The design of an Attitude Control System for the SPS-2 satellite

For the Rate Damping, Sun Acquisition and Sun Pointing Modes

M.M. Oomen

Technische Universiteit Delft

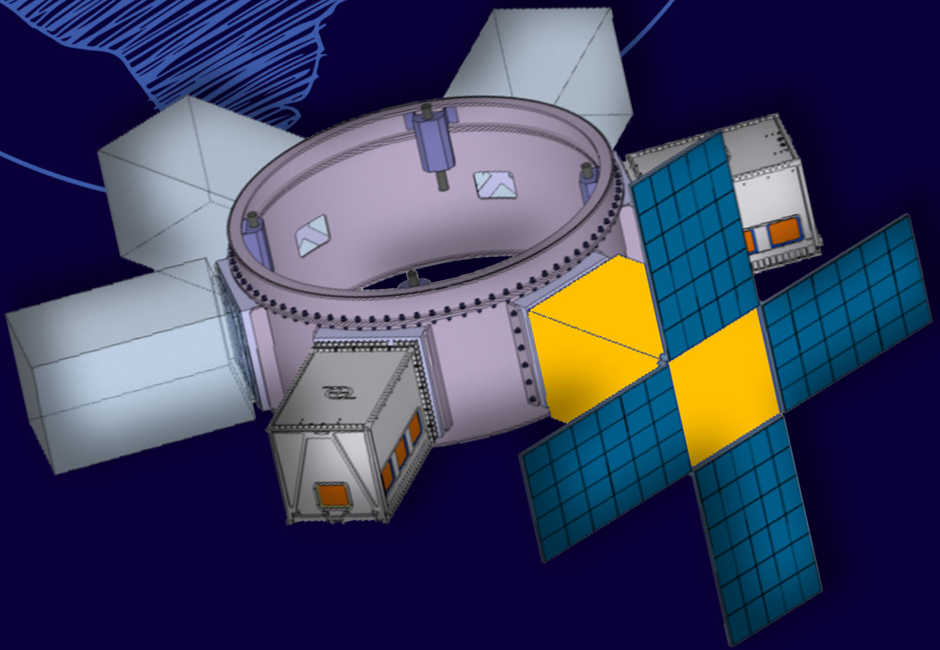

Delft University of Technology

Challenge the future

THE DESIGN OF AN ATTITUDE CONTROL SYSTEM FOR THE SPS-2 SATELLITE

FOR THE RATE DAMPING, SUN ACQUISITION AND SUN POINTING MODES

by

M.M. Oomen

in partial fulfillment of the requirements for the degree of

Master of Science
in Aerospace Engineering

at the Delft University of Technology,
to be defended publicly on Friday August 26th 2016 at 10:00 AM.

Supervisor:	Dr. ir. E. Mooij	
Thesis committee:	Prof. dr. ir. P.N.A.M. Visser,	TU Delft
	Dr. ir. E. van Kampen,	TU Delft
	Ir. L. Meijer,	Airbus Defense and Space the Netherlands
	Ir. M. Visser,	Airbus Defense and Space the Netherlands

This thesis is confidential and cannot be made public until August 26th, 2021.

Delft
University of
Technology

PREFACE

The last couple of months I have been working on a very interesting project: the SPS-2, which is a product being an innovative idea developed at Airbus Defense and Space the Netherlands. The opportunity arose to participate in this project a year and a half ago, which I readily accepted. It has been a good learning experience ever since. The common practice is that a lot of theses are performed within the chair of the faculty. Working on a real mission proposal for Airbus was very exciting. For this, I would like to thank the persons at Airbus who gave me this opportunity.

It is of importance to mention, that this thesis work has been performed in parallel with another graduate student. Prosper Munatsi continued his internship work at Airbus, and worked on the same project. At the start of our thesis work, the work was divided in two parts. My contribution has been the design of the controllers for the Rate Damping, Sun Acquisition and Sun Pointing modes. Furthermore, I have developed the magnetorquer, magnetometer and Sun sensor models. The set-up of the simulator structure, including the verification part, has fully been performed by me. Prosper, on the other hand, developed the Science controller, with the gyro, reaction wheel and star tracker models. The wheel offloading controller has also been developed by Prosper. However, it has not been considered in this thesis work, due to delays from his side, and my work has progressed too much by then. Furthermore, for his own work, Prosper looked into the design of an MEKF. Working together on one project, means that you have overlaps. I have used the gyro and reaction wheel models developed by Prosper, for my thesis work.

I would like to thank my daily supervisors Lex and Martijn at Airbus for their assistance (where-ever it was needed), but also for the joy and laughter during our weekly meetings. I really hope the SPS-2 project will be successful in the future.

At Airbus, Prosper was my daily companion. I would like to thank him for the good and cheerful conversations, but also for thinking with me, when it was required. I wish you all fortune with finishing your thesis work. In a nine month period at Airbus a lot of interns come and go, too many to mention. We have had a great time together, and I hope to see you all again in the near future.

I would also like to thank my supervisor Erwin at Delft University of Technology, for all the help, patience and good will. He will, for sure, miss the most accurate weather prediction the world has ever known, in the form of our biweekly scheduled meeting. The odds were that (almost) every single time I managed to enter his office drained from the rain, even during summertime.

Last, but *certainly* not least, I want to thank my parents for all their support through the years. I hope you also like the report, may it be only for the nice figures.

SUMMARY

This thesis covers the design of the Attitude Control System for the SPS-2 configuration, developed at Airbus Defense and Space the Netherlands. The start of the SPS-2 mission consists of three phases: rate damping, Sun Acquisition and Sun Pointing. The SPS-2 satellite has five available mounting places for different payloads. In the first part of the thesis work, different configurations have been considered, of which three were chosen to be considered further. A choice has been made to develop a simulator in Matlab/Simulink, with inclusion of existing models of the GGNCSim repository. The correctness of the implementation of those models has been verified with ADS, where it has been discovered that there was a sign ambiguity in the aerodynamic model. At this stage, the assumption of modeling the complex SPS-2 geometry as a simple cylinder shape has been verified. The second part of the thesis describes the development of the sensor and actuator models, and the control algorithms which have been designed. The sensor and actuator model error parameters have been obtained from the data sheets of different manufacturers. The models have all been verified. The controllers which have been designed are a nominal B-dot detumble controller in the RD mode, a simple PI controller on the velocity in the SA mode and the quaternion feedback controller in the SP mode. The gains for the different controllers have been selected such that these work for all configurations. The stability has been looked at briefly (gain and phase margins), but no requirements have been imposed on those. In the last part of the thesis, the simulation performance runs have been performed. Here the uncertainties in the error parameters, uncertainties in the satellite geometry, variations in initial conditions and the impact of different actuators have looked at. It has been found that the detumble time is within the requirement of 1.5 orbit, but that the maximum magnetic dipole moment shall be a minimum of 15 Am^2. The SA and SP results show that the Sun is in all cases acquired within 1 orbit and that the time to be actual Sun pointing is less than 10 minutes. The pointing accuracy is within 1.92° for all cases. For both reaction wheels which have been considered, more than enough margin was found for the angular momentum build-up. As such, there is no need to offload the wheels during the first part of the mission. The SunSpace wheel will suffice. The simulation performance runs have shown that the requirements are met, even in presence of the maximum sensor errors. Critical may be the impact of the Earth-albedo error, which has been roughly estimated. More research shall be performed here. The current simulator structure and models which have been developed give a good basis for the further design of the ACS of the SPS-2, but also for other projects.

CONTENTS

SYMBOLS

Table 1: *Symbols (Latin).*

Symbol	**Meaning**
A	frontal area satellite [m^2]
A_{core}	cross-sectional area core [mm^2]
A_{plate}	area plate [m^2]
a	semi-major axis [km] (orbital element)
$\mathbf{B}$	magnetic field vector [T] [3×1]
$\mathbf{b}$	bias [3×1]
C(s)	control output (stability analysis)
C_D	drag coefficient [-]
C_a	absorption coefficient [-]
C_{diff}	diffusive reflection coefficient [-]
C_{spec}	specular reflection coefficient [-]
C_n^m	coefficients gravity field model [-]
$\hat{\mathbf{c}}$	unit vector [3×1]
$\mathbf{e}$	principal/Euler axis [3×1]
$\mathbf{e}$(t)	error signal [3×1]
e	eccentricity [-] (orbital element)
$\mathbf{F}$	force vector [Nm] [3×1]
F_s	sampling frequency [Hz] [3×1]
$\mathbf{f}_{EXT}$	perturbing acceleration vector [m/s^2]
f	modified equinoctial element
G(s)	gain (stability analysis)
$\mathbf{g}^{\mathrm{R}}$	gravity field perturbing acceleration in R-frame [m/s^2] [3×1]
g	modified equinoctial element
g_n^m	Gaussian coefficient magnetic field model (nT)
H(s)	plant (stability analysis)
$\mathbf{H}$	angular momentum vector rigid body [kg m^2/s] [3×1]
$\mathbf{H}_s$	angular momentum vector satellite + wheel system [kg m^2/s] [3×1]
$\mathbf{h}_w$	angular momentum vector wheel [kg m^2/s] [3×1]
h	height cylinder [m]
h	altitude above Earth surface [km]
h	modified equinoctial element
h_n^m	Gaussian coefficient magnetic field model (nT)
I	current [A]
$\mathbf{i}$	unit vector in Cartesian x-direction [3×1]
i	inclination [rad] (orbital element)
i^*	relative inclination spacecraft orbit to geomagnetic field [rad]
$\mathbf{J}$	satellite inertia [kg m^2] [3×3]

Table 1 - *Symbols (Latin), continued from previous page.*

Symbol	**Meaning**
$\mathbf{J}_w$	wheel inertia [kg m^2] [3 × 3]
J_n	coefficients of gravity field model [-]
$J_{n,m}$	coefficients of gravity field model [-]
$\mathbf{j}$	unit vector in Cartesian y-direction [3 × 1]
$\mathbf{K}_p$	proportional gain SA/SP mode
$\mathbf{K}_i$	integral gain SA mode
$\mathbf{K}_d$	integral gain SP mode
$\mathbf{k}$	unit vector in Cartesian z-direction [3 × 1]
k	modified equinoctial element
k_B	gain standard B-dot controller
k_w	gain modified and nominal B-dot controller
L	modified equinoctial element
l_{core}	length core [m]
M_{sat}	mass of the satellite [kg]
M_{core}	magnetization of core [A/m]
$\mathbf{M}$	misalignment matrix
$\hat{\mathbf{M}}$	misalignment matrix including scale factor error
$\mathbf{M}_{EXT}$	sum of all external moments [Nms] [3 × 1]
$\mathbf{m}$	Earth magnetic dipole vector [Am^2] [3 × 1]
$\mathbf{m}$	magnetorquer dipole vector [Am^2] [3 × 1]
m_i	mass body i [kg]
m_{ij}	misalignment terms in misalignment matrix [-]
N_x	angle used to calculated azimuth angle and co-elevation angle of Sun vector
N_y	angle used to calculated azimuth angle and co-elevation angle of Sun vector
$\mathbf{n}^{\mathrm{P}}_{Sun}$	unit vector from Sun towards plate [3 × 1]
$\mathbf{n}^{\mathrm{P}}_{plate}$	unit vector normal to plate [3 × 1]
$\mathbf{n}^{\mathrm{SS}}_{Sun}$	Sun vector in SS-frame [3 × 1]
n	number of windings [-]
P	power consumption [W]
P_n	Legendre polynomials [-]
$P_{n,m}$	Legendre polynomials [-]
$\mathbf{p}^{\mathrm{P}}_{solar}$	solar radiation pressure in P-frame [3 × 1]
$\mathbf{p}_{Sun}$	solar radiation pressure [3 × 1]
p	roll rate [rad/s]
p	modified equinoctial element
$\mathbf{q}$	quaternion [-] [4 × 1]
$\overline{\mathbf{q}}$	vector part of quaternion [-] [3 × 1]
q_4	scalar part of quaternion [-] [1 × 1]
$\delta\mathbf{q}$	error quaternion [-] [4 × 1]
q	pitch rate [rad/s]
$R(s)$	reference signal (stability analyis)
$\mathbf{r}$	position vector [m]
r	yaw rate [rad/s]
r_{core}	radius core [mm]
$\mathbf{S}$	scale factor error [ppm] [3 × 1]

Table 1 - *Symbols (Latin), continued from previous page.*

Symbol	**Meaning**
S_n^m	coefficients gravity field model
$\mathbf{T}$	torque [Nm] [3 × 1]
$\mathbf{T}_{MTQ}$	torque magnetorquer [Nm] [3 × 1]
$\mathbf{T}_W$	torque reaction wheel [Nm] [3 × 1]
T_c	coulomb friction reaction wheel [Nm]
T_f	frictional torque reaction wheel [Nm]
T_m	motor torque reaction wheel [Nm]
T_n	net torque reaction wheel [s]
T_s	sampling time [s]
T_v	viscous coefficient reaction wheel [Nms/rad]
t	time [s]
t_{acc}	acceleration time [s]
t_{coast}	coast time [s]
U	gravitational potential per unit mass [J/kg]
$\mathbf{u}$	arbitrary vector [3 × 1]
$\mathbf{V}$	velocity vector [km/s] [3 × 1]
$V(r, \tau, \delta^*)$	magnetic potential per unit mass [J/kg]
V_{core}	volume core [mm^3]
ΔV	velocity impulse [km/s]
X	axis of Cartesian coordinate system
x	Cartesian coordinate
Y	axis of Cartesian coordinate system
y	Cartesian coordinate
Z	axis of Cartesian coordinate system
z	Cartesian coordinate

Table 2: *Constants.*

Symbol	**Meaning**	**Value**	**Unit**
AU	astronomical unit	$149.59787070 \cdot 10^6$	[km]
c	speed of light	299,792,458	[m/s]
G	gravitational constant	$6.67384 \cdot 10^{-11}$	[m^3/kg/s^2]
R_{Earth}	Earth equatorial radius	$6.371 \cdot 10^3$	[km]
μ	gravitational parameter Earth	$3.986004 \cdot 10^{14}$	[km^3/s^2]

Table 3: *Symbols (Greek).*

Symbol	**Meaning**
α	arbitrary angle [rad]
α	measured angle Sun sensor [rad]
α_{XY}	Sun sensor XY-angle [rad]
β	measured angle Sun sensor [rad]
γ	flight path angle (spherical coordinate) [rad]
δ	geocentric latitude [rad]
δ	elevation [rad]
δ^*	co-elevation [rad]
$\boldsymbol{\eta}$	noise error [3 × 1]
$\boldsymbol{\eta}_{ARW}$	Angular Random Walk [$°/\sqrt{\text{hr}}$] [3 × 1]
$\boldsymbol{\eta}_{RRW}$	Rate Random Walk [$°/\sqrt{\text{s}^3}$] [3 × 1]
Θ	Greenwich Hour Angle [rad]
θ	pitch angle [rad]
θ_{slew}	covered angular distance during whole slew [rad]
θ_{acc}	covered angular distance during acceleration part [rad]
θ_{coast}	covered angular distance during coast part [rad]
$\dot{\theta}$	angular velocity spacecraft [rad/s]
$\ddot{\theta}$	angular rate spacecraft [rad/s^2]
θ	true anomaly [rad]
μ_r	relative permeability [-]
μ_0	permeability of free space [N/A^2]
ρ	atmospheric density [kg/m^3]
τ	time of pericenter passage [s] (orbital element)
τ	geocentric latitude [rad]
τ_n^m	coefficients gravity field model
Φ	solar flux [W/m^2]
ϕ	roll angle [rad]
ϕ	(geocentric) latitude [rad]
ϕ	rotation angle used in rotation matrices [rad]
φ	azimuth angle [rad]
χ	heading angle [rad]
$\boldsymbol{\Xi}(\mathbf{q})$	mathematical operator [4 × 3]
ξ_m	inclination of spacecraft orbit to geomagnetic plane [rad]
ψ	yaw angle [rad]
Ω	right ascension of ascending node [rad] (orbital element)
$\boldsymbol{\Omega}(\boldsymbol{\omega})$	mathematical operator [4 × 4]
$\boldsymbol{\omega}_{BI}$	angular velocity of body with respect to I-frame [rad/s]
ω_{cb}	angular velocity central body (Earth) [rad/s]
ω	argument of pericenter [rad] (orbital element)
ω_W	angular velocity wheel [rad/s]
$\mathcal{V}$	illumination factor
$\boldsymbol{\mathcal{V}}$	nonlinearity error [3 × 1]

Table 4: *Special notations.*

Symbol	Meaning
$\mathbf{C}_x$	rotation matrix indicating rotation around X-axis [3×3]
$\mathbf{C}_y$	rotation matrix indicating rotation around Y-axis [3×3]
$\mathbf{C}_z$	rotation matrix indicating rotation around Z-axis [3×3]
$\mathbf{C}_{A,B}$	rotation matrix from reference frame B to reference frame A [3×3]
♈	First Point of Aries (at vernal equinox) (reference direction to describe directions) [rad]

Table 5: *Reference frames (superscripts).*

Symbol	Meaning
I	Geocentric non-rotating equatorial reference frame
R	Geocentric rotating equatorial reference frame
V	vertical reference frame
B	body reference frame
P	body-fixed geometric reference frame
MTM	magnetometer reference frame
MTQ	magnetorquer reference frame
SS	Sun sensor reference frame
RW	reaction wheel reference frame
GYR	gyroscope reference frame

ABBREVIATIONS

Table 6: *Abbreviations.*

Abbreviation	
ADS	AOCS Design Software
Airbus DS NL	Airbus Defense and Space the Netherlands
A.N.	Ascending Node
A(O)CS	Attitude (and Orbit) Control System
APE	Absolute Pointing Error
AU	Astronomical Unit
AVUM	Attitude Vernier Upper Module
CIRA	COSPAR International Reference Atmosphere
CoM	Center of Mass
COSPAR	Committee on Space Research
COTS	Commercial off-the-shelf
CPU	Central Processing Unit
EOM	Equations Of Motion
ESA	European Space Agency
FoV	Field of View
GGNCSim	Generic Guidance Navigation and Control Simulator Environment
GYR	gyroscope
IGRF	International Geomagnetic Reference Field
IOD	In Orbit Demonstration
IOV	In Orbit Validation
MJD	Modified Julian Date
MoI	Moment of Inertia
MTM	magnetometer
MSIS	Mass Spectrometer and Incoherent Scatter Data
MTQ	magnetorquer
NLRMSISE	US Naval Research Laboratory 'MSIS' through Exosphere
OBC	Onboard Computer
RD	Rate Damping
RW	reaction wheel
SA	Sun Acquisition
SDP	Sensor Data Processing
SP	Sun Pointing
SPS	Stackable Platform Structure
SS	Sun sensor
SVM	Service Module

Chapter 1
INTRODUCTION

This chapter will introduce the thesis work. The structure of this chapter is as follows. First, some background information will be given about the SPS-2 project. Section 1.2 presents the problem statement, the research question and the research objective. Finally, the outline of the report is discussed in Section 1.3.

1.1 Background

Since a couple of years there has been a significant increase in the number of nano/microsatellites, which need a launch, and it is expected that the demand will only grow in the future, see Figure 1.1. Current projections indicate that around 3,000 satellites will require a launch from 2016 through 2022 (SpaceWorks, accessed at 20 June '16).

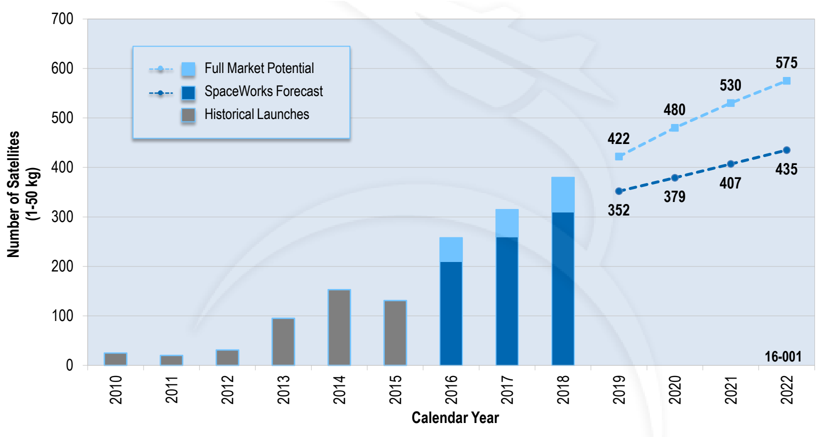

Figure 1.1: *Nano/Microsatellite launch history and forecast (1 - 50 kg) (SpaceWorks, accessed at 20 June '16).*

Airbus Defense and Space the Netherlands answers this demand through an innovative structural product: a small cylinder located between the primary passenger and its adapter, allowing for low-cost launch of small satellites. The structure is named the Stackable Platform Structure (SPS). The product family consists out of four products, evolving from a simple nano/microsatellite dispenser to a fully-functional satellite configuration.

The SPS-1 version is currently in development/production and serves mainly as a technology demonstrator. The structural ring allows for six payloads to be attached, up to 30 kg each. Once in orbit, all SPS payloads are separated from the structural ring. The structural ring itself is passivated in the atmosphere together with the upper stage of the VEGA rocket.

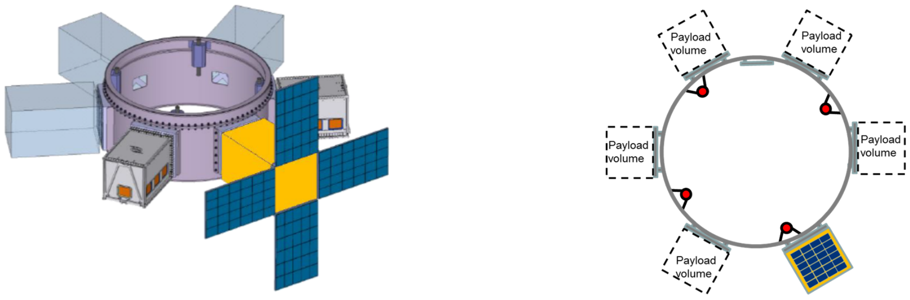

Figure 1.2: *Schematic drawings of the SPS-2 satellite from the preliminary design phase, from (Cruijssen and Hobijn, 2015).*

The follow-up in the family is the SPS-2 satellite, see Figure 1.2 for an illustration. The main difference is that the SPS-2 has a service-module (SVM) package, which allows for In-Orbit Demonstration (IOD) and In-Orbit Validation (IOV) of novel technologies. As the SVM occupies one place, five remaining places are left for either nano/microsatellites, Quadpacks$^{\text{TM}}$ (developed by ISIS) or IOD payloads. Once the SPS-2 satellite is brought into orbit, the nano/microsatellites are detached and the Quadpacks$^{\text{TM}}$ will release four Cubesats each. The IOD payloads remain attached to the structural ring. Note that different payload configurations are possible. The SVM provides power generation, control and distribution, data handling, communications with ground and payloads, thermal control and attitude control for the full satellite structure.

The SPS-2 main mission characteristics are as follows. The orbit is a 350 × 850 km orbit, with an inclination of between 94 and 99 degrees. The operation lifetime will be a maximum of 12 months. The first flight is targeted in 2018. In Chapter 2, the SPS-2 project will be described in more detail. The mission requirements, together with the project constraints, are listed in Section 6.1.

After separation of the launcher upper stage, the SPS-2 satellite will be left with small angular rates. These shall be reduced in the Rate Damping mode (RD), after which a Sun Acquisition (SA) slew maneuver shall be performed, followed by a Sun Pointing (SP) slew maneuver. The design of the Attitude Control System (ACS) for these control modes will be considered in this thesis work.

1.2 Problem statement, research question and objective

In this section the problem statement, the research question and the research objective are addressed. The problem statement gives the purpose of the thesis work. The research question helps to answer the problem statement. The research objective gives an accurate description of the specific actions that have to be performed to answer the research question.

The problem statement is as follows:

PS *For the SPS-2 concept definition study of Airbus DS NL, a preliminary design of the ACS shall be developed to demonstrate that the SPS-2 satellite can autonomously detumble after launcher separation and subsequently get Sun Pointing, whilst being compliant to the requirements and taking into account the limitations enforced by Airbus.*

The research question is as follows:

RQ *Which controllers shall be used in combination of the preselected set of sensors and actuators, to meet the SPS-2 requirements for the detumble and SA & SP control, given the different configurations to be considered, limitations and uncertainties, and what is the performance of the overall system?*

The research question can be split up into the following sub-questions.

- **SQ1** What are the critical design drivers?
  - **SQ1.1** Which configurations result in the minimum performance?
  - **SQ1.2** What sensor and actuator errors have the largest impact on the system?
  - **SQ1.3** What is the impact on the performance when selecting different actuators?
- **SQ2** What control algorithms shall be used for the different modes?
  - **SQ2.1** What are the minimum stability margins (gain and phase margins) for the different controllers?
  - **SQ2.2** Are the controllers sufficiently robust against changes in configurations and uncertainties in the model parameters?
  - **SQ2.3** Is it possible to use one set of gains for all configurations?
- **SQ3** What is the performance during the detumble mode?
  - **SQ3.1** What is the maximum time to detumble?
  - **SQ3.2** What are the maximum remaining angular rates at the end of the detumble mode?
  - **SQ3.3** What is the maximum energy consumption?
- **SQ4** What is the performance during the SA and SP modes?
  - **SQ4.1** What is the maximum time to acquire the Sun?
  - **SQ4.2** What is the maximum time to be Sun pointing?
  - **SQ4.3** What is the minimum pointing accuracy?
  - **SQ4.4** What is the maximum energy consumption?
  - **SQ4.5** Is it necessary to off-load the wheels during the SA and SP slews, and if so, what shall be the frequency of wheel off-loading?

The research objective is as follows:

RO *The objective is to develop a simulator with all relevant ACS components, including the verification of the implemented models and a stability analysis, to perform the verification test-runs to verify whether the requirements for the detumble, SA and SP mode can be met for the SPS-2 mission in presence of the uncertainties.*

The research objective can be split into the following sub-goals:

- **RO1** For each mode a controller shall be designed.
  - **RO1.1** The gain shall be selected such that it works for all configurations.
  - **RO1.2** To analyze the stability of the controller, the gain and phase margins of the control algorithms shall be looked at.
  - **RO1.3** To show the robustness of the ACS, the different configurations, uncertainties in mass distributions and the uncertainties in the model parameters shall be looked into.
- **RO2** In the development of the simulator architecture, the spacecraft state and environment shall be modeled, together with the related ACS components.
  - **RO2.1** The spacecraft environment shall be modeled such that the relevant disturbances are taken into account. A selection of which models implemented in the simulator to use shall be made. The correct implementation of those models shall be verified.
  - **RO2.2** The ACS components include the sensors/actuators/control algorithms. These models shall be developed, verified and validated (if possible).
  - **RO2.3** If it appears to be necessary, a Kalman filter shall be implemented.
- **RO3** To analyze whether the ACS is compliant with the requirements, simulation verification test runs have to be performed for each mode individually.
  - **RO3.1** To identify the critical design drivers, the simulation verification test runs shall be performed such that the impact of the different contributions is clearly visible.

1.3 Outline report

The structure of the report is as follows. The SPS-2 project details are discussed in Chapter 2. Chapter 3 gives the general background information regarding to orbital mechanics. The simulator architecture, design and verification is discussed in Chapter 4. The sensor and actuator theory is described in Chapter 5. The model implementation is discussed after, including the verification of the models. The controller design for each separate mode is discussed in Chapter 6. The stability of the controller is looked at briefly, at the end of this chapter. The simulation performance runs for the detumble mode are discussed in Chapter 7. The simulation performance runs for the SA and SP modes are discussed in Chapter 8. Finally, the conclusions and the recommendations are presented in Chapter 9.

Chapter 2
SPS-2 PROJECT

This chapter will give some background information for the SPS-2 mission. The structure of this chapter is as follows. In Section 2.1 the control modes for the SPS-2 mission are presented. The mode switching diagram is discussed in Section 2.2. An overview of the sensors and actuators, which will be used in the different modes is given in Section 2.3. The different configurations of the SPS-2 satellite are shown in Section 2.4. Finally, the satellite parameters are presented in Section 2.5.

2.1 Modes

The following control modes have been identified in the preliminary design phase (Cruijssen and Hobijn, 2015):

- *Rate Damping* (RD) mode: after separation of the SPS-2 satellite from the launcher upper stage, the satellite will be left with angular rates (up to 1 deg/s). These angular rates shall be reduced towards 0 deg/s. Nonzero remaining angular rates will result in a higher required angular momentum capacity of the reaction wheel.
- *Sun Acquisition* (SA) mode: the objective is to acquire the Sun direction. Two consecutive slews of 360° are performed, after which the Sun shall be acquired. This may not be true in eclipse conditions.
- *Sun Pointing* (SP) mode: after the Sun direction has been acquired, a slew will be performed to get Sun pointing with an accuracy of $< 5°$.
- *Science* (SC) mode: this mode supports the payloads attached to the SPS-2 structure. For this, high accuracy pointing will be required. This control mode is discussed by (Munatsi, 2016a).

2.2 Mode Switching Diagram

To switch from one mode into another, the satellite shall comply to certain conditions. To give a clear overview of the mode switching possibilities, a mode switching diagram is used. The mode switching diagram structure has been constructed based on the project requirements, as described in Section 6.1. The resulting mode switching diagram is shown in Figure 2.1. The description of the sub modes is given in Table 2.1. The description of the symbols is given in Table 2.2. A detailed description will be given now.

At start of the mission, after separation of the launcher upper stage, the SPS-2 satellite is left with small angular rates ($\leqslant 1$ deg/s). The objective of the RD mode is to reduce these angular rates towards 0 deg/s (mode 1). When the norm of the measured rate is below 0.05 deg/s, the satellite will enter the SA mode (mode 2). This 0.05 deg/s was selected in the preliminary design phase because it was found to provide sufficient margin for the remaining angular momentum capacity of the reaction wheel. When it appears (in a later stage) that the remaining angular rates are too high, this condition shall be redefined.

In the SA mode, the objective is to acquire the Sun direction. To do so, a slew of 360 deg will be performed about one of the spacecraft axis (perpendicular to the solar panel). When the Sun has not been acquired after the full slew, another slew will be performed about the other axis (mode 3). One of the constraints (described in Section 6.1) is that no eclipse information is available. As such, it might be that more than 2 slews are required to acquire the Sun direction in case of an eclipse.

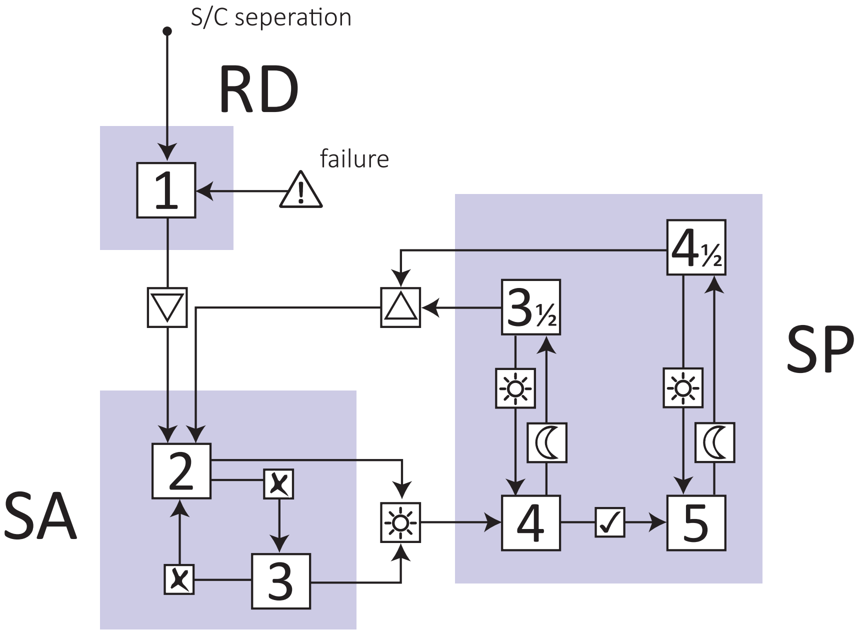

Figure 2.1: *Mode switching diagram. RD = Rate Damping mode, SA = Sun Acquisition mode and SP = Sun Pointing mode.*

When the Sun is in the field of view (FoV), the spacecraft enters the SP mode (mode 4). The objective here is to accurately (< 5 deg) point the satellite towards the Sun. When this requirement is met, mode 5 has been reached. When no Sun vector measurements are obtained in one of these modes, the satellite falls back into modes $3\frac{1}{2}$ or $4\frac{1}{2}$. The last Sun vector measurement is then propagated based on measured angular rates of the spacecraft. When the last Sun vector measurement is more than 1 hr ago (longer than the maximum eclipse duration), the satellite falls back into the SA mode (mode 2).

Table 2.1: *Description sub-modes in the mode switching diagram.*

Mode	**Description**
1	rate damping
2	slew Sun Acquisition (Z-axis) (smallest inertia)
3	slew Sun Acquisition (Y-axis)
4	slew Sun Pointing
5	stable Sun Pointing
$3^1/_2$ and $4^1/_2$	slew Sun Pointing (without Sun vector measurements)

Table 2.2: *Description symbols in the mode switching diagram.*

Symbol	Description
∇	the norm of the measured rate is below 0.05 deg/s
☼	the Sun vector is in the FoV
χ	the SA slew has been finished, but the Sun vector has not been acquired. Continue to the next SA slew.
✓	the satellite is SP
☾	currently no Sun vector measurement
Δ	no Sun vector measurement for >1 hr, return to SA mode

2.3 Sensor and Actuator Baseline

Table 2.3 gives an overview of the sensor and actuators which will be used in the different modes. The modes have been described in Section 2.1.

Table 2.3: *Sensor and actuator baseline for the SPS-2 project. The symbol ○ stands for wheel-offloading.*

Unit	Quantity	RD	SA + SP	SC
magnetorquer	3	✓	○	○
magnetometer	1	✓	○	○
Sun sensor	1		✓	
reaction wheel	3		✓	✓
gyroscope	3	✓	✓	✓
star tracker	1			✓

The magnetorquer will be used to detumble the satellite after separation. The detumble control algorithm makes use of the magnetic field measurement and the spacecraft rate. this requires a magnetometer and a gyroscope. A minimum of three magnetorquers is required for three-axis attitude control. However, as the torque exerted is perpendicular to the magnetic field, no full 3-axis attitude control will be available.

After the detumble mode, the satellite will make several slew maneuvers to acquire and subsequently point towards the Sun. These slews are performed using reaction wheels. A minimum of three reaction wheels is required to enable full 3-axis attitude control. The spacecraft rate is measured with the gyroscope.

The magnetorquers will also be used to offload the wheels. Due to external disturbances, the angular momentum of the reaction wheels will increase. To prevent the wheels from being saturated, these must be offloaded on a regular basis. The wheel offload strategy (including the associated controller) is discussed by (Munatsi, 2016a). In this thesis work, it will only be investigated whether it is necessary to offload the wheels during the SA and SP slews.

As a final remark, note that the science mode is considered by (Munatsi, 2016a). As such, the star tracker will not be considered in this thesis work.

2.4 SPS-2 Satellite Geometry

The SPS-2 project is a non-recurring effort to design a platform, which is compatible with large variety of payloads. This thesis shall address the different payload configurations. In the future, the goal is to make the SPS-project a recurring one. This thesis shall provide the groundwork for those projects. It shall be investigated whether the controller is sufficiently robust against changes in the configuration. Which configurations will be considered in this thesis work is described here.

Please note that the purpose of this work is *not* to find optimal geometrical orientation out of the cases. The goal is to show that for each configuration the requirements can be met.

Several possible payload configurations are shown in Figure 2.2. Those payload configurations meet the regulations of the launcher, which has set a constraint on the center of mass location. The range envelope is ±30 mm radially (most important) and ±30 mm longitudinally (estimate). As such, no cases have been considered with highly non-symmetrical mass distributions. Note that this constraint is only applicable for the launch configuration. In orbit the solar panels will deploy, the Cubesats are released and the Microsats are detached. That situation is depicted in Figure 2.2.

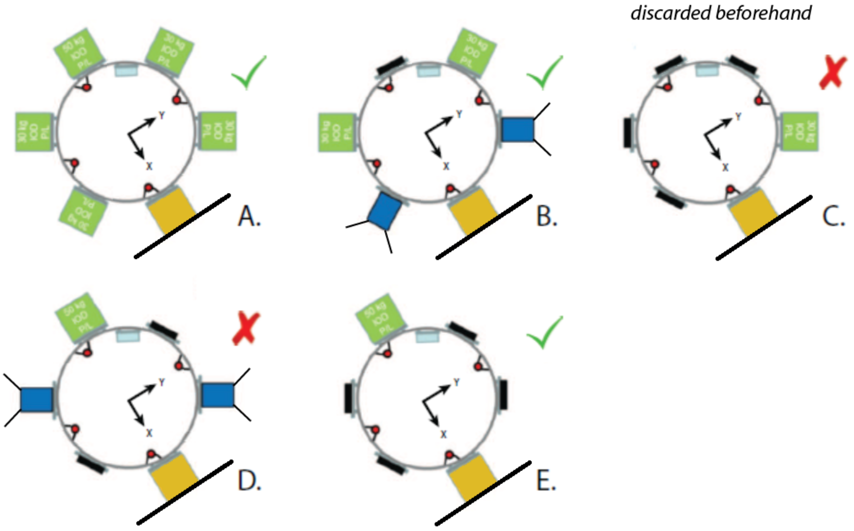

Figure 2.2: *A schematic overview of several different SPS-2 satellite configurations (free-flying configuration). Shown are the SVM with the deployed solar panels (yellow), IOD units (green), empty Quadpacks^{TM} (blue) and empty spots of the Microsats.*

A description of the different configurations is given in Table 2.4.

Table 2.4: *Description of the different configurations.*

Design	Description
A	The worst-case situation, i.e., the situation with the maximum mass.
B	In this case the satellite has a small non-symmetrical mass distribution.
C	In this case the satellite has a highly non-symmetrical mass distribution.
D	In this case the satellite has a small non-symmetrical mass distribution.
E	In this case all the masses are placed along the X-axis.

The configurations which will be selected to be investigated further shall be unique and shall represent extreme cases. In this manner, the robustness of the controller can be shown. Furthermore, the cases need to be realistic. If a better payload placement exists, the option shall therefore be discarded.

Based on these criteria, it has been decided to only consider configurations A, B and E. Configuration C was discarded beforehand, because a better payload placement exists (configuration E). Configuration D is not unique, as it is a combination of configurations B and E.

Apart from the different payload configurations described here, there is an uncertainty in the location of the center of mass (CoM) and the moment of inertia (MoI) for each configuration. These uncertainties will be addressed further in Section 7.3.1.

2.5 SPS-2 Satellite Parameters

In this section the SPS-2 parameters will be discussed which are relevant for this thesis work. The parameters have been obtained from the reference documentation of the preliminary design stages (Cruijssen and Hobijn, 2015) (Munatsi, 2016b).

Figure 2.3 shows the SPS-2 satellite structure, with the associated axis orientation.

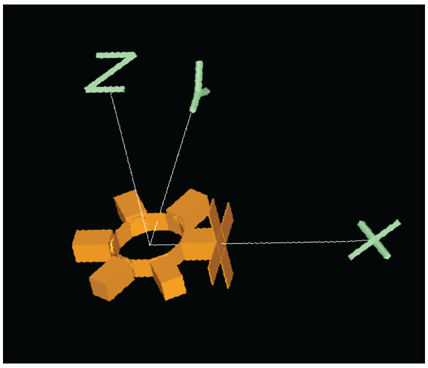

Figure 2.3: *A schematic drawing of the SPS-2 satellite (configuration A).*

The satellite properties are as follows. The radius of the inner ring is 937 mm with a height of 500 mm. The dimensions of the payload volumes and the SVM are 300×300×500 (w×h×l) mm^3. The mass of the inner ring is assumed to be 50 kg. The mass of the SVM and a IOD payload are 30 kg each. The mass of an empty Quadpack$^{\text{TM}}$ is 7 kg.

The resulting CoM and the MoI tensors for the different configurations are listed in Table 2.5.

Table 2.5: *The CoM and MoI matrices for the different configurations (XYZ-frame).*

configuration	**CoM (m)**	**MoI (kg m^2)**	**mass (kg)**
A	$\begin{bmatrix}+0.00962\\-0.02531\\-0.07521\end{bmatrix}$	$\begin{bmatrix}61.29 & +2.854 & -5.335\\+2.854 & 95.55 & -9.18\\-5.335 & -9.18 & 51.35\end{bmatrix}$	250.1
B	$\begin{bmatrix}+0.06789\\-0.0105\\-0.0822\end{bmatrix}$	$\begin{bmatrix}48.45 & -0.414 & -3.064\\-0.414 & 70.54 & -7.636\\-3.064 & -7.636 & 35.1\end{bmatrix}$	174.1
E	$\begin{bmatrix}+0.07842\\-0.01405\\-0.07541\end{bmatrix}$	$\begin{bmatrix}50.03 & -1.528 & -7.733\\-1.528 & 56.3 & -7.396\\-7.733 & -7.396 & 17.52\end{bmatrix}$	130.1

There are some other relevant satellite parameters, which are in particular useful for the calculation of the disturbance torques acting upon the satellite. These will be given now. The residual dipole moment is estimated to be 0.2 Am^2. The drag coefficient C_D is 2 and the specular reflection coefficient C_{spec} is 0.25. The diffuse reflection coefficient C_{diff} is 0 and the absorption coefficient C_a is 0.75.

Chapter 3
ORBITAL MECHANICS

The structure of the chapter is as such. Section 3.1 describes the state variables. The reference frames are discussed in Section 3.2. The theory of transformations is discussed in Section 3.3. How the different reference frames can be transformed into each other, is shown in Section 3.4. The dynamic and kinematic equations of motion are described in Section 3.5. The background theory of the relevant environmental models is discussed in Section 3.6. The Two-Body problem is discussed briefly in Section 3.7. Section 3.8 describes the perturbation analysis, in which the main perturbations relevant for the SPS-2 project are identified.

3.1 State Variables

3.1.1 Position and Velocity

The position and motion of a spacecraft can be expressed in different manners. This section gives an overview of several possibilities.

Cartesian position and velocity

Using Cartesian components, the position and velocity can be expressed with respect to the inertial geocentric frame. The position is defined with $(x(t), y(t), z(t))$ and the velocity by $(\dot{x}(t), \dot{y}(t), \dot{z}(t))$. See Figure 3.5 for an illustration. As the equations of motion are expressed in Cartesian components, these coordinates allow for stable and easy integration. Furthermore, the environmental models are usually expressed in Cartesian coordinates as well, such that these allow for easy inclusion.

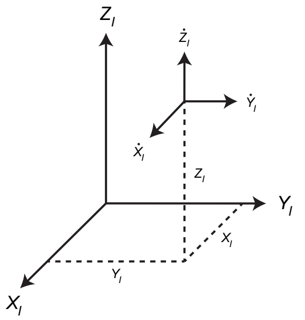

Figure 3.1: *Cartesian coordinates, which are defined in the I-frame.*

Spherical position and velocity

Using spherical components, the position and velocity are expressed with respect to the Geocentric rotating equatorial reference frame (R-frame). Figure 3.2 gives an illustration. The advantage of this set is that the state is directly physically interpretable. However, as these coordinates are in particular useful for re-entry problems, these will not be considered further.

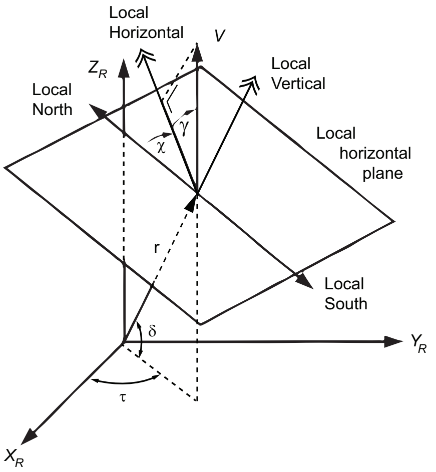

Figure 3.2: *Spherical coordinates in the rotating geocentric frame. Adapted from (Wakker, 2010).*

Classical orbital elements

The position and velocity can also be expressed in the classical orbital elements (also known as Kepler elements). See Figure 3.3 for an illustration. The advantage of classical orbital elements is that these are constant for a unperturbed orbit (except for τ, which links time with the angle θ). The orbital elements vary slightly for a perturbed one.

The disadvantage of using Keplerian elements is that when the eccentricity e and/or the orbital inclination i tend towards zero, the orbital elements Ω and ω become indeterminate. The equations of motion may become singular. As such, the classical orbital elements will not be used for orbit propagation. The use of classical orbital elements is in particular useful for defining the orbit or for the visualization of the results.

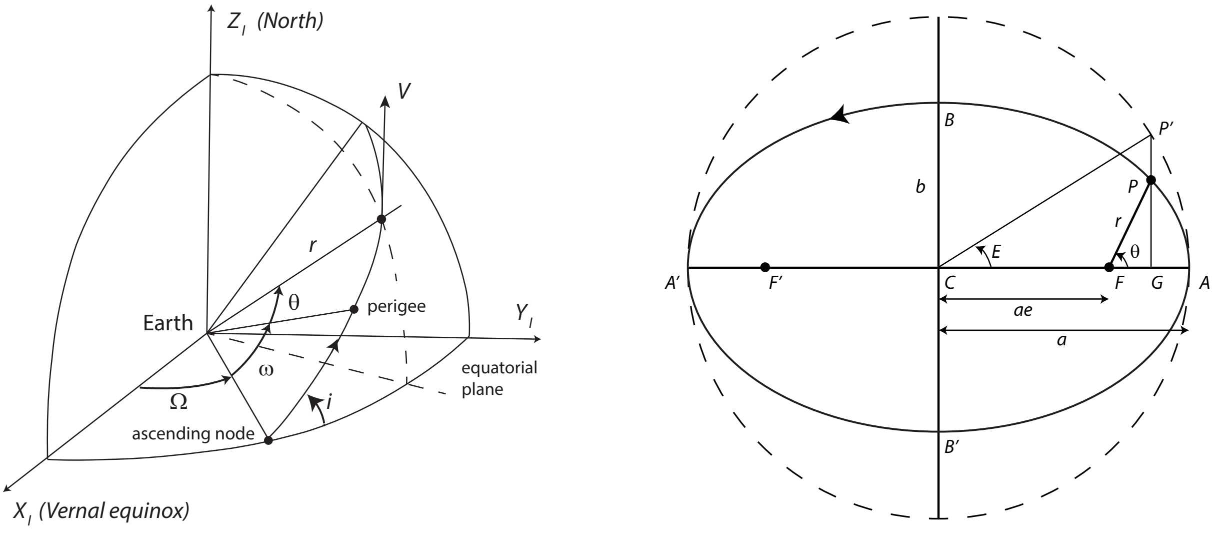

Figure 3.3: *Left: definition of the orbital elements. Adapted from (Wakker, 2010). Right: geometry of an elliptical orbit. Adapted from (Wakker, 2010).*

3.1.2 Attitude Representation

Classical Attitude Angles

The classical attitude angles are the roll angle ϕ, the pitch angle θ and the yaw angle ψ. These can define the attitude w.r.t. the inertial space, but also to another reference frame. These angles form a set of Euler angles. It is important in which order the transformation is executed, and about which axis (Mooij, 2011). Each combination results in a different form of a rotation matrix. The 3-2-1 sequence is commonly used in the aerospace applications. It consists of a yaw rotation around the Z-axis, followed by a pitch rotation about the Y-axis and concluded by a roll rotation around the X-axis (Mooij, 2011).

Quaternions

Instead of using Euler angles, the quaternion (also known as Euler parameters) representation of the attitude can be used. A quaternion is constructed with the principal axis (or Euler axis) $\mathbf{e} = [e_1 \;\; e_2 \;\; e_3]^{\mathrm{T}}$ and a rotation angle θ around that axis. Euler's eigenaxis rotation theorem states that *'by rotating a rigid body about an axis that is fixed to the body and stationary in an inertial reference frame, the rigid body attitude can be changed from any given orientation to any other orientation. Such an axis of rotation, whose orientation relative to both an inertial reference frame and the body remains unchanged throughout the motion, is called the Euler axis or eigenaxis'* (Wie, 2008).

A quaternion $\mathbf{q}$ has a vector part $\vec{\mathbf{q}}$ and a scalar part q_4 (Wie, 2008):

$$\mathbf{q} = \begin{bmatrix} \vec{\mathbf{q}} \\ q_4 \end{bmatrix} = \begin{bmatrix} \mathbf{e}\sin(\theta/2) \\ \cos(\theta/2) \end{bmatrix} \tag{3.1.1}$$

where $\vec{\mathbf{q}} = [q_1 \;\; q_2 \;\; q_3]^{\mathrm{T}}$. Note that the Euler parameters are not independent from each other. The quaternions for attitude representations are unit quaternions, such that its norm is $\|\mathbf{q}\| = 1$. Mathematical rules with regard to quaternions are described in Appendix A.

Trade-off

There are some disadvantages of working with the set of Euler angles. It might be that singularities occur at the second rotation. For the kinematic equations of motion, describing the attitude in terms of Euler angles is not ideal, as these are described with trigonometric functions. This comes at cost of the computational efficiency.

Unlike Euler angles, the quaternions do not contain any trigonometric functions. Furthermore, no singularities can occur. The kinematics of a spacecraft can also be expressed in terms of quaternions. This makes them very useful and efficient for computational purposes. Furthermore, the quaternion has an advantage is size (4×1 against 3×3 with the Euler angles). Multiplications involving quaternions are therefore faster. As such, the quaternions will be used to represent the spacecraft attitude.

3.1.3 Angular Rate Representation

The angular rate of the spacecraft body is here defined as the rotational velocity of the body frame with respect tot the inertial frame, expressed in components along the body axis. The angular rate $\boldsymbol{\omega}$ is defined by the roll rate p, the pitch rate q and the yaw rate r (Ellenbroek et al., 2015).

3.2 Reference Frames

Reference frames are used to describe the position, velocity and forces acting on the spacecraft relative to a fixed point. It depends on the type of problem which reference frame is most convenient to use. Different kinds of reference frames will be discussed here.

Geocentric non-rotating equatorial reference frame

In a Geocentric reference frame the motion is described with respect to the Earth's center of mass. This reference frame is a suitable choice when a satellite orbits Earth. The Geocentric non-rotating equatorial reference frame is indicated with the index I. As the name suggests, the XY-plane coincides with the equatorial plane. The X-axis points towards the Vernal equinox ♈ at 12:00 Terrestrial Time on 1 January 2000, the Z-axis points towards the Earth geometric North pole and is aligned with the rotation axis of the Earth. The Y-axis complements the right-hand-rule. See Figure 3.4 for an illustration.

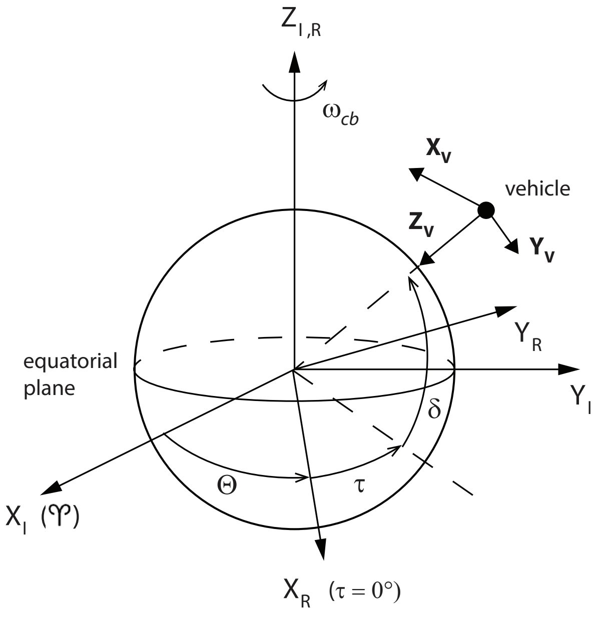

Figure 3.4: *Relation between the inertial and rotating Geocentric frames (index I and R, respectively) and the vertical frame (index V). Here* Θ *is the Greenwich Hour Angle,* τ *is the Geocentric longitude,* δ *is the Geocentric latitude and* ω_{cb} *is the angular rate of the Earth around the Z-axis of the inertial Geocentric frame. Adapted from (Ellenbroek et al., 2015).*

Geocentric rotating equatorial reference frame

The Geocentric rotating equatorial reference frame (index R) is fixed to the Earth. The difference with the Geocentric non-rotating reference frame is the definition of the X- and Y-axis. The X-axis now intersects the equator at zero longitude (Greenwich). Again, the Z-axis points towards the Earth geometric North pole and is aligned with the rotation axis of the Earth. The Y-axis complements the right-hand-rule. See Figure 3.4 for an illustration.

Vertical reference frame

With the vertical reference frame (V-frame), the origin is at the vehicle center of mass. The Z-axis is normal to the Earth surface and positive pointing down. The X-axis lies in the meridian plane and points north. The Y-axis is obtained with the right-hand-rule and by definition positive to the east. See Figure 3.4 for an illustration.

Body-fixed geometric reference frame

The body-fixed geometric reference frame (P-frame) is fixed to the satellite structure. The origin lies in the geometrical center of the ring. The positive X-axis is defined along the central axis of the Service Module. The X-axis is positioned along the longitudinal axis of the satellite. The Y-axis complements the right-hand-rule. See Figure 3.5 for an illustration.

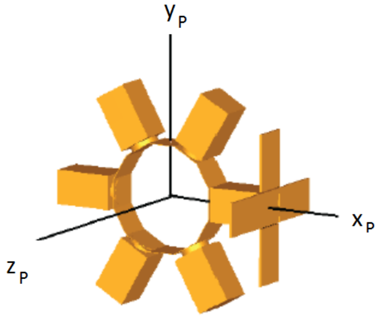

Figure 3.5: *Body-fixed geometric reference frame (P-frame).*

Body reference frame

The body-frame (B-frame) is similar to the P-frame, except that the origin of the B-frame lies in the center of mass of the satellite.

Equipment reference frames

All sensors and actuator frames are defined with respect to the P-frame. Apart from the Sun sensor reference frame, the reference frames are identical. The names of the individual frames are listed in Table 5.

The axis orientation of the Sun sensor is as follows. The Sun sensor Z-axis points towards the X-axis of the P-frame, the X-axis points towards the Y-axis of the P-frame and the Z-axis points towards the Y-axis of the P-frame.

3.3 Transformations

To express the components of one reference frame in another reference frame, transformation matrices are used. It is assumed in the following that the origin of the different reference frames coincide.

The direction transformation matrices are defined as such:

$$\mathbf{C}_x(\phi) = \begin{bmatrix} 1 & 0 & 0 \\ 0 & \cos\phi & \sin\phi \\ 0 & -\sin\phi & \cos\phi \end{bmatrix} \quad \mathbf{C}_y(\phi) = \begin{bmatrix} \cos\phi & 0 & -\sin\phi \\ 0 & 1 & 0 \\ \sin\phi & 0 & \cos\phi \end{bmatrix} \quad \mathbf{C}_z(\phi) = \begin{bmatrix} \cos\phi & \sin\phi & 0 \\ -\sin\phi & \cos\phi & 0 \\ 0 & 0 & 1 \end{bmatrix}$$

where ϕ is the angle of rotation. Here $\mathbf{C}_x$, $\mathbf{C}_y$ and $\mathbf{C}_z$ are the rotations about the X-, Y- and Z-axis of a particular frame (Wie, 2008).

A rotation from an arbitrary frame B to frame A can always be decomposed in a number of sequential unit axis rotations. A transformation from frame B to frame A is usually written as $\mathbf{C}_{A,B}$ or $\mathbf{C}_B^A$. Several powerful relations exists between the DCM matrices. Given that the angles of rotation are known, any rotation can be expressed with a maximum of three subsequent rotations.[1] A DCM matrix preserves the length of a coordinate vector and the angles between the vectors and the product of two transformation matrices results in another transformation matrix. Each of the transformation matrices is orthonormal, and the product is orthonormal again. As such, it holds true that:

$$\mathbf{C}_{A,B} = \mathbf{C}_{B,A}^{-1} = \mathbf{C}_{B,A}^{\mathrm{T}} \tag{3.3.1}$$

As an example, consider a rotation sequence about the positive X-axis, the negative Y-axis and the negative Z-axis to rotate from the B-frame to the A-frame. This can be represented as:

$$\mathbf{C}_{A,B} = \mathbf{C}_z(-\phi_3)\mathbf{C}_y(-\phi_2)\mathbf{C}_x(+\phi_1) \tag{3.3.2}$$

where the order of rotations is defined from right to left. The inverse is now given by:

$$\mathbf{C}_{B,A} = \mathbf{C}_x(-\phi_1)\mathbf{C}_y(+\phi_2)\mathbf{C}_z(+\phi_3) \tag{3.3.3}$$

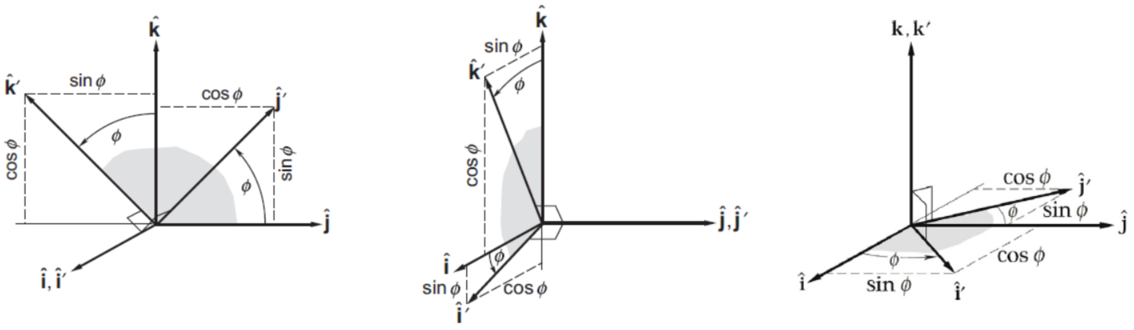

Figure 3.6: *Illustration of $\mathbf{C}_x$, $\mathbf{C}_y$ and $\mathbf{C}_z$ rotations (Curtis, 2010), where $\hat{\mathbf{i}}$, $\hat{\mathbf{j}}$ and $\hat{\mathbf{k}}$ are the unit vectors in the X-, Y- and Z- directions.*

3.4 Transformation between Reference Frames

In Section 3.2 different reference frames were shown. How to transform between these reference frames is discussed here.

---

[1] If not, more rotations could be necessary.

Geocentric rotating equatorial reference frame

The transformation from the rotating (R-frame) to the inertial Geocentric reference frame (I-frame) can be obtained with:

$$\mathbf{C}_{I,R} = \mathbf{C}_z(-\Theta) = \begin{bmatrix} \cos\Theta & -\sin\Theta & 0 \\ \sin\Theta & \cos\Theta & 0 \\ 0 & 0 & 1 \end{bmatrix} \tag{3.4.1}$$

where Θ is the Greenwich Hour Angle (also known as sidereal time). It can be calculated with:

$$\Theta(t) = 100.4606° + 360.9856473° d \tag{3.4.2}$$

where d is the number of days from 1 January 2000, at 12:00 Terrestrial Time (also referred to as *J2000*) (Montenbruck and Gill, 2000).

Vertical reference frame

The transformation from the V-frame to the R-frame can be obtained with:

$$\mathbf{C}_{R,V} = \mathbf{C}_z(-\tau)\mathbf{C}_y(\pi/2+\delta) = \begin{bmatrix} -\cos\tau\sin\delta & -\sin\tau & -\cos\tau\cos\delta \\ -\sin\tau\sin\delta & \cos\tau & -\sin\tau\cos\delta \\ \cos\delta & 0 & -\sin\delta \end{bmatrix} \tag{3.4.3}$$

where τ is the Geocentric longitude and δ is the Geocentric latitude.

Body reference frame

The transformation from the B-frame to the I-frame in terms of Euler angles ϕ, θ and ψ is as follows (Wie, 2008):

$$\mathbf{C}_{I,B} = \mathbf{C}_1(\phi)\mathbf{C}_2(\theta)\mathbf{C}_3(\psi) = \begin{bmatrix} c_\theta c_\psi & s_\phi s_\theta c_\psi - c_\phi s_\psi & c_\phi s_\theta c_\psi + s_\phi s_\psi \\ c_\theta s_\psi & s_\phi s_\theta s_\psi + c_\phi s_\psi & c_\phi s_\theta s_\psi - s_\phi c_\psi \\ -s_\theta & s_\phi c_\theta & c_\phi c_\theta \end{bmatrix} \tag{3.4.4}$$

The direction cosine matrices can also be parametrized in terms of quaternions. The transformation from the B-frame to the I-frame in terms of the quaternion is as such (Wie, 2008):

$$\mathbf{C}_{I,B}(\mathbf{q}) = (q_4^2 - \vec{\mathbf{q}}^T\vec{\mathbf{q}})\mathbf{I}_{3\times3} + 2\vec{\mathbf{q}}\vec{\mathbf{q}}^T - 2q_4\left[\vec{\mathbf{q}}\times\right] \tag{3.4.5}$$

where:

$$[\vec{\mathbf{q}}\times] = \begin{bmatrix} 0 & -q_3 & q_2 \\ q_3 & 0 & -q_1 \\ -q_2 & q_1 & 0 \end{bmatrix} \tag{3.4.6}$$

Fully written out, Equation (3.4.5) yields:

$$\mathbf{C}_{I,B}(\mathbf{q}) = \begin{bmatrix} 1-2(q_2^2+q_3^2) & 2(q_1q_2+q_3q_4) & 2(q_1q_3-q_2q_4) \\ 2(q_2q_1-q_3q_4) & 1-2(q_1^2+q_3^2) & 2(q_2q_3+q_1q_4) \\ 2(q_3q_1+q_2q_4) & 2(q_3q_2-q_1q_4) & 1-2(q_1^2+q_2^2) \end{bmatrix} \tag{3.4.7}$$

Body-fixed geometric reference frame

The origins of the P-frame and the B-frame are separated by the distance vector towards the center of mass of the satellite. The axis orientation is identical.

Equipment reference frame

All sensors and actuators reference frames are identical to the P-frame, except for the Sun sensor frame. The transformation from the SS-frame to the P-frame is defined as:

$$\mathbf{C}_{P,SS} = \mathbf{C}_y(-\pi/2)\mathbf{C}_z(-\pi/2) = \begin{bmatrix} 0 & 0 & 1 \\ 1 & 0 & 0 \\ 0 & 1 & 0 \end{bmatrix} \tag{3.4.8}$$

3.5 Equations of Motion

In this section the equations of motion are described. These consist of the dynamic equation of motion and the kinematic equation of motion.

3.5.1 Dynamic Equations

The total change in angular momentum of a rigid body about its center of mass is given as (Wie, 2008):

$$\dot{\mathbf{H}} = \mathbf{M}_{EXT} \tag{3.5.1}$$

where $\mathbf{H}$ is the angular momentum vector of a rigid body about its mass center and $\mathbf{M}_{EXT}$ is the sum of all external moments acting on the body about its mass center.

Expressed in the inertial reference frame, the change in angular momentum can be written as:

$$\dot{\mathbf{H}} = \left[\frac{d\mathbf{H}}{dt}\right]_I = \left[\frac{d\mathbf{H}}{dt}\right]_B + \boldsymbol{\omega}_{B/I} \times \mathbf{H} \tag{3.5.2}$$

with $\mathbf{H} = \mathbf{J}\boldsymbol{\omega}_{B/I}$ and $\boldsymbol{\omega}_{B/I}$ being the angular rate of the body with respect to the inertial frame. For now, omitting the subscript in $\boldsymbol{\omega}_{B/I}$, this equation can be rewritten as:

$$\begin{aligned} \dot{\mathbf{H}} &= \left[\frac{d}{dt}(\mathbf{J}\boldsymbol{\omega})\right]_B + \boldsymbol{\omega} \times (\mathbf{J}\boldsymbol{\omega}) \\ &= \left[\frac{d\mathbf{J}}{dt}\right]_B \boldsymbol{\omega} + \mathbf{J}\left[\frac{d\boldsymbol{\omega}}{dt}\right]_B + \boldsymbol{\omega} \times (\mathbf{J}\boldsymbol{\omega}) \end{aligned} \tag{3.5.3}$$

With the assumption that the satellite inertia remains constant, that is $\left[\frac{d\mathbf{J}}{dt}\right]_B = 0$, it can be written that:

$$\mathbf{J}\dot{\boldsymbol{\omega}} + \boldsymbol{\omega} \times (\mathbf{J}\boldsymbol{\omega}) = \mathbf{M}_{EXT} \tag{3.5.4}$$

This equation is called Euler's rotation equation of motion. Note that the identities are expressed in the body-frame.

When the external torques of the reaction wheel and the magnetorquer are included, Euler's rotational equations of motion change to (Wie, 2008):

$$\mathbf{J}\dot{\boldsymbol{\omega}} + \boldsymbol{\omega} \times (\mathbf{J}\boldsymbol{\omega} + \mathbf{h}_W) = \mathbf{M}_{EXT} - \mathbf{T}_W - \mathbf{T}_{MTQ} \tag{3.5.5}$$

where $\mathbf{T}_W = \dot{\mathbf{h}}_W$ is the torque output of the wheels, $\mathbf{h}_W = \mathbf{J}_W\ \boldsymbol{\omega}_{W/B}$ is the wheel angular momentum and $\boldsymbol{\omega}_{W/B}$ is the angular rate of the wheel. Furthermore, $\mathbf{T}_{MTQ}$ is the torque output of the magnetorquer and $\mathbf{M}_{EXT}$ is the external moment acting upon the satellite. All are expressed in the B-frame.

3.5.2 Kinematic Equations

The angular orientation of a spacecraft can be solved with quaternions, given a known initial quaternion and angular rate with respect to the inertial frame. Note that the quaternion representation is $\mathbf{q} = [\vec{\mathbf{q}}\ \ q_4]^T$, as also described in Section 3.1.2.

The kinematic equations of motion are (Wie, 2008):

$$\dot{\vec{\mathbf{q}}} = \frac{1}{2}\left[q_4\ \boldsymbol{\omega} - \boldsymbol{\omega}^{\times}\vec{\mathbf{q}}\right] \tag{3.5.6}$$

$$\dot{q}_4 = -\frac{1}{2}\boldsymbol{\omega}^T\vec{\mathbf{q}} \tag{3.5.7}$$

Again, $\boldsymbol{\omega}$ is the angular rate of the body with respect to the inertial frame. The quaternion and its derivative also relate the body to the inertial frame.

In matrix format one can write:

$$\begin{bmatrix} \dot{\vec{\mathbf{q}}} \\ \dot{q}_4 \end{bmatrix} = \frac{1}{2}\begin{bmatrix} -[\boldsymbol{\omega}\times] & \boldsymbol{\omega} \\ -\boldsymbol{\omega}^T & 0 \end{bmatrix}\begin{pmatrix} \vec{\mathbf{q}} \\ q_4 \end{pmatrix} = \frac{1}{2}\begin{bmatrix} 0 & \omega_3 & -\omega_2 & \omega_1 \\ -\omega_3 & 0 & \omega_1 & \omega_2 \\ \omega_2 & -\omega_1 & 0 & \omega_2 \\ -\omega_1 & -\omega_2 & -\omega_3 & 0 \end{bmatrix}\begin{pmatrix} \vec{\mathbf{q}} \\ \dot{q}_4 \end{pmatrix} = \frac{1}{2}\boldsymbol{\Omega}(\boldsymbol{\omega})\mathbf{q} \tag{3.5.8}$$

Alternatively, Equation (3.5.8) can be written as:

$$\begin{bmatrix} \dot{\vec{\mathbf{q}}} \\ \dot{q}_4 \end{bmatrix} = \frac{1}{2}\begin{bmatrix} q_4\mathbf{I}_{3\times 3} + [\vec{\mathbf{q}}\times] \\ -\vec{\mathbf{q}}^T \end{bmatrix}\begin{pmatrix} \omega_1 \\ \omega_2 \\ \omega_3 \end{pmatrix} = \frac{1}{2}\begin{bmatrix} q_4 & -q_3 & q_2 \\ q_3 & q_4 & -q_1 \\ -q_2 & q_1 & q_4 \\ -q_1 & -q_2 & -q_3 \end{bmatrix}\begin{pmatrix} \omega_1 \\ \omega_2 \\ \omega_3 \end{pmatrix} = \frac{1}{2}\boldsymbol{\Xi}(\mathbf{q})\boldsymbol{\omega} \tag{3.5.9}$$

3.6 Environmental Models

In this section the Earth gravity field, the Earth magnetic field, the solar radiation pressure and the atmospheric density are discussed.

3.6.1 Gravity Field

The gravitational acceleration was shown in Equation (3.7.4). However, it was assumed that the Earth is a perfect sphere with a uniform mass distribution. This is not true. The Earth is flattened and 'pear-shaped': it is not a perfect sphere and its mass distribution is not uniform either. This generates differences in the gravitational acceleration. These offsets can be modeled with gravity-field perturbing accelerations.

The gravitational potential of the Earth U is a function of the geocentric distance r, the geocentric latitude δ and the geographic longitude τ (Capderou, 2005):

$$
\begin{aligned}
U &= -\frac{\mu}{r} + \text{gravity-field perturbing potential} \\
U &= -\frac{\mu}{r}\left[1 + \sum_{n=2}^{\infty}\sum_{m=0}^{\infty}\left(\frac{R_{Earth}}{r}\right)^{n} P_n^m(\sin\delta)\{C_n^m \cos m\tau + S_n^m \sin m\tau\}\right] \\
U &= -\frac{\mu}{r}\left[1 - \sum_{n=2}^{\infty} J_n \left(\frac{R_{Earth}}{r}\right)^{2} P_n(\sin\delta) + \sum_{m=1}^{\infty} J_n^m \left(\frac{R_{Earth}}{r}\right)^{n} P_n^m(\sin\delta)\left\{\cos\left(m(\tau-\tau_n^m)\right)\right\}\right]
\end{aligned}
\tag{3.6.1}
$$

where:

$$
\begin{aligned}
C_n^m &= J_n^m \cos\tau_n^m & \qquad J_n &= J_n^0 = -C_n^0 \\
S_n^m &= J_n^m \sin\tau_n^m & \qquad P_n(\sin\delta) &= P_n^0(\sin\delta)
\end{aligned}
$$

In this equation, μ and R_{Earth} are the Earth' gravitational parameter and radius. The C_n^m, S_n^m, J_n^m and τ_n^m terms are coefficients for the gravity-field model. The model order and degree are denoted with n and m respectively. The $P_n^m(\sin\delta)$ terms are Legendre polynomials, for which the following expressions hold:

$$P_n(x) = \frac{1}{(-2)^n n!}\frac{\mathrm{d}^n}{\mathrm{d}x^n}(1-x^2)^n \tag{3.6.2}$$

$$P_n^m(x) = \frac{\mathrm{d}^m P_n(x)}{\mathrm{d}x^m}(1-x^2)^{m/2} \tag{3.6.3}$$

$$x = \sin\delta \tag{3.6.4}$$

Finally, the gravity-field perturbing acceleration in the R-frame can be calculated with:

$$\mathbf{g}^{\mathrm{R}} = -\boldsymbol{\nabla}U = -\tfrac{\partial U}{\partial r}\mathbf{u}_r - \tfrac{1}{r}\tfrac{\partial U}{\partial \delta}\mathbf{u}_\delta - \tfrac{1}{r\cos(\delta)}\tfrac{\partial U}{\partial \tau}\mathbf{u}_\tau$$

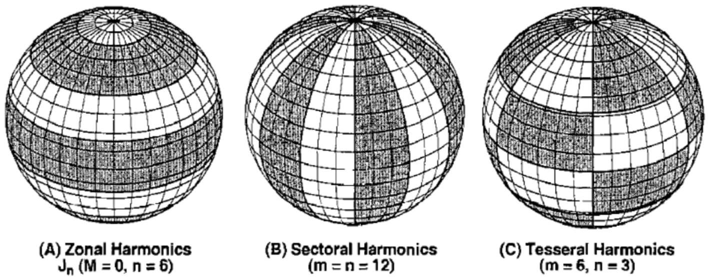
(A) Zonal Harmonics J_n (M = 0, n = 6)
(B) Sectoral Harmonics (m = n = 12)
(C) Tesseral Harmonics (m = 6, n = 3)

Figure 3.7: *Example of zonal harmonics (A), sectoral harmonics (B) and tesseral harmonics (C). White areas represent elevation above a mean spherical surface and black areas represent elevation below a mean spherical surface (Wertz et al., 2009).*

The terms in Equation (3.6.1) represent different gravitational potentials with different mass density distributions. A distinction is made between zonal harmonics, sectoral harmonics and tesseral harmonics:

- terms with $(n \neq 0, m = 0)$ are called zonal harmonics (independent of longitude),
- terms with $m = n \neq 0$ are called sectoral harmonics (independent of latitude),
- and terms with $m \neq n \neq 0$ are called tesseral harmonics. See Figure 3.7 for an illustration.

The accuracy of the gravity field model increases with the higher-order terms. The J_0 term $(n = 0, m = 0)$ represents a spherically symmetric distribution, which was considered up to this point. The J_1 term $(n = 1, m = 0)$ represents the difference in mass between the northern and southern hemispheres. The J_2 term (also referred to as the Earth oblateness) represents the mass distribution of the equatorial bulge and is, by far, the largest of the geopotential terms. Beyond J_2, coefficients becomes small quickly, which can be seen in Table 3.1.

Table 3.1: *Harmonic coefficients J_n for the geopotential, for n up to order 6. The degree m is 0. The data is taken from the GRIM5-C1 model (Capderou, 2005).*

$J_n = -C_{n,0}$	Value (dimensionless)
J_0	1
J_1	0
J_2	+ 1 082.626 220 70 $\times 10^{-6}$
J_3	-2.536 150 69 $\times 10^{-6}$
J_4	-1.619 363 55 $\times 10^{-6}$
J_5	- 0.223 101 38 $\times 10^{-6}$
J_6	+0.540 289 52 $\times 10^{-6}$

3.6.2 Magnetic Field

As with the gravity-field model, also the magnetic field can be modeled as a potential. The magnetic potential is described as follows (Landis Markley and Crassidis, 2014):

$$V(r, \tau, \delta^*) = R_{Earth} \sum_{n=1}^{\infty} \frac{R_{Earth}}{r}^{n+1} \sum_{m=0}^{\infty} \left(g_n^m \cos m\tau + h_n^m \sin m\tau \right) P_n^m(\delta^*) \tag{3.6.5}$$

where r is the geocentric distance, τ is the East longitude from Greenwich, δ^* is the co-elevation and R_{Earth} is the magnetic spherical reference radius. Furthermore, g_n^m and h_n^m

are Gaussian coefficients and the $P_n^m(\delta^*)$ terms are the associated Legendre functions.

The coefficients in Equation (3.6.5) can be found in (Thébault et al., 2015). This document discusses the International Geomagnetic Reference Field (IGRF). The IGRF is a series of mathematical models describing the large-scale internal part of the Earth's magnetic field. Every 5 years an update is provided, because the Earth magnetic field changes constantly. The document gives definitive coefficient values for the past and provides predictions for the coming 5 years. The latest IGRF-model currently available is the IGRF-12 from 2015.

3.6.3 Solar Radiation Pressure

The solar radiation pressure is given by $P_{solar} = {}^{\Phi}\!/_{c}$, where Φ is the solar flux and c is the speed of light. At a distance of 1 AU of the Sun (mean distance Earth to the Sun), the solar flux amounts to $\Phi_{\text{1AU}} \approx 1367$ W/m^2 (Wertz et al., 2009), such that:

$$P_{solar} \approx 4.56 \cdot 10^{-6} \text{ N/m}^2 \tag{3.6.6}$$

To account for the variation in distance to the Sun, the well-known inverse-square law can be applied, resulting in:

$$P_{solar} = 4.56 \cdot 10^{-6} \left(\frac{R_{\text{ 1AU}}}{\|\mathbf{r}_{sat} - \mathbf{r}_{Sun}\|} \right)^2 \tag{3.6.7}$$

where $\mathbf{r}_{sat}$ is the position vector towards the satellite, $\mathbf{r}_{Sun}$ is the position vector towards the Sun and $R_{\text{ 1AU}}$ is the distance of 1 Astronomical Unit.

3.6.4 Atmospheric Density

The atmospheric density varies with altitude. It can be represented by the International Standard Atmosphere. However, the atmospheric density also depends on the solar activity, time, longitude, latitude, the atmospheric composition and even the geomagnetic activity. Modeling the atmospheric density is therefore complex.

CIRA (COSPAR International Reference Atmosphere) provides recommendations for a range of up-to-date semi-empirical models to accurately determine the Earth's upper atmosphere properties (including atmospheric density) above 120 km. The CIRA model baseline is developed by the Committee on Space Research (COSPAR). Several editions of the CIRA models exist. The first edition appeared in 1961, the last (fifth) edition dates from 2012.

The latest version, CIRA-2012 [2], states that the NRLMSISE-00 model is one of the four recommended models currently available. This model is based on a '*very large underlying set of supporting data from satellites, rockets, and radars, with extensive temporal and spatial distribution. It has been extensively tested against experimental data by the international scientific community.* (COSPAR, 2012). A detailed discussion of the NRLMSISE-00 model is given in Appendix B.2.

Other atmospheric density models which will be considered are the CIRA-72 model and the MSIS-86 model, as these are implemented in the simulators which are available.

---

[2] `http://spaceweather.usu.edu/files/uploads/PDF/COSPAR_INTERNATIONAL_REFERENCE_ATMOSPHERE-CHAPTER-1_3(rev-01-11-08-2012).pdf`

What the models have in common, is that these are based on a certain measured solar flux or a prediction of the solar flux for a given date. The solar flux is often measured at the characteristic wavelength of 10.7 centimeters (F10.7 flux). This is a convenient measure largely because the data for the F10.7 index is available for historical periods beginning in 1945 (Wertz, 1978). The F10.7 flux is an indication for the solar activity. High activities at solar maxima result in heating of the atmosphere, causing in to expand and become denser. Note that the solar cycle is approximately 11 years.

3.7 Two-Body Problem

Applying Newton's second law of motion and Newton's law of gravitation, the motion of body i with respect to the inertial reference frame can be written as:

$$m_i \frac{d^2\mathbf{r}_i(t)}{dt^2} = \sum_{j \neq i} G \frac{m_i m_j}{r_{ij}^3(t)} \mathbf{r}_{ij}(t) \tag{3.7.1}$$

where G is the gravitational constant, m denotes the mass of a certain body and $\mathbf{r}$ is the position vector in the inertial reference frame. Here it is assumed that outside the system of n bodies no other bodies exist, that no external forces act on the system and that within the system of n bodies only gravitational forces occur.

Equation (3.7.1) represents the motion of bodies with respect to an inertial reference frame. However, in practical cases one will hardly be interested in the motion of a body with respect to the center of mass of a system of n bodies, but one wants to know the motion with respect to one of the bodies, for example, relative to a non-rotating reference frame with its origin at the center of the Earth. However, such a reference frame experiences translational accelerations and is thus not an inertial one. Therefore, other expressions have to be obtained, which describe the motion of body i relative to another body k. When the motion of body i is considered with respect to a non-rotating reference frame fixed to body k, the following equation holds true (Wakker, 2010):

$$\frac{d^2\mathbf{r}_i(t)}{dt^2} = -G \frac{m_i + m_k}{r_i^3(t)} \mathbf{r}_i(t) + G \sum_{j \neq i,k} m_j \left(\frac{\mathbf{r}_j(t) - \mathbf{r}_i(t)}{r_{ij}^3(t)} - \frac{\mathbf{r}_j(t)}{r_j^3(t)} \right) \tag{3.7.2}$$

In a first-order approximation the effects of the gravitational attraction between the bodies $\{j \neq i, k \text{ and } i\}$ can be neglected with respect to the effect of the gravitational attraction between the bodies i and k. In that case, the relative motion of body i is in a good approximation described by:

$$\frac{d^2\mathbf{r}_i(t)}{dt^2} = -\frac{\mu}{r_i^3(t)} \mathbf{r}_i(t) \tag{3.7.3}$$

μ is also referred to as the standard gravitational parameter of the central body. In many practical cases $\mu = Gm_k$, since $m_i << m_k$, where m_k is the mass of the attracting body.

Introducing the external accelerations (other than the gravitational) $\mathbf{f}_{EXT}$, Equation (3.7.3) can be written as:

$$\frac{d^2\mathbf{r}}{dt^2} + \frac{\mu}{r^3}\mathbf{r} = \mathbf{f}_{EXT} \tag{3.7.4}$$

Note that the index i and the time dependency (t) have been omitted here.

3.8 Perturbation Analysis

The satellite will encounter several perturbations. Which perturbations will be considered for the angular momentum build-up for the satellite will be discussed here. Furthermore, the magnitude of the central and perturbing accelerations will be looked at. From this analysis, it will be decided which perturbing accelerations to model.

3.8.1 Central and Perturbing Accelerations

Figure 3.8 shows the central and perturbing accelerations as function of the altitude of the satellite. The read-outs of the maximum accelerations are shown in Table 3.2.

Table 3.2: *Digital read-outs of Figure 3.8. This table gives an indication of the order of magnitude of the maximum central and perturbing accelerations which occur in a 300×850 orbit.*

Effect (high to low)	**Acceleration [m/s^2]**
GM	≈ 8.8
J2	≈ 8.7e−03
Atm. drag (solar max.)	≈ 1.1e−04
Atm. drag (solar min.)	≈ 1.2e−05
J4	≈ 1.2e−05
J6	≈ 3.5e−06
Moon (third-body)	≈ 1.2e−06
Sun (third-body)	≈ 5.8e−07
Tidal	≈ 4.1e−07
Solar rad. pressure	≈ 7.8e−08
Relativity	≈ 1.8e−08
Albedo	≈ 1.4e−08
Planets	≈ 7.9e−11

The dominant term (after the central field acceleration) is the J2 gravitational effect. The atmospheric drag at a solar maximum is 1.2% of the J2 effect. The J4 effect is only a fraction of the J2 effect (0.1%). Higher-order effects such as the J6 gravitational effect, the third-body perturbation by the Moon and Sun and the tidal effects are even smaller (<∼29.9% compared to J4 effect). It can also be seen that the perturbing acceleration due to the solar radiation pressure is very small.

Implementing third-body accelerations and tidal effects would increase the accuracy of the calculated satellite orbit. However, the simulations performed in this thesis work do not require that level of accuracy for the orbit calculations. It has therefore been decided to only consider gravity-field perturbations up to order J4 and the perturbations due to atmospheric drag.

3.8.2 Disturbance Torques

In the preliminary design phase the maximum disturbance loads have been looked at by (Munatsi, 2016b). Section 4.5.1 gives an overview of the maximum disturbance loads found. The disturbance torques, which will be considered, are due to the gravity-field, the magnetic field, the atmospheric density and the solar radiation perturbations.

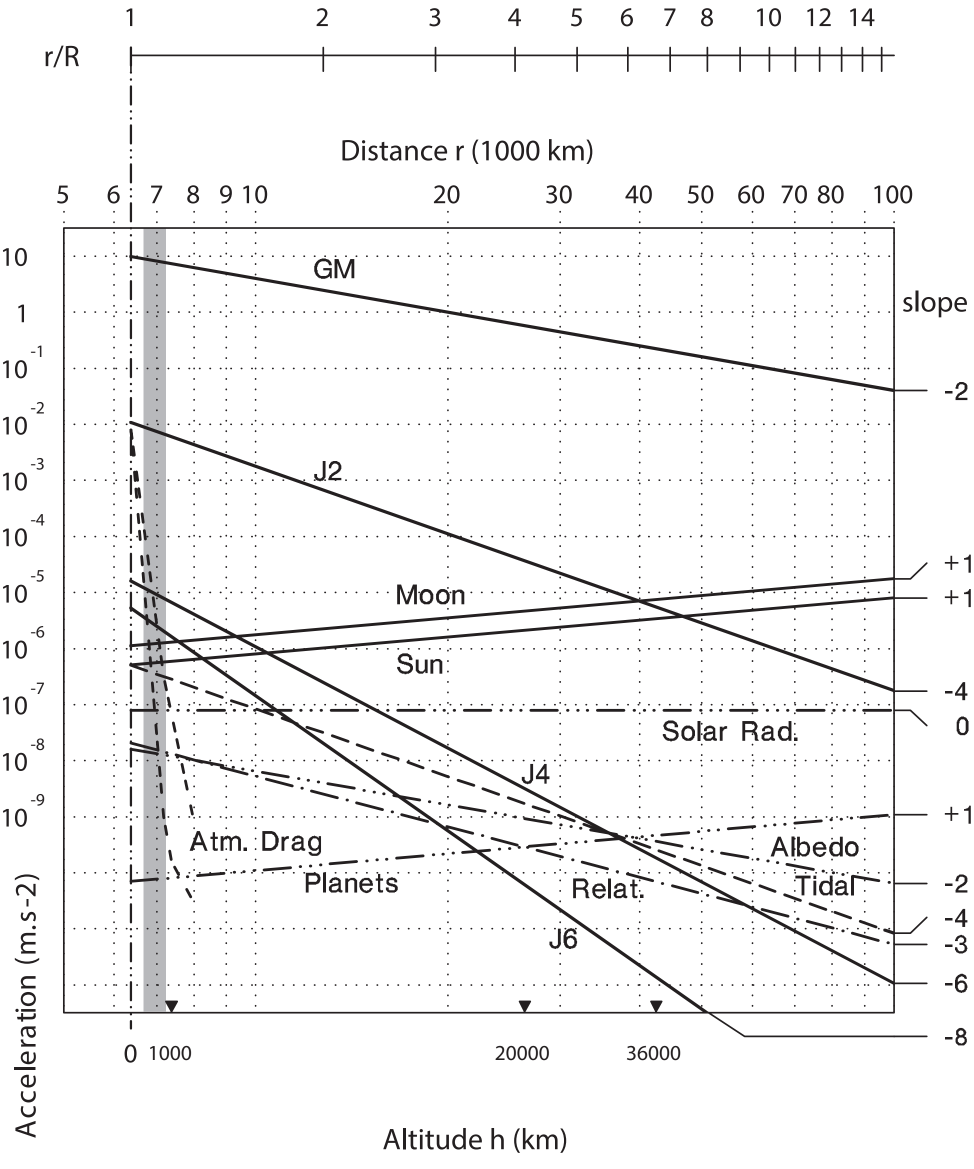

Figure 3.8: *Central and perturbing accelerations as function of the distance r from the satellite from the center of the Earth. Adapted form of (Capderou, 2005)*

.

Chapter 4
SIMULATOR ARCHITECTURE, DESIGN AND VERIFICATION

In this chapter the simulator, which will be used in the simulation performance runs, is presented. In Section 4.1 two different simulators are compared, after which a choice is made. Section 4.2 describes the simulator architecture. The environmental models which have been implemented are discussed in Section 4.3. The perturbation models which have been been implemented are discussed in Section 4.4. Section 4.5 describes the results of the perturbation analysis and shows that the cylindrical shape approximation is valid. Finally, in Section 4.6, it is verified whether the environmental and perturbation models are correctly implemented in the simulator.

4.1 Model Software Baseline

At the start of the project, two specific simulators have been considered to design the AOCS system. No other simulators have been considered, as these are the only available simulators currently available at Airbus DS NL. The simulators which will be considered are:

- AOCS Design Software (ADS);
- Generic Guidance Navigation and Control Simulator Environment (GGNCSim).

A detailed description of both simulators is given here, followed by a trade-off and a selection. At the end of the section, the simulator structure is elaborated on.

ADS

The first simulator, which will be studied is ADS. Airbus DS NL has used the software ADS in multiple projects, mainly to perform disturbance torque analysis for different missions. The software has not been used yet to make an A(O)CS design. Therefore, it has been investigated whether ADS is a suitable tool to design the ACS system.

ADS has been developed in 1998 by ALCATEL (Sghedoni, 2000), under a contract from the ESA. The current (and latest) version which is being used by Airbus DS NL is v3.0, dated from 2005. Since then no updates have been released.

ADS is a computer aided program; its first aim is to assist and facilitate the design of an Attitude and Orbit Control System. ADS has the ability to model and generate Earth orbits, to construct a spacecraft physical design, incorporate mission requirements, select equipment, define modes and build control laws. These elements can be used to build an AOCS-oriented spacecraft model. To perform the simulations, ADS simulates the dynamics of a modeled satellite, including perturbations acting upon it. Furthermore, ADS has comprehensive visualization capabilities.

There are several advantages of using the ADS software:

- The software allows the user to easily investigate the disturbance torques for a specific mission.
- The 3D satellite design tool enables the designer to incorporate an accurate representation of the satellite design (including mass properties) in the model. This is of importance for an accurate modeling of the disturbance torques. The surface contributions are accurately modeled.
- A 3D visualization of the satellite in the orbit is possible.
- From the simulation results the ΔV for orbit maintenance, the mass and power budgets for a mission, the stability performance and the pointing performance can be obtained.
- Several different sensors and actuators models are available in ADS. Alterations in the ACS design are made easily by adding/removing units. This should result in a very easy and convenient way to design the ACS architecture. Furthermore the characteristics of the sensors/actuators can be tuned (such as biases, noises and drifts) and their orientation with respect to the body frame can be changed and visualized.
- ADS allows the user to implement user-defined control algorithms.

There are several disadvantages using ADS. These will be summarized here.

- The satellite dynamics are linearized. As such, it is not possible to implement nonlinear control algorithms.
- Another consequence of the linearized dynamics is that an appropriate reference frame should be selected to avoid large angles maneuvers of the satellite. When no appropriate reference frame is selected, this may result in inaccuracies and disturbed measured angles by the sensors.
- In the descriptive documents (Sghedoni, 2000) it is explained how the different parts have been modeled, but these models cannot accessed or modified. Therefore, no alterations can be made, if that would appear to be necessary. Where the reference documentation is not adequate, the user is left in the dark. An example is how different formula's have been obtained. These have not been referred to any reference documentation.
- Not all results can be saved (e.g., those of the disturbance torque analysis) and the data is not accessible. As such, manual read-outs are required from the resulting plots. Post-processing of these results is therefore very time consuming and prone to errors.

Furthermore, there are some impracticalities from the user-standpoint of view:

- The results may (in some particular cases) ignore the latest modifications imposed by the user. If the user is not aware of this, this can lead to misinterpreted results.
- The axes in the plots are not labeled.
- The order of magnitude on the axes is hard to read.
- The program needs a regular restart, to avoid (unclear) error messages and to prevent the simulator from slowing down.
- The error handling is unclear and undocumented. Examples are: `"3DR: Low on memory, unable to proceed"`, `"driverRC is NULL"`, `"ERROR_MALLOC2"` and `"Echec de l'assert (E:\Users\didier\etc..., line 541)"`.

GGNCSim

The Generic Guidance Navigation and Control Simulator environment (GGNCSim) repository (Ellenbroek, 2011) contains a collection of models which can be used to build a simulator of a spacecraft in its environment. It does not provide the simulator itself, but only the building blocks. The environment consists of a set of MATLAB/Simulink libraries, which are written in C-code. All models have been verified and validated, such that these can be used directly.

The libraries which are relevant for the SPS-2 mission which are available are:

- The *math* library, which contains many mathematical operations, such as vector/matrix multiplications and quaternion transformations.
- The *environment* library, which contains gravity field models, magnetic field models, atmosphere models, solar-radiation models and ephemeris models.
- The *flight dynamics* library, which contain rigid-body models, environmental disturbance load models and the satellite mass properties.
- *Sensor* and *actuator* libraries, in which some generic sensor and actuators have been modeled. However, none of these models have been used in this project (directly), as these were not suitable.

A disadvantage of using GGNCSim is that the simulator structure still has to be build, as well as all the initialization and the post-processing scripts.

Trade-off between ADS and GGNCSim

The many (and serious) disadvantages/limitations of ADS do not compensate for the labor to be put into developing new models for the GGNCSim and setting up the simulator structure. Therefore, it has been decided to use GGNCSim for this project.

The GGNCSim repository offers all models relevant to model the spacecraft state and the environment. Only the sensors, actuators and controllers need to be developed. This is no problem, as it gives a large freedom in the design.

Note that ADS includes, in contrast to GGNCSim, a 3D visualization of the spacecraft position and orientation with respect to the Earth. Such a visualization can help in giving insight in the results obtained from the simulations. Therefore, the author has decided to spend some effort in developing a similar tool.

4.2 Simulator Structure and Development

From the two simulators, it has been decided to use GGNCSim. In this section the simulator structure is presented. First, the overall architecture is discussed, followed by a summary of the common model blocks and the user-defined model blocks. The set-up of the simulator is discussed after. Finally, some practicalities are discussed working with the simulator.

Architecture

The simulator architecture is shown in Figure 4.1. Based on the spacecraft position and orientation, the environmental parameters are calculated (1), with which the the disturbance loads can be calculated (2). The environmental properties and the spacecraft state are passed to the sensors (3), where the sensor measurements are performed. The resulting measurements are processed in the sensor data processing block in the onboard computer (4), after which the spacecraft state is estimated (if applicable) (5). Based on the measurements (and the estimated state) the controller gives a torque command (6). The torque command is processed in an actuator command (7). The torque command is processed by the actuators, which results in a torque output to control the spacecraft attitude (8). The actuator torques and disturbance loads are fed into the dynamics to update the spacecraft state (9).

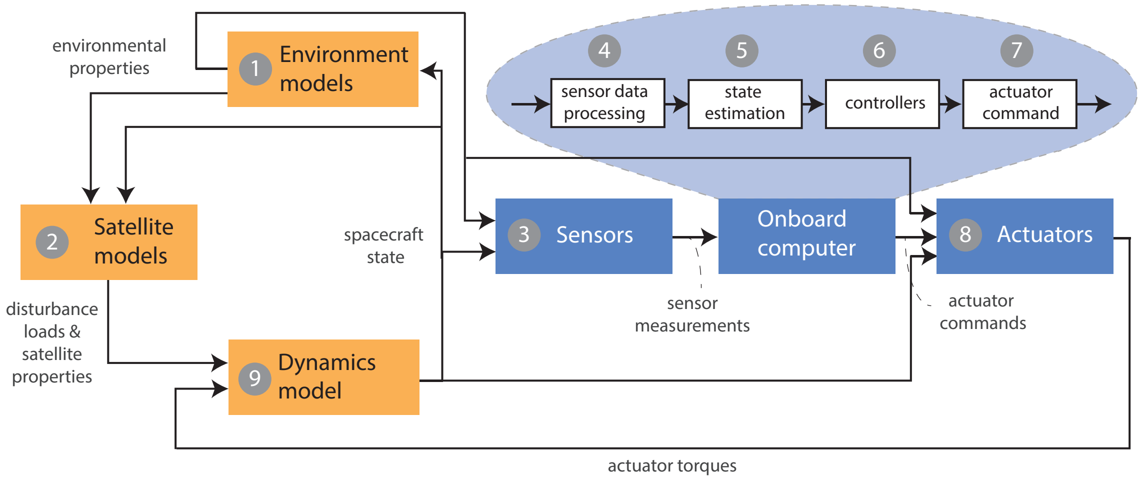

Figure 4.1: *Simulator architecture. The common models blocks (consisting of model blocks from GGNCSim repository) are shown in orange. The other blocks are the user-defined model blocks (index 3-8).*

Common model blocks

With the common model blocks the satellite orbit can be modeled, including its environment. The common model blocks have been taken from the GGNCSim repository. As such, these have already been verified and validated. The common blocks have been grouped in three specific blocks. The structure is as follows.

- In the *environment* block (1) the environmental parameters are calculated. This includes the Earth gravity field, the magnetic field, the atmospheric density, the solar radiation pressure, the time (MJD), the position of the Sun and the eclipse status.
- In the *satellite* (2) block the satellite mass and inertia properties are defined. Furthermore, the gravitational load, the aerodynamic disturbances, the gravitational disturbances, the magnetic disturbances and the solar radiation pressure disturbances are calculated.
- In the *dynamics* (9) block the spacecraft state is propagated.

User-defined model blocks

The user-defined models are grouped in the following parts of the simulator:

- The *sensor* models are grouped in the sensor block (3).
- The *actuator* models are grouped in the actuator block (8).
- The *onboard computer* (OBC) contains the sensor data processing (SDP) model block (4), the state estimation (if applicable, e.g. Kalman filters) model block (5), the control algorithms (6) and the command-model block (7).

Simulator development

Now the development of the simulator is discussed. The approach for the implementation of the common model blocks was as follows:

1. Investigate which model blocks are required.
2. Select the relevant model block from the GGNCSim repository.
3. Implement the relevant model block in the SPS-2 model.
4. Verification of the results.

The resulting environmental and the disturbance load models, which have been selected are discussed in Sections 4.3 and 4.4. The correctness of the implementation of the models has been verified by comparing the results to ADS. This verification will be discussed in Section 4.6.

Once the common model blocks have been implemented, the user-defined model blocks will be developed. The design of the sensor and actuator model blocks is discussed in Section 5. Chapter 6 discusses the design of the control algorithms for the detumble and SA/SP mode.

Working with the simulator

This section discusses briefly how a simulation is initialized and the visualization of the simulation results. Furthermore, the simulator characteristics are briefly discussed.

The solver, which has been used to simulate the dynamic system, is a Fourth-Order Runge-Kutta (RK4) solver. A fixed-stepsize of 1 s has been used. A trade-off between the accuracy and simulation speed has been made here. Considering the large number of simulations, which will be considered in the performance analysis, the computation time is very important. Larger simulation stepsizes affect the accuracy of the simulations. It was found that 1 s was a sufficiently small time-step to maintain a sufficient level of accuracy of the results, for simulations up to (at least) three orbits.

The simulation parameters can be initialized with an Excel script, with which different simulation cases can be defined. Alternatively, the user can choose to use specifically written Matlab functions to set-up a simulation. This is in particular useful when a large number of simulations has to be performed, such as in the verification test-runs.

The 3D visualization tool, of which an example is shown in Figure 4.2, which has been developed, shows for any time instance the spacecraft attitude and position in the orbit. The axis of the I-frame, R-frame, the B-frame and the equipment unit-frame can be illustrated, whereas in ADS only the B-frame is displayed. Furthermore, the Earth rotation is taken into account, as well as the change in Sun position. Finally, the Greenwich Meridian and the Equator are visualized. The 3D visualization tool has been verified by a one to one comparison with ADS. This has been done for different orientations, angular rates, orbits and different time instances. An advantage of the newly developed visualization tool is the possibility to store the resulting trajectory as a movie file (.AVI).

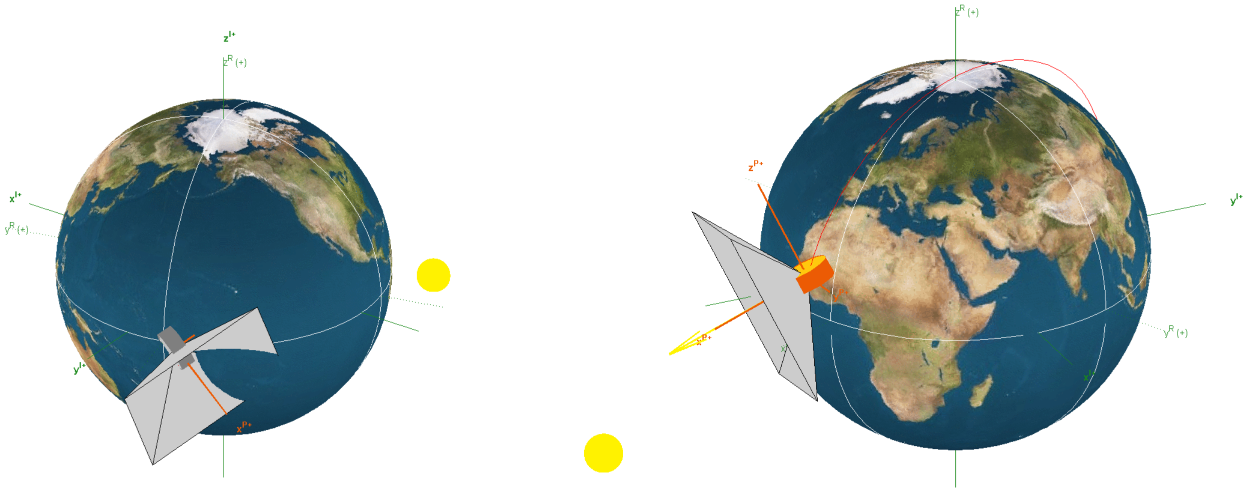

Figure 4.2: *Examples of the 3D orbit and attitude visualization tool. Left: spacecraft in eclipse conditions, right: spacecraft in Sun pointing direction. Note that the FoV of the Sun sensor is indicated with the gray pyramid cone.*

4.3 Environmental Model Implementation

The implementation of the gravity-field model, the magnetic field model, the solar radiation model and the atmospheric density model are discussed now. Note that the theory behind the environmental models was discussed in Section 3.6. At the end of this section, the illumination model is described, which has not been mentioned before.

4.3.1 Gravity-Field Model

In GGNCSim two gravity-field models are available:

- `env_gravity_central_field_zonal_harmonics_sfun` model (simplistic)
- `env_gravity_grim5c1_sfun` model (more advanced)

The simplistic model is based on (Regan, 1993). The gravity-field potential is a reduced form of Equation (3.6.1), where only the zonal harmonics are taken into account. That means that the major effects of the inhomogeneous mass distribution are modeled, but the variations with longitude are ignored with this model. The model order goes up to 4, such that only the effects until J_4 can be modeled.

The more advanced model is based on (Capderou, 2005) and includes the longitudinal dependency of the gravity-field. The gravity-field potential is the full form of Equation (3.6.1). The model order and degree can go up to 99. The coefficients are taken from the GRIM5-C1 model (from the year 2000), described in (Capderou, 2005). Nowadays, even better models are available due to scientific missions as GRACE and GOCE, which have made detailed measurements of the Earth's gravity field.

A very detailed representation of the Earth gravity-field would not improve the analysis in this thesis, as it only considers the design of the Attitude Control System. Therefore, the use of the zonal harmonics or the GRIM5-C1 model will suffice. As the computation time of both models is comparable, the more accurate GRIM5-C1 model has been selected. The only question is, which model order to select. The model order which has been chosen is 4, in accordance with Section 3.8.1.

4.3.2 Magnetic Field Model

In GGNCSim two magnetic field models are implemented, which differ in complexity:

- `env_magnetic_central_field_sfun` model, which gives a first-order approximation of the magnetic field (only the $n = 1$ terms are included). The dipole strength and the dipole unit vector can be inserted manually.
- `env_magnetic_igrf_epoch_1995_sfun` model, which is the more advanced model. The magnetic potential is calculated with Equation (3.6.5). The maximum model order which can be selected is $n = 10$.

The complex model in GGNCSim should yield a more accurate magnetic field. However, this model is based on the epoch of 1995. It will now be investigated what the impact is on the accuracy of the resulting magnetic field. The results of both models will be compared, by looking at the first-order approximation of the magnetic field. Note that for the same epochs, this would yield the same results.

In the first-order approximation of the magnetic field, the Earth's magnetic field can be approximated by a tilted dipole placed at the center of the Earth. Keeping only the $n = 1$ terms in Equation (3.6.5), the dipole approximation is as follows (Landis Markley and Crassidis, 2014):

$$V(\mathbf{r}) = \frac{\mathbf{m}^{\mathrm{R}}_{Earth} \cdot \mathbf{r}}{r^3} \tag{4.3.1}$$

where $\mathbf{m}_{Earth}$ is the Earth magnetic dipole vector and $\mathbf{r}$ is the position vector given in spherical coordinates. As a result, the magnetic field is given by:

$$\mathbf{B}(\mathbf{r}) = -\boldsymbol{\nabla} V(\mathbf{r}) = \frac{3(\mathbf{m}^{\mathrm{R}}_{Earth} \cdot \mathbf{r})\mathbf{r} - r^2 \mathbf{m}^{\mathrm{R}}_{Earth}}{r^5} \tag{4.3.2}$$

Given the longitude τ and latitude δ, the unit vector which represents the South Earth geomagnetic dipole is as follows:

$$\hat{\mathbf{m}}^{\mathrm{R}}_{Earth} = \begin{pmatrix} \cos\tau\cos\delta \\ \sin\tau\cos\delta \\ \sin\delta \end{pmatrix} \tag{4.3.3}$$

The strength of the magnetic field for the first-order model approximation is given by:

$$\left\| \mathbf{m}^{\mathrm{R}}_{Earth} \right\| = R^3_{Earth} \sqrt{{g^0_1}^2 + {g^1_1}^2 + {h^0_1}^2 + {h^1_1}^2} \tag{4.3.4}$$

where the Gaussian coefficients have been listed in Table 4.1.

Table 4.1: *IGRF coefficients for Epochs 1995 (original GGNCSim model), 2015 (IGRF-12) and 2020 (prediction IGRF-12) (Thébault et al., 2015), up to a model order of 4.*

		1995		**2015**		**2020**	
n	**m**	**g (nT)**	**h (nT)**	**g (nT)**	**h (nT)**	**g (nT)**	**h (nT)**
1	0	-29682	0	-29442	0	-29431.7	0
1	1	-1789	5318	-1501	4797.1	-1482.9	4770.5
2	0	-2197	0	-2445.1	0	-2453.8	0
2	1	3074	-2356	3012.9	-2845.6	3009.6	-2873
2	2	1685	-425	1676.7	-641.9	1678.8	-656
3	0	1329	0	1350.7	0	1354.1	0
3	1	-2268	-263	-2352.3	-115.3	-2357.8	-107.1
3	2	1249	203	1225.6	244.9	1224.9	244.5
3	3	769	-406	582	-538.4	571.9	-536.6
4	0	941	0	907.6	0	906.9	0
4	1	782	262	813.7	283.3	813.9	282
4	2	291	-232	120.4	-188.7	111.3	-183.4
4	3	-421	98	-334.9	180.9	-330.8	183.8
4	4	116	-301	70.4	-329.5	66.1	-334.7

Table 4.2: *Location South Geomagnetic pole in 1995 (as in GGNCSim model), 2015 (IGRF-12) and 2020 (prediction IGRF-12) (Thébault et al., 2015).*

year	**latitude (N)**	**longitude (E)**
1995	-78.60°	109.55°
2015	-80.37°	107.37°
2020	-80.65°	106.83°

It will now be investigated what the difference is between the Earth magnetic dipoles for the epochs 1995, 2015 and 2020. This will directly show the difference in the first-order approximation of the magnetic field. The locations of the South Earth geomagnetic dipole for the years 1995, 2015 and 2020 are given in Table 4.2. The Earth geomagnetic dipoles for the years 1995, 2015 and 2020 are calculated to be:

$$\textbf{1995:}\quad \hat{\mathbf{m}}^{\mathrm{R}}_{Earth} = \begin{pmatrix} -0.0661 \\ +0.1863 \\ -0.9803 \end{pmatrix} \text{ which is } \begin{pmatrix} +37.5\% \\ +21.2\% \\ -0.7\% \end{pmatrix} \text{ w.r.t. year 2015} \tag{4.3.5}$$

$$\text{and } \left\|\mathbf{m}^{\mathrm{R}}_{Earth}\right\| = 7.812 \cdot 10^{15}\ \mathrm{Tm}^3 \text{ which is } +1.1\% \text{ w.r.t. year 2015} \tag{4.3.6}$$

$$\textbf{2015:}\quad \hat{\mathbf{m}}^{\mathrm{R}}_{Earth} = \begin{pmatrix} -0.0499 \\ +0.1597 \\ -0.9859 \end{pmatrix} \text{ and } \left\|\mathbf{m}^{\mathrm{R}}_{Earth}\right\| = 7.725 \cdot 10^{15}\ \mathrm{Tm}^3 \tag{4.3.7}$$

$$\textbf{2020:}\quad \hat{\mathbf{m}}^{\mathrm{R}}_{Earth} = \begin{pmatrix} -0.0470 \\ +0.1555 \\ -0.9867 \end{pmatrix} \text{ which is } \begin{pmatrix} -2.2\% \\ +1.1\% \\ -0.0\% \end{pmatrix} \text{ w.r.t. year 2015} \tag{4.3.8}$$

$$\text{and } \left\|\mathbf{m}^{\mathrm{R}}_{Earth}\right\| = 7.721 \cdot 10^{15}\ \mathrm{Tm}^3 \text{ which is -0.1\% w.r.t. year 2015} \tag{4.3.9}$$

$$\tag{4.3.10}$$

It can be seen that there is no use of using the complex model, unless it is updated. In the comparison of both models, the computation time has also been looked at. The difference in computation time is negligible, even when a model order of 10 is selected for the complex model.

The accuracy of the magnetic field is considered to be important, with the main reason that the measured magnetic field is used to control the spacecraft in the detumble mode. The simulation results are more trustworthy with an accurate representation of the magnetic field. The model order which has been selected is 10, which is the maximum model order. For this, the author has updated the complex model with the model coefficients from 2015 using the data in (Thébault et al., 2015).

4.3.3 Solar Radiation Pressure Model

The solar radiation pressure model which has been implemented in GGNCSim is the `env_pressure_sun_radiation_sfun` model. The working principle of the model is identical to the theory described in Section 3.6.3. The variation in distance with respect to the Sun is taken into account.

4.3.4 Atmospheric Density Model

The atmospheric models which are implemented in GGNCSim are:

- `env_atmosphere_msis86_min_sfun`
- `env_atmosphere_msis86_nom_sfun`
- `env_atmosphere_msis86_max_sfun`

These models are based on the MSIS-86 atmospheric model (Wertz and Larson, 2007). The MSIS-86 model (MSIS stands for Mass Spectrometer and Incoherent Scatter Radar) uses the average data for the minimum, nominal and maximum atmospheric densities for a period of several decades:

- The minimum and maximum densities for the MSIS-86 model are chosen such that 10% of all measured densities are above/below the minimum/maximum density.
- The nominal density of the MSIS-86 model is chosen such that 50% of all measured densities are either above or below the nominal density.

Which years have been taken to get to these minimum/nominal/maximum density profiles is not written down explicitly in the reference documentation (Ellenbroek, 2011). Note that the MSIS-86 is more than 30 years old.

There exist several other atmospheric models which relate the atmospheric density to the altitude. A model which is currently widely used is the NLRMSISE-00 model. The question is whether the MSIS-86 model gives sensitive atmospheric density estimations. To verify this, the model has been compared to the NLRMSISE-00 model, which is considered to be the current standard.

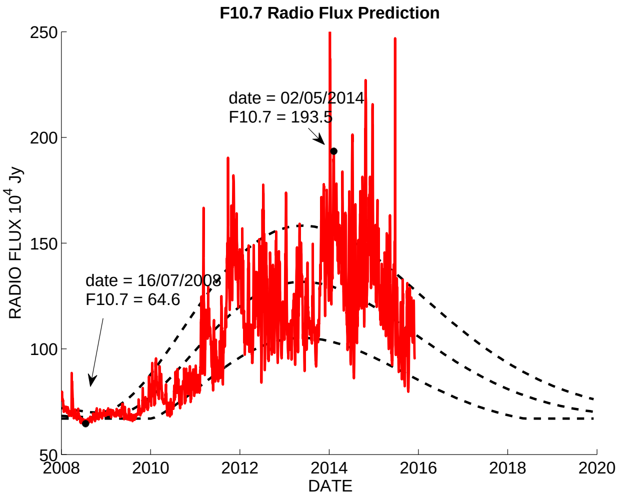

Figure 4.3: *F10.7 Radio Flux Prediction (dotted lines) and measurements (red line). Two dates have been selected.*[1]

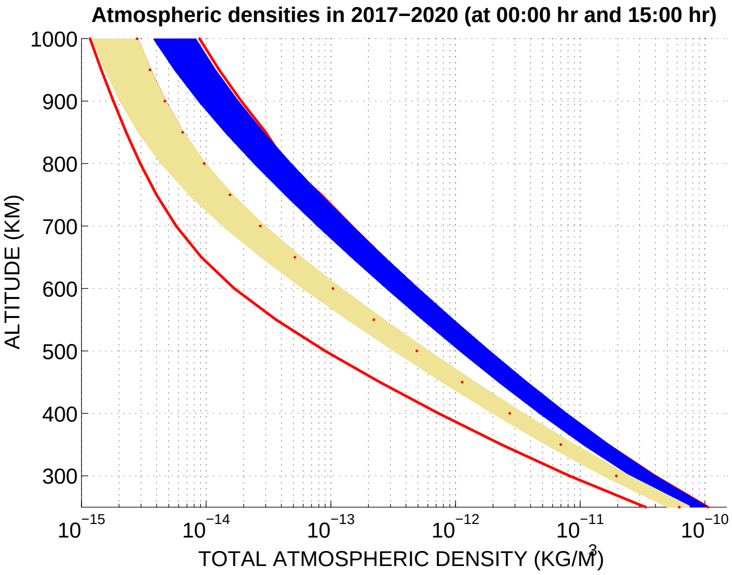

Figure 4.4: *The atmospheric density profile for all days in 2017-2020. The red lines are the minimum, nominal and maximum values obtained with the MSIS-86 model. The results for the NLRMSISE-00 model are shown in yellow (00:00 hr) and blue (15:00 hr).*

A brief summary of the NLRMSISE-00 model is given in Appendix B.2. In this analysis it has been shown that the impact of the F10.7 flux, the magnetic field information and the contribution of anomalous oxygen can be safely be ignored in the upcoming comparison, as these contributions result in lower atmospheric densities. However, it has been found that the time during the day has a large impact on the atmospheric density profile. This needs to be taken into account.

---

[1] The data to generate this plot has been taken from: `ftp://ftp.ngdc.noaa.gov/STP/space-weather/solar-data/solar-features/solar-radio/noontime-flux/penticton/penticton_observed/listings/` and `http://solarscience.msfc.nasa.gov/images/f107_predict.txt`, at 19-01-2016.

The atmospheric densities for the years 2017 till 2020 have been examined with the NLRMSISE-00 model and compared to the minimum, mean and maximum atmospheric density profiles of the MSIS-86 model for two time instances (00:00 hr and 15:00 hr). The results are shown in Figure 4.4. The estimated densities of the NLRMSISE-00 model are within the minimum and maximum density profiles of the MSIS-86 model. As such, the atmospheric densities will *not be* underestimated using the MSIS-86 model. However, to account for the daily change in atmospheric density, which is clearly present, the atmospheric densities should be varied between the minimum and maximum values in the simulations.

4.3.5 Illumination Factor Model

The model which is used to determine the illumination factor is based on (Montenbruck and Gill, 2000). The output of the model `env_sun_illumination_factor_sfun` is ν, which is the illumination factor.

The occulation of the Sun by the Earth is modeled by overlapping disks. Figure 4.5 illustrates the geometry. All formula's described here are directly taken from (Montenbruck and Gill, 2000).

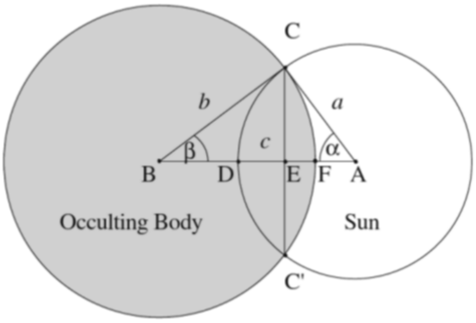

Figure 4.5: *Geometry of the occulting body and the Sun (Montenbruck and Gill, 2000).*

The apparent radius a of the occulted body (the Sun) is calculated as such:

$$a = \arcsin \frac{R_s}{|\mathbf{r}^{\mathrm{I}}_{Sun} - \mathbf{r}^{\mathrm{I}}_{sat}|} \tag{4.3.11}$$

where R_s is the Sun radius equal to 6.96×10^8 m, $\mathbf{r}^{\mathrm{I}}_{Sun}$ is the Sun position expressed in the I-frame, and $\mathbf{r}^{\mathrm{I}}_{sat}$ is the satellite position in the I-frame.

The coordinate of the satellite with respect to the occulting body (the Earth) is simply:

$$\mathbf{s} = \mathbf{r}_{sat} \text{ and } s = |\mathbf{s}| \tag{4.3.12}$$

Now the apparent radius b of the occulting body (the Earth) can be calculated:

$$b = \arcsin \frac{R_e}{s} \tag{4.3.13}$$

With distances a and b, the apparent separation of the centers of both bodies c is known:

$$c = \arccos \frac{-\mathbf{s}^{\mathrm{T}} \left(\mathbf{r}_{Sun} - \mathbf{r}_{sat}\right)}{s|\mathbf{r}_{Sun} - \mathbf{r}_{sat}|} \tag{4.3.14}$$

If $a + b \leqslant c$, there is no eclipse, such that $\nu = 1$. If $a - b < c$, there is a total eclipse, such that $\nu = 0$. For the other situations, the area A of the occulted segment of the apparent solar disk can be calculated.

The occulted area may be expressed as:

$$A = a^2 \arccos \frac{x}{a} + b^2 \arccos \frac{c - x}{b} - cy \tag{4.3.15}$$

where $x = \frac{c^2+a^2-b^2}{2c}$ and $y = \sqrt{a^2 - x^2}$. The remaining fraction of the Sunlight is then given by:

$$\nu = 1 - \frac{A}{\pi a^2} \tag{4.3.16}$$

4.4 Modeling of Perturbations

In this section the modeling of the forces and moments acting on the satellite will be discussed. The combination of the forces and moments acting upon the satellite is referred to as the *load*. Here, the implementation of the gravity-field perturbation, the magnetic-field perturbation, the atmospheric perturbation and the solar radiation perturbation are discussed.

The shape of the SPS-2 satellite is relatively complex: it consists of many surfaces. As a simplification, a cylindrical shape is assumed. In Section 4.5.2 it will be validated that this is a reasonable assumption.

Note that the forces are generally expressed in inertial frame, whereas the disturbance moments will be be expressed in the body frame.

4.4.1 Gravity-Field Load

The gravitation acceleration from the GRIM5-C1 model is expressed in the V-frame. After transformation to the I-frame, the gravitation acceleration force in the I-frame is described as follows:

$$\mathbf{F}^{\mathrm{I}} = M_{\mathrm{sat}}\, \mathbf{g}^{\mathrm{I}} \tag{4.4.1}$$

where M_{sat} is the satellite mass and $\mathbf{g}^{\mathrm{I}}$ is the gravitational acceleration.

By definition, the gravitational moment of a point mass should be zero. However, the satellite is not a point mass. The contribution due to large geometry and mass distribution can be treated as disturbances. The gravitation acceleration moment in the B-frame is defined as:

$$\mathbf{M}^{\mathrm{B}} = \left(M_{\mathrm{sat}}\, \mathbf{r}^{\mathrm{B}}_{CoM}\right) \times \mathbf{g}^{\mathrm{B}} \tag{4.4.2}$$

here $\mathbf{r}^{\mathrm{B}}_{CoM}$ is the vector towards the satellite center of mass in the B-frame. However, the B-frame is defined to coincide with the satellite center of mass, such that $\mathbf{M}^{\mathrm{B}} = \mathbf{0}$.

4.4.2 Gravity-Field Perturbation Moment

The gravitation disturbance moment is due to the varying gravitation field over the spacecraft body. A first-order approximation of this perturbation expressed in the B-frame is as follows (Wie, 2008):

$$\mathbf{M}^{\mathrm{B}} = 3\frac{\mu}{|r|^3}\hat{\mathbf{r}}^{\mathrm{B}} \times \mathbf{J}\hat{\mathbf{r}}^{\mathrm{B}} \;\; \text{with} \;\; \hat{\mathbf{r}}^{\mathrm{B}} = \frac{\mathbf{r}^{\mathrm{B}}}{\|\mathbf{r}^{\mathrm{B}}\|} \tag{4.4.3}$$

where $\mathbf{r}^{\mathrm{B}}$ is the distance between the B-frame and the I-frame, expressed in the I-frame. $\mathbf{J}$ is the moment of inertia of the satellite and μ is the gravitational parameter of the Earth.

4.4.3 Magnetic Field Disturbance Moment

The gravitational disturbance moment due to the magnetic field $\mathbf{M}^{\mathrm{B}}$ is defined as such:

$$\mathbf{M}^{\mathrm{B}} = \mathbf{B}^{\mathrm{B}} \times \mathbf{m}^{\mathrm{B}} \tag{4.4.4}$$

where $\mathbf{m}^{\mathrm{B}}$ is the spacecraft magnetic dipole moment expressed in the B-frame (in Am^2) and $\mathbf{B}^{\mathrm{B}}$ is the magnetic field vector expressed in the B-frame (in T).

4.4.4 Atmospheric Disturbance Load

The atmospheric disturbance load depends on the shape of the satellite. The load at the cylinder is split up in a contribution from the cylinder wall and the top and bottom faces. See Figure 4.6 for an illustration.

In this derivation, use is made of the P-frame. This is the frame which belongs to the geometric shape of the cylinder. The origin is in the center of the cylinder. The force at the top/bottom face expressed in the P-frame is as follows (Ellenbroek, 2011):

$$\mathbf{F}^{\mathrm{P}}_{plate} = \frac{1}{2}\rho C_D(\pi r^2){V^{\mathrm{P}}}^2\,\hat{\mathbf{V}}^{\mathrm{P}} \tag{4.4.5}$$

where ρ is the atmospheric density, C_D is an aerodynamic force coefficient related to the reference surface and r is the radius of the cylinder. Furthermore, $\mathbf{V}^{\mathrm{P}}$ is the velocity vector (relative to the atmosphere) in the direction of the velocity and $\hat{\mathbf{V}}^{\mathrm{P}}$ is the unit vector in direction of the velocity, both expressed in the P-frame.

The force at the wall surface in the P-frame is as follows (Ellenbroek, 2011):

$$\mathbf{F}^{\mathrm{P}}_{wall} = -\frac{1}{2}\rho C_D(2rh)V^2\,\hat{\mathbf{V}}^{\mathrm{P}}\sin(\beta) \;\; \text{with} \;\; \beta = \cos^{-1}\left(-\hat{\mathbf{V}}^{\mathrm{P}}_z\right) \tag{4.4.6}$$

where h is the height of the cylinder.

Now the aerodynamic disturbance forces acting upon the satellite are known. These forces can easily be transformed to the I-frame, as the perturbing forces are generally expressed in the I-frame.

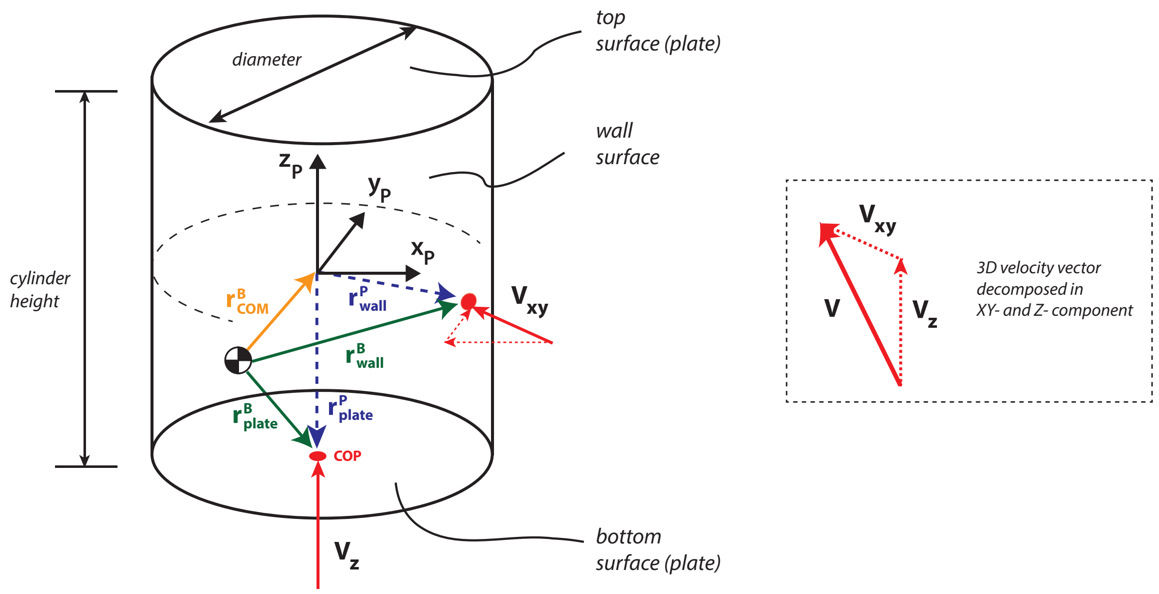

Figure 4.6: *Geometric description of the cylinder in the P-frame, relative to the center of mass. The red points are the pressure points on the wall and the top/bottom surfaces.*

The aerodynamic pressure force (which acts in the center of pressure point) causes a moment around the center of mass of the satellite. To calculate this disturbance moment, the location of the center of pressure needs to be known. The location of the center of pressure, expressed in the P-frame, is:

$$\mathbf{r}^{\mathrm{P}}_{plate} = \begin{pmatrix} 0 \\ 0 \\ \pm\frac{1}{2}h \end{pmatrix} \quad \text{and} \quad \mathbf{r}^{\mathrm{P}}_{wall} = \begin{pmatrix} r\hat{V}_x \\ r\hat{V}_y \\ 0 \end{pmatrix} \tag{4.4.7}$$

where h is the height and r is the radius of the cylinder. $\hat{V}^{\mathrm{P}}_x$ and $\hat{V}^{\mathrm{P}}_y$ are the x- and y-components of the unit vector in direction of the velocity, both expressed in the P-frame. See Figure 4.6 for an illustration of the distances $\mathbf{r}^{\mathrm{P}}_{plate}$ and $\mathbf{r}^{\mathrm{P}}_{wall}$.

The distances $\mathbf{r}^{\mathrm{P}}_{plate}$ and $\mathbf{r}^{\mathrm{P}}_{wall}$ can now easily be expressed in the B-frame. The moment contributions of the plate and the wall then become:

$$\mathbf{M}^{\mathrm{B}}_{plate} = \mathbf{r}^{\mathrm{B}}_{plate} \times \mathbf{F}^{\mathrm{B}}_{plate} \tag{4.4.8}$$

$$\mathbf{M}^{\mathrm{B}}_{wall} = \mathbf{r}^{\mathrm{B}}_{wall} \times \mathbf{F}^{\mathrm{B}}_{wall} \tag{4.4.9}$$

4.4.5 Solar-Radiation Disturbance Loads

The calculation of the solar-radiation disturbance load shows similarities with the calculation of the aerodynamic disturbance load. Again, the cylinder is split up in a contribution from the cylinder wall and the top and bottom faces. The other similarity is the use of the P-frame, which is related to the geometric shape of the cylinder. See Figure 4.6 for an illustration.

First the plate contribution is looked at. The solar radiation pressure at the plate is calculated with (Ellenbroek, 2011):

$$\mathbf{p}^{\mathrm{P}}_{solar} = -\mathrm{p}_{sun}\left(\mathbf{n}^{\mathrm{P}}_{sun}\cdot\mathbf{n}^{\mathrm{P}}_{plate}\right)\left[(1-C_{spec})\mathbf{n}^{\mathrm{P}}_{sun} + 2C_{spec}\left(\mathbf{n}^{\mathrm{P}}_{sun}\cdot\mathbf{n}^{\mathrm{P}}_{plate}\right)\mathbf{n}^{\mathrm{P}}_{plate}\right] \tag{4.4.10}$$

where p_{sun} is the solar radiation pressure, $\mathbf{n}^{\mathrm{P}}_{sun}$ is the unit vector from the Sun towards the plate, $\mathbf{n}^{\mathrm{P}}_{plate}$ is the unit vector normal to the plate surface, C_{spec} is the specular reflection coefficient and C_{diff} is the diffusive reflection coefficient. The effect of absorption is also incorporated, through the relation $C_{spec} + C_a = 1$. Furthermore, the relation takes care of which side of the panel is facing the Sun. This determines the direction of the solar radiation pressure. Note that $C_{diff} = 0$, and therefore has been omitted from the relation.

With the solar radiation pressure, the force in the pressure point of the plate can be calculated as such:

$$\mathbf{F}^{\mathrm{P}}_{plate} = \nu A_{plate}\mathbf{p}^{\mathrm{P}}_{solar} \tag{4.4.11}$$

where ν is the illumination factor (between 0 and 1) and A_{plate} is the area of the plate. The disturbance moment of the solar radiation pressure of the plate is simply obtained by:

$$\mathbf{M}^{\mathrm{P}}_{plate} = \mathbf{r}^{\mathrm{P}}_{plate} \times \mathbf{F}^{\mathrm{P}}_{plate} \tag{4.4.12}$$

where $\mathbf{r}^{\mathrm{P}}_{plate}$ is the moment arm from the center of the cylinder in the P-frame towards the pressure point on the plate.

Now the wall contribution is looked at. First, define angles α and β as such:

$$\alpha = \tan^{-1}\left(\frac{\mathbf{n}^{\mathrm{P}}_{sun,y}}{\mathbf{n}^{\mathrm{P}}_{sun,x}}\right) \tag{4.4.13}$$

$$\beta = \cos^{-1}\left(\mathbf{n}^{\mathrm{P}}_{sun,z}\right) \tag{4.4.14}$$

The generalized force at the surface of the cylinder wall becomes:

$$\mathbf{F}^{\mathrm{P}}_{surface} = -\nu A_{wall}\sin\beta\,\mathbf{p}^{\mathrm{P}}_{sun} \tag{4.4.15}$$

The solar radiation pressure force then can be written as:

$$\mathbf{F}^{\mathrm{P}}_{wall} = \begin{bmatrix} \left(2(1+\frac{1}{3}C_{spec})\sin\beta\right)\cos\alpha \\ \left(2(1+\frac{1}{3}C_{spec})\sin\beta\right)\sin\alpha \\ \left((1-C_{spec})\cos\beta\right) \end{bmatrix}\mathbf{F}^{\mathrm{P}}_{surface} \tag{4.4.16}$$

The moment contribution in the cylinder frame is defined as:

$$\mathbf{M}^{\mathrm{P}}_{wall} = \frac{\pi}{2}r\begin{bmatrix} \sin\alpha \\ -\cos\alpha \\ 0 \end{bmatrix}\cos\beta\,\mathbf{F}^{\mathrm{P}}_{surface} \tag{4.4.17}$$

Now the forces and moment contributions of the wall and plate have been obtained, these can be transformed to the I-frame and the B-frame respectively.

4.5 Disturbance Torque Analysis

This section deals with the disturbance torques acting on the SPS-2 satellite. In the preliminary design phase, the disturbance torques have been looked at. A brief overview of the results is given in Section 4.5.1. In Section 4.5.2 it will be investigated whether a cylindrical shape for the satellite can be assumed.

4.5.1 Perturbation Analysis

In the work of (Munatsi, 2016b) the maximum disturbance loads were investigated to occur with the SPS-2 satellite. The disturbance loads have been investigated using ADS. In this analysis, different configurations, orbits and dates have been considered for the year 2017. It was found that the angular momentum build-up shows a seasonal variation. The highest angular momentum build-up (during one orbit) which has been found was $\sim 280 \times 10^{-3}$ Nms and occurred at July the 21st 2017 for the configuration shown in Figure C.1.

In a later stage, a review of the perturbation analysis was performed. The revisit was necessary because:

- only the Sun-pointing orientation was considered
- only one orbit has been selected per day
- the residual dipole moment was over-estimated[2]
- the ring height was 0.3 m instead of 0.4 m (changed later to 0.5 m due to an additional clamp release system)
- the total mass of the model was 232.5 kg instead of 250 kg

The results are described by (Munatsi, 2016a). In the review of the perturbation analysis, also the Earth-pointing (nadir) and inertial pointing orientations have been considered. It appears that the solar-pointing orientation gives the worst-case disturbance torques. The ring height and the mass change have a negligible effect on the angular momentum build-up. The gravity gradient and magnetic disturbances dominate still. The highest angular momentum build-up (during one orbit), which has been found was $\sim 250 \times 10^{-3}$ Nms.

4.5.2 Cylindrical Shape Investigation

One of the key features of using ADS is that a detailed three-dimensional satellite model can be used to analyze the disturbance torques (see Figure C.1). As a result, the contribution of the individual surfaces can be taken into account separately, which yields a more accurate representation of the disturbance torques acting on the satellite. Important to note is that despite the accurate 3D representation, the shadowing effect is neither taken into account in ADS nor in GGNCsim.

When using the disturbance load models of GGNCSim, the satellite structure can be represented by different shapes: a cylinder, box or plate surface. With these geometries the aerodynamic and solar radiation disturbance torques are analyzed. The combination of these shapes would yield the same level of detail used in ADS. However, it is complicated to correctly define this, as there is no visualization of the satellite structure and the geometry

---

[2] This was discovered in the verification of the magnetic disturbance load model block from the GGNCSim repository, as described in Section 4.6.4.

is relatively complex. Therefore, it has been investigated whether a cylindrical shape can be used to represent the satellite structure.

The resulting angular momentum build-up of the detailed SPS-2 structure will now be compared for three cylindrical shapes. The ring height is identical, but the radius has been varied. The analysis has been performed with ADS. Figure C.1 shows the SPS-2 geometry which has been used in this analysis by (Munatsi, 2016b), for the reference case. The satellite parameters are shown in Table C.1.

What can be observed from the results in Figure 4.7, is that the angular momentum build-up does not differ much from the reference case. The minimum angular momentum is smaller than the reference case, but the maximum angular momentum build-up is larger. Therefore, a simple cylindrical shape for the satellite can be safely be assumed. The satellite will therefore be modeled as a cylinder. As the results of case C are closest to the reference case, this geometry has been selected for the remainder of the report.

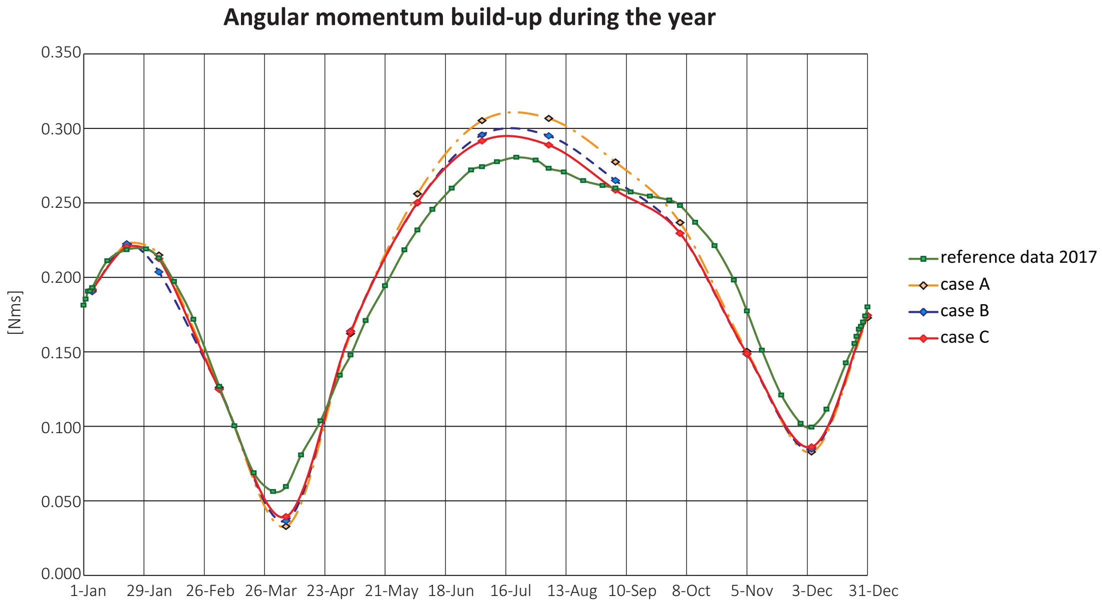

Figure 4.7: *The resulting angular momentum build-up for the different geometries which have been considered for the cylindrical shape investigation.*

4.6 Verification Implementation of GGNCSim Models

The GGNCSim models which have been described in Section 4.4 are here compared with the models in ADS. It will be investigated whether the resulting disturbance torques are identical, and if not, where the discrepancies come from.

A step by step approach has been used in the verification of the disturbance torques. The test cases have been carefully selected and will be discussed now. First simple test cases have been adopted. When these tests have passed successfully, more complex test cases were tested.

The analysis was cumbersome, because the results of ADS cannot be assessed and saved, such that manual read-outs are required. This is a time consuming, labor intensive job and worst of all: not very accurate. Furthermore, with ADS the contributions of a disturbance load cannot be split up in individual components, e.g., only the wall contribution of the aerodynamic load. However, a clever definition of the orientation of the satellite still enables the user to do so. Before comparing the disturbance loads, first the environmental models of both simulators are looked at. Differences in disturbance loads may be traced back to differences here.

4.6.1 Comparison Environmental Parameters

To compare the results in the disturbance loads, first the environmental parameters need to be compared. Difference may result from differences in these models.

The resulting solar radiation pressure, the atmospheric density and the magnetic field in the B-frame are discussed here. These parameters have been compared for orbit B in Table 4.3 and orientation A in Table 4.4 (XY-plane of satellite coplanar to XY-plane I-frame, Z-axis pointed upwards).

Table 4.3: *The orbit simulation parameters. Note that Ω, ω and θ are 0 degrees for all orbits.*

	unit	**orbit A**	**orbit B**	**orbit C**
perigee height	km	575	350	575
apogee height	km	575	800	575
inclination	deg	0	98	0
year	-	2017	2017	2015
date	-	21/07	21/07	20/03
time	hr/m	00:00	00:00	22:45

Table 4.4: *The simulation parameters for the initial attitude. $\mathbf{C}_{I,P}$ is the transformation which defines the initial orientation of the P-frame with respect to the I-frame. With this transformation matrix the initial quaternion is constructed.*

case	$\mathbf{C}_{\mathbf{I},\mathbf{P}}$
A	$\mathbf{I}_{3\times3}$
B	$\mathbf{C}_1(\pi/2)\mathbf{C}_3(\pi/2)$
C	$\mathbf{C}_1(\pi/2)\mathbf{C}_3(\pi/2)\mathbf{C}_1(-\pi/2)\mathbf{C}_2(-\pi/4)\mathbf{C}_3(-\pi/6)$
D	$\mathbf{I}_{3\times3}$
E	$\mathbf{C}_2(\pi/2)$

The comparison has shown that:

- The atmospheric density calculated in the SPS-2 model is larger than in ADS. The density model used in ADS is the CIRA-72, which was described in Section 4.3.4. In

GGNCSim the MSIS-86 model is used. How the densities of both model relate to each other, is shown in Appendix B.1. For now a multiplication factor of 0.52 has been used to balance out this difference, but only in this analysis.
- No discrepancies have been found between the gravitational accelerations of both models.
- The magnetic field vector components in the B-frame have slight offsets of -2.50%, 0.34% and 0.27%, in the X-, Y- and Z- directions respectively. A first-order model has been used in ADS, with a slightly different Earth geomagnetic dipole, which explains the differences. The Earth geomagnetic dipole used in ADS is:

$$\mathbf{m}^{\mathrm{R}}_{Earth} = \begin{pmatrix} -0.065261 \\ +0.179302 \\ -0.981627 \end{pmatrix} 8.056 \cdot 10^{15} \ \ \mathrm{Tm}^3$$

  where the location of the South Earth geomagnetic dipole is 79° South and 110° East.
- The solar radiation pressure in ADS is constant with a value of $4.6{\cdot}10^{-9}$ Nm. A more realistic scenario is achieved in the SPS-2 model, where the solar radiation pressure depends on the position of the satellite with respect to the Sun. The solar radiation pressure in the SPS-2 model is therefore slightly smaller; the maximum offset is -3.99%.

Now the differences in the environmental models have been pointed out, the disturbance loads of both models are compared in the coming sections.

4.6.2 Aerodynamic Disturbance Load

The aerodynamic disturbance load resulting from the original GGNCSim model is different than the results obtained with ADS. To trace back where the differences come from, four test cases have been performed. In these test cases, the wall and the plate contributions could be accessed individually.

The test cases are as such:

- Wall component only (simple case). Orbit A, orientation A (spacecraft body XY-plane in equatorial plane, Z- axis pointing to North). The spacecraft orientation remains inertial fixed in this situation. It appears that the contribution of the aerodynamic force of the wall is opposite in sign compared to ADS. After a careful examination, it was determined that ADS uses the correct sign convention here. Therefore a modification is made to the original GGNCSim model block.
- Plate component only (simple case). Orbit A, orientation B (spacecraft body X-axis parallel to Z-axis of I-frame). The spacecraft rotates 360 degrees around its X-axis during one orbit, such that the aerodynamic force only consists of a plate component. The plate contribution of the aerodynamic force is the same as in ADS. No sign changes are required here.
- Plate and wall component (simple case). Orbit A, orientation B (spacecraft body X-axis parallel to Z-axis of I-frame). The spacecraft orientation is now inertial fixed. In this simulation there is a varying contribution of the wall and plate aerodynamic force. The aerodynamic force components of the SPS-2 model (with the change in the wall contribution of the aerodynamic force) matches the results of ADS. The resulting

aerodynamic disturbance torque, however, does not match the results of ADS. It appears that the GGNCSim model block uses another distance for the arm to calculate the disturbance moment contributions (see Figure 4.6). The moment contributions of the plate and the wall are calculated with distances $\mathbf{r}^B_{plate}$ and $\mathbf{r}^B_{wall}$. In ADS (despite claimed differently) the distance $\mathbf{r}^B_{COM}$ is used calculate the aerodynamic disturbance torques, which is wrong.
- Plate and wall component (complex case). Orbit B, orientation C (the spacecraft is oriented in an arbitrary orientation). In this simulation there is a varying contribution of the wall and plate aerodynamic force. The results of both simulators are identical.

4.6.3 Gravitational Disturbance Load

To compare the gravitational disturbance loads, orbit B and orientation C have been considered (the spacecraft is oriented in an arbitrary orientation). The gravitational loads from both models are identical.

4.6.4 Magnetic Disturbance Load

In this section the magnetic disturbance loads calculated with ADS and GGNCSim will be compared. Also here, orbit B is considered with orientation C (the spacecraft is oriented in an arbitrary orientation).

The resulting magnetic disturbance torques of GGNCSim and ADS are completely different. This can be due to two reasons: either the calculated magnetic field is different for the two models, or the residual dipole moment is defined differently. The magnetic field models have already been compared in Section 4.6.1. As the reference documentation of both models state the same method to calculated the magnetic disturbance torque, no other option can be left than a difference in the residual dipole moment. It was found that the residual dipole moment was initially wrongly defined in ADS (too high). This has been corrected, but the results are still far off.

As the calculation of the magnetic disturbance torque is very straightforward, no other conclusion can be drawn that the results of ADS are not to be trusted. The GGNCSim implementation is assumed to be correct.

4.6.5 Solar Radiation Disturbance Load

In this subsection the resulting solar-radiation disturbance loads from the SPS-2 model are compared to the results of ADS. Three test-cases have been considered here:

- Wall component only (simple case). Orbit C (at Vernal Equinox, such that the Sun crosses the equatorial plane) and orientation D (spacecraft body XY-plane in equatorial plane, X-axis parallel to Sun vector). The spacecraft is inertial fixed. The results of both simulators are identical.
- Plate component only (simple case). Orbit C (at Vernal Equinox, such that the Sun crosses the equatorial plane) and orientation E (spacecraft Z-axis parallel to Sun vector, but in opposite direction, spacecraft XY-plane perpendicular to equatorial plane). The spacecraft is inertially fixed. The results of both simulators are identical.
- Plate and wall component (complex case). Orbit B, orientation C (the spacecraft is oriented in an arbitrary orientation). The results of both simulators are identical.

4.6.6 Summary of Results

The following discrepancies have been found:

- The ADS and GGNCSim aerodynamic models have been compared based on four test cases. It has been found that there was a sign error in the wall contribution of the aerodynamic force in the GGNCSim model implementation, which has been corrected after. Furthermore, in ADS the aerodynamic disturbance torque is wrongly calculated. It appears that the distance $\mathbf{r}^B_{COM}$ is used to calculate the aerodynamic disturbance torque (despite what is claimed in the reference documentation). However, the distances $\mathbf{r}^B_{plate}$ and $\mathbf{r}^B_{wall}$ should be used here.
- As the calculation of the magnetic disturbance torque is very straightforward, no other conclusion can be drawn that the results of ADS are not to be trusted.

Chapter 5
SENSORS AND ACTUATORS

The structure of this chapter is as follows. In Section 5.1, some background information is given for the different sensors and actuators used in the SPS-2 project. In Section 5.2, the sensor and actuator models are discussed.

5.1 General Background Information

This section will give some background information for the different sensors and actuators used in the SPS-2 project. A short description of the magnetometer, magnetorquer and the Sun sensor is given in Sections 5.1.1, 5.1.2 and 5.1.3. For each of these sensors/actuators, an overview will be given of the error sources, which shall be taken into account in the model implementation. The reaction wheel and gyroscope are discussed briefly in Sections 5.1.4 and 5.1.5.

Note that the purpose of this section is only to provide some background information and to identify the error sources. With the identified error sources, the sensor and actuator models will be developed in Section 5.2. The selection of each type of sensor/actuator to be used in the SPS-2 project is left for future work. That selection shall be based on the results of the simulation runs in Chapters 7 and 8.

5.1.1 Magnetometers

Application

A magnetometer measures the direction of the Earth magnetic field vector in the spacecraft frame. To measure the local Earth magnetic field as accurately as possible, it is important to keep the magnetometer away from disturbing magnetic fields in the satellite (Wertz, 1978). The nearby presence of a magnetorquer should thus be avoided, which also holds for high current traces. Magnetometers are in general cheap and reliable (Wittmann, 2009).

Types

The fluxgate magnetometer and the magneto-resistive magnetometer are most commonly used for space applications. These which will be discussed here.

- *Fluxgate magnetometers* are available in two kinds: the ring core and the rod core magnetometers. See Figure 5.1 for an illustration. The working principle of a fluxgate magnetometer is as follows (Primdahl, 1979). A ferromagnetic core is wrapped with a coil of wire, through which an alternating current is passed. This induces an alternating magnetic field, which is strong enough to drive the the ferromagnetic core into an alternating cycle of magnetic saturation. With a ring core magnetometer, a second coil (sensing coil) surrounds the total assembly. With a rod core magnetometer, the sensing coil is wrapped around the ferromagnetic core, but in opposing direction. However, the working principle of both is identical. The change in magnetic field induces an electric current in the sensing coil. The difference between the current in the sensing and drive coil is a measure for the external magnetic field strength. When no external magnetic field would be present, these currents would be identical. As a result of an external field, the core will be more easily saturated in alignment with the field, and less easily saturated in the opposing direction.

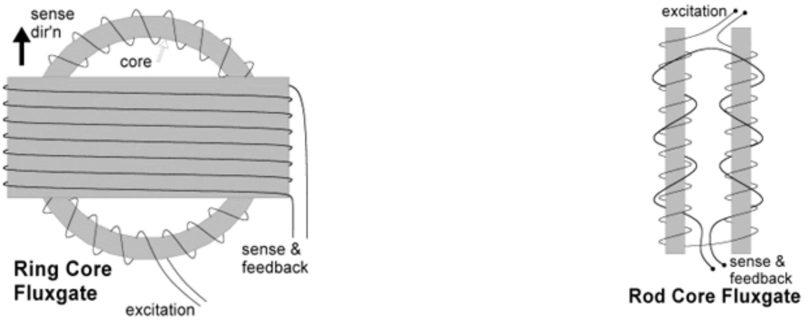

Figure 5.1: *A ring core fluxgate magnetometer (left) and a rod core fluxgate magnetometer (right).*[1]

- *Anisotropic-Magneto-Resistive* (AMR) magnetometers are made of thin strips of permalloy (nickel-iron magnetic alloy) (Ripka, 2003). The electrical resistance of the material varies with a change in the external magnetic field. As such, the magnetic field direction and strength can be obtained.

No specific choice has been made, which type of magnetometer shall be used.

Error identification

The most common error sources for the magnetometers have been obtained from the specification sheets of currently available magnetometers on the market. Table E.1 lists the specifics of these magnetometers.

Based on the specification sheets of the manufacturers, the error sources, which have been identified for the magnetometers are the scale factor error (with a temperature dependency), the zero-field bias, the zero-field bias drift (with a temperature dependency), the linearity error, a noise and a misalignment error. The common error sources are explained in more detail in Section 5.2.2. The implementation of these error sources in the magnetometer model is discussed in Section 5.2.5. The minimum, nominal and maximum errors, which have been defined are listed in Table 5.2.

A concluding remark has to be made about the order of magnitude of the noises, which have been specified. Most noise values, which have been found are 10-150 pT RMS/$\sqrt{}$Hz. The contribution of the noise error is therefore much smaller than other error sources. Outliers are the noise values specified by MEDA and ZARM Technik, which are in the order of 10 nT RMS/$\sqrt{}$Hz. That is remarkable, because these magnetometers are more expensive. The noise values used in a comparative design of (Tuthill, 2009) are 125 nT RMS/$\sqrt{}$Hz, which

---

[1] `http://www.sensorland.com/HowPage071.html#anchor162680`, accessed 30 July '15.

is even higher. That value is in the same order as the zero field bias error, the scale factor error and the nonlinearity error.

5.1.2 Magnetorquers

Application

The torquers will be used to detumble the satellite after separation and to desaturate the reaction wheels. The working principle of a magnetorquer is as follows. A magnetorquer generates a magnetic field when a electric current is applied. This magnetic field in turn interacts with the Earth's magnetic field, producing an output torque, which is in a plane perpendicular to the local geomagnetic field. The nominal torque output of the magnetorquer is as follows:

$$\mathbf{T} = \mathbf{m} \times \mathbf{B} \tag{5.1.1}$$

where $\mathbf{B}$ is the Earth-magnetic-field vector in T and $\mathbf{m}$ is the magnetic dipole moment created by the magnetorquer in Am^2. More details about the magnetic dipole moment of the torquer can be found in Appendix D.1.

Magnetorquers are characterized by their simplicity (no moving parts), a high reliability, low energy consumption and low costs, according to (Wertz, 1978). The use of a magnetorquer brings some disadvantages too. The torque output is perpendicular to the magnetic field. As such, no full 3-axis control is possible. Furthermore, torquers are not very useful for agile maneuvering, as the torque output is limited. The maximum torque output of a 15 Am^2 torquer is $\sim$ 1 mNm, whereas the reaction wheels considered in this thesis work can provide torques of 30 - 50 mNm.

Types

There are three types of magnetorquers, discussed by (Bellini, 2014):

- *Air core* magnetorquers, which consist of a certain number of turns of copper wire wrapped in wide circles. The torque output is limited.
- *Torque rod* magnetorquers, where the windings have the form of a solenoid. Within the solenoid volume, a material with magnetic properties is placed that amplifies the dipole moment the magnetorquer produces. These are the most powerful magnetorquers currently available.
- *Embedded* magnetorquers, which are integrated on a printed circuit board. For (constrained) three-axis control one air core and two torque rod magnetorquers are embedded. The advantage of this approach is that this saves volume, but the torque capacity is limited due to the size.

In the preliminary work by (Munatsi, 2016b), a required magnetic dipole moment of 15 Am^2 was estimated. The torquers, which will be considered in this thesis work will be characterized with magnetic dipole moments in the range of 10 - 30 Am^2. As such, only torque rods will be considered further.

Induced magnetic field

Here, the induced magnetic field of the magnetorquer will be looked at, which is an important property, because the magnetorquer can disturb the magnetometer measurements of the Earth magnetic field. The induced magnetic field strength at different distances can be seen in Table 5.1. The results have been obtained for a torquer with a magnetic dipole moment of 30 Am^2. See Section D.2 for the full analysis. The induced magnetic field at close vicinity to the magnetorquer is much larger than the ambient Earth magnetic field strength (which is around 50 μT).

Table 5.1: *Induced magnetic field strength for the MTR-30 magnetorquer.*

Distance from torquer	Induced magnetic field strength
0.0 m	1786.3 μT
0.1 m	1307.1 μT
0.5 m	105.3 μT
1.5 m	4.9 μT

In the SPS-2 project the distance between the magnetometer and the magnetorquer is smaller than 0.5 m, as both are situated in the service module. Therefore, it will not be possible to perform measurements with the magnetometer whilst actuating with the magnetorquer. This should be taken into account in the detumble control.

Error identification

The most common error sources for the magnetorquers have been obtained from the specification sheets of currently available magnetorquers on the market, summarized in Table E.2. Note that only torque rod magnetorquers have been considered here. The specification sheets have been included in a separate document.

The two error sources, which have been identified for the magnetorquers are the residual dipole moment and the nonlinearity error. In addition, a misalignment error will be considered. The implementation of these error sources in the magnetorquer model is discussed in Section 5.2.6. The minimum, nominal and maximum errors which have been defined are listed in Table 5.3.

5.1.3 Sun sensors

Application

The Sun sensor is used to measure the Sun-vector direction. Sun sensors are characterized by a high reliability. Different types of Sun sensors exist. These can either be analogue or digital. With analogue Sun sensors, photo-diodes are used to generate one or more analogue currents. With digital Sun sensors, an array of photocells may be used, or a CCD (charge-coupled device, which converts electromagnetic radiation into an electric current) (Wittmann, 2009).

Types

Commonly known Sun sensors are pyramid, four-quadrant, digital-slit, digital pin-hole and analogue coarse Sun sensors (Wertz and Larson, 2007).

Figure 5.2: *Bradford pyramid and four-quadrant Sun sensors.*[2]

- The working principle of the *four-quadrant Sun sensor* is as follows. The Sun direction is reconstructed based on the difference in illumination of the 4 quadrants. *Pyramid Sun sensors* work with a similar principle, i.e., the Sun angles can be determined by a simple function of the four output currents, but also offer a near-hemispherical field of view. Another advantage of pyramid Sun sensors is the internal redundancy, as each side has two independent photo-detectors. Both type of sensors are vulnerable to incoming light from non-solar sources, such as the Earth albedo. This decreases the measurement accuracy. The pyramid Sun sensors are expected to be much more expensive (based on the experience of specialists at Airbus) and will not be considered further.
- *Digital Sun sensors* have several advantages over the analogue Sun sensors. These type of sensors achieve higher accuracies and avoid the problems with light being reflected from the Earth's surface (Wittmann, 2009). However, these Sun sensors are much more expensive, based on the experience of experts at Airbus. As such, these will not be considered further.
- *Coarse Sun sensors* (also referred to as Sun presence or Sun acquisition sensors) in general consist of solar cells which are attached to the different sides of the spacecraft. This type of Sun sensors is characterized by low accuracies ($10 - 20°$) (Wittmann, 2009). As such, these will not be considered here.

To summarize: only four-quadrant Sun sensors will be considered further.

Earth-albedo effect

The Earth-albedo contribution can be approximately 30% of the incident Sunlight (Wertz and Larson, 2007), however, this strongly depends on the orbit. Furthermore, it depends whether the satellite is situated above land, water or icy surfaces and possible cloud formations. The disadvantage of analogue Sun sensors is that the reflected light from the Earth (or Moon) surface cannot be distinguished from direct Sunlight. This will affect the Sun-vector measurement. To include this effect, an Earth albedo model should be implemented. However, this analysis has not been performed due to time constraints. This is left as future work. In the model implementation in Section 5.2.7, the impact has studied, based on a pragmatic approach.

---

[2] `http://bradford-space.com/`, accessed June '16.

Error identification

The most common error sources, which have been found for the four-quadrant Sun sensors, based on the specification sheets of currently available Sun sensors on the market, are summarized in Table E.3. Again, these specification sheets have been included in a separate document.

The error sources, which have been identified for the Sun sensors are the noises in boresight direction and for the whole field of view. Furthermore, misalignments will be considered. The implementation of these error sources in the Sun sensor model is discussed in Section 5.2.7. The minimum, nominal and maximum errors which have been defined are listed in Table 5.4.

5.1.4 Reaction wheels

With the reaction wheels, the spacecraft attitude can be controlled. A reaction wheel works on the basis of momentum exchange between the wheel rotor and the spacecraft. The larger the wheel inertia and the higher the wheel speed range, the more momentum can be exchanged. The flywheel rotation is driven by an electric motor, which allows for a variable adjustment of torque. Reaction wheels have a limited lifetime during due to bearing wear. Static and dynamic imbalances produces micro-vibrations. Stiction effects around zero speed causes disturbance torques, therefore zero speed crossings should be avoided (Wittmann, 2009). A disadvantage of the use of reaction wheels is that these do not take out the momentum of the satellite. Reaction wheels can only be used to exchange momentum of the spacecraft with the wheels. In addition with external disturbances, the wheels need to be offloaded frequently.

The reaction-wheel model has been developed by (Munatsi, 2016a). The two reaction wheels, which will be considered are listed in Table 5.7. The minimum, nominal and maximum errors, which have been defined are listed in Table 5.8. The implementation of these error sources in the reaction wheel model is discussed in Section 5.2.8.

5.1.5 Gyroscopes

Gyroscopes are used to measure the rotation of the spacecraft body in the inertial reference frame. However, gyros do not offer direct attitude measurements. Gyroscopes are completely independent of external sources, such that these can be used in all instances (Wittmann, 2009). There are several specific error sources, which affect the gyro measurements. Apart from the common errors (such as the scale factor error, nonlinearity, noise, misalignments) the bias exhibits a drift in time. This drift is caused by the Rate Random Walk (RRW). To compensate for this drift, the gyro measurements can be corrected with the use of a direct attitude measurement. An example is the use of star trackers, in combination with a Extended Kalman Filter (EKF) (Landis Markley and Crassidis, 2014).

The gyroscope model has been developed by (Munatsi, 2016a). The minimum, nominal and maximum errors, which have been defined for the gyro model, are listed in Table 5.9. The implementation of these error sources in the gyroscope model is discussed in Section 5.2.9.

5.2 Sensor and Actuator Model Development

In this section the magnetometer, magnetorquer, Sun sensor model, gyroscope and reaction wheel models will be discussed. First, an overview will be given of the implementation of the unit models. Then, the model parameters will be shown. Finally, the verification of the model will be discussed.

But first, the approach will be described in Section 5.2.1. The commonly described errors will be presented in Section 5.2.2. The implementation of the misalignment and scale factor error is discussed in Section 5.2.3 and the implementation of the nonlinearity error is discussed in Section 5.2.4.

5.2.1 Approach

The models, which will be developed in this section, need to be verified and validated. The approach which has been adopted to, is as follows:

1. Derive the analytic equations for the model, including the error sources. The error sources for each model have been obtained from the error identification in Sections 5.1.1, through 5.1.3.
2. Based on the analytic equations, make a stand-alone model.
3. Verify that the results of the stand-alone model are correct. This is discussed in detail in Sections 5.2.5 through 5.2.9.
4. Validate the model.
5. Integrate the unit model into the full simulator.
6. Verify that the results are according to the expectations. This is done with unit tests and the approach is very trivial. The results will not be discussed here.

If anywhere in the procedure a difference occurs between the simulated and expected outcome, the origin of this discrepancy shall be retraced. Based on that, the model shall be adjusted or this discrepancy shall be explained in the documentation.

The validation part consists of validating the models with the test-data of the actual hardware. However, in this project no such data is available. An alternative is to perform a verification of the results with benchmark tests, which sometimes can be found in literature. Again, no such data could be found. Therefore, unfortunately the validation step has been omitted.

5.2.2 Commonly described error sources

Common error sources for different sensors and actuators are:

- *Biases* are constant errors independent from the underlying specific force or angular rate that add an offset to the true output (Mooij, 2011).
- *Nonlinearity errors* give the errors between the true nonlinear signal and the linear approximation.
- *Scale factor errors* are caused by tolerances in manufacturing or due to aging, and adds an error tot the output proportional to the specific force or angular rate (Mooij, 2011).
- *Noises* are random variations in a signal.

- *Misalignment errors* arise from the misalignments of the sensitive axis (Mooij, 2011).
- *Saturation* occurs when the dynamic range of the measured quantity exceeds the capabilities of the senor, the output will either the minimum or maximum value (Mooij, 2011).
- *Quantization* is the result of using a finite number of digits to represent the measurements. As a consequence, the accuracy of all digital measurements is limited and the output changes step-wise (Mooij, 2011).

The bias, nonlinearity error and the scale factor error are visualized in Figure 5.3.

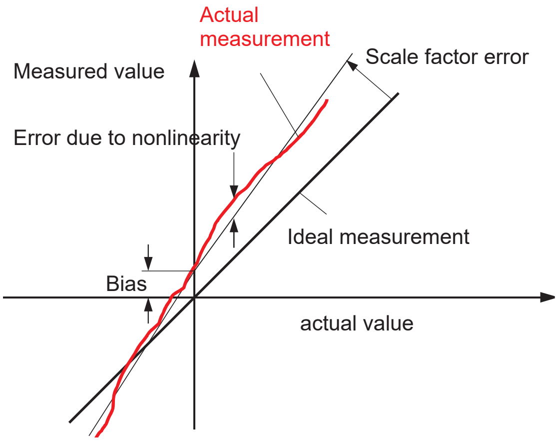

Figure 5.3: *Several error sources for sensors and/or actuators (Wittmann, 2009).*

5.2.3 Implementation misalignment and scale factor error

Different implementations are possible for the misalignment and scale factor error. The implementation used often in literature is presented first. Two alternative implementations are presented. At the end, a choice is made between the different methods.

- **First method**

  The implementation method commonly described in literature (Landis Markley and Crassidis, 2014) is as follows:

$$\mathbf{u}_{meas} = (\mathbf{I}_{3\times3} + \mathbf{M} + \mathbf{S})\,\mathbf{u}_{true} \tag{5.2.1}$$

where $\mathbf{M}$ is the misalignment matrix (3×3), $\mathbf{I}_{3\times3}$ is the identity matrix (3×3) and $\mathbf{S}$ is the scale factor error (3×3). It can be written that:

$$(\mathbf{I}_{3\times3} + \mathbf{M} + \mathbf{S}) = \mathbf{I}_{3\times3} + \begin{bmatrix} 0 & m_{xy} & m_{xz} \\ m_{yx} & 0 & m_{yz} \\ m_{zx} & m_{zy} & 0 \end{bmatrix} + \begin{bmatrix} S_x & 0 & 0 \\ 0 & S_y & 0 \\ 0 & 0 & S_z \end{bmatrix} \tag{5.2.2}$$

$$= \begin{bmatrix} S_x + 1 & m_{xy} & m_{xz} \\ m_{yx} & S_y + 1 & m_{yz} \\ m_{zx} & m_{zy} & S_z + 1 \end{bmatrix} \equiv \hat{\mathbf{M}} \tag{5.2.3}$$

Note that m_{ij} is the contribution of the j-axis measurement (the axis along the measurement is performed) to the i-axis component. The misalignments m_{ij} are calculated with $\sin(\alpha_{ij})$, where α_{ij} are the misalignment angles.

The disadvantages of this implementation method are:

- The norm of the measured vector changes after applying the misalignment error, as the diagonal terms of the misalignment matrix are set to 0.
- The scale factor error is only applied to the measurement axis.
- The scale factor error is applied to the true vector, instead of the (true) misaligned vector.

- **Second method**
  The implementation of the misalignment error and the scale factor error proposed here is slightly different. Again, consider the measurement equation, but now in a slightly different format:

$$\mathbf{u}_{meas} = (\mathbf{I}_{3\times3} + \mathbf{S})\mathbf{M}\,\mathbf{u}_{true} \tag{5.2.4}$$

$$\mathbf{u}_{meas} = \begin{bmatrix} S_x+1 & 0 & 0 \\ 0 & S_y+1 & 0 \\ 0 & 0 & S_z+1 \end{bmatrix} \begin{bmatrix} m_{xx} & m_{xy} & m_{xz} \\ m_{yx} & m_{yy} & m_{yz} \\ m_{zx} & m_{zy} & m_{zz} \end{bmatrix} \mathbf{u}_{true} \tag{5.2.5}$$

It can be seen that with this implementation, the scale factor error is applied to all contributions of the measured (misaligned) vector. The misalignments m_{xx}, m_{yy} and m_{zz} ensure that the norm of the vector is contained:

$$\text{X-axis:} \quad \left.\begin{aligned} m_{yx} &= \sin(\alpha_{yx}) \\ m_{zx} &= \sin(\alpha_{zx}) \end{aligned}\right\} \text{with } m_{xx} = \sqrt{1 - m_{yx}^2 - m_{zx}^2} \tag{5.2.6}$$

$$\text{Y-axis:} \quad \left.\begin{aligned} m_{xy} &= \sin(\alpha_{xy}) \\ m_{zy} &= \sin(\alpha_{zy}) \end{aligned}\right\} \text{with } m_{yy} = \sqrt{1 - m_{xy}^2 - m_{zy}^2} \tag{5.2.7}$$

$$\text{Z-axis:} \quad \left.\begin{aligned} m_{xz} &= \sin(\alpha_{xz}) \\ m_{yz} &= \sin(\alpha_{yz}) \end{aligned}\right\} \text{with } m_{zz} = \sqrt{1 - m_{xz}^2 - m_{yz}^2} \tag{5.2.8}$$

- **Third method**
  A simplification of the second method is as such:

$$\mathbf{u}_{meas} = (\mathbf{I}_{3\times3} + \mathbf{S})\mathbf{M}\,\mathbf{u}_{true} \tag{5.2.9}$$

$$\mathbf{u}_{meas} = \begin{bmatrix} S_x+1 & 0 & 0 \\ 0 & S_y+1 & 0 \\ 0 & 0 & S_z+1 \end{bmatrix} \begin{bmatrix} 1 & m_{xy} & m_{xz} \\ m_{yx} & 1 & m_{yz} \\ m_{zx} & m_{zy} & 1 \end{bmatrix} \mathbf{u}_{true} \tag{5.2.10}$$

With this implementation, the norm of the measured vector is not contained.

Now a decision will be made between the different implementations. Although the first implementation method is used often in literature, the author has decided not to use this method. A more realistic model implementation has been suggested with the second method. The third method is a simplification of the second method, where the norm of the measured vector is not contained after applying a misalignment error.

It appears that the misaligned axis contribute 1.75% to the total scale factor error for a maximum misalignment error of 1°. The ideal implementation of the misalignment error results in a change of only 0.03% in the contribution of the measured axis output. Based on these contributions, it has been chosen to implement the third method.

5.2.4 Implementation nonlinearity error

The nonlinearity error gives the error between the true nonlinear signal and the linear approximation. In literature no information could be found on the implementation of the nonlinearity error. In the specification sheets the nonlinearity error is specified as a percentage of the full range. The manufacturers most probably make the linear fit such that it minimizes the error over the full range. The following approach has been discussed and agreed upon at Airbus.

To construct the nonlinearity error, the measure/output range of the sensor/actuator is divided in 16 equally spaced intervals. For each of the points randomly a nonlinearity error is assigned, with a threshold value of the maximum nonlinearity error specified. Through a 1-D shape-preserving piecewise cubic interpolation method the points are connected. The interval size is 1/1000 of the full scale. The nonlinearity error is seed dependent, where an uniformly distributed pseudorandom generator has been used. Figure 5.4 illustrates the resulting nonlinearity error for a given seed.

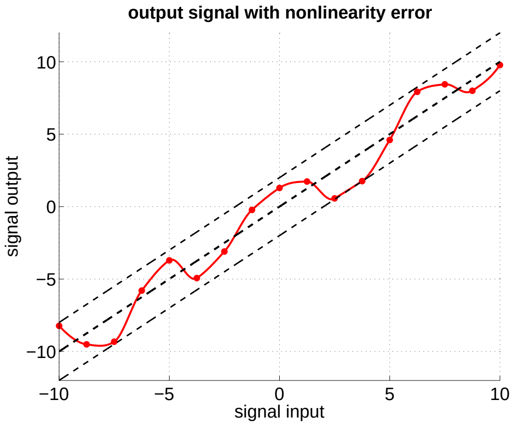

Figure 5.4: *An example of the implementation of the linearity error, for a range of ±10 and a maximum nonlinearity error of 2.*

5.2.5 Magnetometer model development

In this section the magnetometer model is discussed. First, an overview will be given of the implementation of the model. Then, the model parameters will be shown. Finally, the verification of the model will be discussed.

Magnetometer model overview

The input of the magnetometer model is the magnetic field vector in the B-frame. The magnetic field vector is first transformed to the MTM-frame. Then, subsequently the misalignments, the scale factor error, the nonlinearity error, the bias and the noises are applied. At last, the measured signal will be quantized and the measurements will be transformed to the B-frame.

The measurement equation for the magnetometer in the unit frame is described in this form:

$$\mathbf{B}_{meas} = (\mathbf{I}_{3\times 3} + \mathbf{S})\mathbf{M}\,\mathbf{B}_{true} + \mathbf{b} + \boldsymbol{\nu} + \boldsymbol{\eta} \tag{5.2.11}$$

where $\mathbf{B}$ is the magnetic field vector in the unit frame (3×1), $\mathbf{M}$ is the misalignment matrix (3×3), $\mathbf{S}$ is the scale factor error (3×3), $\mathbf{b}$ is the bias, which consists of the zero-field bias and the zero-field bias drift (3×1), $\boldsymbol{\nu}$ is the nonlinearity error (3×1) and $\boldsymbol{\eta}$ is the measurement noise (3×1).

No transport delays have been added. However, this effect will be considered in the stability analysis of the controllers.

Magnetometer model parameters

Table 5.2 lists the minimum, nominal and maximum parameter values for the magnetometer model. These are based on Table E.1.

Table 5.2: *Model parameters for the magnetometers, based on the specification sheets in Table E.1.*

parameter	MIN	NOM	MAX	unit
measurement range	100	100	100	μT
scale-factor error	100	150	600	ppm/°C
linearity error	10	100	500	nT
zero-field bias	50	150	250	nT
zero-field bias drift	1	1	1	nT/°C
temperature	10	30	50	°C
noise (1σ)	20	50	150	pT (RMS/$\sqrt{}$Hz)
misalignment angle	0.1	0.5	1	°
quantization step-size	16	12	8	bits
quantization step-size	0.0031	0.0488	0.7813	μT

Two remarks have to be made about the content of Table 5.2. The noise values are varied towards the largest values as documented in the specification sheets, see Section 5.1.1. After an internal discussion within Airbus it has been decided not to consider the outliers, as there are multiple affordable alternatives. Furthermore, Airbus has specified a thermal range of between 10°C and 50°C.

Magnetometer model verification

To verify the magnetometer model, two simulation verification runs have been performed, which differ in complexity of the input signal. These input profiles are shown in Figure 5.5. The maximum magnetometer errors from Table 5.2 have been considered.

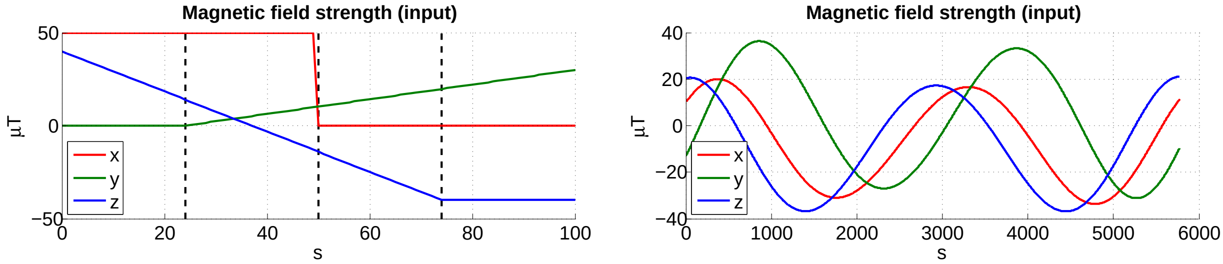

Figure 5.5: *The simple (left) and complex (right) input signals for the verification of the magnetometer model.*

The implementation of the misalignment error, the scale factor error, the nonlinearity error, the bias, the noise and the quantization error will be looked at. The errors have been considered one at a time, unless stated differently.

- **Simple input profile**
  In this test-case a simple input profile has been selected, characterized by four stages. In each of the different stages the contribution of the magnetic field is slightly different. In this manner, it can be easily be verified whether the implementation of the different error sources is correct.

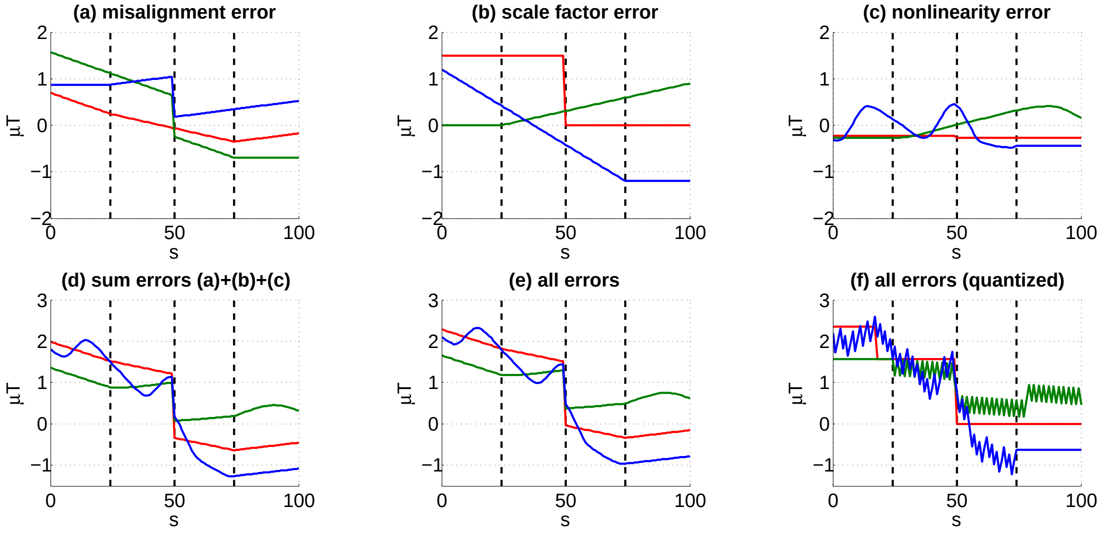

Figure 5.6: *Verification of the magnetometer model. The input signal is a simple magnetic field strength profile, where four different stages can be identified.*

The results are shown in Figure 5.6. The misalignment error (a), the scale factor error (b) and the nonlinearity error (c) have been considered first, after which their summed contribution is shown (d). The bias and noise contributions are independent of the input signal. Their contribution is shown on top of the summed contribution (e). Finally, the difference between the input signal and the quantized signal is shown (f), which includes all error sources.

Two remarks have to be made. First, note that plots (d) and (e) are almost identical. The bias error contribution in (e) is small, and the measurement noise is negligible.

This can be seen in Figure 5.7. The second remark is regarding the quantized signal. It might be that one would expect the outcome of Figure 5.7 (right plot) instead. However, note that the sum of the errors shown in (f) is not quantized, but the measured signal is. Therefore the result as shown in (f) is correct.

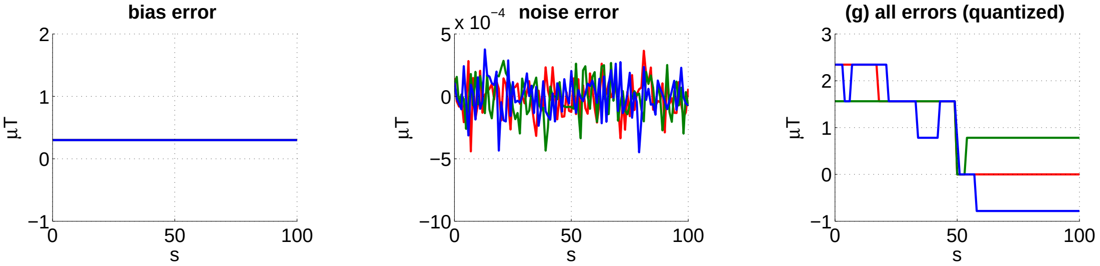

Figure 5.7: *Left: bias error. Middle: noise error. Right: all errors combined (quantized).*

- **Complex input profile**
  Now the complex input profile will be considered. The magnetic field strength profile used here is representative for the SPS-2 orbit. The results are shown in Figure 5.8.

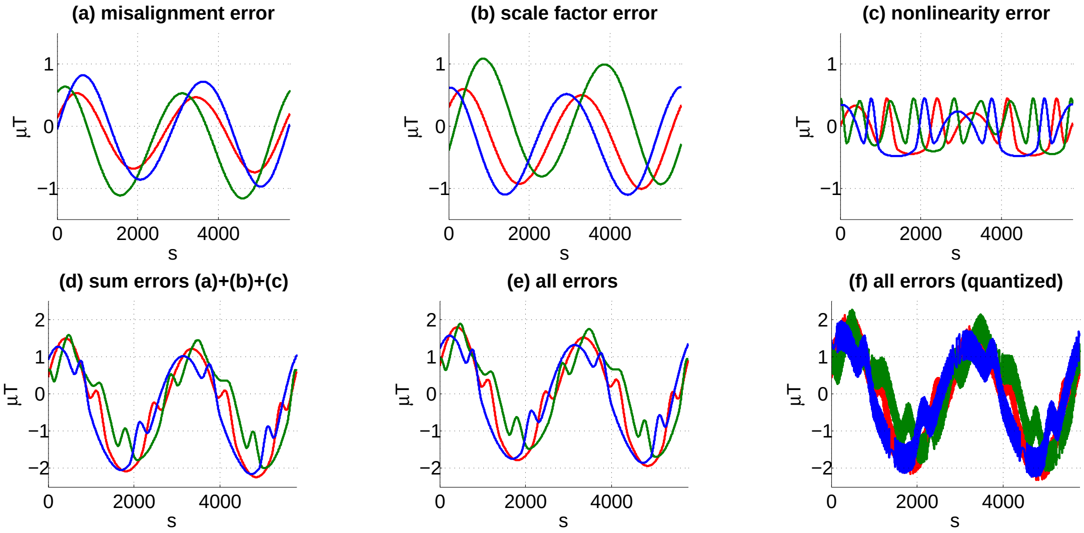

Figure 5.8: *Verification of the magnetometer model. The input signal is the the magnetic field strength profile which can occur during the SPS-2 orbit.*

As with the simple input profile, note that plots (d) and (e) are almost identical, for the same reasons as before. Furthermore, it can be seen that the misalignment error and the scale factor error are the dominant error sources. Note that the quantization error is also significant, because the chosen quantization step-size is very large. However, the performance of the controller will be looked at for different quantization step-sizes, as previously shown in Table 5.2.

The simple and complex input profiles have shown that the implementation of the different error sources is as expected. With this, verification of the magnetometer model has been concluded.

5.2.6 Magnetorquer model development

In this section the magnetorquer model is discussed. First, an overview will be given of the implementation of the model. Then, the model parameters will be shown. Finally, the verification of the model will be discussed.

Magnetorquer model overview

The input of the model is the magnetic dipole moment request in the B-frame. The magnetic dipole moment request is first transformed to the MTQ-frame. The misalignments will be applied, after which the nonlinearity error and the residual dipole moment are added. A saturation block prevents the magnetic dipole moment output to exceed the limit value. The magnetic dipole moment will then be transformed to the B-frame. The torque output follows from the cross product between the magnetic dipole moment and the magnetic field strength, as given by Equation (5.1.1).

The output magnetic dipole moment of the magnetorquer (in the MTQ-frame) is described in this form:

$$\mathbf{m}_{\text{output}} = \text{saturate}\left[\mathbf{M} \cdot \mathbf{m}_{\text{command}} + \mathbf{b} + \boldsymbol{\nu}\right] \tag{5.2.12}$$

where $\mathbf{m}$ is the magnetic dipole moment, $\mathbf{M}$ is the misalignment matrix (3×3), $\mathbf{b}$ is the bias (which consists only of the residual dipole moment) (3×1) and $\boldsymbol{\nu}$ is the nonlinearity error (3×1). The saturation block will limit the magnetic dipole moment output.

Finally, the torque output of the magnetorquer (in the B-frame) is described with:

$$\mathbf{T}_{\text{output}} = \mathbf{m}_{\text{output}} \times \mathbf{B} \tag{5.2.13}$$

where $\mathbf{T}$ is the torque output in the B-frame, $\mathbf{m}$ is the magnetic dipole moment in the B-frame and $\mathbf{B}$ the magnetic field strength in the B-frame.

The residual dipole moment will be implemented as a constant offset (bias) with the maximum residual dipole moment specified by the manufacturers. Note that the residual dipole moment is the measure of the remanence of the hysteresis cycle, which is explained in detail in Section D.3. However, no literature could be found how to accurately model this. The current approach yields the worst-case scenario.

Another aspect, which has not been considered, is the possible delay in the torque output due the coil rise time. The coil rise time is the time it takes to build-up a certain current level, given a voltage input. A typical rise-time is expected to be only a fraction of a second. However, the impact of delays will be investigated in the stability analysis of the controllers.

Magnetorquer model parameters

Table 5.3 lists the minimum, nominal and maximum parameter values for the magnetorquer model. These have been selected from Table E.2.

Table 5.3: *Model parameters for the magnetorquers, based on the specification sheets in Table E.2.*

parameter	**MIN**	**NOM**	**MAX**	**unit**
range	10	15	30	Am^2
nonlinearity error	0.5625	0.75	1.125	Am^2
residual dipole moment	0.075	0.1	0.15	Am^2
misalignment angle	0.1	0.5	1	°

The model parameters, which have been found for the nonlinearity and residual dipole moment error are very consistent. It has been decided to vary the minimum and maximum linearity error and the residual dipole moment have towards 75% and 150% of the nominal value.

Magnetorquer model verification

The magnetorquer model shows similarities with the magnetometer model. Again a misalignment has been included, together with a (constant) bias and the nonlinearity error. It is not necessary to discuss these again in full detail. This section will discuss the resulting torque output.

Given the magnetic field strength in the B-frame shown in Figure 5.9 (left) and the resulting magnetic dipole moment in the B-frame in Figure 5.9 (middle), which has been saturated at 15 Am^2, the resulting torque output in the B-frame is constructed. This is shown in Figure 5.9 (right). Calculations by hand can easily show the correctness of the current implementation.

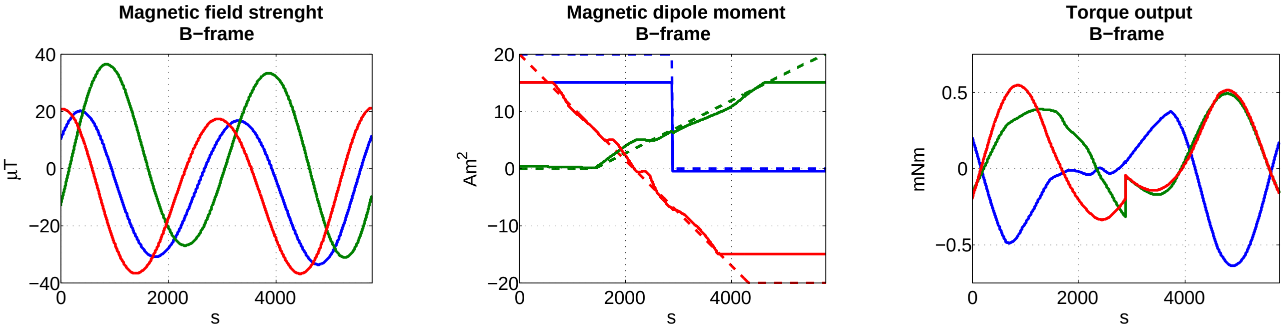

Figure 5.9: *Left: magnetic field strength. Middle: magnetic dipole moment output, including all errors (dotted line is input). Right: resulting torque output of the magnetorquer model.*

5.2.7 Sun sensor model development

In this section the Sun sensor model is discussed. First, an overview will be given of the implementation of the model. Then, the model parameters will be shown. Finally, the verification of the model will be discussed.

The Sun sensor model is partly based on the `'Fine sun sensor'` model from the GGNC-Sim repository (Ellenbroek, 2011). However, in that model no boresight accuracy is implemented. Note that this model also does not include the Earth-albedo error. The impact of not modeling the Earth albedo on the measurements is elaborated on at the end of this section.

Sun sensor model overview

The input of the Sun sensor model is the unit Sun vector in the B-frame. The unit Sun vector is first transformed to the S-frame, after which the misalignments are applied. From the resulting unit Sun vector in the S-frame ($\mathbf{n}^{SS}_{Sun}$) the angles α and β are calculated and subsequently the noises are added. Finally, the measured angles will be quantized. The measured angles are used to reconstruct the Sun vector in the SS-frame.

Note that in practice, the four-quadrant Sun sensor measures four voltages. From these voltages two angles α and β can be obtained. In the Sun sensor model these angles α and β are calculated directly from the incident Sun vector in the Sun-sensor frame (SS-frame).

The angle α denotes the angular distance of the projection of the Sun vector between +Z and +X axis in the S-frame. Note that this angle is measured in the XZ-plane. Angle β denotes the angular distance of the projection of the Sun vector between the +Z and +Y axis in the S-frame. Note that this angle is measured in the YZ-plane. Figure 5.10 shows these angles.

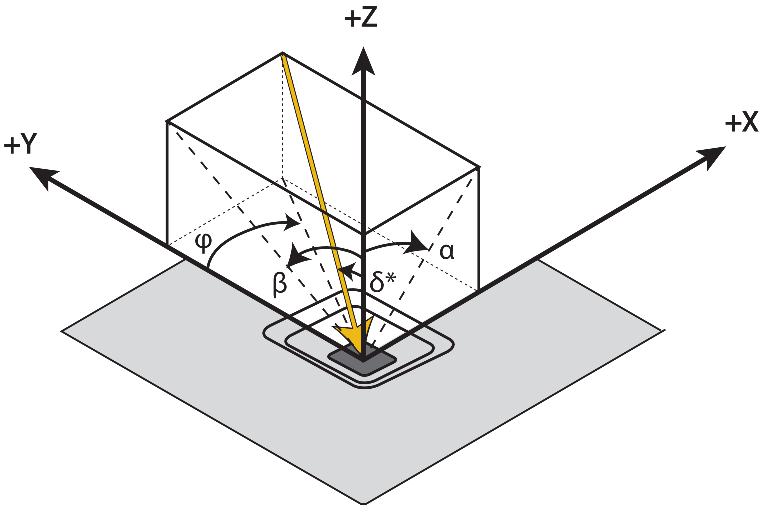

Figure 5.10: *Definition angles α, β, φ and δ in the Sun-sensor frame (SS-frame).*

The first step is to transform the Sun vector from the inertial frame to the S-frame, after which a misalignment is applied. Given the unit Sun vector $\mathbf{n}^{SS}_{Sun}$ in the S-frame, the angles α and β can now be calculated with:

$$\tan(\alpha) = \frac{\mathbf{n}^{SS}_{Sun,x}}{\mathbf{n}^{SS}_{Sun,z}} \equiv N_x \tag{5.2.14}$$

$$\tan(\beta) = \frac{\mathbf{n}^{SS}_{Sun,y}}{\mathbf{n}^{SS}_{Sun,z}} \equiv N_y \tag{5.2.15}$$

Now that the angles α and β have been calculated, it is determined whether the Sun vector is in the Field of View (FoV) of the sensor. For this, these angles shall *both* be smaller than the cut-off angle of the pyramid cone, which is shown in Figure 5.11. Furthermore, it is verified whether the satellite is not in eclipse conditions. If both are true, then the noises are added. The magnitude of the noise value depends on whether the Sun-vector measurement is in boresight direction or just in the whole FoV. Higher accuracies are achieved in the boresight direction. When the satellite happens to be in eclipse conditions, or when the Sun is not in the FoV, the measured angles are zero.

Finally, the measured angles are quantized. No transport delays have been added. However, the effect will be considered in the stability analysis of the controllers.

Up to this point, the physical process of the Sun sensor has been represented, although in a simplified manner. In a different part of the simulator (in the sensor data processing block in the on-board computer) the Sun vector is reconstructed given the measured angles α and β. This can be done as follows. The azimuth angle φ and the co-elevation angle δ^* (see Figure 5.10) need to be calculated first:

$$\tan^2\delta^* = \tan^2\alpha + \tan^2\beta = N_x^2 + N_y^2 \tag{5.2.16}$$

$$\tan(\varphi) = \frac{\tan\alpha}{\tan\beta} = \frac{N_x}{N_y} \tag{5.2.17}$$

Then the unit Sun vector in the S-frame can be reconstructed with:

$$\mathbf{n}_{Sun,x}^{SS} = \sin\varphi\sin\delta^* \tag{5.2.18}$$

$$\mathbf{n}_{Sun,y}^{SS} = \cos\varphi\sin\delta^* \tag{5.2.19}$$

$$\mathbf{n}_{Sun,z}^{SS} = \cos\delta^* \tag{5.2.20}$$

Finally, the measured Sun vector in the S-frame will be transformed to the B-frame.

Note that Equations (5.2.18) till (5.2.20) are not valid for $\alpha = \pm 90°$ or $\beta = \pm 90°$. In that particular situation, the Sun vector lies on the Sun sensor XY-plane. Since the cut-off angle of the Sun sensor is in practice smaller than 90°, this situation will not occur.

The accuracy of the measurement is represented with the XY-angle α_{XY}. The XY-angle is the angle between the Sun vector and the Sun sensor +Z axis, which can be calculated with:

$$\alpha_{XY} = \pi/2 - \operatorname{atan}\left(\frac{\mathbf{n}_{Sun,z}^{SS}}{\sqrt{(\mathbf{n}_{Sun,x}^{SS})^2 + (\mathbf{n}_{Sun,y}^{SS})^2}}\right) \tag{5.2.21}$$

$$\text{when: } \alpha_{XY} > \pi/2, \text{ then: } \alpha_{XY} = \alpha_{XY} - \pi \tag{5.2.22}$$

Sun sensor model parameters

Table 5.4 lists down the minimum, nominal and maximum parameter values for the Sun sensor model. These have been selected from Table E.3.

Table 5.4: *Model parameters for the Sun sensor, based on the specification sheets in Table E.3.*

parameter	MIN	NOM	MAX	unit
cut-off half-angle (whole FoV)	64	57	50	°
cut-off half-angle (boresight)	15	10	5	°
noise (whole FoV) (3σ)	0.3	0.5	1	°
noise (boresight) (3σ)	0.05	0.1	0.2	°
misalignment angle	0.1	0.5	1	°
quantization step-size	16	12	8	bits
quantization step-size	0.0039	0.0557	0.7813	°

The cut-off angle of the boresight direction is an estimate, as it has not been specified by the manufacturers.

Sun sensor model verification

The verification of the model will be performed as follows. Two situations are considered in the verification of the Sun sensor model. First a simple case is considered where the Sun vector stays in the YZ-plane. The angle β varies from 0 towards 2π radians. After this, the more complex case will be considered. Both cases are shown in Figure 5.11.

The simulations have been performed with a FoV of 50° (whole FoV) and 15° in the boresight direction. Unless specified differently, the maximum errors have been considered from Table 5.4.

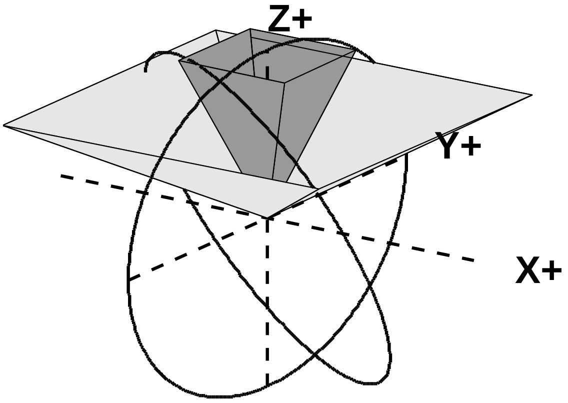

Figure 5.11: *This figure shows the implementation of the Sun sensor model. The Sun sensor FoV is indicated with the large inverted pyramid. The narrow inverted pyramid indicates the boresight direction of the Sun sensor.*

- **Simple case**
  In the simple case, the Sun vector progresses in the YZ-plane of the Sun sensor. As such, the angle β varies from 0 towards 2π radians. See Figure 5.11 for an illustration. Here it is assumed that no eclipse occurs and that there are no misalignment errors.

  Figure 5.12 shows the angles α and β (without any errors sources added) and the flags for the noise. Based on the angles α and β, it is determined whether the Sun is in the FoV. The magnitude of the noise depends whether the Sun vector is in the whole FoV (flag 1) or in the boresight direction (flag 2). If the Sun is not in the FoV, the output measurement is zero (flag 0). The same holds true when an eclipse occurs.

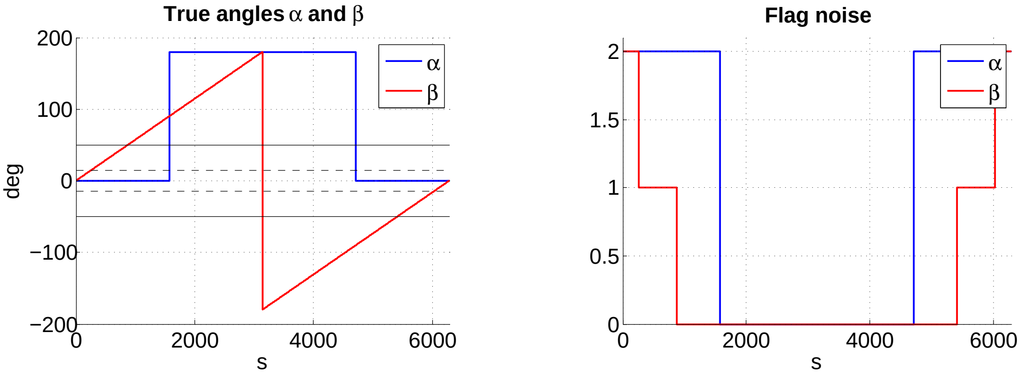

Figure 5.12: *Left: the true angles α and β, which have been calculated with the input Sun vector. Right: the corresponding noise flags.*

Figure 5.13 shows the corresponding noises, which are being added to the angles α and β. Note that unfortunately a mistake was made here. As the angle α is continuously zero (at start), the noise, which is added to that angle is one with the boresight accuracy. However, this should not be the case. A boresight accuracy is only achieved when both angles are within the boresight cut-off angle. Unfortunately, this mistake was only discovered after all simulations had been performed. A detailed discussion about the consequence of this error follows at the end of this section, together with the corrected implementation.

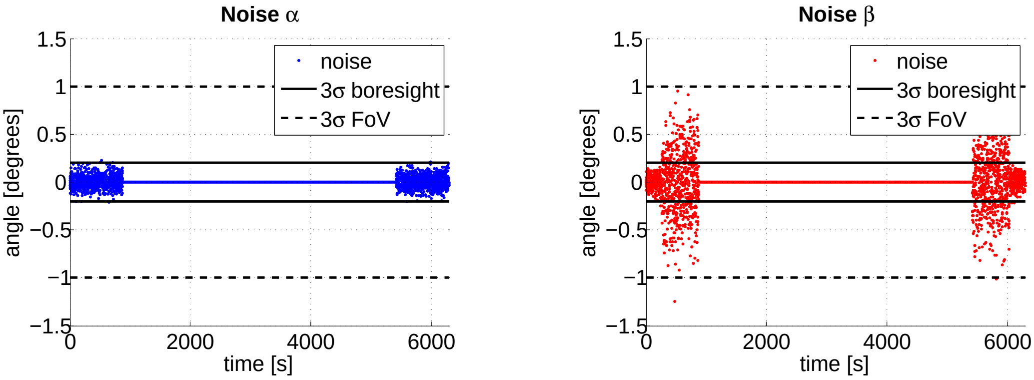

Figure 5.13: *The corresponding noises for the angles α and β.*

After the noise has been applied, the measured angles α and β are quantized. With the quantized angles the Sun vector is reconstructed in the Sun sensor frame. The difference between the true and measured XY-angle is being calculated now. The results are shown in Figure 5.14.

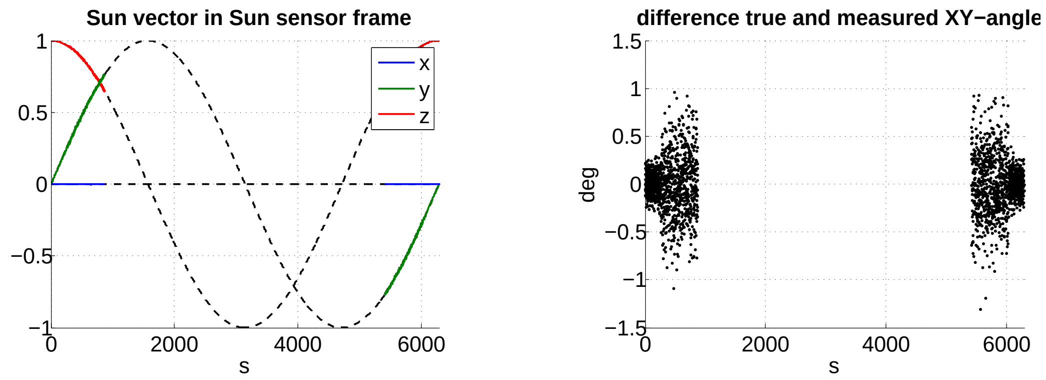

Figure 5.14: *The measured Sun vector, with the reference Sun vector shown with the dotted line.*

As mentioned earlier, an error has been made in the implementation of the noise. The impact of the erroneous implementation of the noise will now be discussed. The corrected noise output and the resulting inaccuracy in the measured XY-angle are shown in Figure 5.15.

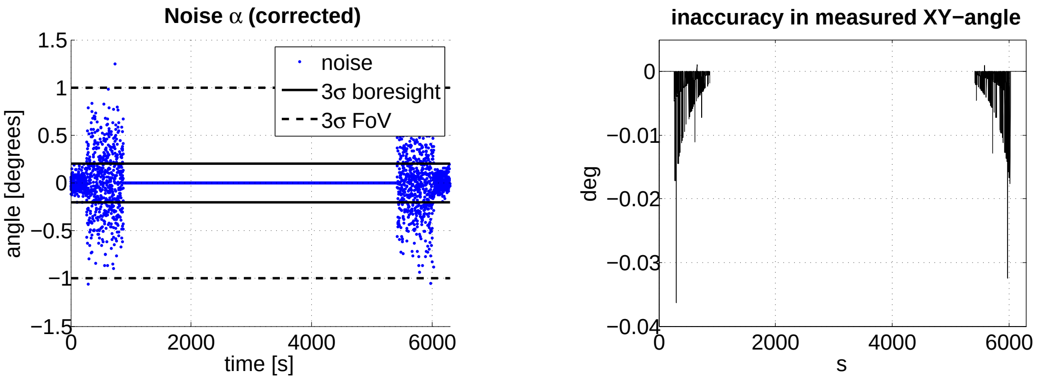

Figure 5.15: *Left: the correct noise output. Right: the inaccuracy in the measured XY-angle due to the erroneous implementation of the noise.*

The impact of the erroneous implementation of the noise is small. The measurement accuracy will be slightly better during the Sun Acquisition. It must be emphasized that the error has no consequence on the accuracy of the measured Sun vector during Sun Pointing. As such, it has been decided not to perform the simulation verification runs again.

- **Complex case**
  In the complex case, the plane in which the Sun vector moves is tilted. See Figure 5.11 for an illustration. Furthermore, a misalignment error of 1 degree is considered. The results are shown in Figures 5.16 through 5.18.

  The results are as expected. The Sun vector is (for a very short period) in the boresight direction of the Sun sensor. In Figure 5.18 it can be seen that the corresponding difference between the true and measured XY-angle is smallest during this time period.

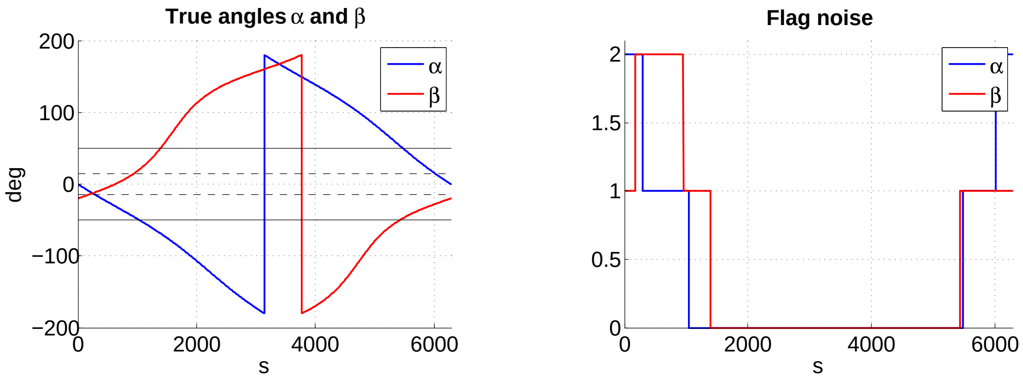

Figure 5.16: *Left: the true angles α and β, which have been calculated with the input Sun vector. Right: the corresponding noise flags.*

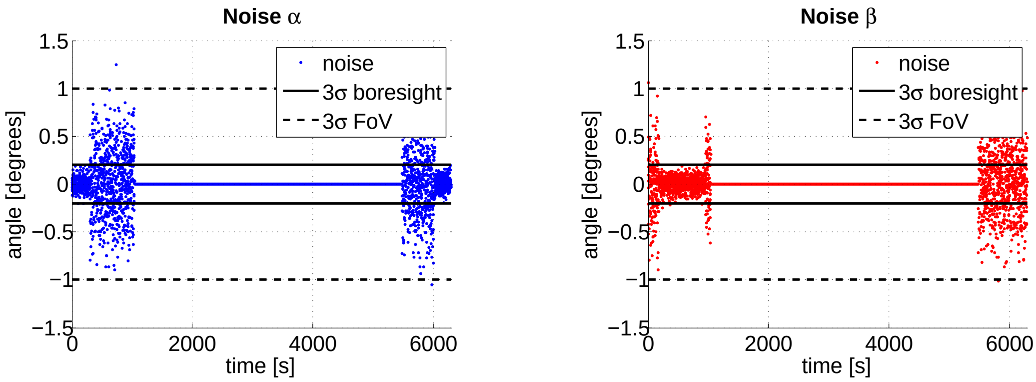

Figure 5.17: *The corresponding noises for the angles α and β.*

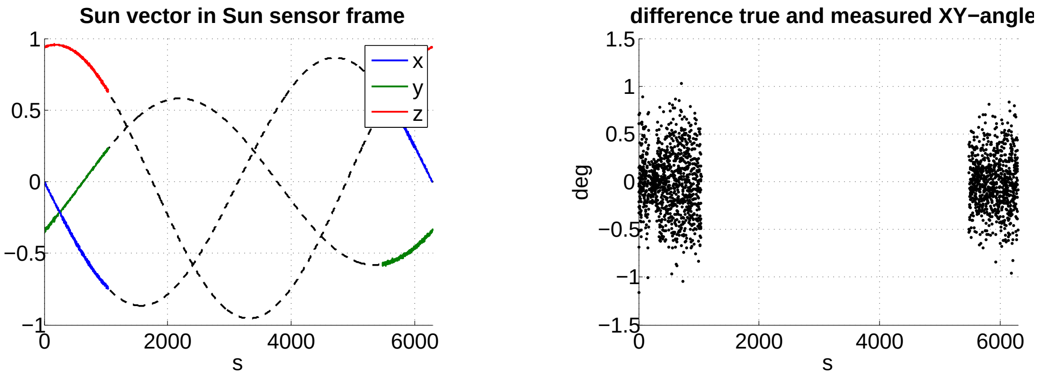

Figure 5.18: *Left: the measured Sun vector, with the reference Sun vector shown with the dotted line. Right: the resulting XY-angle mesaurement of the Sun sensor.*

Earth-albedo error

Not modeling the Earth-albedo error may have an impact on the results. This will be discussed now.

Two cases can be distinguished:

- **Only Earth albedo contribution**
  When the Sun is not in the field of view, the Earth albedo may lead to false Sun-

detection flags. One could argue to set a threshold value to the minimum voltage input to the Solar cells. The Solar flux amounts to approximately 1365 W/m^2 (Wertz, 1978). The Solar flux input is minimum when the Sun vector is on the outer rim of the FoV. The Sun sensor FoV is modeled as an inverted pyramid, see Figure 5.11. At the edges of this pyramid, the incidence angle is larger than the specified FoV. The effective Solar flux at the maximum incidence angles is listed in Table 5.5, for the different FoV.

Table 5.5: *Effective solar flux at maximum incidence angles, for different FoV.*

FoV (deg)	**Maximum incidence angle θ (deg)**	**Effective Solar flux at maximum incidence angle (W/m^2)**
50	59.32	$0.51 \cdot 1365 \approx 696$
57	65.33	$0.42 \cdot 1365 \approx 573$
64	70.97	$0.33 \cdot 1365 \approx 450$

The maximum Earth albedo is around 30% of the Solar flux. When setting a lower bound of 50%, no false sensor read-outs due to the Earth-albedo effect shall arise. The disadvantage of this approach is that there is no benefit any longer of having a larger field of view, because for larger incidence angles the voltage input decreases.

- **Combined Solar and Earth albedo contribution**
  In this case there is a combined effect. The consequence of this is that the resulting Sun-vector measurement will have a reduced accuracy. A pragmatic approach has been adopted to, to estimate the impact.
  - The intensity of the Earth-albedo contribution varies with the incidence angle with the Sun sensor (similar to the Solar flux contribution).
  - It will never occur that the Earth-albedo contribution is maximum *and* that the Sun vector is in the FoV. That is impossible, as the Earth albedo is maximum along the Sun vector in the inertial frame. As such, in all cases the Earth-albedo contribution will only be a fraction of the maximum Earth albedo.
  - The resulting inaccuracy in the XY-angle is shown in Table 5.6 (as function of the contribution):

Table 5.6: *Inaccuracy in the measured XY-angle, as function of the Earth-albedo contribution.*

Earth-albedo contribution (W/m^2)	**Inaccuracy in measured XY-angle when exactly Sun pointing (deg)**
30% of 1365 (maximum)	12.6
20% of 1365	8.9
10% of 1365	4.8

These inaccuracies are not insignificant. In these instances, the requirement of a 5° pointing accuracy during the SP mode cannot be met.

For an orbit with, e.g., zero inclination, at least once per orbit the situation would exist that no Earth albedo effect would be present, with which this problem disappears. However, the primary passenger of the VEGA rocket is brought into SSO (Sun-Synchronous Orbit). The launcher upper stage de-orbit burn will bring the SPS-2 satellite into a 350 × 850 km orbit with SSO inclination. The satellite, though, will not any longer be in a perfect SSO orbit. The small difference in the orbit causes that the orbit precesses with approximately 0.0414°/day or 15.11 °/year.

In the worst-case scenario, when the satellite is in an exact Sun-synchronous orbit, a continuous summed contribution will follow. However, it is very unlikely that this is the full Earth-albedo contribution, or even near 10%. The inner product of the incidence Solar vector and the normal vector pointing out of the Earth (in nadir direction) is small. Furthermore, exactly half of the visible surface area of the Earth (under the satellite) is not Sun-lit.

It is therefore assumed that at least once per orbit, the satellite will be able to see the Sun without the distortion of the Earth albedo. When this is not the case (only for a perfect SSO orbit), the contribution of the Earth albedo is much smaller than 10%.

5.2.8 Reaction-wheel model development

In this section the reaction-wheel model is discussed. First, an overview will be given of the implementation of the model. Then, the model parameters will be shown. The review of the model is discussed at the end of this section. The model is described in full detail by (Munatsi, 2016a), including the verification.

Reaction-wheel model overview

The model is implemented as follows. The misalignment error is applied first. The torque command is translated into a current command. A limit is imposed on the commanded current. Then, this is multiplied by the motor gain, after which the motor torque T_m is obtained. The net torque T_n arising from the reaction wheel is the motor torque minus the frictional torques T_f in the wheel. The net torque in the wheel can easily be translated into the angular acceleration of the wheel with:

$$T_n = T_m - T_f = \dot{h}_w \tag{5.2.23}$$

where the wheel angular momentum is:

$$h_w = J_w \, \omega_w \tag{5.2.24}$$

The angular acceleration of the wheel, $\dot{\omega}_w$, is integrated, after which the velocity of the wheel is obtained. A speed limiter is put here to prevent the wheel from spinning too fast.

Given the wheel rate, the frictional torques can be calculated (along the spin axis of the wheel). These consist of the viscous and the Coulomb friction, and these are calculated with:

$$T_f = T_c + T_v \tag{5.2.25}$$

$$T_c = \mathrm{sign}(\omega_w) K_c \tag{5.2.26}$$

$$T_v = \omega_w K_V \tag{5.2.27}$$

where K_V is the viscous friction coefficient and K_c is the Coulomb-friction coefficient.

The torque acting on the spacecraft equals the net torque of the reaction wheel, but with opposite sign. However, also the cross-coupling of the angular momentum component of the wheel needs to be taken into account. The total torque $\mathbf{T}_W$ acting on the spacecraft, including the cross-coupling term, then becomes:

$$\mathbf{T}_W = -\dot{\mathbf{h}}_w - (\boldsymbol{\omega}_{SC} \times \mathbf{h}_w) \tag{5.2.28}$$

where $\boldsymbol{\omega}_{SC}$ is the true angular rate of the spacecraft.

Furthermore, the static and dynamic imbalances of the wheel are included in the model. Static imbalances are radial asymmetries in mass distribution. Dynamic imbalances are asymmetries in mass distribution across the thickness of the wheel (Liu, accessed in February 2016).

The static imbalance is relatively large (as the moment arm is large), but acts on a very small timescale and cancels out eventually. The dynamic instability is especially important when considering jitter effects and for high-accuracy pointing stability. Both effects occur at high frequencies, which should cancel out eventually. As such, the static and dynamic imbalances will not be considered further.

Reaction-wheel model parameters

The wheel specifics are listed in Table 5.7. Table 5.8 lists the minimum, nominal and maximum parameter values for the reaction-wheel model, as presented in (Munatsi, 2016a).

Table 5.7: *Wheel specifics. The data has been obtained from the specification sheets in (Oomen, 2016).*

parameter	SunSpace	MicroWheel1000	unit
maximum torque	0.050	0.03	Nm
angular momentum capacity	0.65	1.1	Nms
speed limit	4200	10,000	RPM
cut-off speed	3150	6250	RPM
initial speed (for all axis)	0	0	RPM
current limit*	2	9	A
current consumption*	40	300	A Nm^{-1}
motor constant*	1/40	1/300	Nm A^{-1}
wheel inertia**	0.0015	0.00105	kg m^2

* The current limit, current consumption and motor constant of the MicroWheel1000 are not listed in the specification sheets. These have been obtained looking at the power consumption at the maximum torque output. The purpose of these parameters in the reaction wheel model is as follows. The torque request is first converted to a current using the current consumption. A threshold value (current limit) is set, after which the current is converted back towards the torque request with the motor constant. The motor constant is simply the inverse of the current consumption.

** The wheel inertia of the MicroWheel1000 is calculated with: $I_w = 1.1/(10,000 \times 2\pi/60)$.

The cut-off speed is the speed where the wheel offloading shall commence. The cut-off speed has been set to 75% of the maximum wheel speed. The wheel offloading strategy and implementation is discussed by (Munatsi, 2016a). In the simulations in this report, the maximum wheel speed is limited to this cut-off speed.

Table 5.8: *Model parameters for the reaction wheels, as specified in (Munatsi, 2016a).*

parameter	MIN	NOM	MAX	unit
viscous coefficient	$3.872 \cdot 10^{-6}$	$4.84 \cdot 10^{-6}$	$5.808 \cdot 10^{-6}$	Nms rad^{-1}
coulomb friction	$7.036 \cdot 10^{-4}$	$8.795 \cdot 10^{-4}$	0.0011	Nm
misalignment angle	0.1	0.5	1	°

Note that the viscous and the coulomb friction parameter values are assumed to be identical for both wheels. The minimum and maximum values are selected to be 80% and 120% of the nominal value, after an internal discussion with experts at Airbus.

Review of reaction-wheel model

The model is described in full detail by (Munatsi, 2016a), including the verification of the model. However, the author has reviewed the model implementation. This led to the following discoveries:

- No misalignments were implemented. This was corrected.
- The motor torque conversion resulted in a loss of 8.8% in the motor-torque command. This has been corrected as well.
- The speed limiter, which was implemented to avoid the wheel speed to exceed the maximum value, was wrongly positioned in the model block. The net torque was still being calculated with the unlimited wheel speed. As such, the output torque of the reaction-wheel unit was too high.

5.2.9 Gyroscope model development

In this section the gyroscope model is discussed. The model is described in full detail in (Munatsi, 2016a), including the verification. First, an overview will be given of the implementation of the model. Then, the model parameters will be shown. The review of the model is discussed at the end of this section.

Gyroscope model overview

A gyroscope is used to measure the angular rate of the spacecraft. The input of the gyroscope model is the angular rate specified in the B-frame. The angular rate is first transformed to the GYR-frame and subsequently converted to the unit deg/s. After this, the misalignment and scale factor errors are applied. The nonlinearity error is added, together with the contributions of the rate random walk (noise, which causes a bias drift, short-hand notation RRW), the angular random walk (noise, short-hand notation ARW) and the bias repeatability error (constant bias, but seed dependent). After this, a saturation block is placed. At the end of the model the measured signal is quantized.

The measurement equation for the gyro in the unit frame is described in this form:

$$\boldsymbol{\omega}_{meas} = (\mathbf{I}_{3\times3} + \mathbf{S})\mathbf{M}\,\boldsymbol{\omega}_{true} + \boldsymbol{\eta}_{ARW} + \boldsymbol{\eta}_{RRW} + \mathbf{b} + \boldsymbol{\nu} \tag{5.2.29}$$

where $\boldsymbol{\omega}$ is the angular rate vector in the unit frame (3×1), $\mathbf{M}$ is the misalignment matrix (3×3), $\mathbf{S}$ is the scale factor error (3×3), $\boldsymbol{\eta}_{RRW}$ is the rate random walk (3×1), $\boldsymbol{\eta}_{ARW}$ is the angular random walk (3×1), $\mathbf{b}$ is the bias (only containing the bias repeatability error) (3×1) and $\boldsymbol{\nu}$ is the nonlinearity error (3×1).

No transport delays have been added here. However, the effect of delays is considered in the stability analysis of the controllers.

Gyroscope model parameters

Table 5.9 lists down the minimum, nominal and maximum parameter values for the gyroscope model, discussed by (Munatsi, 2016a).

Table 5.9: *Gyroscope model parameters as presented by (Munatsi, 2016a).*

parameter	MIN	NOM	MAX	unit
ARW	0.012	0.035	0.38	$^\circ/\sqrt{\text{hr}}$
RRW	$\frac{1.25}{60} \cdot 10^{-4}$	$\frac{5}{60} \cdot 10^{-4}$	$\frac{1}{60} \cdot 10^{-3}$	$^\circ/\sqrt{\text{s}^3}$
bias repeatability	1	4	10	°/hr
scale factor error	100	500	1500	PPM
nonlinearity error	50	500	1500	PPM
nonlinearity range*	10	10	10	°/s
misalignment angle	0.1	0.5	1	°
quantization step-size	16	12**	12	bits
quantization step-size	0.0031	0.0146**	0.0488	°/s
measure range	100	30**	100	°/s

* After an internal discussion at Airbus, it has been decided to apply a nonlinearity error based on the operating range of the gyroscope, which lies within ±10 °/s.

** The nominal quantization step-size has been selected as follows. During the detumble mode, the spacecraft should be able to reduce the angular rates below 0.05 deg/s. In order to do so (with a safe margin) the axis read-outs should be below $0.05/3 = 0.0167$ °/s. With a quantization step-size of 12 bits, the accompanied measure range should be a maximum of ∼34 °/s.

In the gyroscope specification sheets, shown in (Oomen, 2016), the nonlinearity error has been specified as a percentage of the full range. The full range is specified to be ±100 °/s. With a maximum nonlinearity error of 1500 PPM, this results in a nonlinearity error of 0.15 °/s, which is very large. The manufacturers most probably make the linear fit such that it minimizes the error over the full range. The operating range of the gyro will be ±10 °/s. As such, it can be expected that another linear fit can be made that minimizes the error over this smaller range, at the expense of larger errors outside this range.

The ARW and RRW have not been specified in the specification sheets. These have been carefully determined by (Munatsi, 2016a) and are based on the QRS-166 gyroscope.

Review of gyroscope model

The model is described in full detail by (Munatsi, 2016a), including the verification of the model. However, the author has reviewed the model implementation. This led to the following discoveries:

- No misalignments were implemented. This was corrected.
- The nonlinearity error was implemented identical as the scale factor error. This has been corrected as well.

- The bias repeatability of the gyro was implemented as a noise. This has been corrected, by defining it as a constant bias, which is seed dependent.
- Most importantly, the author has discovered large discrepancies in the RRW implementation in the different model versions. The bias drift was initially estimated too large. A summary is given in Appendix F.

Chapter 6
CONTROL SYSTEM DESIGN AND ANALYSIS

In this chapter the detumble, SA and SP control algorithms will be presented. The requirements for the different control modes are presented first, in Section 6.1. The detumble controller is described in Section 6.2. The SA controller is described in Section 6.3 and the SP controller is described in Section 6.4. The stability of the controllers is looked at in Section 6.5.

6.1 Requirements

The SPS-2 requirements for the detumble mode are as follows:

Table 6.1: *Requirements detumble mode.*

#	REQUIREMENTS
REQ1	The detumbling of the spacecraft shall be performed within 1.5 orbits.
REQ2	The angular rates shall be reduced within 0.05°/s at the end of the detumbling maneuver, given that the satellite angular tip-off rates are $\leqslant 0.6°$/s along the longitudinal axis and $\leqslant 1.0°$/s around the two transversal axes.

The SPS-2 requirements for SA/SP mode are as follows:

Table 6.2: *Requirements SA/SP mode.*

#	REQUIREMENTS
REQ3	The time to acquire the Sun shall be less than 3 hours.
REQ4	The SPS-2 +X axis shall be pointing towards the Sun vector, with a pointing accuracy (APE) of within $5°(3\sigma)$.
REQ4	The maximum rate around the X-axis shall be within 0.1°/s at the end of the SP mode.
REQ6	Re-pointing after eclipse exit shall be achieved within 10 minutes.

Furthermore, there are some project constraints imposed by Airbus. These are as follows:

- For the SPS-2 mission no redundancy in the sensor/actuator components is considered. The main arguments for this decision are the limited volume available in the SVM, the desire to maintain a level of simplicity of the ACS and the accompanied mission costs.
- The ACS design shall be cost driven using COTS components.
- Assume that no information is available whether the satellite is in eclipse condition during the SA.

6.2 Design of the Detumbling Control Algorithm

To detumble the spacecraft, a detumble controller will be used. For this, magnetorquers are used. The generated magnetic dipole moment of the torquer interacts with the Earth's magnetic field, producing an torque output, which is perpendicular to the local magnetic field. Three different detumble controllers are described by (Avanzini and Giulietti, 2012), which are the standard, the modified and the nominal B-dot controller. Each of them will be discussed here in detail, such that these can be compared in the trade-off.

6.2.1 Detumble controllers

Standard B-dot controller

The standard B-dot control law is described as follows:

$$\mathbf{T} = \mathbf{m} \times \mathbf{B} = -k_B \dot{\mathbf{B}} \times \mathbf{B} \tag{6.2.1}$$

where $\mathbf{T}$ is the output torque, $\mathbf{m}$ is the commanded magnetic dipole moment, $\mathbf{B}$ is the magnetic field vector and k_B is the gain. All vectors are described in the B-frame here.

In the simulations, the derivative term of the magnetic-field vector can be calculated with backward differentiating:

$$\dot{\mathbf{B}}_k = \frac{\mathbf{B}_k - \mathbf{B}_{k-1}}{\Delta t} \tag{6.2.2}$$

where Δt is the simulation step size.

To understand what the controller really does, a closer look at Equation (6.2.1) is required. The derivative of the Earth magnetic-field in the body frame can be described as:

$$\mathbf{C}_{B,I} \dot{\mathbf{B}}_I = \dot{\mathbf{B}}_B + \boldsymbol{\omega} \times \mathbf{B}_B \tag{6.2.3}$$

where $\mathbf{C}_{B,I}$ is the transformation matrix from the I-frame to the B-frame. Since it can be assumed that at the start of the detumble mode the angular rates of the spacecraft are much higher than the change of the magnetic field due to the Earth rotation, it can be written that:

$$\dot{\mathbf{B}}_I \approx \mathbf{0}_{3\times 1} \rightarrow \dot{\mathbf{B}}_B \approx -\boldsymbol{\omega} \times \mathbf{B}_B \tag{6.2.4}$$

such that Equation (6.2.1) can be written as:

$$\mathbf{T} \approx k_B \left(\boldsymbol{\omega} \times \mathbf{B}\right) \times \mathbf{B} \tag{6.2.5}$$

which can be rewritten as:

$$\mathbf{T} \approx k_B \mathbf{B}^{\times} \mathbf{B}^{\times} \boldsymbol{\omega} \tag{6.2.6}$$

where $\mathbf{B}^{\times}$ is the skew-symmetric matrix of the vector $\mathbf{B}$. Using the relation:

$$\mathbf{B}^{\times}\mathbf{B}^{\times} = -\left(\|\mathbf{B}\|^2 \mathbf{I}_{3x3} - \mathbf{B}\mathbf{B}^T\right) \tag{6.2.7}$$

Equation (6.2.6) can be rewritten in the form:

$$\mathbf{T} \approx -k_B \|\mathbf{B}\|^2 \left(\mathbf{I}_{3x3} - \frac{\mathbf{B}\mathbf{B}^T}{\|\mathbf{B}\|^2} \right) \boldsymbol{\omega} \tag{6.2.8}$$

Regarding the last term of Equation (6.2.8), note that:

$$\mathbf{B}\mathbf{B}^T \boldsymbol{\omega} = \mathbf{B} \left(\mathbf{B} \bullet \boldsymbol{\omega} \right) \tag{6.2.9}$$

where $(\mathbf{B} \bullet \boldsymbol{\omega})$ is the projection of the angular rate parallel to the Earth magnetic field direction. In other words, only a control torque is exerted in the direction perpendicular to the Earth magnetic field.

Modified B-dot controller

The modified B-dot control law is described as follows:

$$\mathbf{T} = \mathbf{m} \times \mathbf{B} = -k_w \frac{\dot{\hat{\mathbf{B}}}}{\|\mathbf{B}\|} \times \mathbf{B} \tag{6.2.10}$$

with:

$$\hat{\mathbf{B}} = \frac{\mathbf{B}}{\|\mathbf{B}\|} \tag{6.2.11}$$

where $\hat{\mathbf{B}}$ is the normalized Earth magnetic field vector and k_w is the gain.

$\dot{\hat{\mathbf{B}}}$ can be written as:

$$\dot{\hat{\mathbf{B}}} = \frac{d}{dt}\left(\hat{\mathbf{B}}\right) = \frac{d}{dt}\left(\frac{\mathbf{B}}{\|\mathbf{B}\|}\right) = \frac{\|\mathbf{B}\|\, \dot{\mathbf{B}} - \mathbf{B}\left\|\dot{\mathbf{B}}\right\|}{\|\mathbf{B}\|^2} \tag{6.2.12}$$

such that:

$$\mathbf{T} = -k_w \left[\frac{\|\mathbf{B}\|\, \dot{\mathbf{B}} - \mathbf{B}\left\|\dot{\mathbf{B}}\right\|}{\|\mathbf{B}\|^3} \right] \times \mathbf{B} \tag{6.2.13}$$

$$\mathbf{T} = -k_w \left[\frac{\dot{\mathbf{B}}}{\|\mathbf{B}\|^2} - \frac{\mathbf{B}\left\|\dot{\mathbf{B}}\right\|}{\|\mathbf{B}\|^3} \right] \times \mathbf{B} \tag{6.2.14}$$

Since $\mathbf{B} \times \mathbf{B} = \mathbf{0}_{3\times 1}$, Equation (6.2.14) can be rewritten as:

$$\mathbf{T} = -k_w \left(\frac{\dot{\mathbf{B}}}{\|\mathbf{B}\|^2} \right) \times \mathbf{B} \approx k_w \left(\frac{(\boldsymbol{\omega} \times \mathbf{B})}{\|\mathbf{B}\|^2} \right) \times \mathbf{B} \tag{6.2.15}$$

or:

$$\mathbf{T} \approx k_w \frac{\mathbf{B}^\times \mathbf{B}^\times \boldsymbol{\omega}}{\|\mathbf{B}\|^2} \tag{6.2.16}$$

or, using Equation (6.2.7):

$$\mathbf{T} \approx -k_w \left(\mathbf{I}_{3x3} - \frac{\mathbf{B}\mathbf{B}^T}{\|\mathbf{B}\|^2} \right) \boldsymbol{\omega} \tag{6.2.17}$$

The difference with respect to the standard B-dot controller is the multiplication factor $\|\mathbf{B}\|^2$. Note that in this derivation the Earth magnetic field change due to the rotation of the Earth is neglected, as described earlier in Equation (6.2.4).

Nominal B-dot controller

The nominal B-dot control law is described as follows:

$$\mathbf{T} = \mathbf{m} \times \mathbf{B} = -\frac{k_w}{\|\mathbf{B}\|} \left(\hat{\mathbf{B}} \times \boldsymbol{\omega} \right) \times \mathbf{B} \tag{6.2.18}$$

with:

$$\hat{\mathbf{B}} = \frac{\mathbf{B}}{\|\mathbf{B}\|} \tag{6.2.19}$$

Rewriting gives:

$$\mathbf{T} = -\frac{k_w}{\|\mathbf{B}\|} \left(\frac{\mathbf{B}}{\|\mathbf{B}\|} \times \boldsymbol{\omega} \right) \times \mathbf{B} = -\frac{k_w}{\|\mathbf{B}\|^2} \left(\mathbf{B} \times \boldsymbol{\omega} \right) \times \mathbf{B} \tag{6.2.20}$$

$$\mathbf{T} = \frac{k_w}{\|\mathbf{B}\|^2} \mathbf{B}^\times \mathbf{B}^\times \boldsymbol{\omega} \tag{6.2.21}$$

$$\mathbf{T} = -k_w \left(\mathbf{I}_{3x3} - \frac{\mathbf{B}\mathbf{B}^T}{\|\mathbf{B}\|^2} \right) \boldsymbol{\omega} \tag{6.2.22}$$

Trade-off

The differences between the B-dot controllers are summarized in Table 6.3. For ease of understanding, the standard and the modified B-dot controllers are now referred to as the conventional controllers.

Table 6.3: *Summary of the different B-dot detumble controllers.*

Controller	**Magnetic dipole moment command**	**Resulting torque command**
Standard	$-k_B \dot{\mathbf{B}}$	$\mathbf{T} \approx -k_B \|\mathbf{B}\|^2 \left(\mathbf{I}_{3x3} - \frac{\mathbf{B}\mathbf{B}^T}{\|\mathbf{B}\|^2} \right) \boldsymbol{\omega}$
Modified	$-k_w \frac{\dot{\mathbf{B}}}{\|\mathbf{B}\|}$	$\mathbf{T} \approx -k_w \left(\mathbf{I}_{3x3} - \frac{\mathbf{B}\mathbf{B}^T}{\|\mathbf{B}\|^2} \right) \boldsymbol{\omega}$
Nominal	$-\frac{k_w}{\|\mathbf{B}\|} \left(\hat{\mathbf{B}} \times \boldsymbol{\omega} \right)$	$\mathbf{T} = -k_w \left(\mathbf{I}_{3x3} - \frac{\mathbf{B}\mathbf{B}^T}{\|\mathbf{B}\|^2} \right) \boldsymbol{\omega}$

The difference between the nominal B-dot controller compared to the others, is the use of rate measurements. For large angular rates, the resulting torque commands are similar, as can be seen in Table 6.3. However, the this only holds true when large angular rates are considered; then Equation (6.2.4) holds true. For smaller angular rates, the effect of the rate of change of the magnetic field vector becomes more dominating, such that Equation (6.2.4) is not valid any longer.

That also shows the limitation of the conventional B-dot controllers. The magnetic field vector rotates twice per orbit. The orbit rate is on average 0.0011 rad/s, such that the average angular rate of the satellite due to the rotation of the Earth magnetic field vector (relative to the satellite) is a minimum of 0.0022 rad/s $\approx$ 0.12 deg/s. The conventional B-dot controllers are not capable to reduce the angular rates of the satellite below this value. The nominal B-dot controller on the other hand can reduce the angular rates even further, due to the angular rate information by the gyro. Therefore, the nominal B-dot controller will be used.

6.2.2 On/off switching ratio

Since the magnetometer measurements are highly disturbed by the magnetorquer, as shown in Section 5.1.2, periodic measuring/actuation has to be applied. In the following, this is referred to as both the *measuring/actuation cycle*, as the *on/off switching ratio* of the magnetometer and the magnetorquer.

When the measurements are made, the magnetorquer is shut off. In this time period, no torque is exerted. This means that the gain for the controller effectively reduces. Longer periods of measuring results in an ineffective use of the magnetorquer, which will result in a longer detumble time. When actuating for longer periods (without measuring), the commanded torque is not corrected for the change in the direction of the magnetic field. In that case, the controller performance also reduces.

Unfortunately, no literature could be found on appropriate measure/actuation cycles. The most important aspect is that the measure duration should be long enough to ensure the latest measurements are not disturbed. Personal communication at Airbus led to the agreement that the minimum measurement duration shall be 1 s, which is assumed to be sufficiently long. However, to be on the safe side here, the nominal measurement time is selected to be 3 s. With trial and error, an actuation time of 10 s showed good results. This yields a nominal measure/actuation time ratio (i.e., the on/off switching ratio) of 3/10. This on/off switching ratio will be used for all simulations, unless stated differently. Note that the effective gain therefore reduces to 10/13 of the continuous case.

The impact on the controller performance, for other ratios, will be investigated at in Section 7.2.

6.2.3 Gain selection detumble controller

The gain determination of the nominal B-dot controller was performed as such. First, an initial gain of 0.2 was estimated, which was based on (Avanzini and Giulietti, 2012). In this work a circular orbit has been considered. Furthermore, in their work only the principal moments of inertia were taken into account. It therefore has been investigated whether this gain satisfied the needs. The objective was to find a gain with which the detumble time is small, but not affecting the energy consumption too much.

With this initial estimate, a gain variation has been performed. The gain was varied from 0.01 towards 1 in 100 simulation steps, for one specific orbit. The gain variation has been performed for all geometries separately.

The results were hard to interpret, and could not be explained in full detail. However, the results showed that for gains in the range of $k_w \approx 0.15$ towards $k_w \approx 0.50$ the detumble times were smallest, for all geometries. The next step was to narrow down the gains to four specific gains; 0.15, 0.20, 0.35 and 0.50. For each of the four gains, 200 simulations have been performed for varying initial conditions. This time, only geometry A was considered. The results are shown in Table 6.4. The simulation parameters, which have been used, are shown in Table 6.5.

The best results, in terms of the detumble time, have been found for a gain of 0.35. This gain has therefore been selected. Note that this gain results in the minimum detumble time, with the smallest standard deviation.

Table 6.4: *Results of the variation of initial orbital parameters for geometry A, for different gains.*

k_w	μ (s)	$\mu + 3\sigma$ (s)	μ (Whr)	$\mu + 3\sigma$ (Whr)
0.15	5449	9535	4.79	7.31
0.20	4630	7619	4.92	7.46
0.35	4280	7053	5.35	8.16
0.50	4431	7599	5.72	8.85

Table 6.5: *General model parameters used in simulations.*

Dynamics parameters	**variation between min/max**	**nominal**	**unit**
attitude quaternion	all*	$[0; 0; 0; 1]^T$	-
angular rates	$(\pm 0.6; \pm 0.6; \pm 1)^T$	$(0.6; 0.6; 1)^T$	deg/s
apogee height	750/850	800	km
perigee height	300/400	350	km
inclination	95/101	98	deg
RAAN	0/360	270	deg
argument of perigee	0/360	0	deg
Environment parameters	**variation between min/max**	**nominal**	**unit**
scale factor atmospheric density**	0/1	1	-
scale factor external disturbances***	1/1.5	1	-
Generic parameters	**variation between min/max**	**nominal**	**unit**
year	2017	2017	-
month	1/12	7	-
day	1/28	21	-
hour	0/24	0	hr
minute	0/60	0	m

* Uniformly distributed pseudorandom numbers, where the norm of the quaternion is kept unity by normalization. ** This is used to vary the atmospheric density of the MSIS-86 model between the minimum/maximum values, to account for the daily variation in the atmospheric density. When selected 0, the minimum value is used. When selected 1, the maximum value is used. *** This is used to scale the external disturbances, with the worst-case scenario of a factor 1.5.

6.3 Design of the SA Control Algorithm

In this section the SA controller will be discussed. First, the approach during the SA mode will be presented. The PI controller is described in Section 6.3.2. The reference trajectory which will be followed to perform the slew maneuver is described in Section 6.3.3. The SA gains which will be used are described in Section 6.3.4 and the maximum wheel speeds are discussed in Section 6.3.5.

6.3.1 Approach SA mode

The approach for the Sun Acquisition is as follows. First, a slew of 360 degrees will be performed around the Z-axis of the satellite (smallest inertia, fastest slew). When the Sun is in the field of view (FoV) of the Sun sensor, the slew will be stopped immediately. If not, the slew around the Z-axis will be completed, after which a consecutive slew will be performed around the Y-axis of the satellite. Again, when the Sun is in the FoV of the Sun sensor, the slew will be stopped immediately. As the FoV of the Sun sensor is larger than 90°, two slews in theory should be sufficient to acquire the Sun. However, the satellite might be in eclipse and there might be small deficiencies from the reference trajectory. When the Sun has not been acquired after the two slews, the procedure is repeated again. This could be considered as a waste of energy, but one of the project constraints is that no eclipse information is available.

6.3.2 PI control SA mode

The controller used is a PI controller. The motivation for using the PI controller is as follows. The slews which have to be performed during the SA mode are very simple. The preliminary simulations showed good results using a PI controller. To keep the design as simple as possible, it has therefore been decided not to consider more complex controllers for the SA mode.

The general control output of a PI controller is defined as follows:

$$\mathbf{u}(t) = \mathbf{K}_p\mathbf{e}(t) + \mathbf{K}_i \int \mathbf{e}(t)dt \tag{6.3.1}$$

where $\mathbf{u}(t)$ is the control output, $\mathbf{e}(t)$ is the error, $\mathbf{K}_p$ is the proportional gain and $\mathbf{K}_i$ is the integral gain.

As the satellite will follow a reference velocity profile, $\mathbf{e}(t)$ is the difference between the measured angular rate and the reference velocity. The proportional part of the controller minimizes the velocity error with respect to the reference velocity profile. The integral part of the controller minimizes the integrated velocity error (the distance error) with respect to a reference path. In the preliminary design phase the gains have been determined. These will be discussed in Section 6.3.4.

6.3.3 Reference trajectory SA mode

During the Sun Acquisition the satellite will follow a reference velocity profile to perform the slew maneuvers. Each slew maneuver consists of three phases. First, the wheels are spinned up, which make the spacecraft accelerate. When the wheels have reached a certain wheel speed, the acceleration phase is completed. The wheel speeds will be kept around a constant value and no torque is exerted on the spacecraft. The satellite will perform a slew maneuver with a constant angular velocity (coasting part). Finally, the spacecraft is deaccelerated by spinning down the wheels.

A few assumptions have been made to generate the reference velocity profile for the satellite. A pure spacecraft rate around one of the principal axis is assumed and no external disturbances are considered.

The torque exerted on the spacecraft by (de-)accelerating the reaction wheel is as follows:

$$\dot{\mathbf{h}}_W = \mathbf{T}_W = I_W \, \dot{\boldsymbol{\omega}}_W \tag{6.3.2}$$

where $\dot{h}_W$ is the change in angular momentum of the wheel, $\mathbf{T}_W$ is the torque of the wheel, I_W is the wheel inertia and $\dot{\boldsymbol{\omega}}_W$ is the acceleration of the wheel. When a constant (maximum) acceleration is assumed, the velocity of the wheel at the end of the acceleration phase is given by:

$$\boldsymbol{\omega}_W = \frac{\mathbf{T}_W}{I_W} \, t_{acc} \tag{6.3.3}$$

such that the time required to accelerate the wheel to the maximum wheel speed is known. When the spacecraft rate is purely around one of the principal axis and no external disturbances are present, Euler's rotational equation of motion become:

$$J\ddot{\theta} = -\dot{h}_W = -T_W \tag{6.3.4}$$

$$\ddot{\theta} = -\frac{T_W}{J} \tag{6.3.5}$$

where J is the principal satellite moment of inertia around that axis and $\ddot{\theta}$ is the angular acceleration of the satellite. When a constant (maximum) acceleration is assumed, the angular velocity of the spacecraft and the angular distance which has been covered at the end of the acceleration phase become:

$$\dot{\theta}_{acc} = -\frac{T_W}{J} \, t_{acc} \text{ and } \theta_{acc} = -\frac{1}{2}\frac{T_W}{J} \, t_{acc}^2 \tag{6.3.6}$$

The angular distance which shall be covered during the coast part of the slew (with a constant angular velocity) can be calculated with:

$$\theta_{coast} = \theta_{slew} - 2\,\theta_{acc} \tag{6.3.7}$$

Given the angle which shall be covered during the whole slew maneuver θ_{slew}. The time it takes to perform the coast part of slew can be calculated with:

$$t_{coast} = \frac{\theta_{coast}}{\dot{\theta}_{coast}} \quad \text{where} \quad \dot{\theta}_{coast} = \dot{\theta}_{acc} \tag{6.3.8}$$

Given the time durations for the different phases, the velocity profile for the slews can be constructed.

6.3.4 Gain determination SA mode

Two gains have been considered: the proportional and integral gain. The proportional part of the controller minimizes the velocity error with respect to the reference velocity profile. Large gains are advantageous here, because the settle time is reduced. However, a proportional gain which is too large will result large torque outputs (which is energy inefficient), high compensation behavior and the possibility of loosing track of the reference trajectory. The integral gain minimizes the integrated velocity error (the distance error) with respect to the reference path. The integral gain should ensure that a pure rotation is performed around one axis. Any unwanted angular precession around the other two axis is canceled out with time. High integral gains will compensate more for the drift, but also result in larger overshoots in the wheel speeds.

A wide variety of proportional and integral gains has been looked at. An important criterion for the proportional gain was the settling time. The proportional gain was selected to be 20, as this gave a satisfactory results for all three different geometries. The integral gain, which has selected is 3. The distance error can be compensated for slightly. Higher integral gains result in larger wheel overshoots.[1]

The resulting wheel speeds, spacecraft rates and angular distance plots are shown in Figure 6.1.

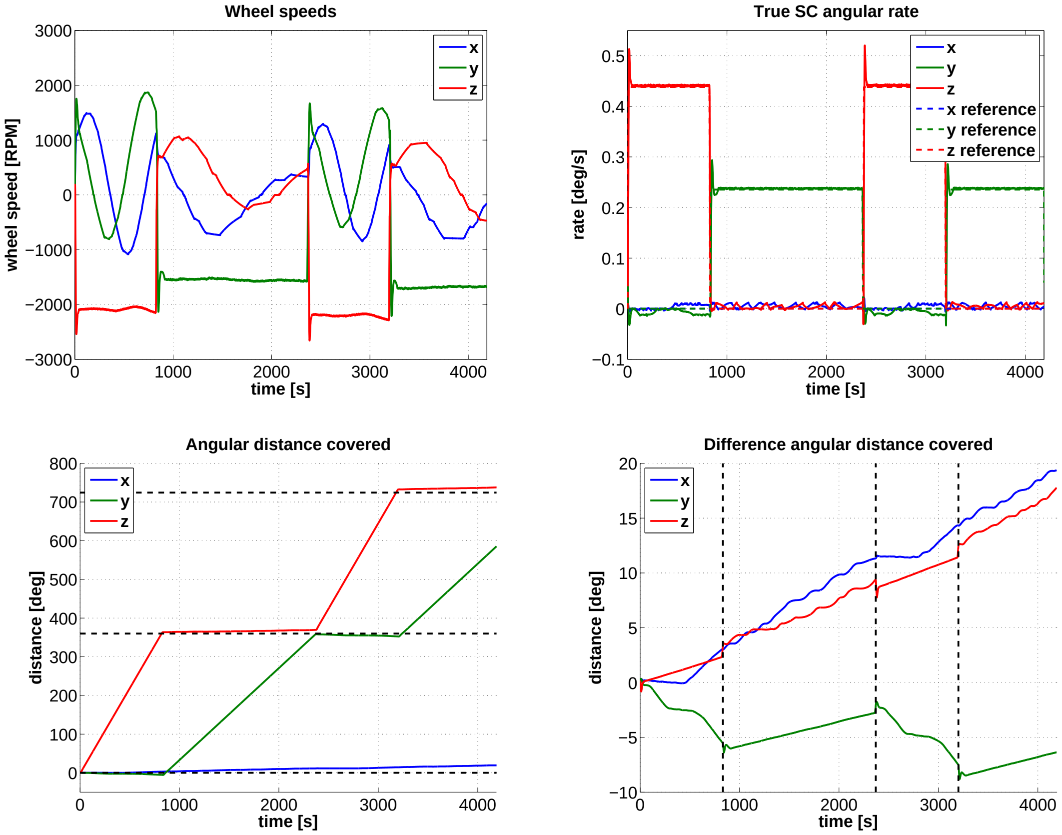

Figure 6.1: *The resulting wheel speeds, spacecraft rates and angular distance plots for the slews in the SA mode.*[2]

---

[1] The overshoot in the wheels speeds with this set of gains is approximately 500 RPM.

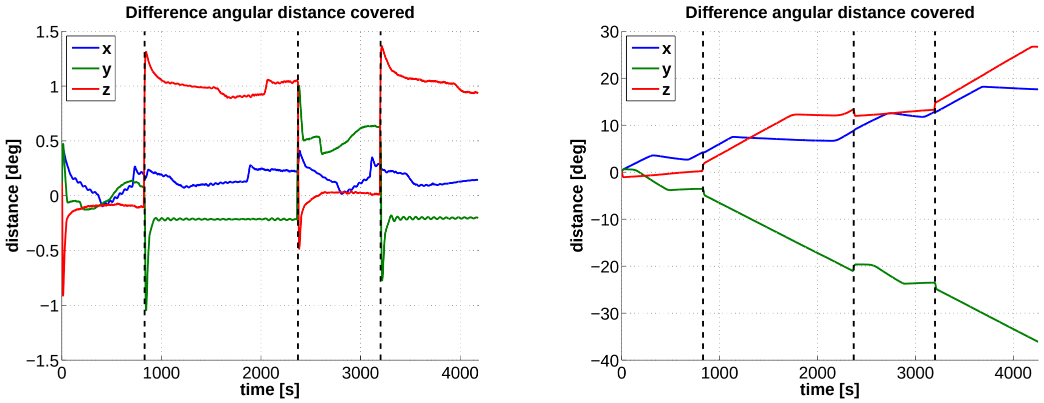

Figure 6.2: *The difference in the angular distance w.r.t. the reference trajectory for the slews in the SA mode. Left: results of the PI-controller using the true angular rate. Right: results of the P-controller.*

In Appendix G it is shown that, despite the deviations from the reference path, the satellite does successfully obtain a double hemispherical view after two successive slews. Why the difference with respect to the reference path cannot be compensated for entirely, has been investigated. This appears to be a result of the measurement error of the gyro. When the true angular rate from the dynamics is fed into the controller, the difference in covered angular distance is much smaller. This is shown in Figure 6.2 (left). Without the integral part of the controller, however, the differences are larger. This is shown in Figure 6.2 (right).

6.3.5 Maximum wheel speeds in SA mode

The maximum wheel speed can be limited with the reference trajectory. The choice for the maximum wheel speed for the two different wheels will be discussed here.

The maximum achievable wheel speed of the SunSpace reaction wheel is 4200 RPM. The wheel offloading will commence at 3150 RPM. The maximum wheel speed for the SA slews has been chosen to be 2500 RPM. This results in a comfortable margin for the angular momentum build-up due to external disturbances, avoiding the necessity of offloading the wheels.

The maximum achievable wheel speed of the MicroWheel1000 is 10,000 RPM. The wheel offloading will commence at 7500 RPM. For the same reasons, the maximum wheel speed for the SA slews has been chosen to be 6250 RPM.

6.4 Design of the SP Control Algorithm

In this section the SP controller will be discussed. The controller which will be used is described in Section 6.4.1. The SP gains which will be used are described in Section 6.4.2. The approach during eclipse periods is discussed in Section 6.4.3 and the maximum wheel speeds are discussed in Section 6.4.4.

---

[2] The figures have been generated using the results from the simulation campaign described in Section 8.3 (geometry A, seed 2120 with the SunSpace wheel).

6.4.1 Quaternion Feedback Controller

The control law used is the Quaternion Feedback Control law, which is described by (Wie, 2008). The control law is of the form:

$$\mathbf{u} = -\mathbf{K}_p \operatorname{sign}(\delta q_4)\delta\overline{\mathbf{q}} - \mathbf{K}_d\,\omega \tag{6.4.1}$$

where $\delta\mathbf{q}$ is the error quaternion which describes the rotation between the measured Sun vector and the boresight axis of the Sun sensor.

Given the measured Sun vector in the body frame the error quaternion can be calculated. The error quaternion describes the rotation from the measured Sun vector to the boresight axis of the Sun sensor. The objective is to align these two axis, with an absolute pointing accuracy within 5 degrees. Furthermore, the angular rate around the Sun vector shall be reduced to 0.1°/s maximum at the end of the SP mode. For this, the derivative term takes care.

Important to note is that always the last Sun vector measurement is used to construct the error quaternion. When the Sun in not in the field of view of the Sun sensor (e.g. in eclipse conditions), the last Sun measurement will be propagated based on the measured rates. This is discussed further in Section 6.4.3.

6.4.2 Gain determination

By manually tuning a suitable set of gains have been selected. Two gains have been considered: the proportional and derivative gain. The proportional part of the controller minimizes the pointing error with respect to the Sun vector. The derivative part of the controller minimizes the angular velocity of the spacecraft.

A large proportional gain result in fast slew maneuvers, at the cost of a high power consumption and resulting torque ripples. On the other hand, a proportional gain which is too small results in long durations to get the satellite Sun pointing. The derivative gain is essential to bring the angular rates towards 0 deg/s. However, increasing the derivative gain results in longer time durations to get the satellite Sun pointing. Another consequence of larger derivative gains is the reduction in pointing accuracy. Small derivative gains naturally result in larger remaining angular rates at the end of the SP mode. Furthermore, the torque ripples cannot be counteracted effectively.

A derivative gain of 20 has been selected. The selected proportional gain is 1.[3] These will be used in the simulation performance runs. The stability for these gains is studied in Section 6.5.3.

6.4.3 Sun pointing after eclipse exit

When the satellite enters an eclipse when the Sun vector has been acquired (mode 4) or when it is already Sun pointing (mode 5), the last measured Sun vector will be propagated based on the measured angular rates. The satellite will be steered towards this propagated

---

[3] It has been found that the derivative gain of the controller shall not be chosen too large. Due to the inaccuracy in the gyro measurement, the Sun vector measurement is propagated inaccurately during eclipse periods, as shown in Section 6.4.3. This effect strengthens with larger derivative gains.

Sun vector. With this approach, the goal is to ensure that the Sun is still in the FoV after the eclipse exit.

First the situation is looked at where the Sun vector has been acquired, but the satellite is not yet Sun pointing when the satellite enters an eclipse. Figure 6.3 shows the results for two different cases, with the gyro parameters listed in Table 6.6. It can be seen that at the start the true XY-angle is effectively reduced towards 0 deg, but then starts to increase for the remainder of the eclipse period. This is due to the inaccuracy in the gyro measurements.

Another situation which has been looked at, is when the satellite was already Sun pointing (mode 5) at the start of the eclipse. Again a drift in the measured XY-angle became apparent.

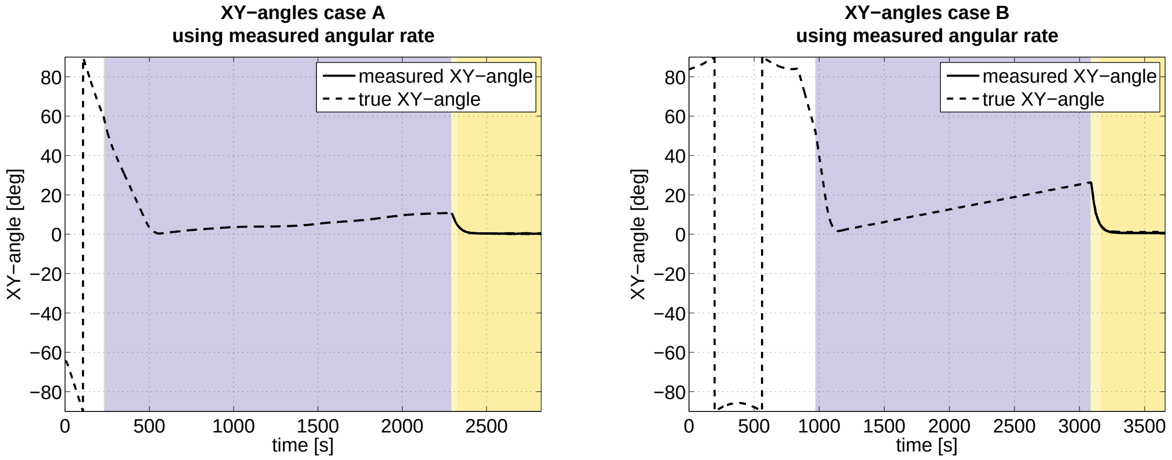

Figure 6.3: *The true and measured XY-angles during and after the eclipse, for two different simulation cases, which are described in Table 6.6.*

Table 6.6: *Gyro parameters for cases A, B, C and D. The initial bias drift which has been specified, comes from the bias drift at the end of the detumble maneuver.*[4]

error	**unit**	**case A**	**case B**	**case C**	**case D**
ARW	$\mathrm{deg}/\sqrt{\mathrm{hr}}$	0.035	0.14418	0.035	0.080447
RRW	$\mathrm{deg}/\sqrt{\mathrm{s}^3}$	8.3333e-06	1.438e-05	8.3333e-06	3.1487e-06
initial bias drift	deg/s	$\begin{pmatrix}-0.0046\\+0.0046\\-0.0046\end{pmatrix}^T$	$\begin{pmatrix}+0.0046\\+0.0046\\-0.0046\end{pmatrix}^T$	$\begin{pmatrix}-0.0046\\+0.0046\\-0.0046\end{pmatrix}^T$	$\begin{pmatrix}-0.0046\\+0.0046\\+0.0046\end{pmatrix}^T$
bias repeatability	deg/hr	4	2.2647	4	4.3945
scale factor error	PPM	500	438.9373	500	145.7921
nonlinearity	PPM	500	1415.5	500	1114.7
quantization interval	deg/s	0.014648	0.0030518	0.014648	0.048828
misalignment angle	deg	0.5	0.47765	0.5	0.85805

---

[4] In cases A (seed 3074) and C (seed 3189) the nominal gyro errors have been used. These test-cases follow from the simulation test-runs where the initial parameters have been varied, described in Section 8.3. The gyro errors in cases B (seed 1188) and D (seed 3054) follow from the Monte Carlo run parameter variation, see Section 8.4. Note that for all cases, geometry A was considered, using the SunSpace wheel. With simulation case B, an adjusted field of view of 53 degrees for the Sun sensor has been used.

Table 6.7 summarizes all results. Differences can be observed between the XY-angles at the end of the eclipse exit, for the different simulation cases. This is expected to be caused due to the differences in the gyro errors. However, more research should be performed to confirm these findings.

Table 6.7: *True XY-angles before and after eclipse exit, for the different simulation cases.*

(with gyro errors) **case**	 **mode**	**XY-angle before eclipse (°)**	**XY-angle after eclipse exit (°)**
case A	mode 4	58.3	10.9
case B	mode 4	52.1	26.4
case C	mode 5	0.8	12.3
case D	mode 5	1.1	38.5
(without gyro errors) **case**	 **mode**	**XY-angle before eclipse (°)**	**XY-angle after eclipse exit (°)**
case A	mode 4	58.8	0.6
case B	mode 4	52.5	0.7
case C	mode 5	0.5	0.6
case D	mode 5	1.1	1.0

Important to note is that the inaccuracy in the gyro measurement cannot be solved for. An alternative approach has been looked at, in which the slew maneuver is stopped when in eclipse. However, this might not work for particular cases. For example, when the Sun is just in the FoV when the satellite enters the eclipse. Therefore, this option has been discarded.

In the performance analysis in Section 8.4.3, the resulting XY-angles after the eclipse exit will be shown, for the simulations results of the full Monte Carlo run.

6.4.4 Maximum wheel speeds in SP mode

The choice for the maximum wheel speed for the two different wheels will be discussed here.

The maximum achievable wheel speed of the SunSpace reaction wheel is 4200 RPM. The wheel offloading will commence at 3150 RPM. The maximum wheel speed during the SP slew has been set to this value. It is expected that the satellite will reach this wheel speed (to spin up the satellite for the slew maneuver), after which the wheel speeds decrease rapidly when the satellite de-accelerates. As the total duration of the SP slew is short, no problems should occur.

The maximum achievable wheel speed of the MicroWheel1000 is 10,000 RPM. The wheel offloading will commence at 7500 RPM. The maximum wheel speed during the SP slew has been set to this value, for the same reasons as above.

6.5 Stability of the Controllers

In this section the performance of the controllers will be looked at in terms of stability. The stability of the controllers can be determined with Bode plots, which give a clear overview of the stability margins. One of the key values of stability margins is that these allow to determine the overall stability of the closed loop system directly from the open loop design. The stability margin can guarantee a certain level of performance and can protect against uncertainties and unmodeled perturbations in the system dynamics.

The Bode plot shows the frequency response of the system, in which the magnitude (dB) and phase (deg) are shown for the different frequencies on a log scale. From these figures, the gain and phase margins can be easily determined.

The gain margin gives an indication of the allowable range of gains before the system becomes unstable. Making the gain too large results in that the controller will end up over-correcting and overshooting, eventually departing from the reference and becoming unstable. The gain margin is measured as the reciprocal of the magnitude, at the point where the phase crosses -180 degrees. The reciprocal in a logarithmic scale means a sign change, so to ensure stability the gain margin needs to be a positive value. A lower bound of 3-5 dB is usually recommended (Osorio, accessed in February 2016).

The phase margin gives insight in the range of delays the system can handle. When the response is delayed for a small time period, it might be that the controller is still stable. However, for larger delays it may be that the controller becomes unstable. The phase margin is measured as the difference between the phase trace and the -180 degrees line, at the frequency where the magnitude crosses zero dB. For stability, the phase margin shall be greater than zero. A lower bound of 30-45 degrees is generally recommended, whereas a phase margin of at least 60 degrees is usually recommended for relatively smooth and well damped system behavior (Osorio, accessed in February 2016).

Note that in this analysis, a simplified, linearized system will be looked at. In reality, the system is nonlinear. Contributions of, e.g., the errors in the measurements, the cross-coupling of the reaction wheels, external disturbances and transient effects will not be considered here. Furthermore, a continuous system is considered, whilst the controller is discrete. As such, the control is kept constant for the duration of a simulation step-size. This affects the stability of the controller. The impact of the continuous time representation, is that the control actions during the minor time-steps[5] of the RK4 integration are falsely taken into account. For all these reasons, the analysis performed in this section *only* gives an indication for the stability of the controllers. The conclusions do not even have to be valid. Further work needs to be done here, but this is beyond the scope of this project.

The maximum time delays which are expected to occur, is one signal delay. As the simulator frequency is 1 Hz, this is equivalent to 1 second.

In the next sections, the gain and phase margins of the detumble, SA en SP modes will be looked at. First the open loop transfer functions will be derived, after which the gain and phase margins will be read from the open-loop Bode plots. One example of a resulting Bode plot will be shown in Section 6.5.2.

---

[5] The major time-steps represent the true physical state of the satellite, whilst the minor time-steps do not.

6.5.1 Stability of the detumble controller

The control loop for the detumble mode, in discrete time, can be represented as in Figure 6.4.

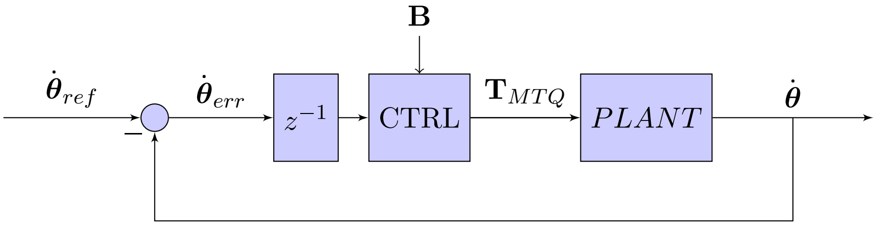

Figure 6.4: *The representation of the closed-loop control, for the detumble controller (in the discrete time-frame).*

In symbolic form (assuming a constant magnetic field strength **B**), the closed-loop control can be represented as in Figure 6.5. As explained in the introduction, a continuous system has been considered here.

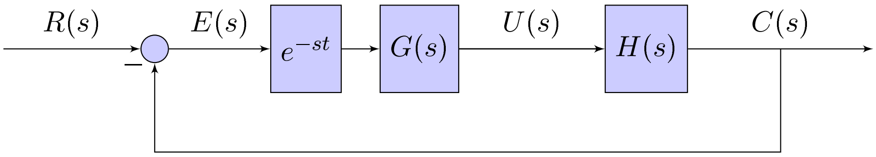

Figure 6.5: *The symbolic representation of the closed-loop control, for the detumble controller (in the continuous time-frame).*

In Figure 6.5, $R(s)$ is the Laplace transform of the reference velocity, $E(s)$ is the Laplace transform of the error velocity and $C(s)$ is the Laplace transform of the output velocity. The torque output is denoted with $U(s)$. The controller is represented with $G(s)$ and the plant with $H(s)$. The signal delay is represented with e^{-st}. Note that the measurement block has been omitted and that it has been assumed that no external disturbances are present.

The relation between the magnetic dipole moment command and the resulting torque command was previously defined in Table 6.3. The controller used in the detumble mode is a P controller on the velocity, described with:

$$G(s) = +k_w \left(\mathbf{I}_{3x3} - \frac{\mathbf{B}\mathbf{B}^T}{\|\mathbf{B}\|^2} \right) \tag{6.5.1}$$

where a constant magnetic field strength **B** will be assumed.

The plant equation can be obtained from Euler's rotational equation of motion:

$$\mathbf{J}\dot{\boldsymbol{\omega}} + \boldsymbol{\omega} \times \mathbf{J}\boldsymbol{\omega} = \mathbf{M}_{EXT} + \mathbf{u} \tag{6.5.2}$$

where $\mathbf{u}$ is the internal torque of the actuators, equal to $\mathbf{T}_{MTQ}$. No external disturbances have been considered, such that $\mathbf{M}_{EXT} = 0$. As a major simplification, when it assumed that that $\boldsymbol{\omega} \times \mathbf{J}\boldsymbol{\omega} \approx 0$ (because the angular rates are small), this results in:

$$\mathbf{J}\dot{\boldsymbol{\omega}} = \mathbf{T}_{MTQ} \tag{6.5.3}$$

The plant equation can therefore described with:

$$H(s) = \frac{1}{Js} \tag{6.5.4}$$

The closed loop transfer function then becomes:

$$\frac{C(s)}{R(s)} = \frac{G(s)H(s)}{1 + G(s)H(s)} \tag{6.5.5}$$

The open loop control loop for the detumble mode can be described with Figure 6.6.

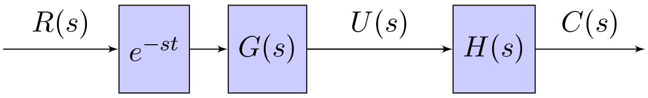

Figure 6.6: *The resulting open-loop control loop for the detumble control.*

The open loop transfer function then becomes:

$$\frac{C(s)}{R(s)} = e^{-st}G(s)H(s) \tag{6.5.6}$$

Only left to consider is $G(s)$, which is dependent on the magnetic field vector, as shown in Equation (6.5.1). For the stability analysis, a constant magnetic field will be assumed. This will result in a constant $G(s)$ term, of which the magnitude shall be determined. For convenience, the term between brackets is referred to as G^*. In full form, it can be written that:

$$G^* = \left(\mathbf{I}_{3x3} - \frac{\mathbf{B}\mathbf{B}^T}{\|\mathbf{B}\|^2}\right) = \begin{bmatrix} 1 - B_x^2/\|\mathbf{B}\|^2 & -B_yB_x/\|\mathbf{B}\|^2 & -B_zB_x/\|\mathbf{B}\|^2 \\ -B_xB_y/\|\mathbf{B}\|^2 & 1 - B_y^2/\|\mathbf{B}\|^2 & -BzB_y/\|\mathbf{B}\|^2 \\ -B_xB_z/\|\mathbf{B}\|^2 & -B_yB_z/\|\mathbf{B}\|^2 & 1 - B_z^2/\|\mathbf{B}\|^2 \end{bmatrix} \tag{6.5.7}$$

Alternatively, in symbolic form:

$$G^* = \left(\mathbf{I}_{3x3} - \frac{\mathbf{B}\mathbf{B}^T}{\|\mathbf{B}\|^2}\right) = \begin{bmatrix} G_{11} & G_{12} & G_{13} \\ G_{21} & G_{22} & G_{23} \\ G_{31} & G_{32} & G_{33} \end{bmatrix} \tag{6.5.8}$$

For this analysis, only the stability around the separate axes will be considered, where the coupling between the different axes will be neglected. For this reason, only the diagonal terms will be considered in G^*. Figure 6.7 shows the variation of the diagonal terms of G^*.

As only the diagonal terms are of interest, G^* will now be represented as a scalar, for each of the three axes. This can be assumed, when the stability around the separate axes will be considered separately. Note that G^* varies from approximately 0.2 to 1. With a safety margin applied, the range of values G^* can obtain is 0.1 to 1.

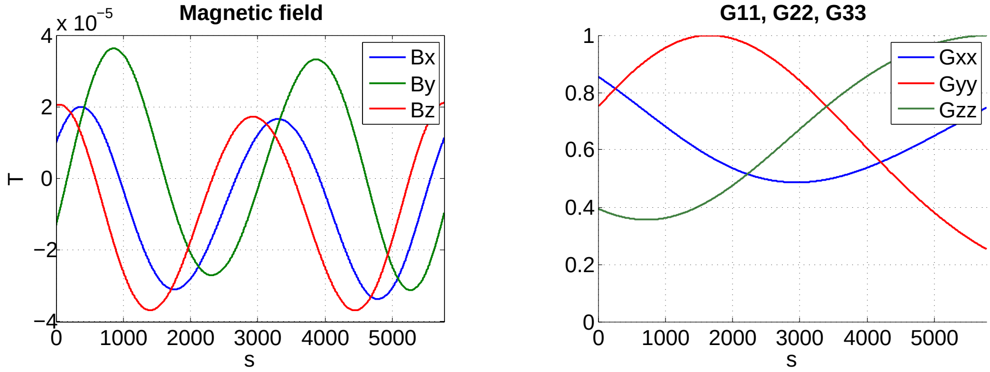

Figure 6.7: *Variation of the diagonal terms of* G^**.*

Stability margins

In this section the resulting gain and phase margins will be discussed for the detumble controller. The detumble gain which has been selected in Section 6.2.3 is 0.35. The resulting gain and phase margins will be looked at for different inertia's and time delays.

The lowest and highest inertia terms will be considered. These are 17.52 and 95.5 kg m^2 respectively. Time delays up to 1 s (equivalent to a full signal delay) will be considered here. Table 6.8 summarizes the gain and phase margins, which have been found.

Table 6.8: *Phase and gain margins for the detumble controller, for different inertia's and time delays.*

Inertia (kg m^2)	Delay (s)	Gain margin (dB)	At frequency (rad/s)	Phase margin (deg)	Delay margin (s)	At frequency (rad/s)
95.5 ($G^* = 0.1$)	0	∞	-	90	4286.0	$3.67 \cdot 10^{-4}$
...	0.1	92.6	15.71	90.0	4285.9	$3.67 \cdot 10^{-4}$
...	0.5	78.7	3.14	90.0	4285.5	$3.67 \cdot 10^{-4}$
...	1.0	72.6	1.57	90.0	4285.0	$3.67 \cdot 10^{-4}$
17.52 ($G^* = 0.1$)	0	∞	-	90	786.3	$2.00 \cdot 10^{-3}$
...	0.1	77.9	15.71	90.0	786.2	$2.00 \cdot 10^{-3}$
...	0.5	63.9	3.14	89.9	785.8	$2.00 \cdot 10^{-3}$
...	1.0	57.9	1.57	89.9	785.3	$2.00 \cdot 10^{-3}$

In this analysis, a constant magnetic field was assumed, resulting in an estimated G^* from 0.1 to 1. The results in Table 6.8 are only shown for $G^* = 0.1$. The gain and delay margins for other G^* can be derived directly from these results.

However, the assumption that the magnetic field can be assumed to be (quasi-)constant, is incorrect for this analysis. A delay margin of 4286 s acts on the time-scale of one orbital revolution, in which the Earth magnetic field certainly is not constant. Therefore, no conclusions can be made about the stability of the detumble controller. This requires further research, which is left as future work.

6.5.2 Stability of the SA controller

The control loop for the SA mode, in discrete time, can be represented as in Figure 6.8.

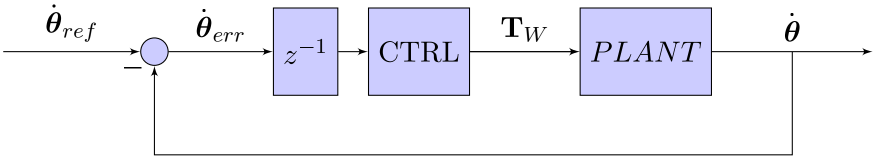

Figure 6.8: *The representation of the closed-loop control, for the SA controller (in the discrete time-frame).*

The controller used in the SA mode is a PI controller on the velocity, described with:

$$G(s) = \frac{K_p s + K_i}{s} \tag{6.5.9}$$

The plant equation can be obtained from Euler's rotational equation of motion:

$$\mathbf{J}\dot{\boldsymbol{\omega}} + \dot{\mathbf{h}}_W + \boldsymbol{\omega} \times (\mathbf{J}\boldsymbol{\omega} + \mathbf{h}_W) = \mathbf{M}_{EXT} \tag{6.5.10}$$

With the same assumptions as in Section 6.5.1, this reduces to:

$$\mathbf{J}\dot{\boldsymbol{\omega}} = \mathbf{u} = -\left(\dot{\mathbf{h}}_W + \boldsymbol{\omega} \times \mathbf{h}_W\right) \tag{6.5.11}$$

where $\mathbf{u}$ is the internal torque from the actuators, in this case $\mathbf{T}_W$. The plant equation (for one-dimensional case) can now be described with $H(s) = \frac{1}{Js}$.

The derivation for the open loop transfer function is identical to Section 6.5.1. Note the difference in the definition of $G(s)$.

Stability margins

In this section the resulting Bode plots will be discussed for the SA controller. The SA gains which have been selected in Section 6.3.4 are $K_p = 20$ and $K_i = 3$. The resulting gain and phase margins will be looked at for different inertia's and time delays.

The inertia terms, which will be considered are J_{yy} and J_{zz}, which correspond to the two axis where the satellite will be rotating around. The lowest and highest inertia terms are 17.52 and 95.5 kg m^2. Time delays up to 1 s (equivalent to a full signal delay) will be considered here. Table 6.9 summarizes the gain and phase margins which have been found. An example of a resulting Bode plot is shown in Figure 6.9.

Table 6.9: *Phase and gain margins for the SA controller, for different inertia's and time delays.*

Inertia (kg m^2)	**Delay** (s)	**Gain margin** (dB)	**At frequency** (rad/s)	**Phase margin** (deg)	**Delay margin** (s)	**At frequency** (rad/s)
95.5	0	∞	-	58.6	4.16	0.25
...	0.1	37.5	15.71	57.2	4.06	0.25
...	0.5	23.2	3.04	51.5	3.66	0.25
...	1	16.9	1.47	44.5	3.16	0.25
17.52	0	∞	-	82.6	1.25	1.15
...	0.1	22.8	15.71	76.0	1.15	1.15
...	0.5	8.5	3.04	49.6	0.75	1.15
...	1	2.1	1.47	16.6	0.25	1.15

For the smallest inertia term, the phase margin is lower than the recommended value of 30 deg, when the signal delay is 1 s. Sufficiently large phase margins (> 30 deg) are obtained for signal delays up to 0.79 s. For these delays, the gain margin is a minimum of 4.34 dB.

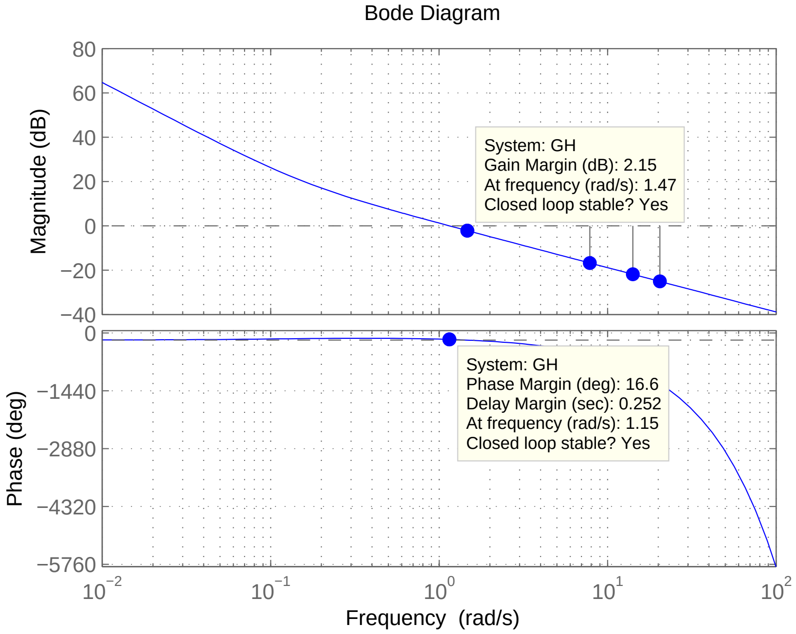

Figure 6.9: *Bode plot for a signal delay of 1 s and an inertia of 17.52 kg m^2.*

It has been investigated which proportional and integral gains would result in sufficiently large gain and phase margins, given the minimum and maximum inertia terms as described above. This analysis has been performed for a signal delay of 1 s. The results are shown in Figure 6.10. The shaded area represents combinations of the proportional and integral gains, where the gain and phase margins are sufficiently large.

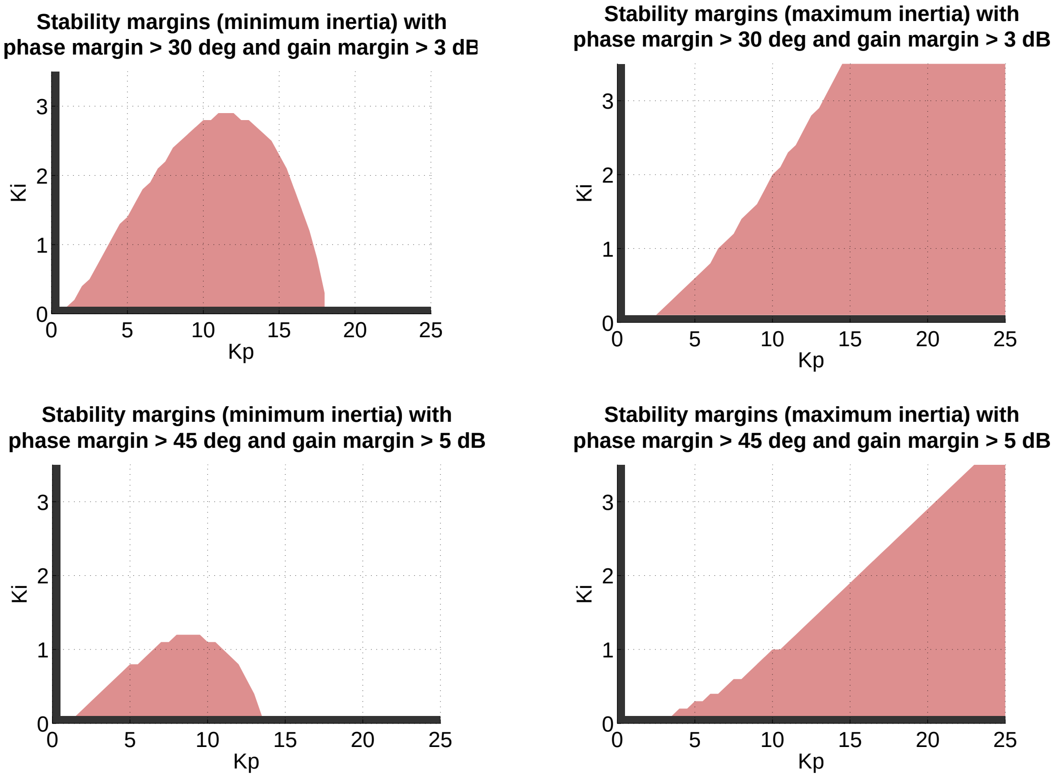

Figure 6.10: *Stability margins for different proportional and integral gains, for a signal delay of 1 s.*

In this section the gain and phase margins of the SA controller have been looked at, for the gains which have been selected in Section 6.3.4. Naturally, the resulting gain and phase margins are very different, due to the large differences in inertia's. The results show that for signal delays up to 0.79 s, sufficiently large gain margin (>3 dB) and phase margins (> 30°) are achieved. Note that, despite these sufficiently large stability margins, the stability of the controller is not ensured. This is only an indication for the stability.

It has also been investigated what the proportional and integral gains should be, to allow for a larger signal delay of 1 s. However, the simulations in Chapter 8 have been performed with the original set of gains.

6.5.3 Stability of the SP controller

The control law used is the Quaternion Feedback Control law, which is described in (Wie, 2008). The control law is of the form:

$$\mathbf{T}_W = -K_p \,\text{sign}(\delta q_4)\delta\overline{\mathbf{q}} - K_d\,\boldsymbol{\omega} \tag{6.5.12}$$

with gains K_p and K_d, the error quaternion $\delta\mathbf{q}$ (with vector $\delta\overline{\mathbf{q}}$ and scalar part δq_4), the angular rate of the satellite $\boldsymbol{\omega}$ and torque of the reaction wheel $\mathbf{T}_W$. Note that the proportional K_p and the derivative gains K_d are identical for the three axis.

Based on this control law, the control loop for the SP mode, in continuous time, can be represented as the schematic in Figure 6.11.

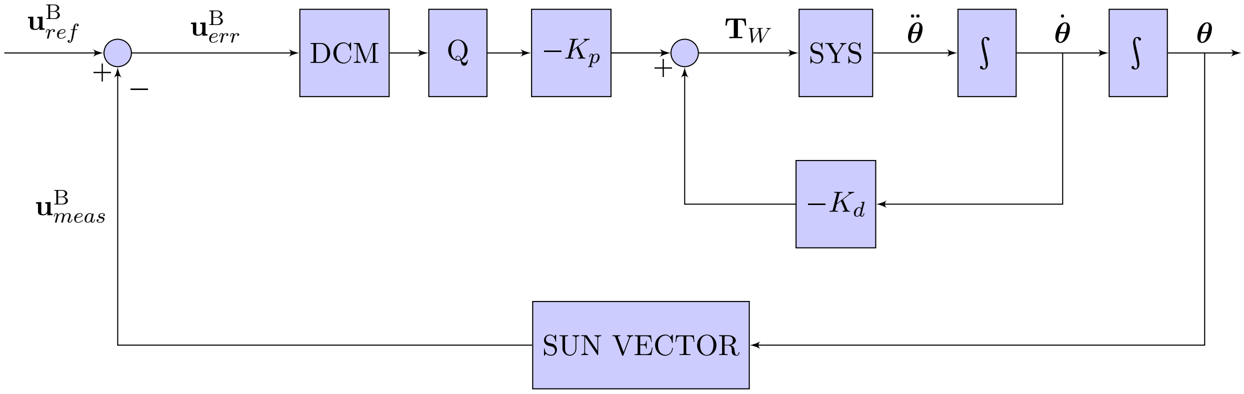

Figure 6.11: *The representation of the closed-loop control, for the SP controller, in the continuous time-frame.*

The process is as follows. First, the measured Sun vector in B-frame is reconstructed from the obtained attitude. The measured Sun vector is then compared with the reference vector, and based on this difference a rotation matrix DCM is defined. The rotation matrix DCM is converted into an error quaternion.

The control loop as shown above can be simplified. With the small angle approximation, one can steer on the angle pointing error instead of steering on the error quaternion. Furthermore, defining a reference speed of 0 deg/s, the control loop simplifies to the schematic in Figure 6.12.

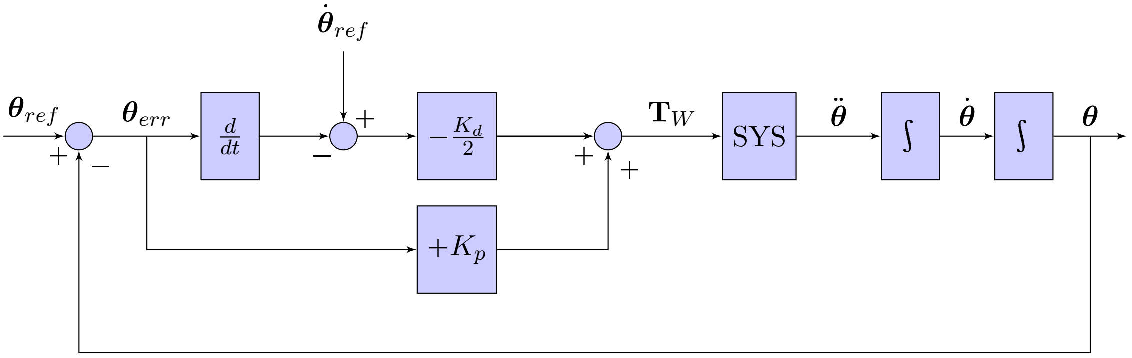

Figure 6.12: *Simplification of the closed-loop control for the SP controller.*

This control loop can simplified further to the schematic shown in Figure 6.13.

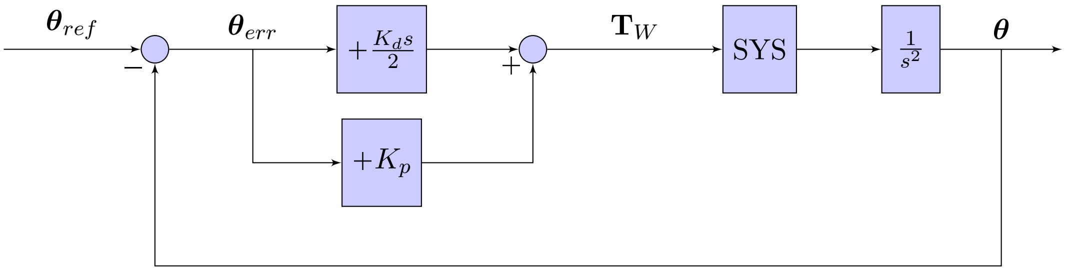

Figure 6.13: *Simplification of the closed-loop control for the SP controller.*

Alternatively, in symbolic form, the control loop can be represented as in Figure 6.14.

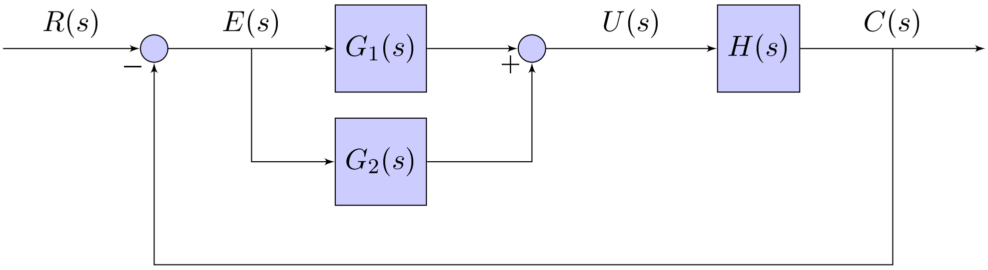

Figure 6.14: *Symbolic representation of the closed-loop control for the SP controller.*

In Figure 6.14, $R(s)$ is the Laplace transform of the reference angles, $E(s)$ is the Laplace transform of the error angles and $C(s)$ is the Laplace transform of the output angles. The controllers are represented with $G_1(s)$ and $G_2(s)$ and the plant with $H(s)$.

The controller used in the SP mode is a PD controller on the position (thus a PI controller on the velocity), described with:

$$G(s) = G_1(s) + G_2(s) = \frac{K_d s}{2} + K_p \tag{6.5.13}$$

The plant equation can be obtained from Euler's rotational equation of motion:

$$\mathbf{J}\dot{\boldsymbol{\omega}} + \dot{\mathbf{h}}_W + \boldsymbol{\omega} \times (\mathbf{J}\boldsymbol{\omega} + \mathbf{h}_W) = \mathbf{M}_{EXT} \tag{6.5.14}$$

With the same assumptions as in Section 6.5.1, this reduces to:

$$\mathbf{J}\dot{\boldsymbol{\omega}} = \mathbf{u} = -\left(\dot{\mathbf{h}}_W + \boldsymbol{\omega} \times \mathbf{h}_W\right) \tag{6.5.15}$$

where $\mathbf{u}$ is the internal torque from the actuators, in this case $\mathbf{T}_W$.

The plant equation is now described as such:

$$H(s) = \frac{1}{Js^2} \tag{6.5.16}$$

The closed loop transfer function and the open loop transfer function are similarly derived as in Section 6.5.1, except for the differences in the definition of $G(s)$ and $H(s)$.

Stability margins

In this section the stability margins will be discussed for the SP controller. The SP gains which have been selected in Section 6.4.2 are $K_d = 20$ and $K_p = 1$. The resulting gain and phase margins will be looked at for different inertia's and time delays.

The inertia term which will be considered is J_{xx}, which corresponds to the axis where the satellite will be rotating around at the end of the SP slew. The lowest and highest inertia terms are 48.45 and 61.29 kg m^2. Time delays up to 1 s (equivalent to a full signal delay) will be considered here. Table 6.10 summarizes the gain and phase margins which have been found.

Table 6.10: *Phase and gain margins for the SP controller, for different inertia's and time delays.*

Inertia (kg m^2)	**Delay (s)**	**Gain margin (dB)**	**At frequency (rad/s)**	**Phase margin (deg)**	**Delay margin (s)**	**At frequency (rad/s)**
61.29	0	∞	-	61.7	5.80	0.19
...	0.1	39.7	15.71	60.6	5.70	0.19
...	0.5	25.5	3.08	56.3	5.30	0.19
...	1	19.3	1.50	51.0	4.80	0.19
48.45	0	∞	-	66.1	5.11	0.23
...	0.1	37.6	15.71	64.8	5.01	0.23
...	0.5	23.5	3.08	59.6	4.61	0.23
...	1	17.2	1.50	53.2	4.11	0.23

The gain and phase margins have also been looked at for the case for a pure derivative controller. This would be the case when the satellite is exactly Sun pointing. Table 6.11 summarizes the results.

Table 6.11: *Phase and gain margins for the SP controller, in case a pure derivative controller is considered.*

Inertia (kg m^2)	**Delay (s)**	**Gain margin (dB)**	**At frequency (rad/s)**	**Phase margin (deg)**	**Delay margin (s)**	**At frequency (rad/s)**
61.29	0	∞	-	90	9.63	0.16
...	0.1	39.7	15.71	89.1	9.53	0.16
...	0.5	25.7	3.14	85.3	9.13	0.16
...	1	19.7	1.57	80.7	8.63	0.16
48.45	0	∞	-	90	7.61	0.21
...	0.1	37.6	15.71	88.8	7.51	0.21
...	0.5	23.6	3.14	84.1	7.11	0.21
...	1	17.6	1.57	78.2	6.61	0.21

The gain and phase margins which have been found, are sufficiently large. This gives an indication for the stability of the controller. However, as mentioned before, the stability of the controller is not ensured. Further research shall be done, but that is beyond the scope of this project.

Chapter 7
PERFORMANCE ANALYSIS DETUMBLE MODE

In this chapter it will be demonstrated that the requirements on the detumble time can be met, which have been presented in Section 6.1. The requirements shall be met in presence of uncertainties. Those uncertainties shall be looked at, with which the critical design drivers will be identified.

The SPS-2 project is a non-recurring effort to design a platform, which is compatible with large variety of payloads. In the future, the goal is to make the SPS-project a recurring one. This thesis shall therefore provide the groundwork for those projects, such that the different payload configurations shall be addressed. Therefore, the simulation runs in this chapter will be performed for all configurations separately.

The approach is as follows. First the influence of varying the initial conditions is looked at. This is described in Section 7.1. These simulation results will also serve as a reference for the further simulations. In Section 7.2 it is shown how the measuring/actuation ratio affects the control performance. In Section 7.3, it is investigated how the uncertainties in the geometry affect the performance of the detumble controller. Section 7.4 describes the impact on the results by varying the torquer strength. Section 7.5 shows how sensitive the system is to variations in the sensor and actuator parameters, and which parameters have a large impact on the design. In Section 7.6 a full Monte Carlo analysis is performed, where all uncertainties are varied simultaneously. These Monte-Carlo simulations have been performed for different torque capacities, to clearly see the effect on the results. This is shown in Section 7.6.1. As some assumptions have been made regarding the measuring/actuation ratio of the torquer, these simulations have been repeated for different measuring/actuation ratios. This is described in Section 7.6.2.

Unfortunately, an error has been made in the initialization stage of the simulations. For all simulations discussed in Sections 7.1 to Section 7.6, the initial angular-rate components are 0.6 deg/s in both lateral directions and 1 deg/s in the longitudinal direction. However, this should be 1 deg/s in both lateral directions and 0.6 deg/s in the longitudinal direction. In Section 7.7 another full Monte Carlo test-run has been performed, such that the impact on the impact on the results is known.

Unless stated differently, all results in this chapter have been obtained with the nominal parameters. Those are listed in Table 6.5.

7.1 Variation of Initial Conditions

In this section the performance will be looked at when the initial parameters are varied. This will be done for all configurations. The initial parameters are varied between their minimum and maximum values, shown in Table 6.5.

The number of simulations per run is 200. To show the consistency of the results, the simulations will be repeated for four different seed numbers. As such, the total number of simulations per geometry is 800. Different seeds has been used for each simulation.

The results are shown in Figure 7.1. The results for each simulation run are listed in Table 7.1.

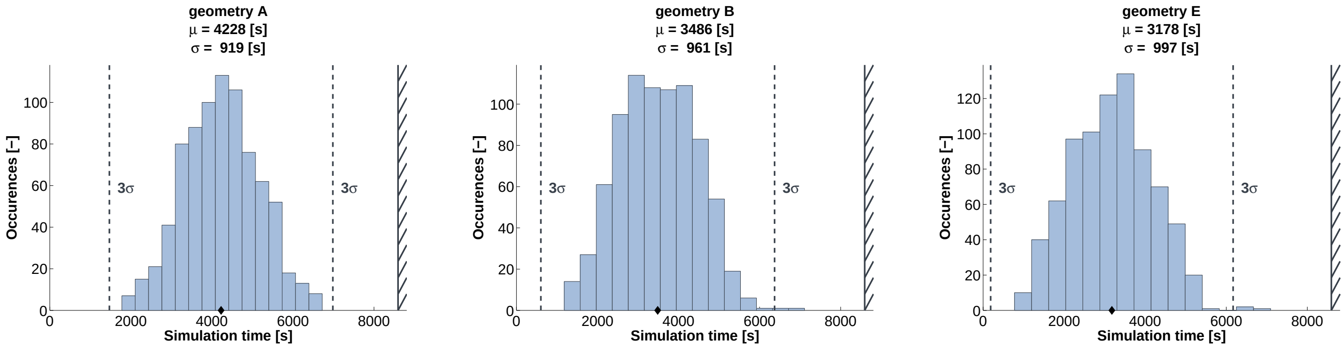

geometry A
μ = 4228 [s]
σ = 919 [s]

geometry B
μ = 3486 [s]
σ = 961 [s]

geometry E
μ = 3178 [s]
σ = 997 [s]

Figure 7.1: *Resulting detumble times (combined results) for the variation of initial conditions for configuration A (left), B (middle) and E (right).*

Table 7.1: *Results for the variation of initial orbital parameters.*[1]

case	**seed0**	**runs**	**MIN (s)**	**MAX (s)**	**μ (s)**	**σ (s)**	**$\mu + 3\sigma$ (s)**	**μ (Whr)**	**σ (Whr)**	**$\mu + 3\sigma$ (Whr)**
A	1	200	1988	6524	4361	919	7119	5.47	0.96	8.41
A	1000	200	2009	6507	4191	958	7064	5.30	0.96	8.24
A	2000	200	2234	6485	4221	851	6774	5.31	0.76	7.93
A	3000	200	1778	6724	4138	937	6949	5.22	0.91	8.09
	average	800	-	-	4228	917	-	5.33	0.95	-
	outliers	-	1778	6724	-	-	7119	-	-	8.41
B	1	200	1332	6107	3545	943	6375	4.11	0.72	6.66
B	1000	200	1230	7108	3493	984	6446	4.00	0.75	6.60
B	2000	200	1310	5682	3454	976	6381	3.98	0.68	6.46
B	3000	200	1180	5530	3453	945	6288	3.93	0.68	6.41
	average	800	-	-	3486	962	-	4.00	0.84	-
	outliers	-	1180	7108	-	-	6446	-	-	6.66
E	1	200	1220	5264	3211	909	5939	3.34	0.74	5.92
E	1000	200	776	6543	3102	972	6017	3.21	0.82	5.92
E	2000	200	1179	7093	3217	1082	6462	3.22	0.77	5.85
E	3000	200	895	5491	3180	1021	6242	3.20	0.81	5.90
	average	800	-	-	3178	998	-	3.24	0.89	-
	outliers	-	776	7093	-	-	6462	-	-	5.92

---

[1] Different seeds has been used for each simulation, indicated with the starting seed *seed0*. The minimum and maximum detumble times are indicated with *MIN* and *MAX*. The gray bars show the averages and outliers for each configuration.

For all cases, the detumble time is well within the constraint of 1.5 orbit (8593 s). It can be seen that the individual simulation runs of each geometry give consistent results. Depending on the initial conditions, the detumble time varies from 776 towards 7108 s. The initial position in the orbit seems to be very important. Note that the detumble times are generally smallest for geometry E.

7.2 Variation On/Off Switching Ratio

An important effect which is looked at, is the on/off switching ratio of the magnetometer and the magnetorquer, which was discussed in Section 6.2.2. The nominal on/off switching ratio selected was 3/10, which indicates 3 s of measuring, followed by 10 s of actuation. Here it will be investigated how the on/off switching ratio influences the controller performance.

In the first test campaign the effect of varying the measure time will be looked at. The measure times which will be considered are 1, 5 and 10 s, where the actuation period is kept at 10 s. As the effective gain is changed, this should have an impact on the resulting detumble times. A shorter measure time of 1 s results in a higher effective gain (10/11), which will most likely result in shorter detumble times. Increasing the time to measure results in lower effective gains (10/15 and 10/20), which will most likely result in longer detumble times. The simulations in Section 7.1 will be repeated with these adjusted measure/actuation ratios. For this analysis, only configuration A will be considered.

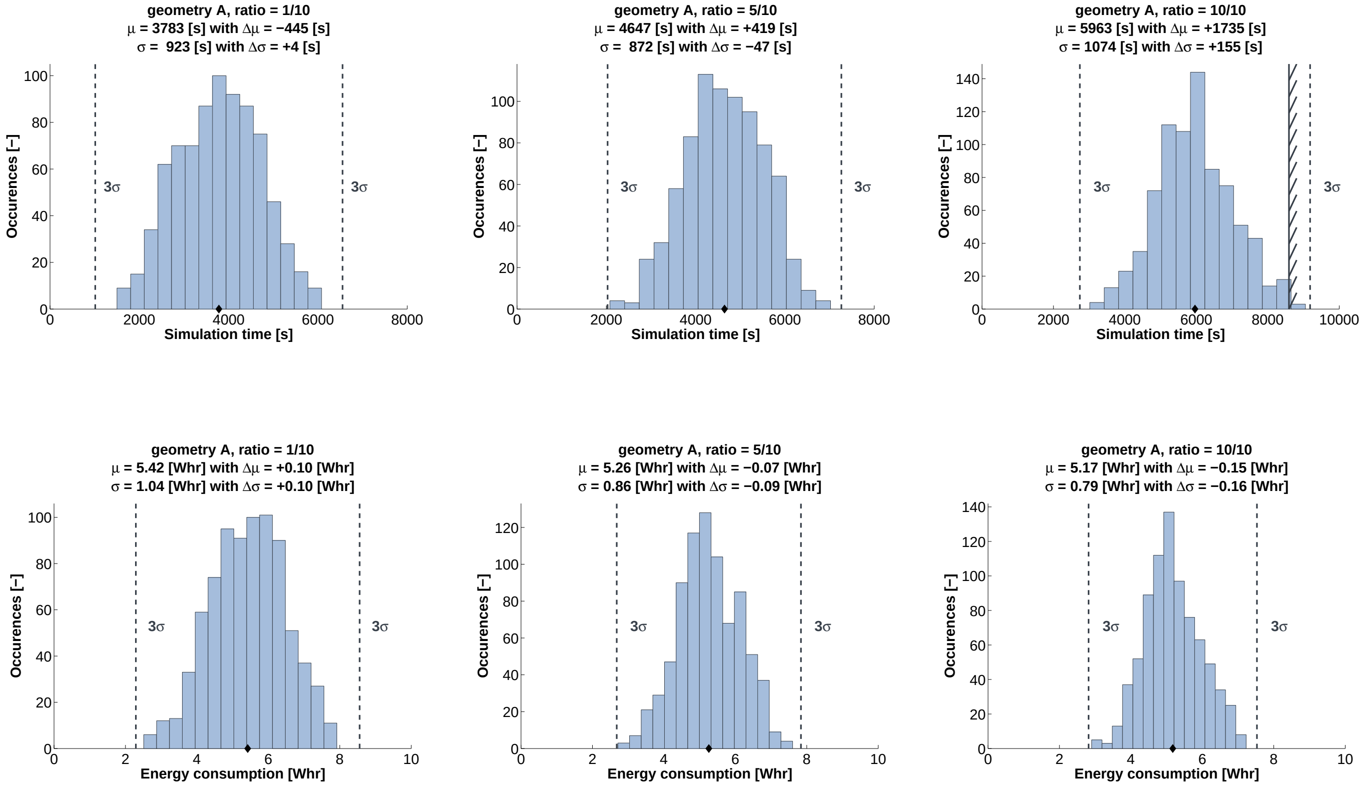

Figure 7.2: *The resulting detumble times and power consumptions for the variation of initial conditions, for configuration A. From left to right: a measure/actuation ratio of 1/10, 5/10 and 10/10.*

Figure 7.2 show the resulting detumble times and energy consumptions for configuration A. The results confirm the predictions made earlier. It can be seen that the average detumble time decreases with a measurement/actuation cycle of 1/10. The increase in power consumption is very small. The average detumble time becomes significantly higher with a higher measure/actuation cycle. The benefit in the power consumption is small though. For a measure/actuation cycle of 10/10, the detumble time constraint is violated a number of times.

In the other test campaign which has been performed, the measurement/actuation ratio is kept the same, such that the effective gain is not altered. As such, this should have no impact on the detumble time. In these simulations, the time to measure is changed to 6 s and the time to actuate is changed to 20 s.

The results can be found in Table 7.2. The minimum and maximum detumble times are indicated with *MIN* and *MAX*. The differences with respect to the reference orbits are indicated with Δ*MIN* and Δ*MAX*. As expected, the results show that the detumble times do not change significantly.

Table 7.2: *Results of the variation of initial orbital parameters, with different measure/actuation cycles, for geometry A.*

on/off ratio	$\boldsymbol{\mu}$ **(s)**	$\boldsymbol{\Delta\mu}$ **(s)**	$\boldsymbol{\sigma}$ **(s)**	$\boldsymbol{\Delta\sigma}$ **(s)**	$\boldsymbol{\mu+3\sigma}$ **(s)**	$\boldsymbol{\Delta(\mu+3\sigma)}$ **(s)**	**MIN (s)**	**ΔMIN (s)**	**MAX (s)**	**ΔMAX (s)**
1/10	3783	-445	923	+4	6552	-433	1501	-277	6082	-642
3/10	4228	-	919	-	6985	-	1778	-	6724	-
6/20	4253	+25	937	+18	7064	+79	1760	-18	7368	+644
5/10	4647	+419	872	-47	7265	+279	2080	+302	7022	+298
10/10	5963	+1735	1074	+155	9185	+2200	3019	+1241	9055	+2331

In this section the impact of varying the measurement/actuation ratio has been discussed, where 800 different initial conditions were looked at. At the end of the chapter a full Monte Carlo run will be performed, where again different measure/actuation ratios will be considered. This is described in Section 7.6.2.

7.3 Variation in the Geometry

Up to this point, three different configurations have been looked at. These were introduced in Section 2.4. However, there is an uncertainty in the mass and inertia distribution for each configuration. In this section it will be investigated whether the controller is sufficiently robust against those changes.

First, the uncertainty in mass distributions is discussed. Then, the results of the simulation campaigns are discussed. Two different simulation campaigns have been performed. In the first simulation campaign, the geometry variation was performed for different initial conditions, similar to Section 7.1. However, this analysis did not result in any insight how the geometry variation affects the controller performance. Therefore, only the geometry variation for specific orbits is discussed.

7.3.1 Uncertainties in mass and inertia distributions

The variation of the CoM and MoI tensors is described in Table 7.3.

Table 7.3: *Description and justification how the CoM and MoI will be varied.*

Variation	**Justification**
• Variation of the CoM location to ±0.06 m along the X- and Y- axis and ±0.05 m along the Z-axis.	The CoM location may change in orbit when solar panels are deployed.
• Variation of the diagonal terms of the inertia matrix with ±15%.	Uncertainty of placement payload masses.
• Variation of the off-diagonal terms of the inertia matrix with ±10%.	Uncertainty of placement payload masses.

The number of geometry variations is as follows. The number of variations in the CoM location is 12 (3 for each axis ×3 for the three axis + 3 variations in all axis simultaneously). Multiplied with a factor 3×3 for the variation of the (off-)diagonal terms of the MoI, this yields in total 108 simulation cases. From this set, 27 cases are identical. That means that 81 unique geometries will be considered.

7.3.2 Geometry variation for specific orbits

In this simulation campaign the different geometries will be looked at for specific orbits. The specific orbits which have been selected are two minimum, an average and two maximum orbits. These have been selected from the results in Section 7.1.

The results of the geometry variation for the specific orbits are summarized in Table 7.4. Here t_{ref} is the detumble time of the reference orbit, μ is the mean detumble time of all 81 simulations and $\Delta\mu$ is the difference with respect to the reference orbit. The minimum and maximum detumble times are denoted with MIN and MAX. The differences with respect to the reference orbits are indicated with ΔMIN and ΔMAX.

Table 7.4: *Results for the variation of the geometry, where specific seeds have been used for each simulation.*

case	**orbit**	**seed**	$\mathbf{t_{ref}}$ **(s)**	$\boldsymbol{\mu}$ **(s)**	$\boldsymbol{\Delta\mu}$ **(s)**	**MIN (s)**	**ΔMIN (s)**	**MAX (s)**	**ΔMAX (s)**
A	min (1)	3039	1778	1777	-1	1325	-453	2390	+612
B	min (1)	3039	1180	1148	-32	859	-321	1503	+323
E	min (1)	1036	776	1083	+307	542	-234	1948	+1172
A	min (2)	179	1988	2324	+336	1354	-634	3248	+1260
B	min (2)	1014	1230	1658	+428	1074	-156	2327	+1097
E	min (2)	3109	895	1203	+308	852	-43	2754	+1859
A	avg	2090	4228	3647	-581	2211	-2017	5128	+900
B	avg	1092	3495	3581	+86	2550	-945	5323	+1828
E	avg	135	3210	3667	+457	2722	-488	5481	+2271
A	max (1)	59	6524	6074	-450	4351	-2173	6966	+442
B	max (1)	26	6107	5565	-542	4179	-1928	6565	+458
E	max (1)	1158	6543	4926	-1617	4039	-2504	7258	+715
A	max (2)	3132	6724	5952	-772	4305	-2419	7043	+319
B	max (2)	1016	7108	4449	-2659	2500	-4608	7108	0
E	max (2)	2076	7093	3739	-3354	1812	-5281	7093	0

It might not be very clear from Table 7.4, but the results for the average and maximum orbits are highly segmented, in some cases around specific detumble times. The histograms in Figure 7.3 illustrate this.

The most important conclusion which can be drawn from the results in Table 7.4 is that the detumble time of the maximum orbits do not, or just slightly increase. This can be seen clearly in the histograms in Figure 7.3.

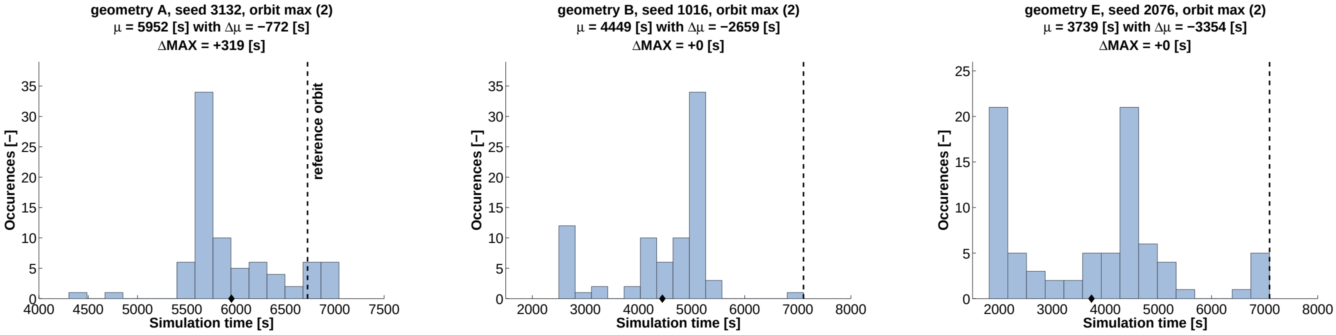

Figure 7.3: *The results for the geometry variation for the maximum orbits. The spread is highly segmented, but the maximum detumble time does not (or only slightly) increase.*

On the other hand, the detumble time for the minimum orbits in most cases increase due to the geometry variation. The average orbits only show a segmented spread around the reference value.

It appears that the geometry variation has only a small effect on the detumble-time performance. The choice of initial conditions is driving the performance of the detumble controller.

7.4 Variation in the Torquer Capability

Up to this point, a torque capacity of 15 Am^2 has been assumed. In this section, the effect is looked at of using magnetorquers with different strengths. It is to be expected that the detumble time decreases with higher torque capacities. The range of the torquer will be varied between 10 Am^2 and 30 Am^2.

The torque range will be changed for specific orbits. The specific orbits which have been selected are two minimum, an average and two maximum orbits for each configuration. These have been selected from the simulation campaign discussed in Section 7.1. The results of the torque range variation for the different configurations and orbits is shown in Figure 7.4.

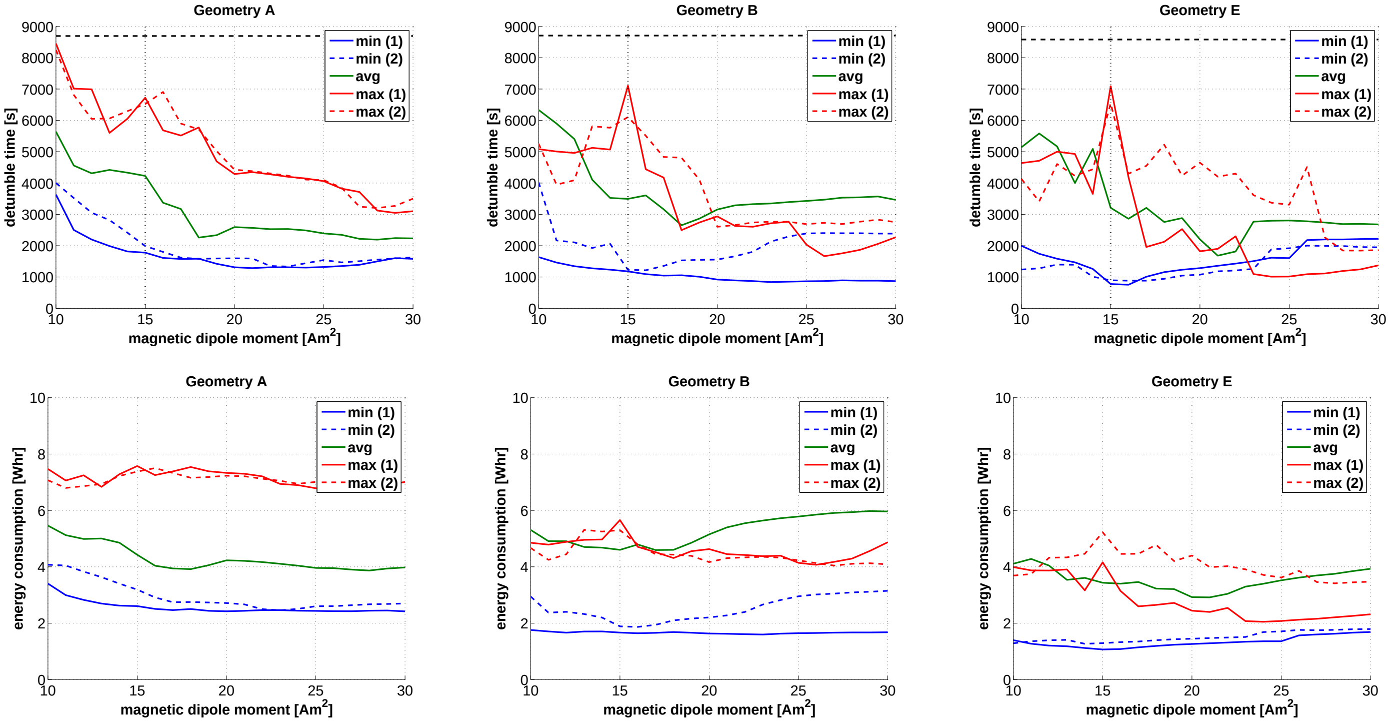

Figure 7.4: *The results for the variation of the torque capacity for configurations A, B and E. Top: detumble times, bottom: energy consumptions.*

The results are shown in Figure 7.4. From these results, some conclusions can be drawn:

- In general a decreasing trend can be observed in the detumbling times for larger torque capabilities, as to be expected. However, this trend is not linear; the detumble time can be higher for larger torque capacities. It can be explained as follows. The simulations have been performed for the exact same initial conditions. However, for the different torque capacities considered here, the torque outputs will be different, causing differences in the angular velocity reduction. As such, the spacecraft attitude profile in time is different as well. It therefore can be concluded, that the control efficiency is strongly related with the spacecraft orientation, together with its position in the orbit.
- There seems to be an upper boundary for the amount in detumble time reduction by increasing the torque capability. This is different per configuration. A possible explanation might be as follows. It might be that, the controller has to 'wait' until the satellite position along the orbit has progressed, to effectively reduce the remaining part of the angular velocity, as the magnetic field has rotated slightly by then.
- Decreasing the torque capability to 10 Am^2 does not result in violating the detumble time requirement in any case. However, the results show that for configuration A the detumble time is very close to the limit value.
- The detumble time of the maximum orbits is decreased significantly by increasing the torque capacity. The detumble time for the minimum or average orbits on the other hand may increase, but these are still below 4000 s.
- Furthermore, it seems as if the power consumption does not increase with higher torque capabilities. This is partly explained by the reduction in detumble time.

From these results, it seems as if a large reduction in detumbling time can be achieved when the torque capability is adjusted to higher values. However, as described above, this reduction in detumbling time mainly applicable for the maximum orbits. Next to this, there are some outliers in the results. This shows the necessity for a Monte Carlo run. In Section 7.6 a full Monte Carlo analysis will be performed. This Monte Carlo run will be performed for five different torque capacities (10, 15, 20, 25 and 30 Am^2). This will support the claims and answer some of the questions listed above.

7.5 Sensor and Actuator Parameter Variation

The structure of this section is as follows. First, the impact of each individual sensor/actuator error will be looked at. The purpose of this analysis is to find which sensor and actuator errors are driving the performance of the controller. After this, the parameters will be grouped. In this analysis, it will be investigated whether a linear relationship exist between the individual error sources. That would be beneficial, because the impact of the combined sensor/actuator errors can then easily be predicted. Finally, a Monte Carlo run has been performed to show the interaction between the individual error sources.

7.5.1 One-at-the-time variation

In this section, it shall be identified which sensor/actuator parameters have the largest impact on the detumble time. The total number of sensor/actuator parameters is 17, containing seven error sources for the magnetometer, seven for the gyro and three for the magnetorquer.

Global search

In the global search, the one-at-the-time parameter variation will be performed for all 17 sensor/actuator parameters. The minimum and maximum errors of each parameter will be considered in the simulations. Two specific orbits are considered (an average and the maximum orbit). These orbits have been selected from the results in Section 7.1. These reference orbits are referred to as nominal orbits, because these results were obtained using the nominal errors.

The results are compared with the nominal orbits. For the constant error sources, only one simulation will be performed. Some error sources are seed dependent; those are noises, nonlinearities and the gyro bias repeatability. For these error sources 15 simulations will be performed. In this manner, the spread in results due to this seed dependency can be observed.

The results of the one-at-the-time variation simulation campaign are listed in Table H.1. From this table, it appears that eight parameters seem to have a relative large impact on the detumble time. These will be looked at in the detailed analysis.

Detailed analysis

In this detailed analysis, eight parameters have been looked at. For this simulation campaign, two average and two maximum orbits have been considered. However, the results for the maximum orbits have been omitted here, as the detumble times decrease significantly and the spread is in general very large. As such, no conclusions can be drawn from these results. This is elaborated on in more detail in Appendix H.2.1.

The set-up for the detailed analysis was as follows. The number of simulations for the seed dependent parameters was increased to 40. Not only the minimum and maximum errors will be considered here (as in the global search), but also the nominal errors, to investigate the spread in detumble times for the nominal errors as well.

The results are shown in Table H.2. The following conclusions can be drawn from the one at the time variation of the different error sources:

- The impact of the magnetometer and the gyro misalignment errors are negligible.
- The impact of the gyro RRW is small. The difference between the minimum and maximum detumble times is generally small, except for one particular orbit, where the spread was 582 seconds. The mean detumble time for the 40 simulation runs differs only 29 seconds.
- The gyro bias repeatability, the gyro nonlinearity and the magnetorquer nonlinearity have a moderate influence on the detumble time. For all orbits, there was a significant spread in the results, often larger than 500 seconds. The maximum spread which have been found was 812 seconds. The mean detumble time for the 40 simulation runs is not affected much; the maximum difference is 126 seconds.
- The impact of the gyro ARW is large. It appears that increasing this error result in a (significant) *decrease* in the detumble time. The mean detumble time for the 40 simulations runs reduces with 65 to 786 seconds. Below, a possible explanation will be given for these results. Remarkable is that the spread in the results is very small (<70 seconds) for the minimum and nominal errors, with exception of one orbit (a spread of 371 seconds). For the maximum errors, the spreads are larger. The maximum spreads which have been found there, are 457 and 339 seconds.
- The impact of the gyro quantization interval is large. These results are remarkable as well. For larger quantization errors, a maximum *decrease* of 588 seconds in the detumble time has been found. Some suggestions will be made which can explain these effects.

Furthermore, there are some additional remarks to be made:

- The results show a highly segmented spread. Therefore, the standard deviations do not give much information of the distribution.
- For the gyro and the magnetorquer nonlinearity errors, the effect of the variation of the magnitude of the errors is not trivial. The detumble time does not always decrease for smaller errors, or increase with higher errors.
- The largest outliers in the results can be found for geometry E, followed by geometry B. There are no outliers for geometry A. Apart from those outliers, the impact of the error sources are more or less similar for the different geometries.
- Note that the gyro errors also have an impact on the angular velocity of the satellite after detumbling. This has not been considered here. With larger gyro errors, the *true* angular rates at the end of the detumbling might be larger, due to the higher inaccuracies in the measurements. This is relevant for the analysis described in Chapter 8 and as such, it will considered there.

A possible explanation for the decrease in detumble time due to a larger ARW error might be as follows. The ARW is an error source, which acts at small time scales. A reverse effect might be present here. In cases where the rates are low, the resulting torque command is small. However, due to the ARW error, the measured rate might be higher, and therefore the commanded torque increases to compensate for this. This compensation behavior does not generally result in a better performance, but may be partly beneficial.

The quantization stepsize determines how accurate the measured signal is represented. The detumble maneuver is ended when the measured rates are below a threshold value of 0.05 deg/s. The quantization of the signal may result in a slightly decreased measured angular rate, such that the detumble maneuver is completed prematurely. This effect might be stronger for larger quantization stepsizes.

Note that further research needs to be done to confirm these two hypotheses. This is beyond the scope of this project.

7.5.2 Variation of sensor/actuator errors in groups

Up to this point, only the impact of the individual parameter errors has been looked at. In this section, it will be investigated whether their combined contribution exhibit a linear relationship. For this, the error contributions are grouped per sensor/actuator. If a linear relationship exist, the impact of the combined sensor/actuator errors can easily be predicted. If not, an additional Monte Carlo run shall be performed to show the interaction between the individual error sources.

The set-up is as follows. The error sources have been grouped per sensor/actuator. Again, two specific average orbits will be considered per geometry. In total 40 simulations will be performed for each group, in which the minimum and maximum errors will be considered. At the end of the simulations, the results of the error variations in groups will be compared to the sum of the individual errors, which have been obtained in the detailed analysis described in Section 7.5.1.

The results for the grouped gyro errors are discussed now. Note that, in this analysis, the scale factor error has not been taken into account, to allow for a fair comparison with the results in Section 7.5.1. The results are listed in Table 7.5. There is a large discrepancy between the results of the variation of error sources in groups, and the summed results of the one-at-the-time variation. From these results, it is very clear that there does not exist a linear relationship between the individual error sources. As such, the obtained results of a similar analysis, for the grouped magnetometer or magnetorquer errors, will not be discussed here.

Despite the fact that no linear relationship exist, there are some conclusions which can be drawn from the simulation results.

- Table 7.5 confirms that the detumble time decreases for the maximum gyro errors. This decrease in detumble time is presumably caused by the ARW and quantization stepsize errors, discussed in Section 7.5.1.
- In Section 7.5.1, a choice was made between the most influencing error parameters per sensor/actuator. It appears that:
  - For the magnetometer, the misalignment error clearly has not the largest impact on the results. See Table H.4 for the results.
  - The nonlinearity error of the magnetorquer does indeed contribute for a large

extent to the results. Interesting to see though, is that the spread in detumble times is affected by the other parameters. The results are shown in Table H.5.

- The combined magnetometer errors do not have much influence at the results. This is as expected.
- The same holds true for the combined magnetorquer errors, except that the spread in the results is larger. Interesting to see, is that the spread in detumble times is affected by the other parameters.

Table 7.5: *The results of the variation of the gyro errors in group, compared to the sum of the results of the one-at-the-time variation. How to read this table, is described in Appendix H.3.*

Results variation error sources in groups (all seven error sources have been considered)													
						$\Delta\mu^*$ (s)		σ (s)			σ (%)		
set	**runs**	**case**	**t_{ref} (s)**	**t^*_{ref} (s)**	**orbit**	**MIN**	**MAX**	**MIN**	**NOM**	**MAX**	**MIN**	**NOM**	**MAX**
GYR	40	A	4228	4334	avg (1)	13	-533	14	199	233	0%	5%	5%
GYR	40	B	3495	3504	avg (1)	24	-119	4	14	31	0%	0%	1%
GYR	40	E	3210	3069	avg (1)	71	-264	12	157	72	0%	5%	2%
GYR	40	A	4143	4235	avg (2)	172	-573	21	159	270	0%	4%	6%
GYR	40	B	3443	3418	avg (2)	66	-574	4	33	73	0%	1%	2%
GYR	40	E	3101	3032	avg (2)	89	-873	7	206	35	0%	7%	1%
Sum results one-at-the-time variation (note that GYR.SF_error has not been considered)													
						$\Delta\mu^*$ (s)		σ (s)			σ (%)		
set	**runs**	**case**	**t_{ref} (s)**	**t^*_{ref} (s)**	**orbit**	**MIN**	**MAX**	**MIN**	**NOM**	**MAX**	**MIN**	**NOM**	**MAX**
GYR	40	A	4228	4293	avg (1)	15	-306	84	112	132	2%	3%	3%
GYR	40	B	3495	3502	avg (1)	-11	-230	12	70	189	0%	1%	3%
GYR	40	E	3210	3172	avg (1)	121	-706	3	8	17	0%	0%	1%
GYR	40	A	4143	4161	avg (2)	107	-101	3	55	128	0%	1%	3%
GYR	40	B	3443	3425	avg (2)	68	-708	8	69	117	0%	1%	2%
GYR	40	E	3101	3076	avg (2)	27	-1377	9	22	60	0%	1%	2%

Discussion points

There are some discussion points relating to the approach in this section. These will be discussed here.

To investigate the impact of the combination between the error sources, these have to be considered simultaneously. One can argue to group the different error sources. Note that the choice of groups in this subsection is not adequate. It might seem a very obvious choice to group the parameters per sensor/actuator. However, note that this choice is purely arbitrary. Currently it is assumed that only those parameters interact with other, without further reasoning. It might well be that there is an interaction with other parameters. This simulation campaign has shown such correlation.

Another aspect, which has not been considered here, is that some parameters in a group might be characterized by a large error, whilst other error sources may be smaller. That is another reason not to group the parameters, because there is an uncertainty in the distribution of the input parameters.

The results show that it is very difficult, or maybe impossible, to predict the influence of one parameter, as there is no linear relationship between the different error sources. There is a strong cross-correlation with other error parameters, but also with the dynamics of the system. If the errors were to be grouped, it must be known how the individual parameters influence each other. Furthermore, there is a large uncertainty about the input distribution, which is a disadvantage when grouping the different error sources. These results prove a Monte Carlo run is necessary to see how the different parameters interact with each other and what the impact of the sensor and actuator errors is on the system performance.

7.5.3 Variation of all sensor/actuator errors

In accordance with the concluding remarks in Section 7.5.2, a Monte Carlo run will be performed here.

A Monte Carlo run has been performed for two average orbits per geometry. The results are shown in Figure 7.5. The dashed lines represent the reference orbits. The dotted lines illustrate the "3σ boundaries". For most cases however, it can be clearly be seen that these do not represent the actual boundaries of the distributions. In some figures, the shape of the distribution resembles a bimodal distribution.

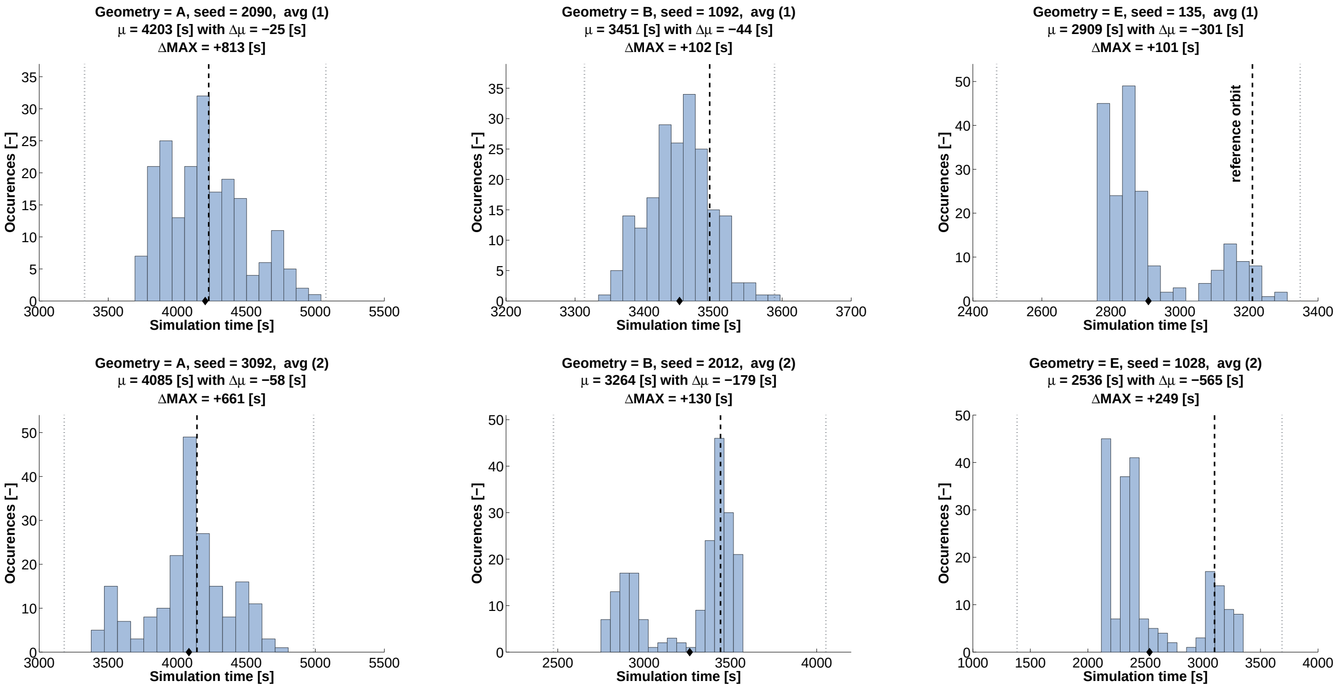

Figure 7.5: *Results of the variation of all sensor/actuator errors simultaneously by a Monte Carlo run.*

These results show that the spread in detumble times is a maximum of ≈1300 seconds. The maximum increase in detumble time occurs for geometry A, where the detumble time increases with 813 and 661 s respectively.

Now that the impact of the sensor and actuator errors has been looked at, the full Monte Carlo runs will be performed.

7.6 Full Monte Carlo Runs

In the preceding sections, the impact of various kinds of uncertainties has been investigated. In this section, the combined effect of all these uncertainties will be looked at, through a full Monte Carlo run. First, the general results are discussed, where different torque capabilities are considered. This is described in Section 7.6.1. In Section 7.6.2 the impact of different measuring/actuation cycles will be looked at.

7.6.1 Variation of torque capability

In this Monte Carlo run, the following variations will be considered simultaneously:

- The variation of the initial parameters (orbit parameters, date, initial attitude and rate direction), as described in Section 7.1.
- The variation in the geometry, as described in Section 7.3.
- The variation in the sensor and actuator parameter errors, as described in Section 7.5.

To investigate the influence of different torque capabilities, this simulation campaign is repeated for four other torque capabilities (10, 20, 25 and 30 Am^2). Each Monte Carlo run consists of 800 simulation runs. The results are shown in Figure 7.6, and have been summarized in Table 7.6. There are several important conclusions which can be made:

- Higher torque capabilities clearly result in faster detumble times. The difference is significant.
- For torque capabilities of 15 Am^2 and larger, the detumble time is always well within the requirement of 8593 s. The margin is more than 1000 s.
- For a torque capability of 10 Am^2, the detumble time requirement is violated in eight instances[2]. However, for 99% of the cases, the requirement on detumble time is still satisfied.

A very interesting result is that the power consumption, as shown in Table 7.6, hardly changes for larger torque capabilities. This is caused by the decrease in detumble time, which requires the torquers to be operated for shorter time periods. But, it might even be more extreme than that. For these simulations, it has been assumed that the power consumption scales linearly with the torque capability. This is a very crude approximation. Some specification sheets state that the torquers become more efficient for larger torque capabilities. As such, one can expect that for higher torque capabilities, the power consumption decreases. That means that for higher torque capabilities, both the detumble time and the power consumption decrease.

---

[2] The violations in detumble times are 8694, 8712, 8739, 8846, 9295, 9357 and 9722 s for configuration A, and 9831 s for configuration E.

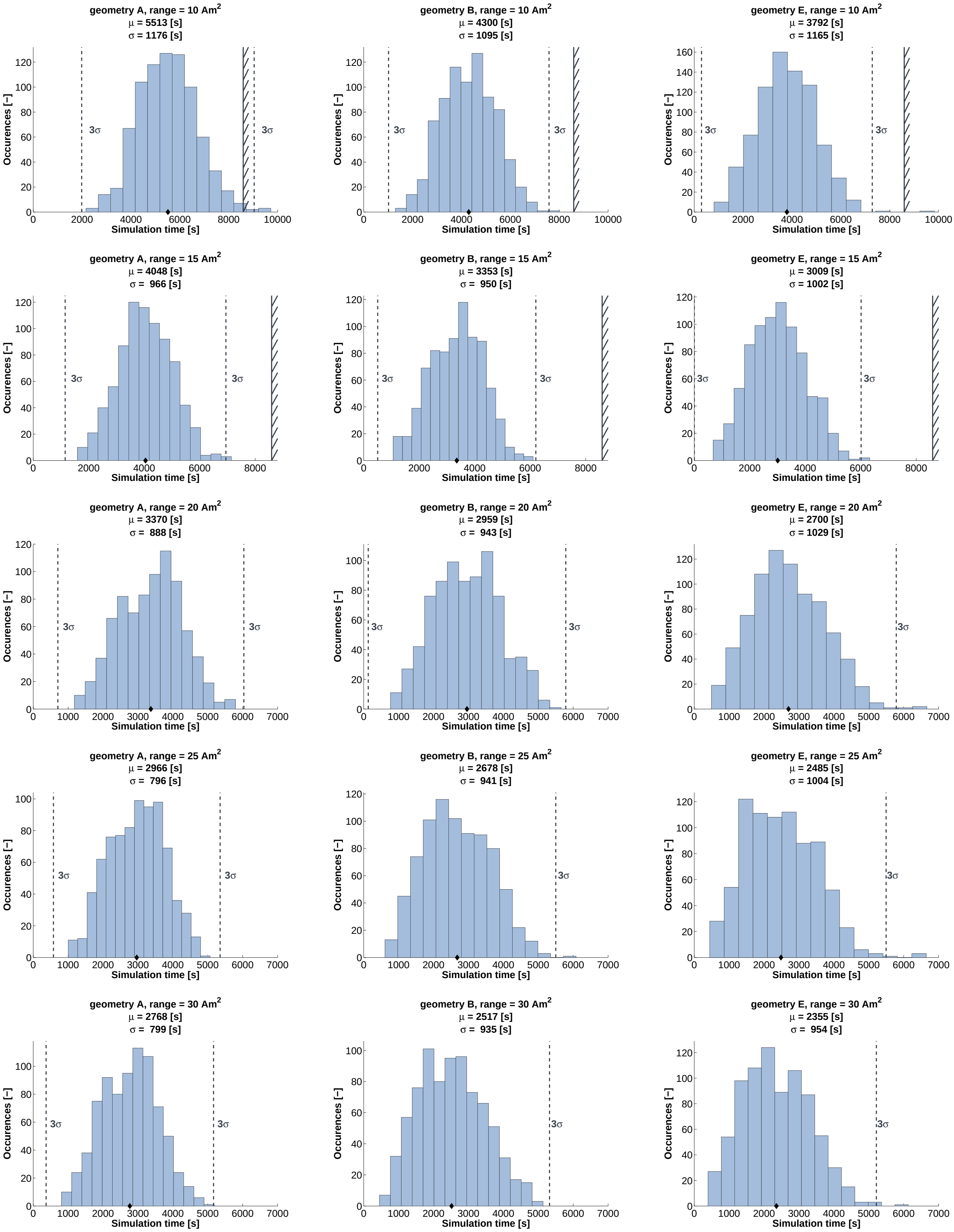

Figure 7.6: *Results of the full Monte Carlo variation, for different configurations and different torque capabilities.*

Table 7.6: *Results of the full Monte Carlo simulation, for different configurations and different torque capabilities.*

case	**range** [Am^2]	μ [s]	σ [s]	$\mu + 3\sigma$ [s]	**MIN** [s]	**MAX** [s]	μ [Whr]	σ [Whr]	$\mu + 3\sigma$ [Whr]
A	10	5513	1176	9041	2159	9722	5.31	1.04	8.44
	15	4048	966	6944	1592	7142	5.21	1.12	8.58
	20	3370	888	6034	1180	5793	5.09	1.16	8.58
	25	2966	796	5353	1003	5066	5.00	1.19	8.58
	30	2768	799	5166	810	5186	4.95	1.24	8.67
B	10	4300	1095	7583	1296	8004	3.96	0.89	6.64
	15	3353	950	6202	1060	6105	3.93	0.94	6.75
	20	2959	943	5788	767	5655	3.93	1.02	6.98
	25	2678	941	5502	609	6084	3.92	1.11	7.24
	30	2517	935	5322	452	5137	3.93	1.14	7.35
E	10	3792	1165	7287	810	9831	3.22	0.90	5.94
	15	3009	1002	6014	683	6327	3.17	0.93	5.97
	20	2700	1029	5787	493	6664	3.18	1.03	6.26
	25	2485	1004	5496	444	6646	3.19	1.07	6.41
	30	2355	954	5218	395	6131	3.20	1.08	6.45

7.6.2 Variation of measuring/actuation cycle

The simulations in Section 7.6.1 will be repeated here, for different measure/actuation ratios. A fixed torque strength of 15 Am^2 hsa been used.

The results are shown in Figure 7.7. Table 7.7 summarizes the results. For almost all simulations, the resulting detumble time is within the requirement. Only for configuration A, when the measure time is 10 s, the detumble time requirement of 8593 s is violated in ten occasions[3]. It can be seen that the detumble time increases for lower on/off switching ratios. The energy consumption slightly decreases when longer measure periods are used.

Table 7.7: *Results of the full Monte Carlo variation, for different measure/actuation ratios.*

case	**ratio**	μ (s)	σ (s)	$\mu + 3\sigma$ (s)	**MIN** (s)	**MAX** (s)	μ (Whr)	σ (Whr)	$\mu + 3\sigma$ (Whr)
A	1/10	3647	966	6545	1309	6718	5.31	1.20	8.90
	3/10	4048	966	6944	1592	7142	5.21	1.12	8.58
	6/20	4061	969	6968	1601	7340	5.25	1.14	8.67
	5/10	4481	1037	7591	1726	7411	5.13	1.08	8.36
	10/10	5730	1229	9418	2267	9199	5.04	0.99	8.00
B	1/10	3199	1036	6306	812	7356	4.11	1.04	7.24
	3/10	3353	950	6202	1060	6105	3.93	0.94	6.75
	6/20	3363	954	6225	1060	6025	3.97	0.94	6.80
	5/10	3612	976	6541	1141	6304	3.83	0.89	6.49
	10/10	4364	1052	7520	1735	7644	3.71	0.82	6.19
E	1/10	2909	1112	6245	472	7094	3.33	1.05	6.49
	3/10	3009	1002	6014	683	6327	3.17	0.93	5.97
	6/20	3009	1006	6028	665	7051	3.20	0.95	6.04
	5/10	3174	945	6010	728	5846	3.08	0.88	5.72
	10/10	3819	1083	7067	856	7190	2.99	0.83	5.49

---

[3] The violations in the detumble times are 8608, 8615, 8675, 8683, 8736, 8831, 8921, 8991, 9013 and 9199 s.

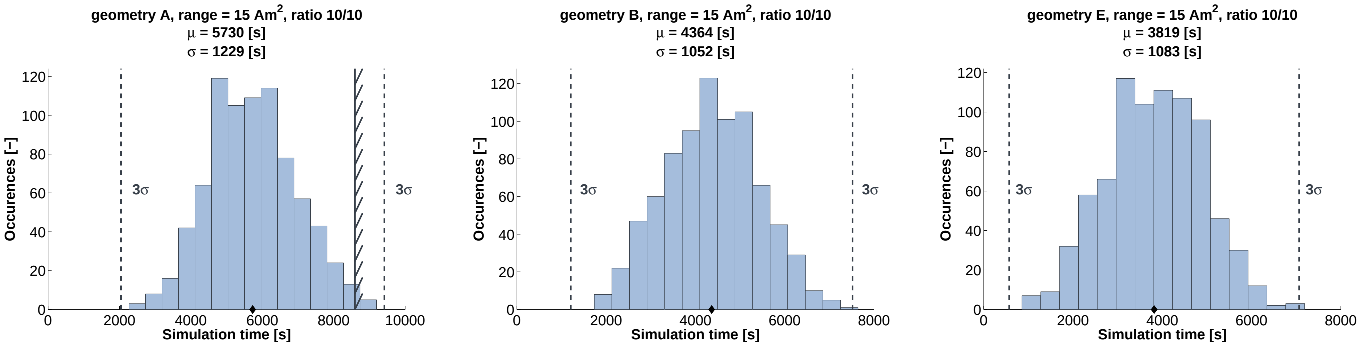

Figure 7.7: *Results of the full Monte Carlo variation, for different measure/actuation ratios.*

The results found here, confirm the results found in Section 7.2. The most important observation is that the detumble time can be decreased further, when shorter measure periods are taken. However, as described in Section 7.2, at this stage there is an uncertainty about the time for the magnetic field to dissipate such that the magnetometer measurements are not disturbed.

7.7 Results for Corrected Initial Rate

Unfortunately, an error has been made in the initialization stage of the simulations. For all simulations discussed in Sections 7.1 to Section 7.6.2, the initial angular rate components are 0.6 deg/s in both lateral directions, and 1 deg/s in the longitudinal direction. However, this should be 1 deg/s in the lateral directions, and 0.6 deg/s in the longitudinal direction.

To see the impact on the results, the analysis of Section 7.6.1 has been repeated. However, only torque capabilities of 10 Am^2 and 15 Am^2 have been considered. The results are shown in Figure 7.8. A summary of the results is given in Table 7.8.

The simulations show that the impact on the detumble time is severe. For a torque strength of 15 Am^2, it can be seen that the detumble time increases significantly. However, for almost all cases the detumble time is still within the detumble time requirement.[4] For a torque strength of 10 Am^2, the detumble time requirement is violated in many cases. Furthermore, note that the increase in the energy consumption is proportional to the increase in detumble time.

On one hand, this result is surprising. In the 'wrong' simulations, the highest components of the rate were around the axis with the highest inertia terms. Therefore, it was to be expected that the detumble times would improve for the correct situation. This appears not to be the case. As the norm of the rate is higher, this apparently means that more effort needs to be done to detumble the satellite.

Despite the fact that the results in this section show that the detumble time increases significantly, the requirement on the detumble can still be fulfilled with a torque capacity of 15 Am^2. It is left as future work to redo the simulations of Sections 7.1 through 7.6 .

---

[4] The detumble time requirement is violated in only two cases (8609 and 8815 s).

Table 7.8: *Results of the full Monte Carlo variation, for the corrected angular rate.*

case	torque (Am^2)	rate (deg/s)	μ (s)	σ (s)	$\mu + 3\sigma$ (s)	MIN (s)	MAX (s)	μ (Whr)	σ (Whr)	$\mu + 3\sigma$ (Whr)
A	15	$(0.6;0.6;1)^T$	4048	966	6944	1592	7142	5.21	1.12	8.58
	15	$(1;1;0.6)^T$	5492	1068	8695	2362	8815	7.32	1.26	11.11
	10	$(1;1;0.6)^T$	7606	1471	12018	3809	11654	7.44	1.31	11.38
B	15	$(0.6;0.6;1)^T$	3353	950	6202	1060	6105	3.93	0.94	6.75
	15	$(1;1;0.6)^T$	4525	1024	7598	1689	7649	5.67	1.05	8.82
	10	$(1;1;0.6)^T$	6033	1164	9524	2534	9547	5.71	0.97	8.61
E	15	$(0.6;0.6;1)^T$	3009	1002	6014	683	6327	3.17	0.93	5.97
	15	$(1;1;0.6)^T$	4250	1044	7382	1591	8190	5.05	1.00	8.06
	10	$(1;1;0.6)^T$	5578	1110	8908	2178	8381	5.14	0.91	7.86

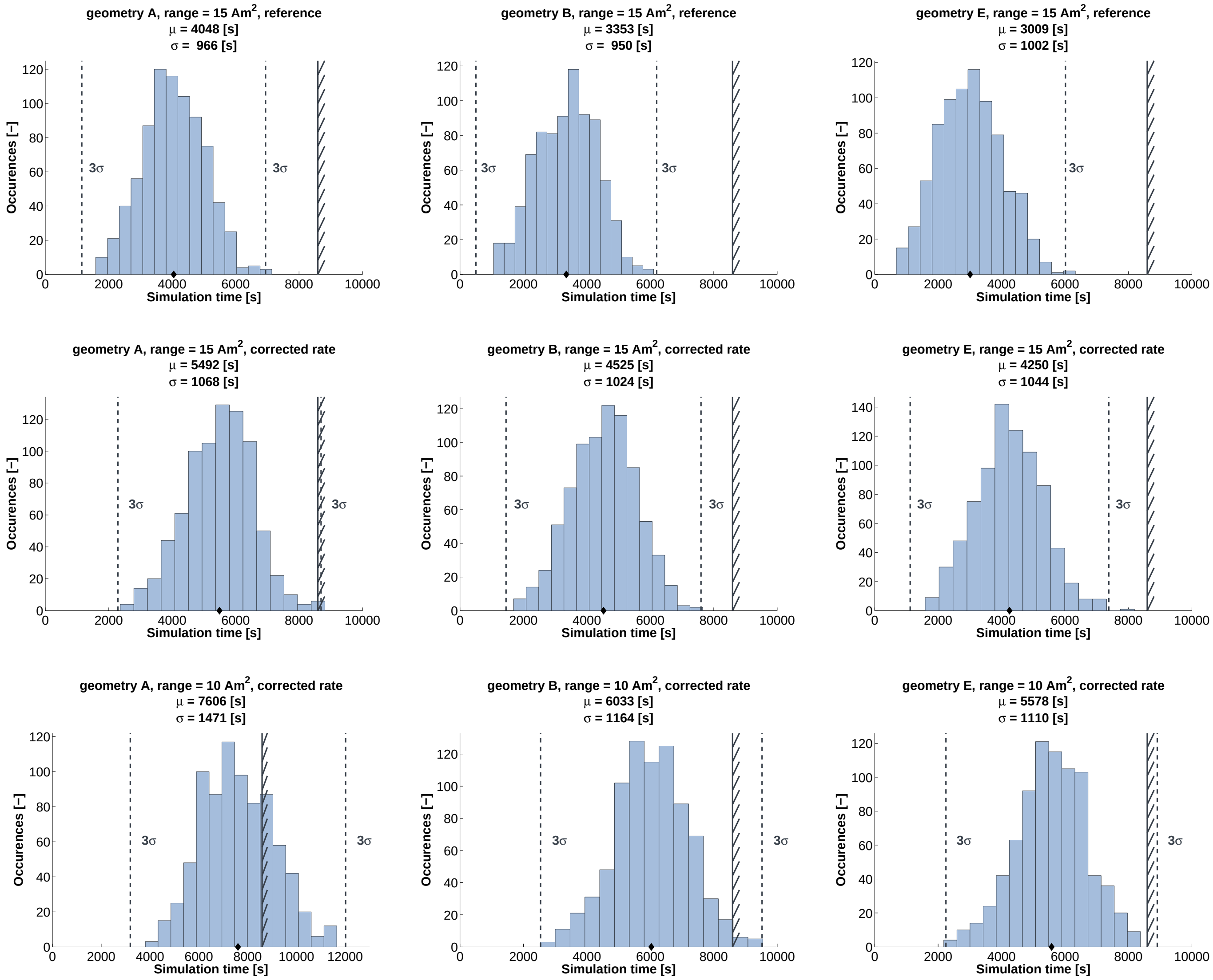

Figure 7.8: *Top: reference detumble times for (wrong) initial angular rate of (0.6;0.6;1) deg/s. Middle: detumble times for correct initial angular rate of (1;1;0.6) deg/s. Bottom: detumble times for correct initial angular rate of (1;1;0.6) deg/s, where the torque capacity is only 10 Am^2.*

Chapter 8
PERFORMANCE ANALYSIS SA AND SP MODES

This chapter deals with the performance analysis of the SA and SP controllers. It will be investigated whether the requirements, as shown in Section 6.1, can be met.

In the performance analysis for the detumble mode, which was discussed in Chapter 7, a detailed analysis was performed to see the impact of the variation of the initial conditions, the geometry and the sensor and actuator parameters separately. The analysis performed there was very time consuming. As the current stage of the project does not allow for more time exceeding, the following approach has been agreed upon. In a similar fashion as the detumble performance analysis, the variation of initial conditions will be considered first. When these results show a comfortable margin to satisfy the the requirements, a full Monte Carlo test run will be performed. If it appears that there are cases where the requirements cannot be satisfied, it will be investigated why. If necessary, more simulations will be performed.

The structure of the chapter is as follows. First, the mode switching possibilities are presented in Section 8.1. This is essential in order to understand the results in the upcoming sections. Then, the simulation parameters are shown in Section 8.2. Section 8.3 will then discuss the results due to the variation of the initial conditions. The results of the full Monte Carlo run are shown in Section 8.4. Finally, the conclusions are written in Section 8.5, together with some recommendations.

8.1 Mode Switching Possibilities

During the simulation campaign different mode switching profiles will occur. Before discussing the results of the simulation campaign, this section will first give a brief overview of the different situations which can occur. Please refer to Section 2.2 to see the mode switching diagram.

The figures in this section can be read as follows. The light yellow regions shows when the Sun has been acquired, i.e. the Sun is in the FoV of the Sun sensor (mode 4). The satellite will then start a slew maneuver to get Sun pointing. If the XY-angle is within 5 deg, the satellite is Sun pointing (mode 5). This is indicated with the dark yellow region. The simulations are stopped when the satellite is SP for 500 s. The blue region shows when an eclipse occurs. The time spend in each mode is also indicated in the figures.

8.1.1 Case without eclipse

It might be that the initial conditions are such that no eclipse occurs. In this situation there are still two possibilities. Either one can start with the Sun directly in the FoV. That means that one can start in mode 4 (left figure). If this is not the case, one or two slew maneuvers are required to acquire the Sun (right figure).

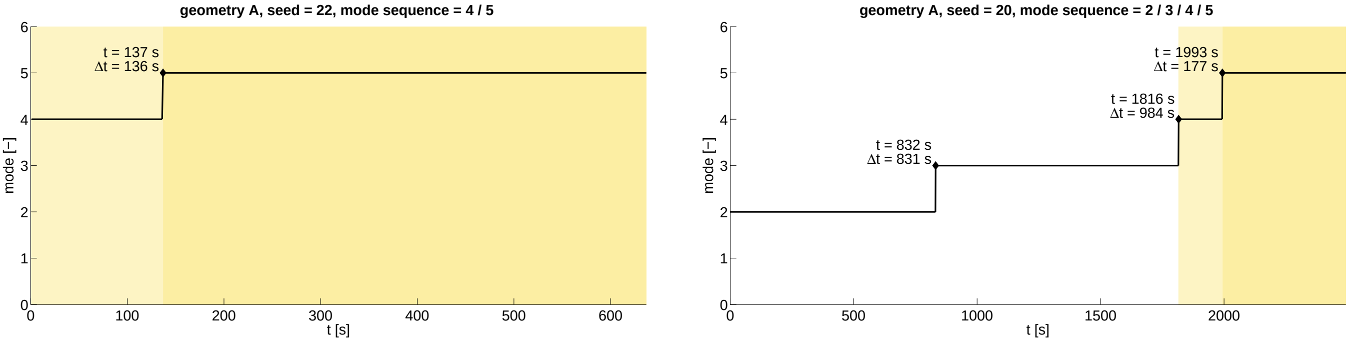

Figure 8.1: *Two examples of a mode switching diagram, without an eclipse.*

8.1.2 Case with eclipse at start

There are several different scenarios one can think of when an eclipse occurs. The first scenario is when one starts in an eclipse. After the eclipse, one or two slew maneuvers are required to acquire the Sun.

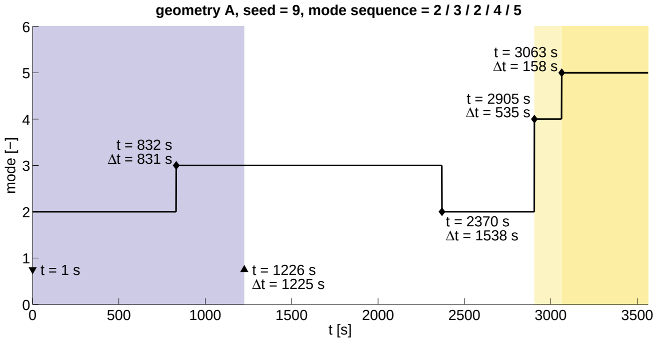

Figure 8.2: *Example of a mode switching diagram, with an eclipse at the start.*

8.1.3 Case with modes 2 / 3 before eclipse

It might be that an eclipse occurs before Sun has been acquired. In that situation, the satellite is still in mode 2 (left figure) or mode 3 (right figure). After the eclipse, one or two slew maneuvers are required to acquire the Sun. This situation results in the longest simulation time.

Note that there is no information whether an eclipse occurs (Section 6.1). Therefore, the satellite will continue to perform the SA slews in an eclipse. It might be (coincidentally) that after the eclipse exit the Sun is in the FoV. In such a situation, the satellite continues in mode 4 or 5.

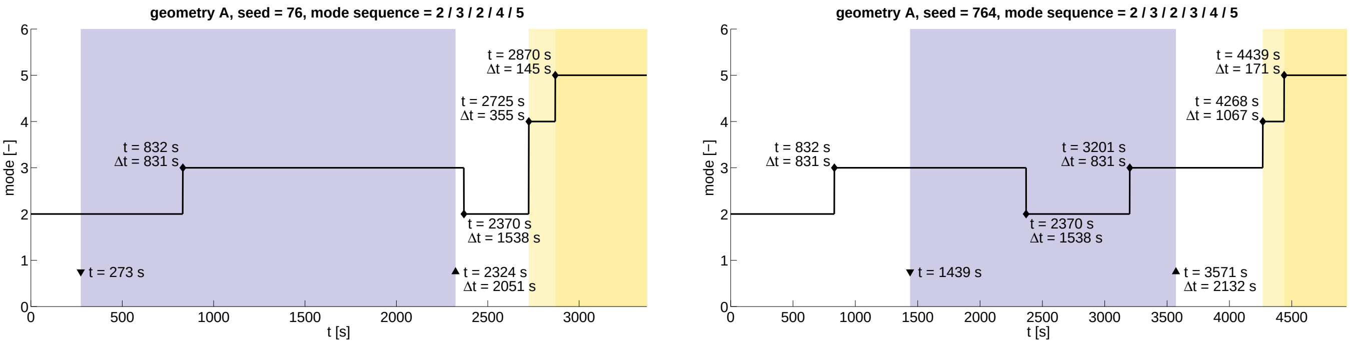

Figure 8.3: *Two examples of a mode switching diagram. Here, an eclipse occurs when the satellite is in control mode 2 (left) or 3 (right).*

8.1.4 Case with modes 4 / 5 before eclipse

The last scenario is that the Sun has been acquired already (left figure), or may be even Sun pointing (right figure), when an eclipse occurs. During the eclipse, the satellite remains Sun pointing, based on propagated last Sun measurement (see Section 6.4.3). After the eclipse, given the Sun is still in the FoV, the satellite will continue in mode 4.

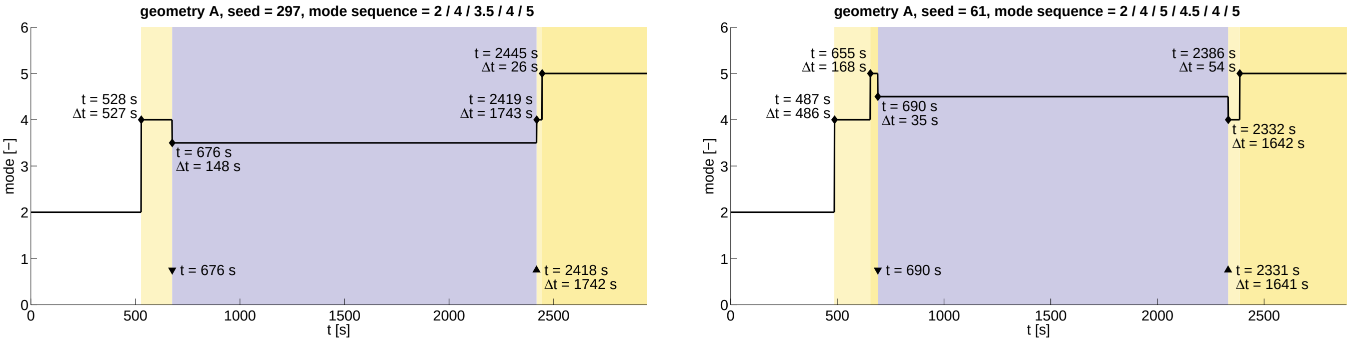

Figure 8.4: *Two examples of a mode switching diagram. Here, an eclipse occurs when the satellite is in control mode 4 (left) or 5 (right).*

8.2 Simulation Parameters

In the simulations in this chapter, the three different configurations from Section 2.4 will be considered. Unless stated differently, all results in this chapter have been obtained with the nominal simulation parameters.

All simulations will be performed for the SunSpace and the MicroWheel1000 reaction wheels separately. The maximum wheel speeds with which the SA and SP slews will be performed, have been discussed in Sections 6.3.5 and 6.4.4.

At the end of the detumble mode, a remaining component of the angular velocity will be present. The highest remaining *true* angular velocities at the end of the detumble mode, which has been found, are $(-0.0991; -0.0939; -0.0846)^{\mathrm{T}}$ deg/s. These results follow from the analysis in Section 7.7. For the simulations in this chapter, it is assumed that the angular velocity has a magnitude of 0.1 deg/s, in each axis. Furthermore, the drift in the gyro bias shall be taken into account. The maximum bias drift, which has been found at the end of the detumble mode, was 0.0046 deg/s. This bias drift will be used as the initial drift in the bias.

The simulations performed in this chapter will be stopped when the satellite is Sun pointing for 500 s. The satellite is considered to be Sun pointing when the measured XY-angle is smaller than 5 degrees.

8.3 Variation of Initial Conditions

In this section the results will be discussed due to the variation of the initial conditions. How these have been varied, is shown in Table 6.5.

The full results are shown in Appendices I.1 and I.2.

Tables I.1 and I.3 show the simulation times for the two different wheel systems. In these tables a detailed overview is given of the time spend in each mode. The time to acquire the Sun after an eclipse exit can also be read from these tables. There are some minor outliers in the simulations; however these do not affect the performance. The outliers have been described in detail in those appendices.

The detailed results for the other performance criteria are listed in Tables I.2 and I.4. Table 8.1 shows the maximum values, which have been obtained for these performance criteria.

Table 8.1: *The results of the simulation campaign where the initial parameters has been varied. The values shown here are the maximum values found in 800 simulations.*

	SunSpace	**MicroWheel1000**	**requirement**
simulation time (including 500 s stable SP)	5029 s	4619 s	< 5880 s
time to acquire Sun after eclipse exit	80 s	76 s	< 600 s
XY-angle measured	1.06 deg	1.08 deg	-
XY-angle true	1.42 deg	1.44 deg	< 5 deg
||SC angular rate||	0.018 deg/s	0.0019 deg/s	< 0.1 deg/s
||wheel speed||	2174 RPM	3628 RPM	-
energy consumption	0.28 Whr	0.48 Whr	-

The spread in the results is shown with Figure 8.5. These results have been obtained with the SunSpace wheel system. The top row shows the resulting simulation times for the different geometries. The second row shows the measured (light) and true (dark) XY-angles. The third and fourth rows show the final spacecraft angular rates and wheel speeds. The X, Y and Z-components are indicated as follows: X in dark blue (background), Y in normal blue (middle) and Z in light blue (front).

The results in this simulation performance run, show that all requirements can be fulfilled with a very comfortable margin. The next step is to perform a full Monte Carlo test run, again for both wheel systems.

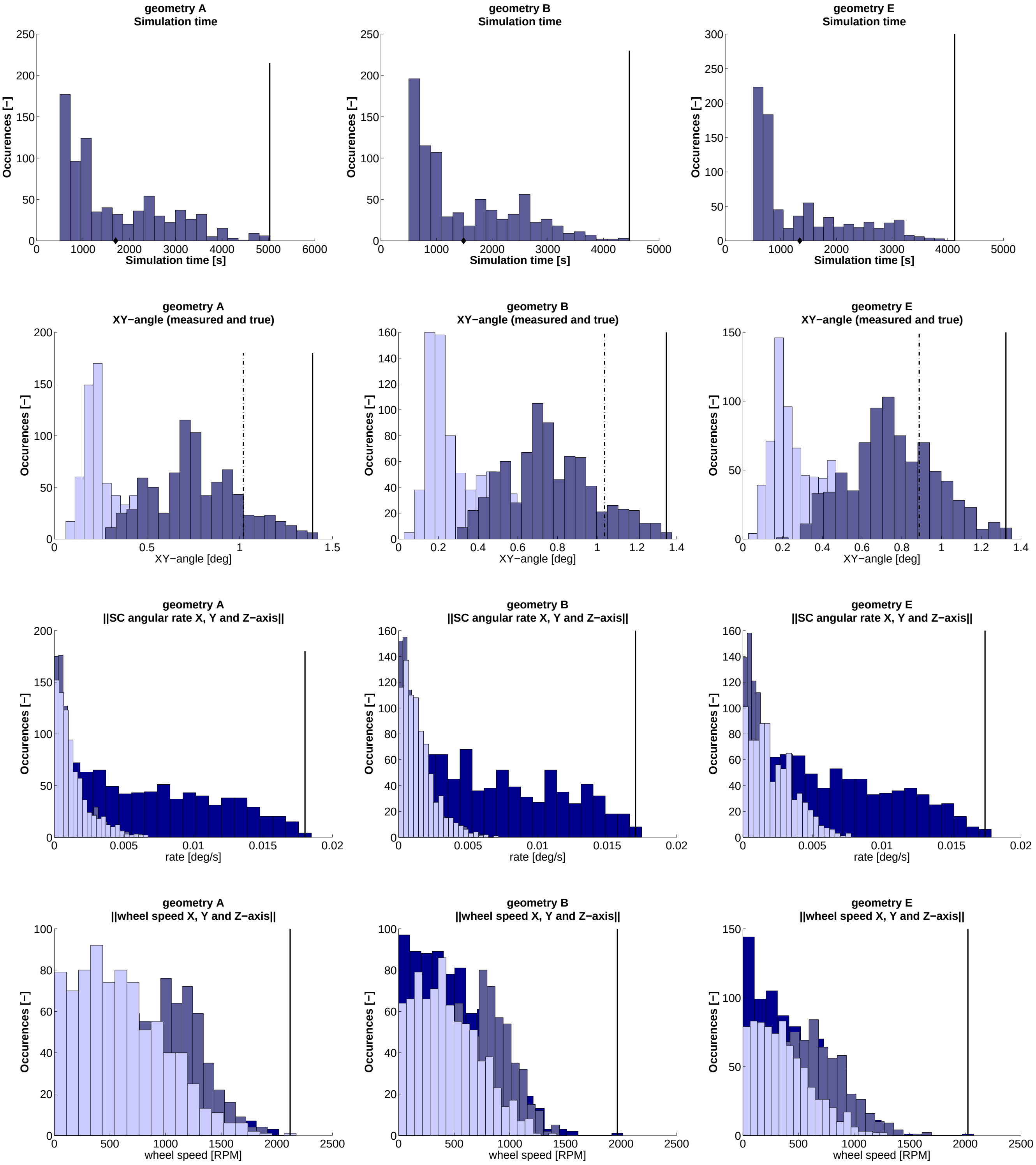

Figure 8.5: *The results for the variation of initial parameters for the SunSpace wheel system.*

8.4 Full Monte Carlo Runs

The results of the full Monte Carlo runs are presented in this section. The simulations in this section have been performed with the initial conditions listed in Table 6.5, where the parameters have been varied between the minimum and maximum values. Furthermore, all sensor and actuator errors are varied from the minimum and maximum errors. The variation in the satellite geometry is also considered, which was discussed in Section 7.3.1.

In Section 8.4.1 the results are presented. Section 8.4.2 discusses the time required to reach a stable Sun pointing state. In Section 8.4.3 the XY-angles after eclipse exit are shown.

8.4.1 Results

The full results are shown in Appendices I.3 and I.4.

The simulation times for the two different wheel systems are shown in Tables I.5 and I.7. Again, these tables provide a detailed overview of the time spend in each mode. Also, the time to acquire the Sun after eclipse exit can be read from these tables. The outliers in the simulation results are discussed those appendices. The outliers do not affect the controller performance.

The detailed results for the other performance criteria are listed in Tables I.6 and I.8. Table 8.2 lists the performance criteria, with the maximum values found in the simulation campaign.

Table 8.2: *The results of the simulation campaign for the full Monte Carlo run. The values shown here are the maximum values found in 800 simulations.*

	SunSpace	**MicroWheel1000**	**requirement**
simulation time (including 500 s stable SP)	5531 s	4581 s	< 5880 s
time to acquire Sun after eclipse exit	113 s	96 s	< 600 s
XY-angle measured	1.14 deg	1.24 deg	-
XY-angle true	1.92 deg	1.90 deg	< 5 deg
||SC angular rate||	0.042 deg/s	0.041 deg/s	< 0.1 deg/s
||wheel speed|| around X-axis	2405 RPM	3222 RPM	-
energy consumption	0.46 Whr	0.56 Whr	-

8.4.2 Time required to reach a stable SP state

The satellite is considered to be Sun pointing when the measured XY-angle is smaller than 5 degrees. At that point the XY-angle can still be further decreased and the angular rates are still relative large. As such, the simulation has been run for another 500 s.

Tables I.6 and I.8 show the variation of performance criteria during the last 500 s. What can be seen is that the parameters are constant after approximately 200 s, from which it can be derived that this is the time required to reach a stable Sun pointing state.

8.4.3 Resulting XY-angles after eclipse exit

In Section 6.4.3 the approach was described when the satellite enters the eclipse, while it has acquired the Sun already (mode 4) or when it is Sun pointing already (mode 5). In this section, the resulting XY-angles after the eclipse exit are shown.

Figure 8.6 and 8.7 show the resulting XY-angles before and after the eclipse, for the different satellite configurations.

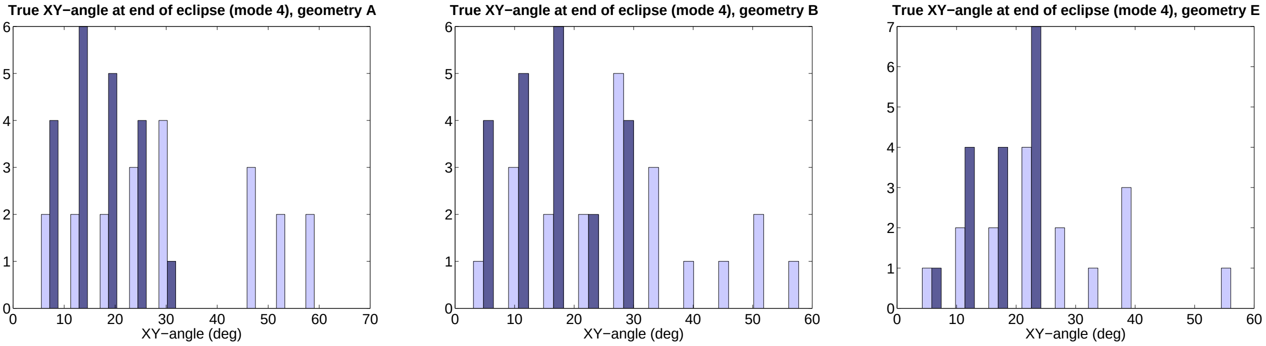

Figure 8.6: *Resulting XY-angles before (light blue) and after (darker blue) the eclipse exit, when the Sun vector has been acquired before the start of the eclipse (mode 4).*

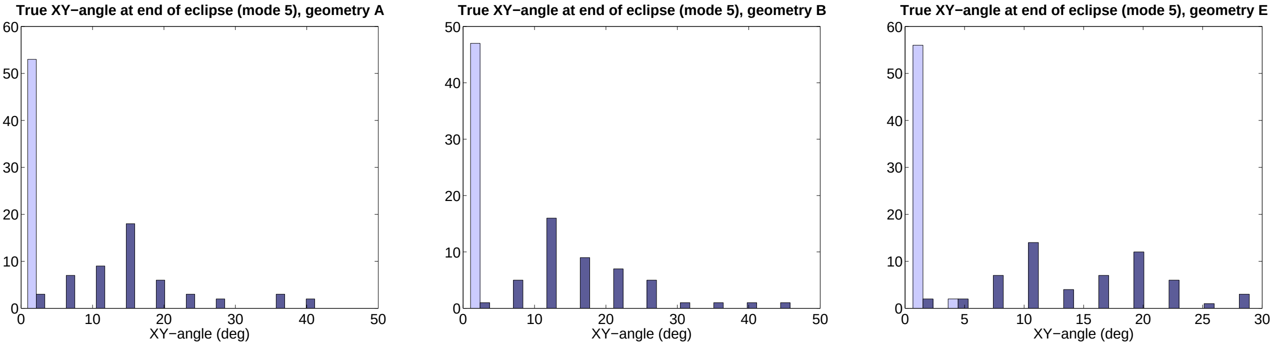

Figure 8.7: *Resulting XY-angles before (light blue) and after (darker blue) the eclipse exit, when the Sun vector has been acquired before the start of the eclipse (mode 5).*

The results are summarized in Table 8.3. It appears when the Sun has been acquired before the start of the eclipse, the XY-angles in most cases improve. However, in the case that the satellite is already Sun pointing before the start of the eclipse, the XY-angles after eclipse exit are considerably larger. These results are similar to the findings in Section 6.4.3.

Table 8.3: *Maximum XY-angles before and after the eclipse.*

	MODE 4		**MODE 5**	
geometry	**start**	**end**	**start**	**end**
A	61.9	32.2	3.8	42.0
B	60.7	29.5	3.5	46.8
E	58.9	24.3	4.9	29.6

The drift in the XY-angle is caused due to the gyro errors. However, this does not yet explain the differences between Figures 8.6 and 8.7. An explanation is given below.

During the eclipse period, the last measured Sun vector is propagated based on the measured angular velocity. The controller tries to minimize the attitude error. For the results shown in Figure 8.6, this attitude error is large. This term is dominant in Equation (6.5.12). Only after a certain time period, the attitude error is reduced towards zero degrees. At this stage, the angular velocity error in (6.5.12) is larger. The drift in the XY-angle starts from this point. For the situation in Figure 8.7, the attitude error is already small at the start. The drift in the XY-angle already starts immediately. As such, the resulting XY-angles are larger at the end of the eclipse period.

Important to note, is that despite the large XY-angles at the end of the eclipse period, the Sun is still in the FoV.

8.5 Conclusions

With the analysis performed in this chapter, it has been shown that all requirements for the SA and SP modes can be met with a comfortable margin. Due to the time constraints, the impact of the different sensor and actuator errors has not been looked into. This is left as future work.

It has been shown that the propagated XY-angles after eclipse exit can be large. Which gyro errors do contribute most to the drift in the XY-angle, is not known. Only suggestions can be made here. More research should be performed in this area.

Finally, the impact of the Earth-albedo error shall be looked at in further studies.

Chapter 9
CONCLUSIONS AND RECOMMENDATIONS

This chapter gives an overview of the conclusions and provides recommendations for future work.

9.1 Conclusions

To state the conclusions, use will be made of the research question, as shown in Section 1.2:

RQ *Which controllers shall be used in combination of the preselected set of sensors and actuators, to meet the SPS-2 requirements for the detumble and SA & SP control, given the different configurations to be considered, limitations and uncertainties, and what is the performance of the overall system?*

The research question was split up into sub-questions SQ1 - SQ4. In this discussion, it will be looked at whether these have been answered. Furthermore, it will be determined if the requirements listed in Section 6.1 are met.

Conclusions for detumble mode

For the detumble mode, a nominal B-dot controller has been selected with a gain of 0.35, which has been used for all configurations. The performance simulation runs, described in Chapter 7, have shown that the controller is sufficiently robust against changes in configurations and uncertainties in the model parameters. Apart from this, the stability margins have been looked at. However, this analysis has shown to be insufficient. Further research is required there.

The results of the performance simulation runs are summarized in Table 9.1, for a torque capability of 15 Am^2. The requirement on the maximum detumble time of 1.5 orbit (8593 s) is complied to. For the 800 simulation cases which have been considered, only in two instances this constraint was violated (8609 s and 8815 s). Furthermore, the measured angular rates have been successfully reduced to 0.05 deg/s for all simulation cases. The highest remaining component of the true angular rate from the dynamics, was 0.0991 deg/s at the end of the detumble mode.[1]

---

[1] Note that the remaining angular rates have been taken into account for the performance analysis for the SA/SP modes. A remaining angular rate of 0.1 deg/s, in each axis, has been assumed there. The maximum bias drift found was 0.0046 deg/s at the end of the detumble mode.

Table 9.1: *The resulting detumble times and energy consumptions from detumble performance test-runs, as discussed in Section 7.7, for a torque capability of 15 Am^2.*

configuration	μ **(s)**	σ **(s)**	$\mu + 3\sigma$ **(s)**	**MIN (s)**	**MAX (s)**	μ **(Whr)**	σ **(Whr)**	$\mu + 3\sigma$ **(Whr)**
A	5492	1068	8695	2362	8815	7.32	1.26	11.11
B	4525	1024	7598	1689	7649	5.67	1.05	8.82
E	4250	1044	7382	1591	8190	5.05	1.00	8.06

The critical design drivers which have been identified, are the choice of the configuration and the torquer strength. It has been found that the minimum torque capability shall be 15 Am^2. A significant decrease in detumble times can be achieved with higher torque capabilities. Furthermore, the minimum performance has been obtained for configuration A. With the simulation performance runs, it has been shown that the variation of the initial conditions has a very large impact on the resulting detumble time. At the end of Chapter 7, it has been shown that the required detumble time mainly depends on the angular rate components in the lateral directions.

The sensor and actuator errors which have the largest impact on the system, are the gyro ARW and the gyro quantization interval (for which a decrease in detumble time was found), followed by the gyro bias repeatability, the gyro nonlinearity and the magnetorquer nonlinearity errors. However, none of the sensor and actuator errors is driving the performance in this stage of the mission. As such, the author suggest to use *low budget* magnetometers and magnetorquers.

It can be concluded that all research questions have successfully been answered, except for the stability analysis of the detumble controller.

Conclusions for SA/SP modes

For the Sun acquisition, a simple PI controller on the velocity has been selected, with a proportional gain of 20 and an integral gain of 3. A quaternion feedback controller was designed for the SP mode, with a derivative gain of 20 and a proportional gain of 1. These gains have been obtained with trial-and-error. The simulations for the different configurations have all been performed with this set of gains.

The stability of both controllers has been looked at in Section 6.5. The minimum gain and phase margins, which have been found, are 2.1 dB and 16.6 deg for the SA controller (minimum inertia term), when the signal delay is 1 s (full signal delay). The resulting gain and phase margins for smaller signal delays, have found to be larger than the generally recommended 3 dB and 30 deg. These margins suggest that the controllers are stable. However, a simplified, linearized system has been looked at, with a continuous time representation. As such, it is only an indication for stability. The limitations of this analysis have been described in full detail in Section 6.5. Further work needs to be done here, but this is beyond the scope of this project.

The results for the performance analysis of the SA/SP modes, are summarized in Table 9.2. These show that the requirements as specified in Section 6.1 are met with a comfortable margin.

Table 9.2: *The results from SA/SP performance test-runs, as discussed in Section 8.4.*

	SunSpace	**MicroWheel1000**	**requirement**
time to get Sun pointing*	5531 s	4581 s	< 5880 s
time to acquire Sun after eclipse exit	113 s	96 s	< 600 s
XY-angle true	1.92 deg	1.90 deg	< 5 deg
||SC angular rate around X-axis||	0.042 deg/s	0.041 deg/s	< 0.1 deg/s
||wheel speed||	2405 RPM	3222 RPM	-
energy consumption	0.46 Whr	0.56 Whr	-

* These results include 500 s of stable Sun pointing.

The maximum wheels speeds which have been found at the end of the simulations, are well within the maximum wheel speeds of 4200 RPM and 10,000 RPM for the SunSpace wheel system and the MicroWheel1000 wheel system. As such, the wheels do not have to be offloaded (yet). When the satellite is Sun pointing for longer periods of time (multiple hours, up to a day), the angular momentum build-up in the wheels will require these to be offloaded. Note that it has *not* been investigated what the frequency of wheel offloading shall be. This is left as future work. The reaction-wheel offloading routine has not been looked at, in agreement with Airbus.

The performance simulation runs have shown that the controllers are sufficiently robust against uncertainties in the model parameters. The minimum performance, again, was found for configuration A. Here, the time required to get Sun pointing was largest, as shown in Table 9.2. Average time durations have found to be 4619 s for the SunSpace wheel system, and 3755 s for the MicroWheel1000 wheel system. Note that these values include 500 s of stable Sun pointing. It became clear, with the chosen limits of the wheel-speeds, that the MicroWheel1000 allows for faster Sun acquisition and Sun pointing. The differences in the results for resulting XY-angles, remaining angular rates or energy consumptions were negligible for the different configurations and wheel systems. The simulations have been performed for threshold wheel speeds, which are a percentage of their maximum wheel speeds. These values might be reconsidered, to allow for faster slews.

Which sensor and actuator errors have the largest impact on the system, has not been shown, due to time constraints. The other research questions have been successfully been answered.

The author suggest the use of the MicroWheel1000 wheel system, as it has a larger angular momentum capacity. Furthermore, all Sun sensors shown in Appendix E will satisfy the mission requirements. However, the author recommends to select a gyro with characteristic errors in the minimum/nominal range, as shown in Table 5.9. This will be beneficial for the pointing accuracy, the propagation of the XY-angle in eclipse periods and the reduction of remaining angular rates at the end of the detumble mode.

General conclusions

Finally, there are some general conclusions, which will be listed here.

- Different measuring/actuation cycles were looked at for the detumble controller. The detumble time can be decreased for smaller measure times (i.e., a higher effective gain).

The detumble time was found to be unaffected, for a doubled measure/actuation period (same effective gain).

- In the Sun-sensor model, the Earth-albedo error has not been modeled. However, it has been estimated which impact the Earth-albedo error might have on the pointing accuracy in the SP mode. In theory, the effect might be as large as 12.6°, but that would be only if the full Earth-albedo contribution is considered. It has been explained why this situation would never occur. The pointing accuracy, however, will be affected during a greater part the orbit. More research shall be performed here, this is left as future work.
- During the thesis work, the design of a MEKF has been looked into. At that time, the bias of the gyro measurements was overestimated. However, the bias was far less worse than anticipated, henceforth there was no further need for the MEKF.

9.2 Recommendations

The following recommendations are made for future work:

- The detumble time can be reduced significantly with larger torque capabilities. However, larger torquers might not fit in the SVM. This shall be investigated.
- The impact of the Earth albedo-error shall be looked into. This can be achieved by the inclusion of an Earth-albedo model. This is future work. The possibility of using Sun sensors, which have an Earth-albedo correction, can also be investigated. However, these might be more expensive.
- The errors with respect to the reference path for the Sun acquisition slews, may be decreased futhre by implementing an additional control action on the path. This shall be investigated further.
- More research should be performed to estimate the time, which is required, for the induced magnetic field of the magnetorquer to dissipate.
- Further research is required to explain why the detumble time decreases significantly in the case of larger gyro ARW errors and larger gyro quantization stepsize errors.
- The author suggest a regression analysis, to further investigate the correlation between the different sensor and actuator error sources.
- Optimizing the gains for each configuration individually, will increase the performance. Not only in terms of performance, but also in terms of stability.
- The stability of the controller shall be investigated further, in a more detailed analysis.

Furthermore, there are some recommendations, specifically for the sensor and actuator model implementation:

- A more precise modeling of the residual dipole moment of the torquer shall be looked into.
- The power output of in the torquer model, has been scaled linearly with torque output. It shall be investigated whether this assumption is valid.
- More research shall be performed in a more accurate modeling of the nonlinearity effect. Manufacturers might specify this.

Appendix A
QUATERNIONS

The conjugate quaternion has an inverted vector component (Landis Markley and Crassidis, 2014):

$$\mathbf{q}^* = \begin{bmatrix} -\vec{\mathbf{q}} \\ q_4 \end{bmatrix} \tag{A.0.1}$$

The inverse of a quaternion is its normalized conjugate:

$$\mathbf{q}^{-1} = \frac{\mathbf{q}^*}{\|\mathbf{q}\|} \tag{A.0.2}$$

Since only unit quaternions are considered, $\mathbf{q}^{-1} = \mathbf{q}^*$.

Vector transformations can be performed using quaternions, and are defined as such:

$$\mathbf{v}_B = \mathbf{q}_{AB} \otimes \begin{bmatrix} \mathbf{v}_A \\ 0 \end{bmatrix} \otimes \mathbf{q}_{AB}^{-1} \tag{A.0.3}$$

Successive transformations through intermediate frames can be accomplished by multiplying successive quaternions as follows:

$$\mathbf{q}_{AC} = \mathbf{q}_{AB} \otimes \mathbf{q}_{BC} \tag{A.0.4}$$

where $\otimes$ denotes the product of two quaternions. This quaternion product is defined by (note the vector and scalar parts):

$$\mathbf{q}_{AB} \otimes \mathbf{q}_{BC} = \begin{bmatrix} q_{AB}\, \vec{\mathbf{q}}_{BC} + q_{BC}\, \vec{\mathbf{q}}_{AB} + \vec{\mathbf{q}}_{AB} \times \vec{\mathbf{q}}_{BC} \\ q_{AB}\, q_{BC} - \vec{\mathbf{q}}_{AB}^T \vec{\mathbf{q}}_{BC} \end{bmatrix} \tag{A.0.5}$$

where q is the scalar part of the quaternion. Note that the order by which the successive transformations are applied using quaternions is from left to right, which is opposite to the direction cosine matrices.

Appendix B
CIRA-72 AND NLRMSISE-00 MODELS

B.1 Comparison MSIS-86 and CIRA-72 models

The atmospheric density model used in ADS is the CIRA-72 (COSPAR International Reference Atmosphere) model. This model is described in (Wertz, 1978) (Table L-6). The MSIS-86 model was described in Section 4.3.4.

Table B.1 lists the nominal atmospheric densities for the MSIS-86 and the CIRA-72 models for the different altitudes. It can be seen that there is a large difference (up to 29.81%) between the densities of both models models.

Table B.1: *The nominal atmospheric densities for different altitudes, based on the MSIS-86 model (used in GGNCSim) and the CIRA-72 model (used in ADS).*

h (km)	$\rho_{\text{MSIS-86}}$ **(kg/m^3)**	$\rho_{\text{CIRA-72}}$ **(kg/m^3)**	$\rho_{\text{MSIS-86}}$ **compared to** $\rho_{\text{CIRA-72}}$ **(%)**
100	4.79×10^{-7}	5.297×10^{-7}	90.43%
150	1.81×10^{-9}	2.070×10^{-9}	87.44%
200	2.53×10^{-10}	2.789×10^{-10}	90.71%
250	6.24×10^{-11}	7.248×10^{-11}	86.09%
300	1.95×10^{-11}	2.418×10^{-11}	80.65%
350	6.98×10^{-12}	9.158×10^{-12}	76.22%
400	2.72×10^{-12}	3.725×10^{-12}	73.02%
450	1.13×10^{-12}	1.585×10^{-12}	71.29%
500	4.89×10^{-13}	6.967×10^{-13}	70.19%
600	1.04×10^{-13}	1.454×10^{-13}	71.53%
700	2.72×10^{-14}	3.614×10^{-14}	72.50%
800	9.63×10^{-15}	1.170×10^{-14}	82.31%
900	4.66×10^{-15}	5.245×10^{-15}	88.85%
1000	2.79×10^{-15}	3.019×10^{-15}	92.41%

B.2 Overview of the NRLMSISE-00 model

The NRLMSISE-00 model will be discussed here. The NRLMSISE-00 model is incorporated in the Aerospace toolbox of Matlab, with the function `atmosNRLMSISE00.m`. Characteristics of the NRLMSISE-00 model are (Picone, 2001):

- The atmospheric density is dependent on the date and time selected.
- In this model the satellite position (longitude, latitude) is also considered.
- As an additional option, the user can choose to include the effects of the daily F10.7 flux of the previous day, the average of the F10.7 flux of the 81 days around the selected date and the magnetic index information. For larger altitudes (above 80 km), this

increases the accuracy of the estimated atmospheric density. These specific tables can be found at:

- `ftp://ftp.ngdc.noaa.gov/STP/space-weather/solar-data/solar-features/solar-radio/noontime-flux/penticton/penticton_observed/listings/`
- `ftp://ftp.ngdc.noaa.gov/STP/GEOMAGNETIC_DATA/INDICES/KP_AP/`.

Note that these effects can not be modeled for dates ahead, as these tables are only available for dates in the past.

- The effect of anomalous oxygen on the atmospheric density profile can be included.

How these individual effects affect the resulting density, has been investigated in detail for two specific dates. The dates were chosen such that one was around a solar flux minimum (16/07/2008) and the other around a solar flux maximum (02/05/2014), see also Figure 4.3.

B.2.1 Impact daily change

The daily variation of the atmospheric density is looked at here. The resulting atmospheric density profiles at 00:00 hr and 15:00 hr are shown in Figure B.1 for the two selected dates (± 40 days). In this analysis, the longitude and latitude have been set to 0 degrees. The atmospheric density was found to be highest around 15:00 hr and smallest around (00:00 hr).

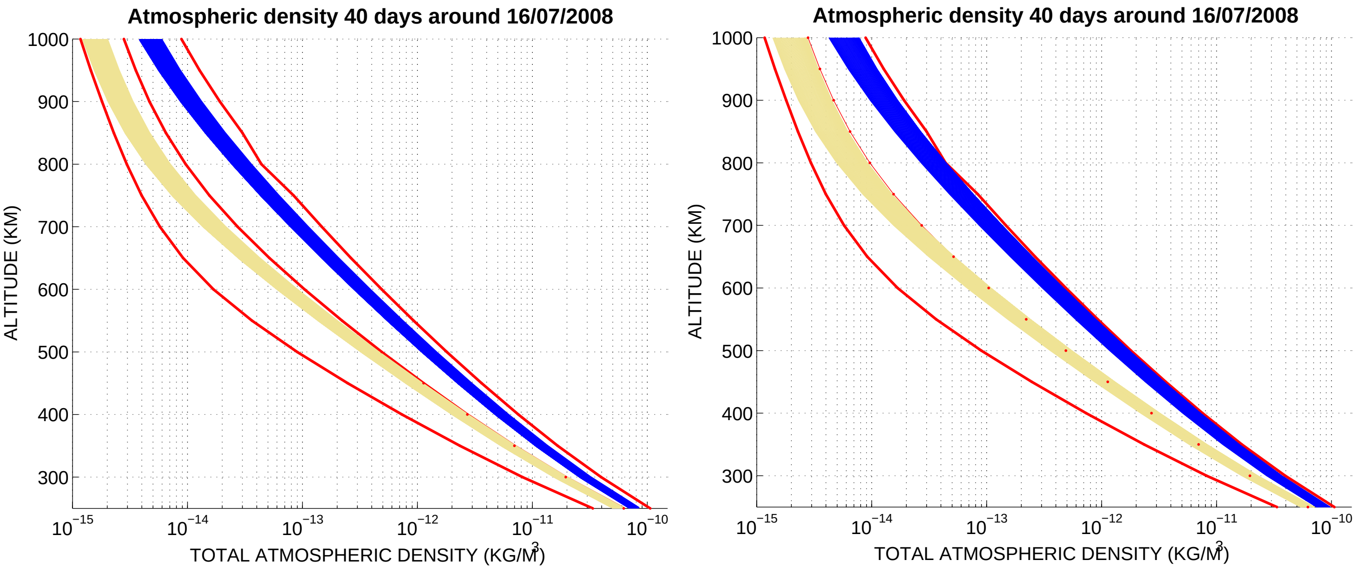

Figure B.1: *The daily variation of the atmospheric density using the NRLMSISE-00 model. The results are shown in yellow (00:00 hr) and blue (15:00 hr). The atmospheric density profiles have been obtained for 40 days around 16/07/2008 (solar minimum) and 02/05/2014 (solar maximum). The red lines are the minimum, nominal and maximum values from the MSIS-86 model.*

B.2.2 Impact F10.7 flux and the magnetic index information

How the F10.7 flux and the magnetic index information affect the atmospheric density is looked at here. Figure B.2 (left figure) shows the ratio between the densities calculated with and without these effects for ±40 days around the solar minimum and the solar maximum. What can be seen is that the ratios between the calculated densities are in general smaller than 1, what means that the the atmospheric densities are estimated lower when including the effects of F10.7 and the magnetic indexes information. The difference is larger at higher altitudes. The ratio between the densities is highest at the solar minimum.

B.2.3 Impact contribution of anomalous oxygen

The effect of including the contribution of anomalous oxygen is looked at here. The results are shown in Figure B.2 (right figure). At lower altitudes there is no contribution of anomalous oxygen to the atmospheric density profile. The effect at high altitudes is still relatively small.

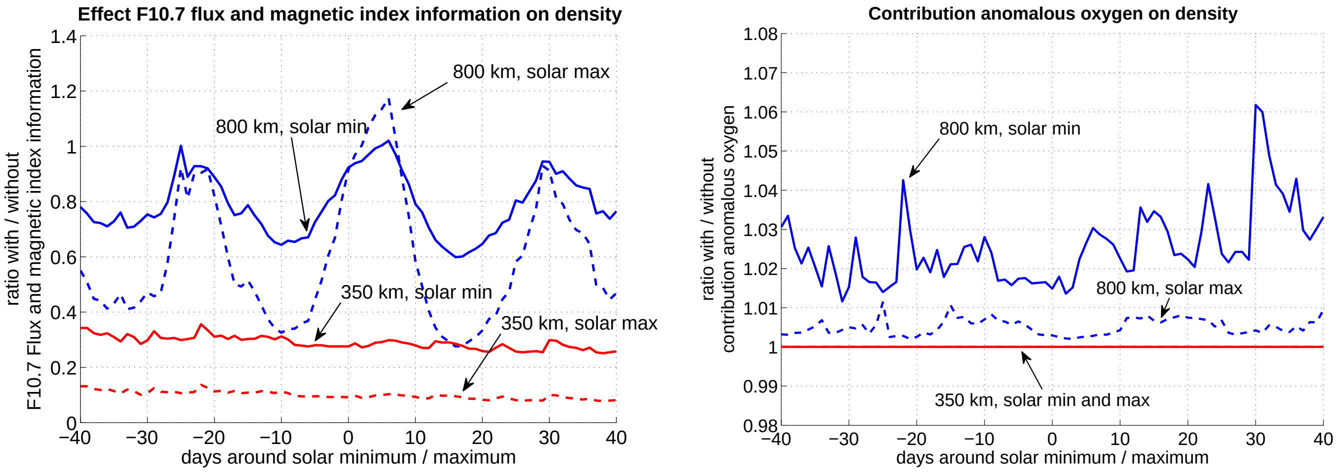

Figure B.2: *Effect of including the F10.7 flux and the magnetic index information (left figure) and the contribution of anomalous oxygen (right figure) on the density, using the NRLMSISE-00 model.*

Appendix C
CYLINDRICAL SHAPE INVESTIGATION

The satellite geometry and satellite parameters are shown separately in this appendix. At the start of the project, a different axis orientation has been used (YZX). As this might be confusing, this figure and table have been excluded from the main report. Note that this axis orientation is only used for the analysis in Section 4.5.2.

The reference satellite geometry is shown in Figure C.1. The dimensions of the cylindrical ring are 468.5×400 mm (radius×height). The dimensions of the box are 500 × 300 × 500 mm (length×width×height).

The satellite parameters for the cylindrical shape approximation are shown in Table C.1. The values have been obtained from the preliminary work by (Munatsi, 2016b).

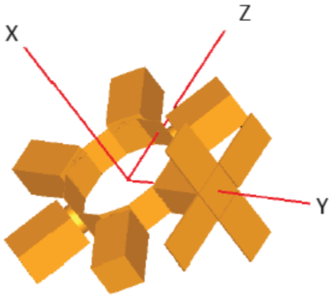

Figure C.1: *The SPS-2 geometry used to analyze the maximum disturbance loads.*

Table C.1: *The satellite parameters used in Chapter 4.5.*

	unit	**cylinder A**	**cylinder B**	**cylinder C**
cylinder radius	m	0.9685	0.7185	0.55
cylinder height	m		0.4*	
mass	kg		232.54	
CoM (YZX)	m		$\begin{bmatrix} -0.06366 & +0.01409 & -0.02495 \end{bmatrix}$	
MoI (YZX)	kg m^2		$\begin{bmatrix} 91.3 & -8.909 & 2.928 \\ -8.909 & 46.81 & -5.186 \\ 2.928 & -5.186 & 57.31 \end{bmatrix}$	
C_D (3-axis)	-		2	
$C_{specular}$ (3-axis)	-		0.25	
$C_{diffuse}$ (3-axis)	-		0	
$C_{absorption}$ (3-axis)	-		0.75	
residual dipole moment (3-axis)	Am^2		0.2	

* At this stage, it was not yet known that the cylinder height would be 0.5 m. The results in (Munatsi, 2016a) show that the effect on the angular momentum build-up is negligible.

Appendix D
MAGNETORQUER THEORY

This chapter provides some background information, which was referred to in Section 5.1.2. How the magnetic dipole moment of the torquer can be calculated is shown in Section D.1. The derivation of the induced magnetic field is shown in Section D.2. The hysteresis cycle is discussed in Section D.3.

D.1 Magnetic dipole moment

The magnetic dipole moment of a magnetorquer is expressed with (Bellini, 2014):

$$\mathbf{m} = \left(nIA + V_{\text{core}}M_{\text{core}}\right)\hat{\mathbf{c}} \tag{D.1.1}$$

The first term in the equation describes the dipole contribution of the solenoid. Here n is the number of windings, I is the applied current in A and A is the cross-sectional area in m^2. The second term describes the dipole contribution due to the core's magnetization. The volume of the core is described with V_{core} in m^3 and the magnetization of the core is denoted with M_{core} in A/m. Finally, $\hat{\mathbf{c}}$ is the unit vector which describes the orientation of the magnetorquer.

When a cylindrical shaped torque rod is considered, the magnetic dipole moment is as follows (assuming that the wire is is negligible thin compared to the core):

$$\mathbf{m} = nIA\left(1 + \frac{(\mu_r - 1)}{(1 - N_d + \mu_r N_d)}\right)\hat{\mathbf{c}} \tag{D.1.2}$$

where μ_r is the relative permeability of the material (in most cases a permalloy, which is a nickel-iron magnetic alloy). Here N_d is expressed as follows:

$$N_d = \frac{4\ \ln\left(\frac{l_{\text{core}}}{r_{\text{core}}} - 1\right)}{\left(\frac{l_{\text{core}}}{r_{\text{core}}}\right)^2 - 4\ \ln\left(\frac{l_{\text{core}}}{r_{\text{core}}}\right)} \tag{D.1.3}$$

The magnitude of the magnetic dipole moment which can be obtained thus depends on the length l_{core} and the radius r_{core} of the core and its permeability.

D.2 Induced magnetic field

The induced magnetic field by the magnetorquer can be calculated with (Jensen and Vinther, 2010):

$$B = nI\mu_0 \frac{l_{\text{core}}^2}{2\pi\left(l_{\text{distance}}^2 + l_{\text{core}}^2/4\right)\sqrt{l_{\text{distance}}^2 + l_{\text{core}}^2/2}} \tag{D.2.1}$$

Where l_{distance} is the distance from the magnetorquer. The number of windings is usually not specified, but can be calculated with Equation (D.1.2).

The resulting induced magnetic field for the Surrey MTR-30 magnetorquer are shown in Table 5.1. The relevant parameter values are listed in Table D.1.

Table D.1: *Simulation parameters to estimate the maximum induced magnetic field for the MTR-30 magnetorquer.*

Quantity	Value	Unit	Comments
m	30	Am^2	magnetic dipole moment
n	2984	-	estimated number of windings
I	200	mA	maximum current
l_{core}	378	mm	length core
d_{core}	74	mm	diameter core
A	4300.8	mm^2	enclosed area
μ_0	$4\pi10^{-7}$	N/A^2	permeability of free space*
μ_R	8000	-	relative permeability permalloy*

* `https://en.wikipedia.org/wiki/Permeability_(electromagnetism)`, accessed 4 August '15.

D.3 Hysteresis cycle

Before the hysteresis cycle is explained, the concept of permeability will be introduced. Permeability is the degree of magnetization that a material obtains in response to an applied magnetic field, indicated with magnetic flux (Bellini, 2014). Ferromagnetic materials have a high permeability, which means that for low magnetic field strengths a large magnetic flux is generated. An important characteristic of ferromagnetic materials is that these saturate at certain magnetic field strengths, limiting the magnetic flux.

When in the presence of a ferromagnetic material an external field is applied, the level of magnetization increases. This is shown with the blue line in Figure D.1. Note that the flux density does not increase linearly with the applied external field. At a certain applied external magnetic field, saturation occurs and the flux density will not increase any further. But, when a reverse magnetic field is applied (or the field is removed), the material will not be demagnetized to its original state. The remanence is a measure of the remaining magnetization when the driving field is dropped to zero, and the coercivity is a measure of the reverse field needed to drive the magnetization to zero after being saturated. This effect is largest for hard ferromagnetic material, and smallest for soft ferromagnetic materials. This cycle is referred to as the hysteresis cycle.

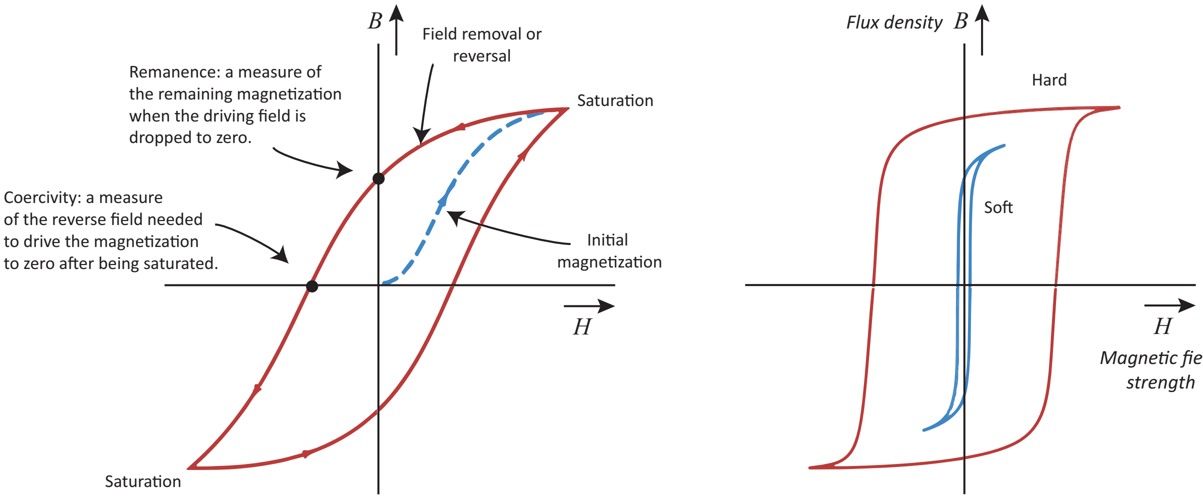

Figure D.1: *A typical hysteresis cycle and the difference between soft and hard ferromagnetic matericals (Bellini, 2014).*

In general ferromagnetic materials are divided in "soft ferromagnetic" and "hard ferromagnetic" materials. A soft ferromagnetic material will experience a thin hysteresis cycle, which means a low energy loss (see Figure D.1). Saturation occurs for low magnetic field strengths. Soft ferromagnetic materials allow for easy magnetization and demagnetization, which results in a low power consumption. An example of a soft ferromagnetic material is a permalloy, which is a commonly used material for torque rods.

Appendix E
SPECIFICATION SHEETS

A summary of the specification sheets of the manufacturers for the magnetometers, the magnetorquers and the four-quadrant Sun sensors are listed in Tables E.1, E.2 and E.3. The specification sheets are listed in (Oomen, 2016).

Table E.1: *Characteristics of magnetometers, which are currently available on the market.*[1]

#	Company	Name	Type	Range (μT)	Accuracy (%FS)
1.	Honeywell *	HMR2300	Magneto-resistive	100	0.52
2.	SpaceQuest *	MAG-3	Fluxgate	100	0.75
3.	Bartington	Spacemag	Fluxgate	100	0.5
4.	Bartington	Spacemag-Lite	Fluxgate	60	0.5
5.	Bartington	MAG-03	Fluxgate	100	0.5
6	MEDA *	TAM-2	Fluxgate	100	1
7.	ZARM Technik	FGM-A-75	Fluxgate	75	0.5
8.	ZARM Technik	AMR-422-LV	Magneto-resistive	100	1

#	Sensitivity (μV/nT)	Scale Factor error (ppm/°C)	Zero Field bias (nT)	Zero Field drift (nT/°C)	Linearity error (nT)
1.	-	600	30	-	500
2.	100	150	250	0.6	150
3.	100	100	100	1	3.3
4.	50	100	100	-	-
5.	100	20	5	0.1	1.5
6	100	-	150	-	50
7.	66.67	PM	900	PM	75
8.	**	100	350	5	100

#	Noise (1σ RMS/$\sqrt{\text{Hz}}$ at 1 Hz)	Alignment error (°)	Mass (g)	Dimensions (mm^3)	Price
1.	-	-	98	38×83×22	\$907
2.	20 pT	-	100	35×32×83	\$12500
3	10-20 pT	1	175	40×40×31	\$8415
4.	10-150 pT	0.5	50	20×20×20	-
5.	10-20 pT	0.5	95	25×25×(105-211)	-
6	10 nT	0.25	500	45×143×76	\$125000
7.	***	1	300	100×82×34	PM
8.	PM	1	60	56×36×17	PM

PM indicates that this information was obtained by personal communication and should not be shared. * ITAR regulations (in the USA) prevents the company from providing any technical data including (especially) performance parameters, unless a license has been given. ** the sensitivity of the AMR-422-LV magnetometer is 10 nT/bit. *** the noise value of the FGM-A-75 magnetometer is 5 nT at a frequency of 2 Hz.

---

[1] The blue cell indicates that this information was obtained by request.

Table E.2: *Characteristics of magnetorquers, which are currently available.*[2]

#	Company	Name	Linear Dipole Range (Am^2)	Linearity Error	Residual Dipole Moment (Am^2)	Voltage (V)	Power (mW)	Dimensions (mm^2 or mm^3)	Mass (g)	Price
1.	ZARM Technik	MT10-2-H to MT30-2	10 - 30	-	-	-	1000 - 1500	(330 - 404.5)×(17 - 29)	350-1400	-
2.	ZARM Technik	MT0.1-1 to MT1-1	0.1 - 1	$< 2\%$	$\leqslant 0.5\%$	5	230 - 315	(55 - 132)×(3.5 - 13.5)	3-60	-
3.	Andrews-Space	TQ-15 (single wind)	15	-	-	28	2800	228×(TBD)	400	11 k$
4.	Andrews-Space	TQ-30 (dual wind)	30	-	-	28	2800	237×(TBD)	727	12 k$
5.	Andrews-Space	TQ-42 (single wind)	42	-	-	28	2800	338×(TBD)	825	14 k$
6.	Surrey	MTR-5	5	5%	< 0.1	5	500	252×66	500	126.8 k$
7.	Surrey	MTR-30	30	5%	< 0.1	5	1000	378×74	1800	125.1 k$
8.	SSBV	-	1 - 100	$< 5\%$	< 0.1	5	1000	(80 - 600)×(6 - 12)	55 g/cm	-

Table E.3: *Characteristics of four-quadrant Sun sensors, which are currently available.*[3]

#	Company	Name	Field of view ($^\circ$)	Accuracy whole FoV ($^\circ$) (3σ)	Accuracy boresight ($^\circ$) (3σ)	Mass (g)	Size (mm^3)	Power (mA)	Price (A)	Price (D)
1.	SSBV	Cubesat Sun Sensor	114	< 0.5	-	<5	33×11×6	<10	$3300	-
2.	SolarMEMS	nanoSSOC-A/D60	120	< 0.5	< 0.1	6.5	43×14×5.9	<23	€2200	€3600
3.	SolarMEMS	SSoC-D60	120	< 0.3	< 0.05	35	60×30×12	120	€4890	€7890
4.	MOOG Bradford	Fine Sun Sensor	128	< 0.3	-	365	108×108×52.5	12	-	-

---

[2] Not all data was provided by the manufacturers. Direct contact with Andrew-Space did not yield further information.

[3] The blue cell indicates that this information was obtained by request.

Appendix F
REVIEW OF THE RRW

In this chapter the RRW of the gyro model will be discussed. The gyro model is described in (Munatsi, 2016a). The author has discovered large discrepancies in the RRW implementation in the different model versions. These discrepancies caused a large delay in the project.

The implementation of the RRW is as follows. The RRW is implemented as a noise, which is integrated with time. This results in a bias drift. The variance of the noise is defined as:

$$\sigma = \left(RRW \sqrt{\frac{1}{T_s}} \right)^2 \tag{F.0.1}$$

where T_s is the sampling time (s), which is the inverse of the gyro sampling frequency F_s (Hz). The RRW is specified in the units deg/$\sqrt{\mathrm{s}^3}$.

The RRW values for the different model versions are listed in Table F.1. The RRW values have been obtained from the Alan-Variance plots, which have been constructed for the QRS-116 rate sensor. This is described in (Munatsi, 2016a).

Table F.1: *RRW values specified in the different model versions.*

Model version	**Date**	**RRW (deg/$\sqrt{\mathrm{s}^3}$)**	**$\mathrm{T_s}$ (s)**	**$\mathrm{F_s}$ (Hz)**
original version (verified)	August 8th	0.0002	1/100	100
updated version	September 23th	0.0002	1/100	1
correction of the model	end of November	$0.0002\cdot\frac{1}{60}$	1	1
final model parameters	December 4th	$0.0005\cdot\frac{1}{60}$	1	1

The originally verified model originates from early August, but it was only at the end of September that the gyro model was needed in this work. The author received the latest model version by then. The author assumed that the model was correct, as a great deal of effort was put into this model. Note that at that time, the model was already verified more than a month ago.

During the initial simulations of the detumble controller it became apparent that the bias drift was large. After 1 orbit, the bias drift was around 1 deg/s. As the bias drift was so large, the nominal controller in the detumble mode could not be used. Therefore, the angular rates could not be decreased further than 0.15 deg/s. These results have been discussed at the meetings at Airbus, in the presence of our supervisors and Prosper. None of them was surprised by this large drift in the gyro bias, despite the fact that they all have looked into the models (including the model parameters) specifically.

The large bias drift would most certainly also cause problems during the SA and SP slews. As such, it has been decided to look into the design of a MEKF (Multiplicative Extended Kalman Filter) to estimate the bias drift, by which the gyro measurements could be corrected. As the author had no experience with Kalman filters, a great deal of effort has been spent in understanding how these filters work and in the implementation of the actual filter. Simultaneously, Prosper worked on the design of a MEKF for the science mode, but using different sensor measurements.

With the MEKF filter, the Sun sensor measurements would be used to estimate the bias drift. There was scepticism about this approach, as the Sun sensor measures only two components of the attitude. An alternative, would be to make use of the magnetic field measurements. This option was discarded by Airbus because it requires the knowledge of the position in the orbit and it required the implementation of a magnetic field model in the onboard computer of the actual spacecraft. A star tracker could not be used, as there was a possibility that the star tracker may face the Sun or Earth.

The MEKF implementation in Simulink was performed as such. It was decided to use the MEKF model developed by Prosper, but in a modified form. When the modified MEKF had been implemented, several simulations were performed to test the performance. However, it soon turned out that the bias drift of the gyro was completely different than in the previous model versions. Meanwhile in the process, Prosper had updated the model again, not realizing the impact on the bias drift. After one orbit, the bias drift was only 0.001 deg/s.

After a careful analysis, it turned out that there were two discrepancies between the original and updated model versions:

- The sampling frequency in Equation (F.0.1) was originally hard-coded.
- The unit conversion for the RRW was wrong. In the update of the model a conversion factor $\frac{1}{60}$ is present.

When it was discovered that the actual bias drift was much smaller, an internal discussion has been taken place at Airbus. It has been decided to not to consider the MEKF any further. The filter did not work yet, and there was no necessity of the use of this filter any longer. Furthermore, there was still a large doubt about the ability of the filter to estimate the bias drift using the Sun sensor measurements. By then, the work was delayed with approximately two months.

Appendix G
COVERED VIEW FOR SUN ACQUISITION SLEWS

In Chapter 6.3 the SA controller was discussed. In this section, it became apparent that there is a difference in the covered angular distance w.r.t. the reference profile, which could not be compensated for entirely. Here it will be shown that a double hemispherical view is obtained after two successive slews.

Simulation parameters

The analysis in this chapter will be performed for the results shown in Figure 6.1. In this instance, four slews were required before the Sun was acquired. The minimum FoV of 50° is used, as this yields the worst-case scenario.

Covered view after two successive slews

Figure G.1 shows the covered view for the first and seconds slews. In this figure, it is shown how the pointing direction of the boresight axis of the Sun sensor moves in the inertial frame. During the slew maneuver, this axis rotates, sweeping a covered area. This is explained in more detail in Figure G.2. To obtain a double hemispherical view, the area which has been covered after the two slews, shall overlap.

It can be clearly seen that the followed path still deviates from the reference path. However, after two successive slews, there are no regions left which have not been covered. A double hemispherical view thus has been obtained. There is even a comfortable margin for larger deviations in the slew profile. The same holds true for the third and fourth slews. As such, these have not been shown here.

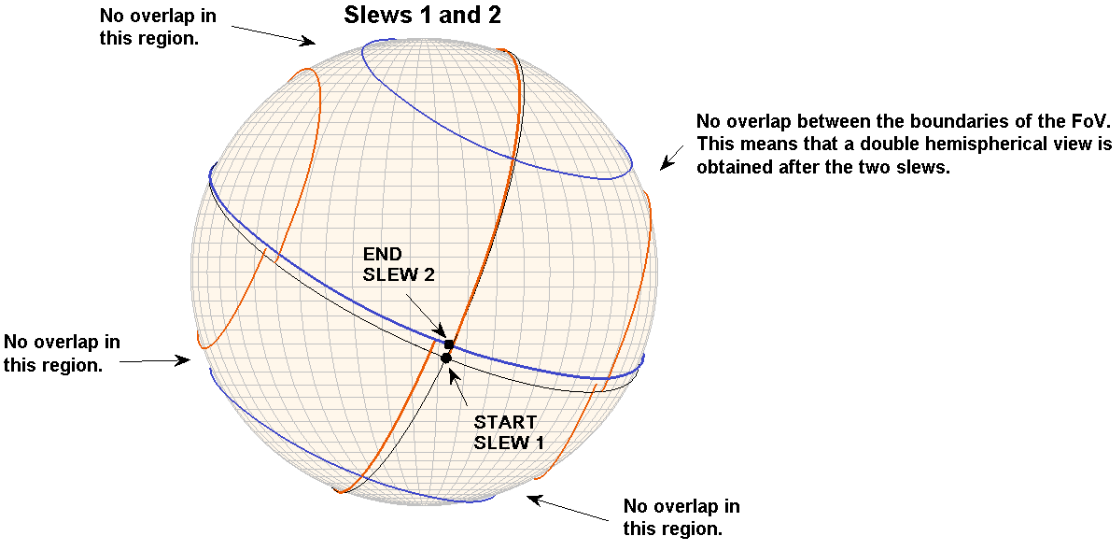

Figure G.1: *After two successive slews, a double hemispherical view has been obtained. See Figure G.2 how to interpret this figure.*

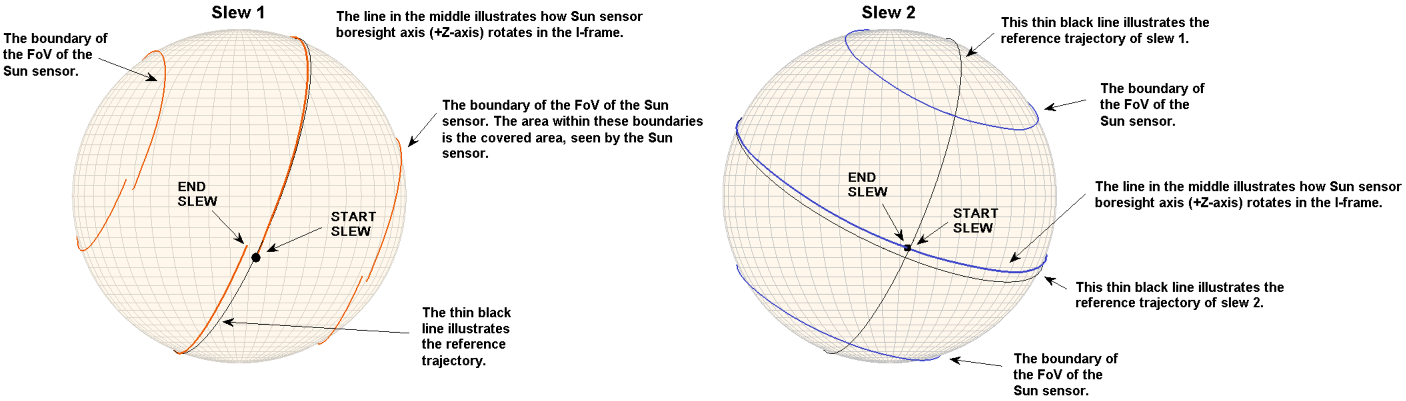

Figure G.2: *Explanation of Figure G.1.*

Appendix H
RESULTS PARAMETER VARIATION DETUMBLE

The results of the one-at-the-time parameter variation described in Section 7.5 are listed in Table H.1. The results of the detailed analysis are listed in Table H.2. The results for the maximum orbits are listed in Table H.3. The results for the grouped error variation are shown in Tables H.4 and H.5.

H.1 Results one-at-the-time variation

Table H.1 lists down the results of the one-at-the-time variation. How to read this table:

- t_{ref} is the detumble time of the reference orbit.
- $\Delta\mu$ is the difference in detumble time with respect to the reference orbit, where $\Delta\mu = \mu - t_{ref}$ and μ is the mean detumble time.
- The standard deviation is indicated with σ.
- *MIN*, *NOM* and *MAX* denote the minimum, nominal and maximum errors.

Table H.1: *The results of the one-at-the-time parameter variation in the detumble mode. All 17 parameters have been considered here.*

MTM.zero_field_bias				$\Delta\mu$ (s)		$\Delta\mu$ (%)					
runs	**case**	**$\mathbf{t_{ref}}$ (s)**	**orbit**	**MIN**	**MAX**	**MIN**	**MAX**				
1	A	4228	avg	-1	-21	-0%	-0%				
1	A	6724	max	-149	-22	-2%	-0%				
1	B	3495	avg	2	12	+0%	+0%				
1	B	7108	max	-5	15	-0%	+0%				
1	E	3210	avg	-2	14	-0%	+0%				
1	E	7093	max	1	-14	+0%	-0%				
MTM.SF_error				$\Delta\mu$ (s)		$\Delta\mu$ (%)					
runs	**case**	**$\mathbf{t_{ref}}$ (s)**	**orbit**	**MIN**	**MAX**	**MIN**	**MAX**				
1	A	4228	avg	-1	-1	-0%	-0%				
1	A	4228	avg	-1	-1	-0%	-0%				
1	A	6724	max	0	-155	0%	-2%				
1	B	3495	avg	2	-1	+0%	-0%				
1	B	7108	max	0	-152	0%	-2%				
1	E	3210	avg	-4	-5	-0%	-0%				
1	E	7093	max	-23	10	-0%	+0%				
MTM.nonlinearity				$\Delta\mu$ (s)		$\Delta\mu$ (%)		σ (s)		σ (%)	
runs	**case**	**$\mathbf{t_{ref}}$ (s)**	**orbit**	**MIN**	**MAX**	**MIN**	**MAX**	**MIN**	**MAX**	**MIN**	**MAX**
15	A	4228	avg	15	17	+0%	+0%	48	76	1%	2%
15	A	6724	max	0	-38	+0%	-1%	1	58	0%	1%
15	B	3495	avg	1	2	+0%	+0%	1	4	0%	0%
15	B	7108	max	5	-23	+0%	-0%	22	76	0%	1%
15	E	3210	avg	-4	0	-0%	+0%	2	8	0%	0%
15	E	7093	max	0	-14	+0%	-0%	6	33	0%	0%

MTM.noise				$\Delta\mu$ (s)		$\Delta\mu$ (%)		σ (s)		σ (%)	
runs	**case**	**t$_{ref}$ (s)**	**orbit**	**MIN**	**MAX**	**MIN**	**MAX**	**MIN**	**MAX**	**MIN**	**MAX**
15	A	4228	avg	0	0	0%	0%	0	0	0%	0%
15	A	6724	max	0	-10	0%	-0%	0	38	0%	1%
15	B	3495	avg	0	0	0%	-0%	0	0	0%	0%
15	B	7108	max	0	0	0%	+0%	0	3	0%	0%
15	E	3210	avg	-2	-2	-0%	-0%	0	1	0%	0%
15	E	7093	max	-12	-8	-0%	-0%	4	4	0%	0%

MTM.temperature				$\Delta\mu$ (s)		$\Delta\mu$ (%)	
runs	**case**	**t$_{ref}$ (s)**	**orbit**	**MIN**	**MAX**	**MIN**	**MAX**
1	A	4228	avg	-22	-1	-1%	-0%
1	A	6724	max	-9	-17	-0%	-0%
1	B	3495	avg	-1	2	-0%	+0%
1	B	7108	max	83	0	+1%	0%
1	E	3210	avg	-3	-3	-0%	-0%
1	E	7093	max	0	-8	0%	-0%

MTM.misalignment				$\Delta\mu$ (s)		$\Delta\mu$ (%)	
runs	**case**	**t$_{ref}$ (s)**	**orbit**	**MIN**	**MAX**	**MIN**	**MAX**
1	A	4228	avg	230	0	+5%	0%
1	A	6724	max	-17	-9	-0%	-0%
1	B	3495	avg	0	0	0%	0%
1	B	7108	max	3	-23	+0%	-0%
1	E	3210	avg	-3	14	-0%	+0%
1	E	7093	max	-8	10	-0%	+0%

MTM.qbits				$\Delta\mu$ (s)		$\Delta\mu$ (%)	
runs	**case**	**t$_{ref}$ (s)**	**orbit**	**MIN**	**MAX**	**MIN**	**MAX**
1	A	4228	avg	-1	-1	-0%	-0%
1	A	6724	max	0	-29	0%	-0%
1	B	3495	avg	11	2	+0%	+0%
1	B	7108	max	-5	-1	-0%	-0%
1	E	3210	avg	-2	-3	-0%	-0%
1	E	7093	max	-8	-13	-0%	-0%

GYR.bias_repeat.				$\Delta\mu$ (s)		$\Delta\mu$ (%)	
runs	**case**	**t$_{ref}$ (s)**	**orbit**	**MIN**	**MAX**	**MIN**	**MAX**
1	A	4228	avg	-50	-235	-1%	-6%
1	A	6724	max	0	-276	0%	-4%
1	B	3495	avg	-1	14	-0%	+0%
1	B	7108	max	-1742	-104	-25%	-1%
1	E	3210	avg	13	156	+0%	+5%
1	E	7093	max	-35	-2468	-0%	-35%

GYR.SF_error				$\Delta\mu$ (s)		$\Delta\mu$ (%)	
runs	**case**	**t$_{ref}$ (s)**	**orbit**	**MIN**	**MAX**	**MIN**	**MAX**
1	A	4228	avg	0	-22	0%	-1%
1	A	6724	max	0	-6	0%	-0%
1	B	3495	avg	-1	12	-0%	+0%
1	B	7108	max	0	10	0%	+0%
1	E	3210	avg	-4	-4	-0%	-0%
1	E	7093	max	-3	-8	-0%	-0%

GYR.nonlinearity				$\Delta\mu$ (s)		$\Delta\mu$ (%)		σ (s)		σ (%)	
runs	**case**	**t$_{ref}$ (s)**	**orbit**	**MIN**	**MAX**	**MIN**	**MAX**	**MIN**	**MAX**	**MIN**	**MAX**
15	A	4228	avg	-2	161	-0%	+4%	65	175	2%	4%
15	A	6724	max	-176	-196	-3%	-3%	8	418	0%	6%
15	B	3495	avg	27	16	+1%	+0%	3	36	0%	1%
15	B	7108	max	33	-825	+0%	-12%	12	960	0%	14%
15	E	3210	avg	-42	-110	-1%	-3%	150	187	5%	6%
15	E	7093	max	-204	-1912	-3%	-27%	7	1138	0%	16%

GYR.ARW				$\Delta\mu$ (s)		$\Delta\mu$ (%)		σ (s)		σ (%)	
runs	**case**	**t_{ref} (s)**	**orbit**	**MIN**	**MAX**	**MIN**	**MAX**	**MIN**	**MAX**	**MIN**	**MAX**
15	A	4228	avg	95	-114	+2%	-3%	116	45	3%	1%
15	A	6724	max	-2	-442	-0%	-7%	4	69	0%	1%
15	B	3495	avg	6	-70	+0%	-2%	4	21	0%	1%
15	B	7108	max	17	-2165	+0%	-30%	29	126	0%	2%
15	E	3210	avg	0	-273	0%	-8%	5	127	0%	4%
15	E	7093	max	0	-2540	-0%	-36%	8	54	0%	1%
GYR.RRW				$\Delta\mu$ (s)		$\Delta\mu$ (%)		σ (s)		σ (%)	
runs	**case**	**t_{ref} (s)**	**orbit**	**MIN**	**MAX**	**MIN**	**MAX**	**MIN**	**MAX**	**MIN**	**MAX**
15	A	4228	avg	115	157	+3%	+4%	176	179	4%	4%
15	A	6724	max	-150	-90	-2%	-1%	34	86	1%	1%
15	B	3495	avg	0	2	+0%	+0%	1	6	0%	0%
15	B	7108	max	53	-309	+1%	-4%	58	719	1%	10%
15	E	3210	avg	-3	4	-0%	+0%	4	8	0%	0%
15	E	7093	max	-24	-36	-0%	-1%	8	43	0%	1%
GYR.misalignment				$\Delta\mu$ (s)		$\Delta\mu$ (%)					
runs	**case**	**t_{ref} (s)**	**orbit**	**MIN**	**MAX**	**MIN**	**MAX**				
1	A	4228	avg	-1	-1	-0%	-0%				
1	A	6724	max	-140	-79	-2%	-1%				
1	B	3495	avg	11	-2	+0%	-0%				
1	B	7108	max	34	-138	+0%	-2%				
1	E	3210	avg	-328	97	-10%	+3%				
1	E	7093	max	29	-8	+0%	-0%				
GYR.qbits				$\Delta\mu$ (s)		$\Delta\mu$ (%)					
runs	**case**	**t_{ref} (s)**	**orbit**	**MIN**	**MAX**	**MIN**	**MAX**				
1	A	4228	avg	138	-282	+3%	-7%				
1	A	6724	max	-50	-563	-1%	-8%				
1	B	3495	avg	16	-95	+0%	-3%				
1	B	7108	max	82	-2263	+1%	-32%				
1	E	3210	avg	39	-422	+1%	-13%				
1	E	7093	max	-26	-3891	-0%	-55%				
MTQ.residual_dipole				$\Delta\mu$ (s)		$\Delta\mu$ (%)					
runs	**case**	**t_{ref} (s)**	**orbit**	**MIN**	**MAX**	**MIN**	**MAX**				
1	A	4228	avg	132	-1	+3%	-0%				
1	A	6724	max	-17	-9	-0%	-0%				
1	B	3495	avg	3	2	+0%	+0%				
1	B	7108	max	0	106	0%	+1%				
1	E	3210	avg	-3	0	-0%	0%				
1	E	7093	max	-8	-3	-0%	-0%				
MTQ.nonlinearity				$\Delta\mu$ (s)		$\Delta\mu$ (%)		σ (s)		σ (%)	
runs	**case**	**t_{ref} (s)**	**orbit**	**MIN**	**MAX**	**MIN**	**MAX**	**MIN**	**MAX**	**MIN**	**MAX**
15	A	4228	avg	207	178	+5%	+4%	162	222	4%	5%
15	A	6724	max	28	50	+0%	+1%	105	183	2%	3%
15	B	3495	avg	-8	-7	-0%	-0%	6	6	0%	0%
15	B	7108	max	-537	-775	-8%	-11%	899	1047	13%	15%
15	E	3210	avg	-117	-127	-4%	-4%	155	152	5%	5%
15	E	7093	max	-2132	-1841	-30%	-26%	849	1119	12%	16%
MTQ.misalignment				$\Delta\mu$ (s)		$\Delta\mu$ (%)					
runs	**case**	**t_{ref} (s)**	**orbit**	**MIN**	**MAX**	**MIN**	**MAX**				
1	A	4228	avg	-1	-21	-0%	-0%				
1	A	6724	max	-91	8	-1%	+0%				
1	B	3495	avg	0	0	0%	0%				
1	B	7108	max	2	-14	+0%	-0%				
1	E	3210	avg	7	7	+0%	+0%				
1	E	7093	max	-13	-8	-0%	-0%				

H.2 Results detailed analysis

Table H.2 lists down the results of the one-at-the-time variation. How to read this table:

- t_{ref} is the detumble time of the reference orbit.
- $\Delta\mu$ is the difference in detumble time with respect to the reference orbit, where $\Delta\mu = \mu - t_{ref}$ and μ is the mean detumble time.
- t^*_{ref} is the corrected average detumble time of the reference orbit (where nominal parameters have been used) with $\Delta\mu^* = \mu - t^*_{ref}$.
- The standard deviation is indicated with σ.
- *MIN*, *NOM* and *MAX* denote the minimum, nominal and maximum errors.

Table H.2: *The results of the detailed analysis, of the one-at-the-time parameter variation in the detumble mode. Eight parameters have been considered here.*

MTM.misalignment (1 run)						$\Delta\mu$ (s)							
case	**orbit**	**seed**	**t_{ref} (s)**			**MIN**	**MAX**						
A	avg (1)	2090	4228			230	0						
B	avg (1)	1092	3495			0	0						
E	avg (1)	135	3210			-3	14						
A	avg (2)	3092	4143			-1	0						
B	avg (2)	2012	3443			-53	14						
E	avg (2)	1028	3101			-33	13						
A	max (1)	3132	6724			-17	-9						
B	max (1)	1016	7108			3	-23						
E	max (1)	2076	7093			-8	10						
A	max (2)	59	6524			0	0						
B	max (2)	26	6107			-1	4						
E	max (2)	1158	6543			42	2						
GYR.bias_repeatability (40 runs)						$\Delta\mu^*$ (s)			σ (s)			σ (%)	
case	**orbit**	**seed**	**t_{ref} (s)**	**Δt_{ref}**	**t^*_{ref} (s)**	**MIN**	**MAX**	**MIN**	**NOM**	**MAX**	**MIN**	**NOM**	**MAX**
A	avg (1)	2090	4228	+0	4228	-30	89	10	100	223	+0%	+2%	+5%
B	avg (1)	1092	3495	-1	3494	0	-2	2	7	17	+0%	+0%	+0%
E	avg (1)	135	3210	+3	3213	9	-41	7	55	155	+0%	+2%	+5%
A	avg (2)	3092	4143	+5	4148	-6	67	3	62	201	+0%	+2%	+5%
B	avg (2)	2012	3443	+10	3453	6	-10	10	35	71	+0%	+1%	+2%
E	avg (2)	1028	3101	-121	2980	41	-111	141	219	292	+5%	+7%	+9%
A	max (1)	3132	6724	+10	6734	-3	11	3	54	167	+0%	+1%	+2%
B	max (1)	1016	7108	-1703	5405	-45	370	6	400	842	+0%	+6%	+12%
E	max (1)	2076	7093	-202	6891	180	-510	14	563	992	+0%	+8%	+14%
A	max (2)	59	6524	-39	6485	-3	-4	12	28	97	+0%	+0%	+1%
B	max (2)	26	6107	+6	6113	2	-7	9	30	74	+0%	+0%	+1%
E	max (2)	1158	6543	-92	6451	-10	-2	46	82	262	+1%	+1%	+4%
GYR.nonlinearity (40 runs)						$\Delta\mu^*$ (s)			σ (s)			σ (%)	
case	**orbit**	**seed**	**t_{ref} (s)**	**Δt_{ref}**	**t^*_{ref} (s)**	**MIN**	**MAX**	**MIN**	**NOM**	**MAX**	**MIN**	**NOM**	**MAX**
A	avg (1)	2090	4228	+121	4349	-126	14	50	171	138	+1%	+4%	+3%
B	avg (1)	1092	3495	+24	3519	3	-10	4	18	35	+0%	+1%	+1%
E	avg (1)	135	3210	-152	3058	126	66	131	173	186	+4%	+5%	+6%
A	avg (2)	3092	4143	+68	4211	-60	-22	3	120	229	+0%	+3%	+6%
B	avg (2)	2012	3443	-34	3409	-12	16	12	25	40	+0%	+1%	+1%
E	avg (2)	1028	3101	+25	3126	-5	-54	4	59	220	+0%	+2%	+7%
A	max (1)	3132	6724	-144	6580	-32	-73	7	136	415	+0%	+2%	+6%
B	max (1)	1016	7108	-238	6870	269	-785	13	574	992	+0%	+8%	+14%
E	max (1)	2076	7093	-1022	6071	819	-1003	7	1130	1041	+0%	+16%	+15%
A	max (2)	59	6524	-109	6416	95	-106	9	162	245	+0%	+2%	+4%
B	max (2)	26	6107	+6	6113	-5	-330	11	29	396	+0%	+0%	+6%
E	max (2)	1158	6543	+38	6581	89	-385	24	142	675	+0%	+2%	+10%

GYR.ARW (40 runs)						$\Delta\mu^*$ (s)		σ (s)			σ (%)		
case	**orbit**	**seed**	$\mathbf{t_{ref}}$ **(s)**	$\mathbf{\Delta t_{ref}}$	$\mathbf{t^*_{ref}}$ **(s)**	**MIN**	**MAX**	**MIN**	**NOM**	**MAX**	**MIN**	**NOM**	**MAX**
A	avg (1)	2090	4228	+28	4256	45	-155	109	97	43	+3%	+2%	+1%
B	avg (1)	1092	3495	+1	3496	4	-65	4	6	18	+0%	+0%	+1%
E	avg (1)	135	3210	-3	3207	4	-312	4	6	94	+0%	+0%	+3%
A	avg (2)	3092	4143	-3	4140	10	-167	4	7	66	+0%	+0%	+2%
B	avg (2)	2012	3443	-24	3419	5	-130	11	18	118	+0%	+1%	+3%
E	avg (2)	1028	3101	-11	3090	7	-786	7	10	45	+0%	+0%	+1%
A	max (1)	3132	6724	-43	6681	42	-412	3	66	75	+0%	+1%	+1%
B	max (1)	1016	7108	+18	7126	-8	-2185	26	47	88	+0%	+1%	+1%
E	max (1)	2076	7093	-4	7089	4	-2549	8	14	44	+0%	+0%	+1%
A	max (2)	59	6524	-4	6520	7	-277	8	8	91	+0%	+0%	+1%
B	max (2)	26	6107	+7	6114	3	-321	5	7	323	+0%	+0%	+5%
E	max (2)	1158	6543	+4	6547	3	-83	10	14	72	+0%	+0%	+1%

GYR.RRW (40 runs)						$\Delta\mu^*$ (s)		σ (s)			σ (%)		
case	**orbit**	**seed**	$\mathbf{t_{ref}}$ **(s)**	$\mathbf{\Delta t_{ref}}$	$\mathbf{t^*_{ref}}$ **(s)**	**MIN**	**MAX**	**MIN**	**NOM**	**MAX**	**MIN**	**NOM**	**MAX**
A	avg (1)	2090	4228	+113	4341	-10	29	167	163	182	+4%	+4%	+4%
B	avg (1)	1092	3495	+2	3497	-1	0	3	4	6	+0%	+0%	+0%
E	avg (1)	135	3210	-1	3210	-3	4	3	5	8	+0%	+0%	+0%
A	avg (2)	3092	4143	-0	4143	1	6	2	8	43	+0%	+0%	+1%
B	avg (2)	2012	3443	-22	3421	2	6	13	25	36	+0%	+1%	+1%
E	avg (2)	1028	3101	+5	3106	-1	-2	3	8	14	+0%	+0%	+0%
A	max (1)	3132	6724	-136	6588	-18	4	30	63	89	+0%	+1%	+1%
B	max (1)	1016	7108	+18	7126	42	-318	70	306	733	+1%	+4%	+10%
E	max (1)	2076	7093	-21	7072	1	-7	8	17	43	+0%	+0%	+1%
A	max (2)	59	6524	+29	6553	-15	6	9	40	67	+0%	+1%	+1%
B	max (2)	26	6107	+13	6120	0	-5	3	13	28	+0%	+0%	+0%
E	max (2)	1158	6543	-22	6521	6	-26	21	55	91	+0%	+1%	+1%

GYR.misalignment (1 run)				$\Delta\mu$ (s)	
case	**orbit**	**seed**	$\mathbf{t_{ref}}$ **(s)**	**MIN**	**MAX**
A	avg (1)	2090	4228	-1	-1
B	avg (1)	1092	3495	-34	-58
E	avg (1)	135	3210	-22	-22
A	avg (2)	3092	4143	15	-27
B	avg (2)	2012	3443	11	-2
E	avg (2)	1028	3101	-22	-22
A	max (1)	3132	6724	-140	-79
B	max (1)	1016	7108	34	-138
E	max (1)	2076	7093	29	-8
A	max (2)	59	6524	23	-6
B	max (2)	26	6107	12	-1
E	max (2)	1158	6543	10	20

GYR.qbits (1 run)				$\Delta\mu$ (s)	
case	**orbit**	**seed**	$\mathbf{t_{ref}}$ **(s)**	**MIN**	**MAX**
A	avg (1)	2090	4228	138	-282
B	avg (1)	1092	3495	16	-95
E	avg (1)	135	3210	7	-401
A	avg (2)	3092	4143	147	43
B	avg (2)	2012	3443	55	-588
E	avg (2)	1028	3101	7	-401
A	max (1)	3132	6724	-50	-563
B	max (1)	1016	7108	82	-2263
E	max (1)	2076	7093	-26	-3891
A	max (2)	59	6524	122	-410
B	max (2)	26	6107	41	-1219
E	max (2)	1158	6543	51	-2278

MTQ.nonlinearity (40 runs)						$\Delta\mu^*$ (s)		σ (s)			σ (%)		
case	**orbit**	**seed**	$\mathbf{t_{ref}}$ **(s)**	$\mathbf{\Delta t_{ref}}$	$\mathbf{t^*_{ref}}$ **(s)**	**MIN**	**MAX**	**MIN**	**NOM**	**MAX**	**MIN**	**NOM**	**MAX**
A	avg (1)	2090	4228	+224	4452	-14	-9	146	173	223	+3%	+4%	+5%
B	avg (1)	1092	3495	-6	3489	0	0	5	5	6	+0%	+0%	+0%
E	avg (1)	135	3210	-150	3060	32	-45	230	256	283	+7%	+8%	+9%
A	avg (2)	3092	4143	+96	4239	-32	13	155	193	213	+4%	+5%	+5%
B	avg (2)	2012	3443	+23	3466	0	-4	31	41	53	+1%	+1%	+2%
E	avg (2)	1028	3101	-150	2951	32	-45	230	256	283	+7%	+8%	+9%
A	max (1)	3132	6724	+5	6729	-15	-23	92	148	203	+1%	+2%	+3%
B	max (1)	1016	7108	-659	6449	44	-243	884	970	1033	+12%	+14%	+15%
E	max (1)	2076	7093	-1875	5218	-335	118	730	1067	1136	+10%	+15%	+16%
A	max (2)	59	6524	+74	6598	-2	18	86	116	164	+1%	+2%	+3%
B	max (2)	26	6107	-11	6096	2	-11	21	27	41	+0%	+0%	+1%
E	max (2)	1158	6543	-72	6471	-9	13	62	74	80	+1%	+1%	+1%

H.2.1 Results for the maximum orbits

Table H.3 shows the results for the maximum orbits only, from the results of the one-at-the-time parameter variation in Table H.2. How to read this table:

- $\Delta\mu^*$ is the (corrected) difference in detumble time between the mean of all simulations and the reference orbit.
- The standard deviation is indicated with σ.
- *MIN*, *NOM* and *MAX* denote the minimum, nominal and maximum errors.

What can be observed, is that the results are very extreme for the maximum orbits (in particular for geometries B and E). The detumble times decrease significantly and the spread is in general very large. These maximum orbits give no insight in the impact of the variation of the error sources. Note that in none of the cases, the detumble time has increased or violates the detumble time constraint.

Table H.3: *Summarized results of the one-at-the-time parameter variation. Only the results for the maximum orbits are shown here.*

Maximum orbit (1)			$\Delta\mu^*$ (s)		σ (s)		
error source	**case**	**runs**	**MIN**	**MAX**	**MIN**	**NOM**	**MAX**
GYR.bias_repeatability	B	40	-45	370	6	400	842
GYR.bias_repeatability	E	40	180	-510	14	563	992
GYR.nonlinearity	B	40	269	-785	13	574	992
GYR.nonlinearity	E	40	819	-1003	7	1130	1041
GYR.ARW	B	40	-8	-2185	26	47	88
GYR.ARW	E	40	4	-2549	8	14	44
GYR.RRW	B	40	42	-318	70	306	733
GYR.RRW	E	40	1	-7	8	17	43
GYR.qbits	B	1	82	-2263			
GYR.qbits	E	1	-26	-3891			
MTQ.nonlinearity	B	40	44	-243	884	970	1033
MTQ.nonlinearity	E	40	-335	118	730	1067	1136
Maximum orbit (2)			$\Delta\mu^*$ (s)		σ (s)		
error source	**case**	**runs**	**MIN**	**MAX**	**MIN**	**NOM**	**MAX**
GYR.nonlinearity	B	40	-5	-330	11	29	396
GYR.nonlinearity	E	40	89	-385	24	142	675
GYR.qbits	B	1	41	-1219			
GYR.qbits	E	1	51	-2278			

H.3 Results grouped error variation

Here the results will be shown of the grouped error variation, for the magnetometer and the magnetorquer. The results are shown in Tables H.4 and H.5.

How to read these tables:

- t_{ref} is the detumble time of the reference orbit.
- $\Delta\mu$ is the difference in detumble time with respect to the reference orbit, where $\Delta\mu = \mu - t_{ref}$ and μ is the mean detumble time.
- t^*_{ref} is the corrected average detumble time of the reference orbit (where nominal parameters have been used) with $\Delta\mu^* = \mu - t^*_{ref}$.
- The standard deviation is indicated with σ.
- *MIN*, *NOM* and *MAX* denote the minimum, nominal and maximum errors.

Table H.4: *The results of the variation of the grouped magnetometer errors.*

Results variation error sources in groups (all seven error sources have been considered)													
						$\Delta\mu^*$ (s)		σ (s)			σ (%)		
set	**runs**	**case**	**t_{ref} (s)**	**t^*_{ref} (s)**	**orbit**	**MIN**	**MAX**	**MIN**	**NOM**	**MAX**	**MIN**	**NOM**	**MAX**
MTM	40	A	4228	4235	avg (1)	187	175	137	58	146	3%	1%	3%
MTM	40	B	3495	3497	avg (1)	-1	-1	1	4	5	0%	0%	0%
MTM	40	E	3210	3207	avg (1)	1	11	11	2	15	0%	0%	0%
MTM	40	A	4143	4142	avg (2)	-4	-5	4	3	15	0%	0%	0%
MTM	40	B	3443	3430	avg (2)	-40	-13	1	27	36	0%	1%	1%
MTM	40	E	3101	3095	avg (2)	-303	-123	311	11	270	10%	0%	9%
Sum results one-at-the-time variation (only MTM.misalignment error has been considered)													
						$\Delta\mu$ (s)		σ (s)			σ (%)		
set	**runs**	**case**	**t_{ref} (s)**	**t^*_{ref} (s)**	**orbit**	**MIN**	**MAX**	**MIN**	**NOM**	**MAX**	**MIN**	**NOM**	**MAX**
MTM	40	A	4228	-	avg (1)	230	0	-	-	-	-	-	-
MTM	40	B	3495	-	avg (1)	0	0	-	-	-	-	-	-
MTM	40	E	3210	-	avg (1)	-3	14	-	-	-	-	-	-
MTM	40	A	4143	-	avg (2)	-1	0	-	-	-	-	-	-
MTM	40	B	3443	-	avg (2)	-53	14	-	-	-	-	-	-
MTM	40	E	3101	-	avg (2)	-33	13	-	-	-	-	-	-

Table H.5: *The results of the variation of the grouped magnetorquer errors.*

Results variation error sources in groups (all three error sources have been considered)													
						$\Delta\mu^*$ (s)		σ (s)			σ (%)		
set	**runs**	**case**	$\mathbf{t_{ref}}$ **(s)**	$\mathbf{t^*_{ref}}$ **(s)**	**orbit**	**MIN**	**MAX**	**MIN**	**NOM**	**MAX**	**MIN**	**NOM**	**MAX**
MTQ	40	A	4228	4452	avg (1)	-8	-11	133	173	202	3%	4%	5%
MTQ	40	B	3495	3489	avg (1)	-1	-1	5	5	7	0%	0%	0%
MTQ	40	E	3210	3087	avg (1)	88	-80	70	153	165	2%	5%	5%
MTQ	40	A	4143	4239	avg (2)	-108	34	47	193	218	1%	5%	5%
MTQ	40	B	3443	3466	avg (2)	27	-23	25	41	51	1%	1%	1%
MTQ	40	E	3101	2951	avg (2)	-12	-57	265	256	288	9%	9%	10%
Sum results one-at-the-time variation (only MTQ.nonlinearity error has been considered)													
						$\Delta\mu^*$ (s)		σ (s)			σ (%)		
set	**runs**	**case**	$\mathbf{t_{ref}}$ **(s)**	$\mathbf{t^*_{ref}}$ **(s)**	**orbit**	**MIN**	**MAX**	**MIN**	**NOM**	**MAX**	**MIN**	**NOM**	**MAX**
MTQ	40	A	4228	4452	avg (1)	-14	-9	146	173	223	3%	4%	5%
MTQ	40	B	3495	3489	avg (1)	0	0	5	5	6	0%	0%	0%
MTQ	40	E	3210	3060	avg (1)	32	-45	230	256	283	7%	8%	9%
MTQ	40	A	4143	4239	avg (2)	-32	13	155	193	213	4%	5%	5%
MTQ	40	B	3443	3466	avg (2)	0	-4	31	41	53	1%	1%	2%
MTQ	40	E	3101	2951	avg (2)	32	-45	230	256	283	7%	8%	9%

Appendix I
RESULTS SA + SP MODES

This appendix contains all results for the SA and SP simulation performance runs. Sections I.1 and I.2 give the results for the variation of the initial parameters for the SunSpace and MicroWheel1000. Sections I.3 and I.4 gives the results for the full Monte Carlo run for both wheels.

I.1 Results variation initial parameters SunSpace

Table I.1 gives an detailed overview of the time spend in each mode. Table I.2 gives a detailed overview of the performance at the end of the simulation.

Table I.1: *Results for the variation of initial orbital parameters. Different seeds has been used for each simulation. The total number of simulations is 800 per geometry.*

		time modes 2 + 3 [s]		**time mode 4 (I)** [s]		**time mode 4 (II)** [s]		**eclipse time** [s]		**total time** [s]	
geometry A	#	**mean**	**max**	**mean**	**max**	**mean**	**max**	**mean**	**max**	**mean**	**max**
no eclipses	419	363	1846	129	298	-	-	-	-	993	2489
eclipse at start	253	1461	3468	128	234	-	-	923	2098	2090	4111
mode 2 before eclipse	41	2513	4156	145	306	-	-	1731	2165	3159	4816
mode 3 before eclipse	13	3709	4197	129	151	-	-	1869	2196	4340	4840
mode 4 before eclipse	16	392	1739	55	147	42	74	1863	2170	2854	4479
mode 5 before eclipse	58	434	1831	142	251	36	80	1883	2196	3218	5029
geometry B	#	**mean**	**max**	**mean**	**max**	**mean**	**max**	**mean**	**max**	**mean**	**max**
no eclipses	435	271	1340	110	197	-	-	-	-	882	1961
eclipse at start	253	1253	3061	110	249	1*	157*	923	2098	1865	3679
mode 2 before eclipse	31	2247	3045	108	135	-	-	1700	2165	2856	3675
mode 3 before eclipse	6	3069	3205	88	128	-	-	1737	2157	3658	3736
mode 4 before eclipse	19	244	1272	51	148	39	72	1820	2133	2656	3875
mode 5 before eclipse	56	290	1330	115	179	34	73	1904	2196	3094	4466
geometry E	#	**mean**	**max**	**mean**	**max**	**mean**	**max**	**mean**	**max**	**mean**	**max**
no eclipses	450	159	890	102	155	-	-	-	-	762	1502
eclipse at start	253	1201	2819	102	142	1*	143*	923	2098	1805	3431
mode 2 before eclipse	15	2012	2546	101	143	-	-	1731	2131	2614	3141
mode 3 before eclipse	7	2743	3267	116	158	-	-	1994	2165	3361	3885
mode 4 before eclipse	14	66	175	43	91	40	66	1748	2133	2399	2723
mode 5 before eclipse	61	210	874	107	151	33	62	1813	2177	2898	4124
	#	**mean**	**max**	**mean**	**max**	**mean**	**max**	**mean**	**max**	**mean**	**max**
maximum values geometry A	800	3709	4197	145	306	42	80	1883	2196	4340	5029
maximum values geometry B	800	3069	3205	115	249	39	73	1904	2196	3658	4466
maximum values geometry E	800	2743	3267	116	158	40	66	1994	2177	3361	4124

Outlier in the results

There are 5 outliers in the simulations, which occur for geometries B (2x) and E (3x).

For all outliers, mode 4 occurs twice. It can be seen that in these situations the Sun is directly in the FoV after eclipse exit (coincidentally). Therefore, the satellite makes a slew maneuver to get SP. However, during this slew, it looses the Sun for a few seconds from its FoV. However, it can also be seen that based on the propagated last Sun measurement the satellite is still able to get SP.

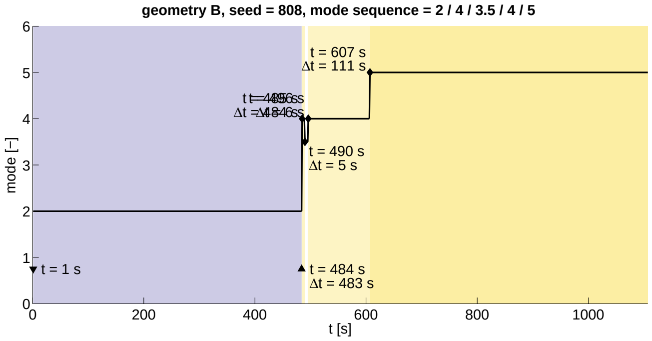
geometry B, seed = 808, mode sequence = 2 / 4 / 3.5 / 4 / 5

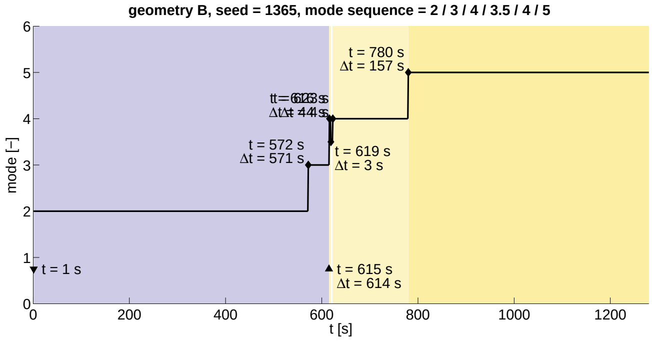
geometry B, seed = 1365, mode sequence = 2 / 3 / 4 / 3.5 / 4 / 5

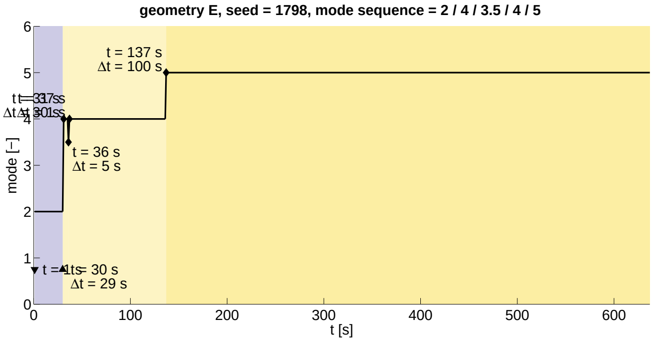
geometry E, seed = 1798, mode sequence = 2 / 4 / 3.5 / 4 / 5

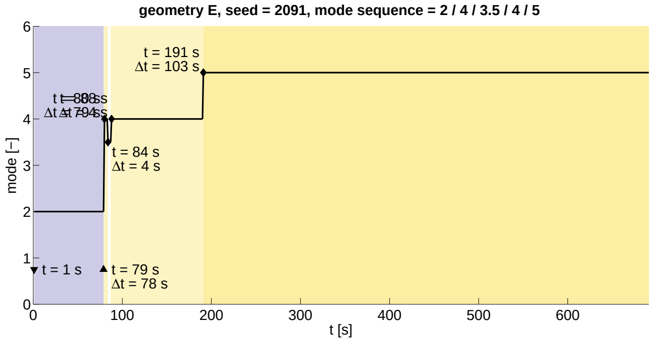
geometry E, seed = 2091, mode sequence = 2 / 4 / 3.5 / 4 / 5

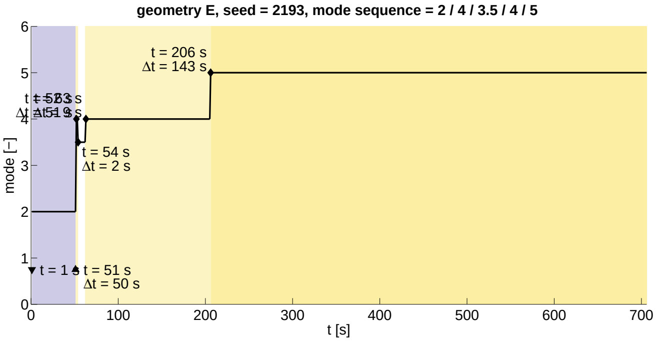
geometry E, seed = 2193, mode sequence = 2 / 4 / 3.5 / 4 / 5

Table I.2 lists the variation of the performance parameters during the last 500 s of the simulation. The results are shown from the instance the satellite is just SP (t_0) until the end of the simulation (t_{end}). The columns of the table show the average and maximum values for all simulations, given the different time instances. Note that the values in the table are independent of each other. Furthermore, please note that the table lists the *absolute* spacecraft angular rate and wheel speeds. With this table, it can be seen that after approximately 200 s the XY-angle and the spacecraft angular rates are have been reduced towards the minimum values. A stable state has been reached.

Table I.2: *Detailed results of the performance parameters for the variation of initial parameters, for the SunSpace wheel system.*

	unit	**average values**				**maximum values**			
geometry A		$\mathbf{t_0}$	$\mathbf{t_{100}}$	$\mathbf{t_{200}}$	$\mathbf{t_{end}}$	$\mathbf{t_0}$	$\mathbf{t_{100}}$	$\mathbf{t_{200}}$	$\mathbf{t_{end}}$
XY-angle measured	deg	4.89	0.37	0.34	0.36	5.00	0.98	0.99	1.04
XY-angle true	deg	4.90	0.76	0.76	0.77	5.69	1.39	1.40	1.42
||SC angular rate X||	deg/s	0.007	0.007	0.007	0.007	0.073	0.018	0.018	0.018
||SC angular rate Y||	deg/s	0.094	0.006	0.002	0.001	0.156	0.014	0.006	0.006
||SC angular rate Z||	deg/s	0.064	0.005	0.002	0.001	0.139	0.015	0.006	0.007
||wheel speed X||	RPM	649	647	651	669	1894	1900	1888	2018
||wheel speed Y||	RPM	936	829	849	852	3071	1853	1886	1914
||wheel speed Z||	RPM	553	585	595	601	1936	1966	2039	2174
energy consumption	Whr	0.06	0.06	0.07	0.08	0.15	0.16	0.16	0.17
	unit	**average values**				**maximum values**			
geometry B		$\mathbf{t_0}$	$\mathbf{t_{100}}$	$\mathbf{t_{200}}$	$\mathbf{t_{end}}$	$\mathbf{t_0}$	$\mathbf{t_{100}}$	$\mathbf{t_{200}}$	$\mathbf{t_{end}}$
XY-angle measured	deg	4.89	0.39	0.33	0.34	5.00	0.96	1.00	1.06
XY-angle true	deg	4.92	0.77	0.76	0.77	5.71	1.37	1.37	1.38
||SC angular rate X||	deg/s	0.007	0.007	0.007	0.007	0.070	0.019	0.018	0.017
||SC angular rate Y||	deg/s	0.089	0.006	0.002	0.001	0.145	0.015	0.007	0.006
||SC angular rate Z||	deg/s	0.069	0.005	0.002	0.001	0.135	0.015	0.008	0.007
||wheel speed X||	RPM	479	478	481	496	1669	1773	1830	2017
||wheel speed Y||	RPM	673	620	634	638	2437	1498	1424	1446
||wheel speed Z||	RPM	402	424	431	437	1344	1307	1350	1421
energy consumption	Whr	0.06	0.07	0.07	0.08	0.16	0.16	0.17	0.18
	unit	**average values**				**maximum values**			
geometry E		$\mathbf{t_0}$	$\mathbf{t_{100}}$	$\mathbf{t_{200}}$	$\mathbf{t_{end}}$	$\mathbf{t_0}$	$\mathbf{t_{100}}$	$\mathbf{t_{200}}$	$\mathbf{t_{end}}$
XY-angle measured	deg	4.89	0.43	0.34	0.33	5.00	1.04	0.87	0.91
XY-angle true	deg	4.92	0.79	0.76	0.76	5.67	1.42	1.36	1.35
||SC angular rate X||	deg/s	0.007	0.007	0.007	0.007	0.074	0.019	0.018	0.018
||SC angular rate Y||	deg/s	0.087	0.006	0.001	0.001	0.345	0.016	0.006	0.006
||SC angular rate Z||	deg/s	0.071	0.006	0.002	0.002	0.137	0.017	0.009	0.008
||wheel speed X||	RPM	407	402	405	424	1617	1799	1858	2075
||wheel speed Y||	RPM	544	533	548	558	2108	1672	1671	1695
||wheel speed Z||	RPM	345	356	360	366	1325	1303	1313	1296
energy consumption	Whr	0.08	0.08	0.08	0.10	0.26	0.26	0.27	0.28

I.2 Results variation initial parameters MicroWheel1000

Table I.3 gives an detailed overview of the time spend in each mode. Table I.4 gives a detailed overview of the performance at the end of the simulation.

Table I.3: *Results for the variation of initial orbital parameters. Different seeds has been used for each simulation. The total number of simulations is 800 per geometry.*

		time modes 2 + 3 [s]		**time mode 4 (I)** [s]		**time mode 4 (II)** [s]		**eclipse time** [s]		**total time** [s]	
geometry A	#	**mean**	**max**	**mean**	**max**	**mean**	**max**	**mean**	**max**	**mean**	**max**
no eclipses	441	247	1146	107	165	-	-	-	-	854	1759
eclipse at start	253	1220	3204	105	161	2*	149*	923	2098	1828	3806
mode 2 before eclipse	28	2266	3505	115	144	-	-	1743	2165	2882	4121
mode 3 before eclipse	5	3206	4008	114	157	-	-	1939	2157	3821	4619
mode 4 before eclipse	19	220	1130	51	95	39	68	1701	2133	2513	3763
mode 5 before eclipse	54	263	1139	112	154	36	76	1883	2183	3034	4260
geometry B	#	**mean**	**max**	**mean**	**max**	**mean**	**max**	**mean**	**max**	**mean**	**max**
no eclipses	448	176	818	100	133	-	-	-	-	777	1421
eclipse at start	253	1152	2935	102	146	0*	122*	923	2098	1756	3538
mode 2 before eclipse	20	2098	2928	99	118	-	-	1761	2165	2698	3532
mode 3 before eclipse	5	2834	2926	104	106	-	-	1940	2141	3438	3532
mode 4 before eclipse	15	69	253	53	117	35	73	1625	2133	2284	2718
mode 5 before eclipse	59	213	807	103	125	39	72	1851	2177	2958	3871
geometry E	#	**mean**	**max**	**mean**	**max**	**mean**	**max**	**mean**	**max**	**mean**	**max**
no eclipses	461	112	562	96	124	-	-	-	-	709	1161
eclipse at start	253	1075	2551	96	134	0*	98*	923	2098	1673	3151
mode 2 before eclipse	11	1974	2364	99	116	-	-	1790	2131	2574	2957
mode 3 before eclipse	5	2239	2818	97	99	-	-	1673	2090	2838	3418
mode 4 before eclipse	17	82	520	45	92	44	70	1835	2141	2509	3123
mode 5 before eclipse	53	87	550	98	114	35	68	1814	2177	2773	3688
	#	**mean**	**max**	**mean**	**max**	**mean**	**max**	**mean**	**max**	**mean**	**max**
maximum values geometry A	800	3206	4008	115	165	39	76	1939	2183	3821	4619
maximum values geometry B	800	2834	2935	104	146	39	73	1940	2177	3438	3871
maximum values geometry E	800	2239	2818	99	134	44	70	1835	2177	2838	3688

Outlier in the results

There are 6 outliers in the simulations, which occur for geometries A (4x), B (1x) and E (1x). Two examples are shown here.

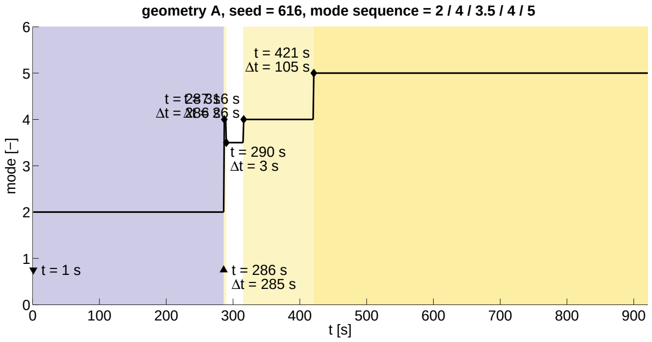

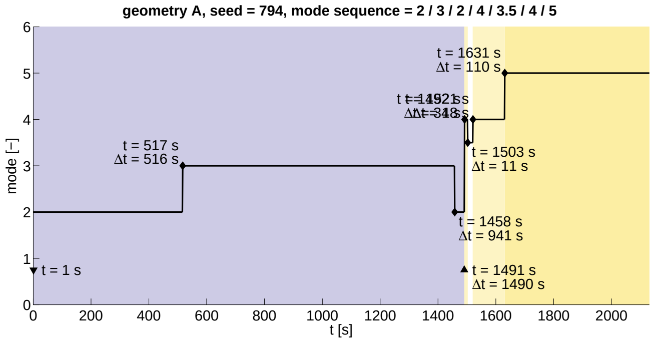

For all outliers, mode 4 occurs twice. The Sun is directly in the FoV after eclipse exit (by coincidence). Therefore, the satellite makes a slew maneuver to get SP. However, during this slew, it looses the Sun for a few seconds from its FoV. However, it can also be seen that based on the propagated last Sun measurement the satellite is still able to get SP.

Table I.4 lists the variation of the performance parameters during the last 500 s of the simulation. The results are shown from the instance the satellite is just SP (t_0) until the end of the simulation (t_{end}). The columns of the table show the average and maximum values for all simulations, given the different time instances. Note that the values in the table are independent of each other. Furthermore, please note that the table lists the *absolute* spacecraft angular rate and wheel speeds. With this table, it can be seen that after approximately 200 s the XY-angle and the spacecraft angular rates are have been reduced towards the minimum values. A stable state has been reached.

Table I.4: *Detailed results of the performance parameters for the variation of initial parameters, for the MicroWheel1000 wheel system*

	unit	**average values**				**maximum values**			
geometry A		$\mathbf{t_0}$	$\mathbf{t_{100}}$	$\mathbf{t_{200}}$	$\mathbf{t_{end}}$	$\mathbf{t_0}$	$\mathbf{t_{100}}$	$\mathbf{t_{200}}$	$\mathbf{t_{end}}$
XY-angle measured	deg	4.89	0.39	0.36	0.37	5.00	0.97	1.06	1.08
XY-angle true	deg	4.93	0.78	0.76	0.78	5.69	1.52	1.41	1.44
||SC angular rate X||	deg/s	0.008	0.007	0.007	0.007	0.073	0.018	0.019	0.019
||SC angular rate Y||	deg/s	0.093	0.006	0.002	0.001	0.377	0.015	0.007	0.006
||SC angular rate Z||	deg/s	0.072	0.005	0.002	0.001	0.254	0.015	0.007	0.007
||wheel speed X||	RPM	928	923	929	955	2986	3201	3324	3628
||wheel speed Y||	RPM	1319	1177	1208	1210	4289	2659	2688	2737
||wheel speed Z||	RPM	801	843	857	865	2795	2536	2584	2639
energy consumption	Whr	0.08	0.09	0.09	0.10	0.29	0.30	0.30	0.31
	unit	**average values**				**maximum values**			
geometry B		$\mathbf{t_0}$	$\mathbf{t_{100}}$	$\mathbf{t_{200}}$	$\mathbf{t_{end}}$	$\mathbf{t_0}$	$\mathbf{t_{100}}$	$\mathbf{t_{200}}$	$\mathbf{t_{end}}$
XY-angle measured	deg	4.90	0.40	0.34	0.35	5.00	1.00	0.96	1.01
XY-angle true	deg	4.93	0.78	0.76	0.77	5.71	1.39	1.37	1.40
||SC angular rate X||	deg/s	0.007	0.007	0.007	0.007	0.070	0.019	0.018	0.018
||SC angular rate Y||	deg/s	0.087	0.006	0.002	0.001	0.143	0.015	0.007	0.006
||SC angular rate Z||	deg/s	0.074	0.006	0.002	0.002	0.136	0.015	0.007	0.007
||wheel speed X||	RPM	678	679	682	700	2478	2650	2718	2996
||wheel speed Y||	RPM	902	860	882	888	3163	1939	2024	2068
||wheel speed Z||	RPM	583	624	635	643	1843	1922	1938	1949
energy consumption	Whr	0.08	0.09	0.09	0.10	0.26	0.26	0.27	0.28
	unit	**average values**				**maximum values**			
geometry E		$\mathbf{t_0}$	$\mathbf{t_{100}}$	$\mathbf{t_{200}}$	$\mathbf{t_{end}}$	$\mathbf{t_0}$	$\mathbf{t_{100}}$	$\mathbf{t_{200}}$	$\mathbf{t_{end}}$
XY-angle measured	deg	4.91	0.43	0.34	0.34	5.00	1.01	0.91	0.95
XY-angle true	deg	4.94	0.79	0.76	0.76	5.71	1.53	1.36	1.35
||SC angular rate X||	deg/s	0.007	0.007	0.007	0.007	0.072	0.019	0.018	0.019
||SC angular rate Y||	deg/s	0.087	0.006	0.001	0.001	0.142	0.015	0.007	0.007
||SC angular rate Z||	deg/s	0.073	0.006	0.002	0.002	0.140	0.016	0.010	0.008
||wheel speed X||	RPM	585	579	584	612	2333	2606	2700	3003
||wheel speed Y||	RPM	789	751	767	778	3086	2421	2388	2384
||wheel speed Z||	RPM	490	517	523	534	1509	1713	1703	1682
energy consumption	Whr	0.11	0.12	0.12	0.13	0.45	0.46	0.46	0.48

I.3 Results full Monte Carlo run SunSpace

Table I.5 gives an detailed overview of the time spend in each mode. Table I.6 gives a detailed overview of the performance at the end of the simulation.

Table I.5: *Results for the variation of initial orbital parameters. Different seeds has been used for each simulation. The total number of simulations is 800 per geometry.*

		time modes 2 + 3 [s]		**time mode 4 (I)** [s]		**time mode 4 (II)** [s]		**eclipse time** [s]		**total time** [s]	
geometry A	#	**mean**	**max**	**mean**	**max**	**mean**	**max**	**mean**	**max**	**mean**	**max**
no eclipses	422	363	2008	129	368	-	-	-	-	994	2686
eclipse at start	253	1431	3902	127	284	-	-	923	2098	2060	4544
mode 2 before eclipse	39	2642	4057	132	233	-	-	1745	2177	3275	4693
mode 3 before eclipse	13	3976	4882	142	172	-	-	1851	2157	4619	5531
mode 4 before eclipse	20	315	1848	56	135	49	84	1737	2160	2658	4229
mode 5 before eclipse	53	420	2163	135	249	47	113	1913	2197	3258	5034
geometry B	#	**mean**	**max**	**mean**	**max**	**mean**	**max**	**mean**	**max**	**mean**	**max**
no eclipses	441	273	1550	110	236	-	-	-	-	884	2188
eclipse at start	253	1308	3239	110	226	1*	153*	923	2098	1919	3840
mode 2 before eclipse	29	2312	3366	108	156	-	-	1742	2165	2921	3987
mode 3 before eclipse	9	3145	3571	102	142	-	-	1855	2157	3749	4159
mode 4 before eclipse	21	284	1500	53	122	43	77	1774	2177	2655	4289
mode 5 before eclipse	47	230	1417	111	174	48	109	1871	2183	2994	4361
geometry E	#	**mean**	**max**	**mean**	**max**	**mean**	**max**	**mean**	**max**	**mean**	**max**
no eclipses	450	156	1046	102	175	-	-	-	-	759	1657
eclipse at start	253	1186	2956	103	156	-	-	923	2098	1789	3556
mode 2 before eclipse	17	2086	2826	110	123	-	-	1732	2131	2698	3425
mode 3 before eclipse	6	2632	2877	104	113	-	-	1978	2165	3237	3475
mode 4 before eclipse	16	170	991	44	91	49	70	1797	2133	2563	3622
mode 5 before eclipse	58	210	1008	106	154	42	87	1811	2177	2905	4289
	#	**mean**	**max**	**mean**	**max**	**mean**	**max**	**mean**	**max**	**mean**	**max**
maximum values geometry A	800	3976	4882	142	368	49	113	1913	2197	4619	5531
maximum values geometry B	800	3145	3571	111	236	48	109	1871	2183	3749	4361
maximum values geometry E	800	2632	2956	110	175	49	87	1978	2177	3237	4289

Outlier in the results

There is one outlier in the simulations, which occurs for geometry B.

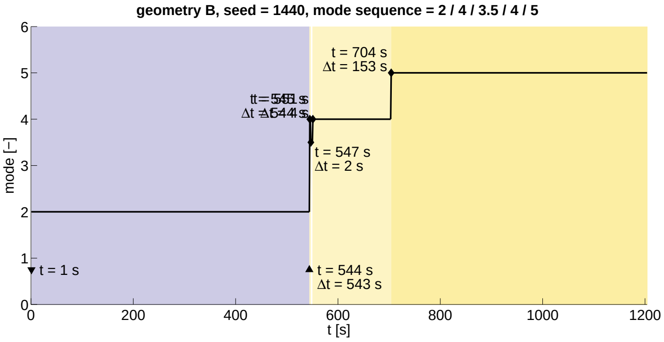

It can be seen that mode 4 occurs twice here. The Sun is directly in the FoV after eclipse exit (by coincidence). Therefore, the satellite makes a slew maneuver to get SP. However, during this slew, it looses the Sun for a few seconds from its FoV. However, it can also be seen that based on the propagated last Sun measurement the satellite is still able to get SP.

Table I.6 lists the variation of the performance parameters during the last 500 s of the simulation. The results are shown from the instance the satellite is just SP (t_0) until the end of the simulation (t_{end}). The columns of the table show the average and maximum values for all simulations, given the different time instances. Note that the values in the table are independent of each other. Furthermore, please note that the table lists the *absolute* spacecraft angular rate and wheel speeds. With this table, it can be seen that after approximately 200 s the XY-angle and the spacecraft angular rates are have been reduced towards the minimum values. A stable state has been reached.

Table I.6: *Detailed results of the performance parameters for the Monte Carlo run, for the SunSpace wheel system.*

	unit	**average values**				**maximum values**			
geometry A		$\mathbf{t_0}$	$\mathbf{t_{100}}$	$\mathbf{t_{200}}$	$\mathbf{t_{end}}$	$\mathbf{t_0}$	$\mathbf{t_{100}}$	$\mathbf{t_{200}}$	$\mathbf{t_{end}}$
XY-angle measured	deg	4.86	0.43	0.35	0.35	5.00	1.50	1.19	1.10
XY-angle true	deg	4.94	0.88	0.84	0.84	6.20	2.00	1.88	1.91
||SC angular rate X||	deg/s	0.011	0.011	0.011	0.011	0.077	0.038	0.038	0.042
||SC angular rate Y||	deg/s	0.095	0.007	0.003	0.003	0.163	0.023	0.023	0.016
||SC angular rate Z||	deg/s	0.064	0.006	0.004	0.003	0.157	0.024	0.019	0.018
||wheel speed X||	RPM	624	624	629	649	2145	2042	2077	2154
||wheel speed Y||	RPM	961	815	834	834	3045	2187	2054	2178
||wheel speed Z||	RPM	546	580	595	602	1910	2365	2375	2405
energy consumption	Whr	0.08	0.09	0.10	0.11	0.42	0.43	0.44	0.45
	unit	**average values**				**maximum values**			
geometry B		$\mathbf{t_0}$	$\mathbf{t_{100}}$	$\mathbf{t_{200}}$	$\mathbf{t_{end}}$	$\mathbf{t_0}$	$\mathbf{t_{100}}$	$\mathbf{t_{200}}$	$\mathbf{t_{end}}$
XY-angle measured	deg	4.87	0.44	0.33	0.34	5.00	1.63	1.30	1.14
XY-angle true	deg	4.97	0.89	0.84	0.84	6.26	1.98	1.74	1.92
||SC angular rate X||	deg/s	0.011	0.011	0.011	0.010	0.072	0.040	0.040	0.037
||SC angular rate Y||	deg/s	0.091	0.008	0.003	0.003	0.160	0.024	0.019	0.021
||SC angular rate Z||	deg/s	0.069	0.007	0.004	0.003	0.475	0.028	0.022	0.019
||wheel speed X||	RPM	462	460	465	482	1535	1562	1591	1764
||wheel speed Y||	RPM	673	608	626	627	2333	1538	1573	1683
||wheel speed Z||	RPM	385	418	429	435	1574	1465	1425	1470
energy consumption	Whr	0.08	0.09	0.10	0.11	0.39	0.41	0.42	0.44
	unit	**average values**				**maximum values**			
geometry E		$\mathbf{t_0}$	$\mathbf{t_{100}}$	$\mathbf{t_{200}}$	$\mathbf{t_{end}}$	$\mathbf{t_0}$	$\mathbf{t_{100}}$	$\mathbf{t_{200}}$	$\mathbf{t_{end}}$
XY-angle measured	deg	4.86	0.47	0.34	0.34	5.00	1.44	1.24	1.10
XY-angle true	deg	4.99	0.92	0.84	0.84	6.38	1.89	1.83	1.77
||SC angular rate X||	deg/s	0.010	0.010	0.010	0.010	0.072	0.038	0.036	0.039
||SC angular rate Y||	deg/s	0.088	0.007	0.003	0.003	0.149	0.025	0.018	0.020
||SC angular rate Z||	deg/s	0.072	0.007	0.005	0.005	1.204	0.049	0.035	0.037
||wheel speed X||	RPM	404	394	399	421	1551	1531	1607	1790
||wheel speed Y||	RPM	550	522	541	548	2373	1754	1791	1807
||wheel speed Z||	RPM	344	361	365	372	1632	1335	1318	1295
energy consumption	Whr	0.09	0.10	0.10	0.12	0.42	0.43	0.44	0.46

I.4 Results full Monte Carlo run MicroWheel1000

Table I.7 gives an detailed overview of the time spend in each mode. Table I.8 gives a detailed overview of the performance at the end of the simulation.

Table I.7: *Results for the variation of initial orbital parameters. Different seeds has been used for each simulation. The total number of simulations is 800 per geometry.*

		time modes 2 + 3 [s]		**time mode 4 (I)** [s]		**time mode 4 (II)** [s]		**eclipse time** [s]		**total time** [s]	
geometry A	#	**mean**	**max**	**mean**	**max**	**mean**	**max**	**mean**	**max**	**mean**	**max**
no eclipses	442	246	1322	107	201	-	-	-	-	854	1935
eclipse at start	253	1234	2992	107	161	1*	117*	923	2098	1843	3598
mode 2 before eclipse	27	2134	3482	96	136	9*	139*	1728	2165	2743	4095
mode 3 before eclipse	6	3152	3968	101	120	-	-	1802	2157	3755	4581
mode 4 before eclipse	22	228	1133	58	109	40	81	1773	2177	2601	3770
mode 5 before eclipse	50	251	1286	109	150	50	96	1880	2183	3031	4292
geometry B	#	**mean**	**max**	**mean**	**max**	**mean**	**max**	**mean**	**max**	**mean**	**max**
no eclipses	447	177	955	100	150	-	-	-	-	778	1559
eclipse at start	253	1143	2979	101	147	1*	125*	923	2098	1746	3578
mode 2 before eclipse	21	2057	2635	91	120	5*	101*	1727	2165	2655	3229
mode 3 before eclipse	5	2820	3256	98	101	-	-	1940	2141	3419	3857
mode 4 before eclipse	13	67	468	45	91	57	77	1781	2133	2452	2714
mode 5 before eclipse	61	226	925	102	132	47	89	1823	2177	2936	4128
geometry E	#	**mean**	**max**	**mean**	**max**	**mean**	**max**	**mean**	**max**	**mean**	**max**
no eclipses	459	110	654	96	125	-	-	-	-	707	1255
eclipse at start	253	1067	2532	94	131	2*	109*	923	2098	1664	3139
mode 2 before eclipse	10	2064	2696	99	116	-	-	1751	2131	2664	3288
mode 3 before eclipse	3	2143	3184	95	97	-	-	1448	2088	2739	3779
mode 4 before eclipse	20	69	483	43	92	47	92	1825	2133	2486	3017
mode 5 before eclipse	55	119	629	98	127	46	89	1808	2177	2814	3693
geometry E	#	**mean**	**max**	**mean**	**max**	**mean**	**max**	**mean**	**max**	**mean**	**max**
maximum values geometry A	800	3152	3968	109	201	50	96	1880	2183	3755	4581
maximum values geometry B	800	2820	3256	102	150	57	89	1940	2177	3419	4128
maximum values geometry E	800	2143	3184	99	131	47	92	1825	2177	2814	3779

Outlier in the results

There are 11 outliers in the simulations, which occur for geometries A (4x), B (4x) and E (3x). Two examples are shown here.

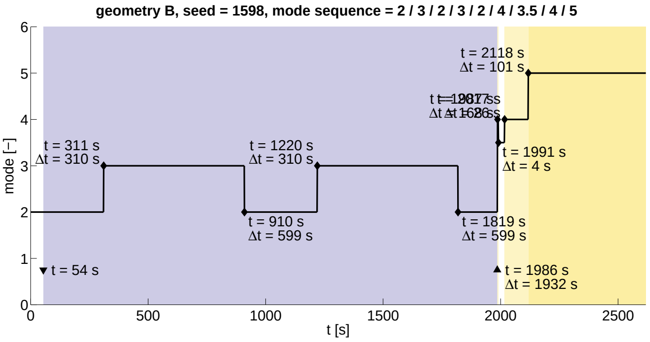

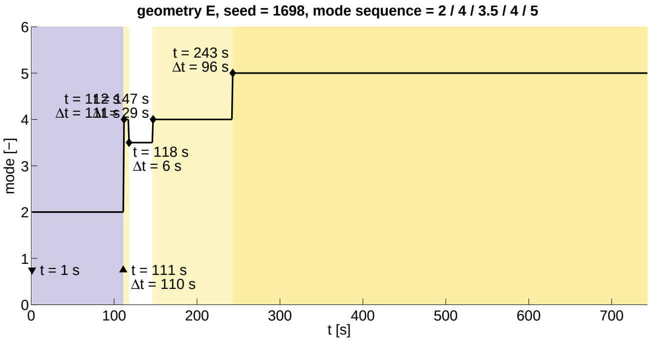

For all outliers, mode 4 occurs twice. The Sun is directly in the FoV after eclipse exit (by coincidence). Therefore, the satellite makes a slew maneuver to get SP. However, during this slew, it looses the Sun for a few seconds from its FoV. However, it can also be seen that based on the propagated last Sun measurement the satellite is still able to get SP.

Table I.8 lists the variation of the performance parameters during the last 500 s of the simulation. The results are shown from the instance the satellite is just SP (t_0) until the end of the simulation (t_{end}). The columns of the table show the average and maximum values for all simulations, given the different time instances. Note that the values in the table are independent of each other. Furthermore, please note that the table lists the *absolute* spacecraft angular rate and wheel speeds. With this table, it can be seen that after approximately 200 s the XY-angle and the spacecraft angular rates are have been reduced towards the minimum values. A stable state has been reached.

Table I.8: *Detailed results of the performance parameters for the Monte Carlo run, for the MicroWheel1000 wheel system.*

	unit	**average values**				**maximum values**			
geometry A		t_0	t_{100}	t_{200}	t_{end}	t_0	t_{100}	t_{200}	t_{end}
XY-angle measured	deg	4.85	0.44	0.37	0.36	5.00	1.52	1.29	1.14
XY-angle true	deg	4.96	0.89	0.84	0.85	6.27	2.00	1.92	1.90
||SC angular rate X||	deg/s	0.011	0.011	0.011	0.011	0.078	0.039	0.037	0.039
||SC angular rate Y||	deg/s	0.094	0.007	0.003	0.002	0.437	0.022	0.017	0.021
||SC angular rate Z||	deg/s	0.072	0.007	0.003	0.003	0.144	0.025	0.021	0.024
||wheel speed X||	RPM	895	891	899	927	2775	2851	2906	3222
||wheel speed Y||	RPM	1323	1149	1179	1180	4539	2752	2835	3061
||wheel speed Z||	RPM	789	830	851	858	3063	2695	2753	2687
energy consumption	Whr	0.09	0.10	0.11	0.12	0.52	0.53	0.54	0.56
	unit	**average values**				**maximum values**			
geometry B		t_0	t_{100}	t_{200}	t_{end}	t_0	t_{100}	t_{200}	t_{end}
XY-angle measured	deg	4.87	0.44	0.35	0.35	5.00	1.50	1.28	1.13
XY-angle true	deg	4.97	0.89	0.84	0.84	6.41	2.08	1.81	1.90
||SC angular rate X||	deg/s	0.011	0.011	0.011	0.011	0.072	0.039	0.036	0.037
||SC angular rate Y||	deg/s	0.089	0.008	0.003	0.003	0.152	0.025	0.022	0.021
||SC angular rate Z||	deg/s	0.074	0.007	0.004	0.004	0.142	0.024	0.024	0.021
||wheel speed X||	RPM	658	657	663	687	2275	2300	2353	2599
||wheel speed Y||	RPM	904	851	879	883	3245	2076	2142	2227
||wheel speed Z||	RPM	569	609	624	630	2667	2025	2101	2075
energy consumption	Whr	0.09	0.10	0.11	0.12	0.43	0.45	0.46	0.48
	unit	**average values**				**maximum values**			
geometry E		t_0	t_{100}	t_{200}	t_{end}	t_0	t_{100}	t_{200}	t_{end}
XY-angle measured	deg	4.86	0.47	0.35	0.36	5.00	1.50	1.26	1.24
XY-angle true	deg	4.97	0.92	0.84	0.85	6.30	2.08	1.89	1.83
||SC angular rate X||	deg/s	0.010	0.010	0.010	0.010	0.073	0.041	0.040	0.041
||SC angular rate Y||	deg/s	0.087	0.007	0.003	0.003	0.148	0.025	0.021	0.018
||SC angular rate Z||	deg/s	0.072	0.007	0.004	0.005	0.148	0.031	0.026	0.026
||wheel speed X||	RPM	568	559	566	602	2277	2245	2306	2564
||wheel speed Y||	RPM	797	747	769	775	3318	2499	2594	2632
||wheel speed Z||	RPM	491	515	523	536	1753	1681	1710	1837
energy consumption	Whr	0.12	0.13	0.14	0.15	0.51	0.52	0.53	0.55

Bibliography

Avanzini G. and Giulietti F., “Magnetic Detumbling of a Rigid Spacecraft,” *Journal of Guidance, Control, and Dynamics*, vol. 35, no. 4, 2012.

Bellini N., “*Magnetic Actuators for Nanosatellite Attitude Control*,” Universita’ di Bologna, 2014.

Capderou M., *Satellites Orbits and missions.* Springer, 2005.

COSPAR, *CIRA-2012 Models of the Earth’s Upper Atmosphere.* Committee on Space research (COSPAR), 2012.

Cruijssen H. and Hobijn C., *The preliminary design of the SPS-2 microsatellite.* Airbus Defense and Space NL, 2015.

Curtis H.D., *Orbital Mechanics for Engineering Students*, 3rd ed. Elsevier, 2010.

Ellenbroek M., Mooij E., Kouwen J., and Meijboom F., *Generic AOCS Simulation Environment In Matlab/Simulink.* Airbus Defense and Space the Netherlands / Dutch Space, 2015.

Ellenbroek M., *Generic GNC Simulator Environment in Matlab / Simulink Software User Manual (Detailed Design Document)*, 2nd ed. Dutch Space, 2011.

Jensen K.F. and Vinther K., “*Attitude Determination and Control System for AAUSAT3*,” Aalborg University, 2010.

Landis Markley F. and Crassidis J., *Fundamentals of spacecraft attitude and control.* Springer, 2014.

Liu L., “*Jitter and Basic Requirements of the Reaction Wheel Assembly in the Attitude Control System*,” http://web.mit.edu/lululiu/Public/TESS%20things/acs_analysis.pdf, accessed in February 2016.

Montenbruck O. and Gill E., *Satellite orbits : models, methods, and applications.* Springer, 2000.

Mooij E., *Lecture notes course AE4870B (Re-Entry Systems).* Delft University of Technology, 2011.

Munatsi P., “*Design of the Attitude Control System for the SPS-2 satellite for the science mode*,” Airbus Defense and Space the Netherlands, TU Delft, 2016.

——, “*Internship report AOCS Design Stackable Platform Structure*,” Airbus Defense and Space the Netherlands, TU Delft, 2016.

Oomen M., *An overview of the specification sheets of the sensors and actuators which have been considered for the SPS-2 mission.* Airbus Defense and Space NL, 2016.

Osorio C., "*Control Tutorials for Matlab & Simulink (Using Bode Plots, Part 1: Closed-Loop Systems)*," http://nl.mathworks.com/videos/using-bode-plots-closed-loop-systems-1-of-5-77057.html, accessed in February 2016.

Picone A., *NRLMSISE-00 Empirical Model of the Atmosphere: Statistical Comparison and Scientific Issues.* Journal of Geophysical Research, 2001.

Primdahl F., "The fluxgate magnetometer," *Journal of Physics and Scientific Instruments*, vol. 12, no. 4, 1979.

Regan F., *Dynamics of Atmospheric Re-Entry.* AIAA Education Series, 1993.

Ripka P., "AMR magnetometer," *Journal of Magnetism and Magnetic Materials*, vol. 254-255, no. 4, 2003.

Sghedoni M., *ADS Software User's Manual (issue 3).* ALCATEL, 2000.

SpaceWorks, "*NANO/ MICROSATELLITE MARKET ASSESSMENT 2016*," http://spaceworksforecast.com/, accessed at 20 June '16.

Thébault E., Finlay C., Beggan C., Alken P., and Aubert J., "International Geomagnetic Reference Field: the 12th generation," *Earth, Planets and Space*, 2015.

Tuthill J., "*DESIGN AND SIMULATION OF A NANO-SATELLITE ATTITUDE DETERMINATION SYSTEM*," NAVAL POSTGRADUATE SCHOOL, MONTEREY, CALIFORNIA, 2009.

Wakker K., *Lecture notes course AE4874 (Astrodynamics I).* Delft University of Technology, 2010.

Wertz J.R., *Spacecraft Attitude Determination and Control.* Kluwer Academic Publishers, 1978.

Wertz J.R. and Larson W.R., *Space Mission Analysis and Design*, 3rd ed. Microcosm Press, Inc., 2007.

Wertz J.R., Meissinger H.F., Kraft Newman L., and Smit G.N., *Orbit & Constellation Design & Management*, 2nd ed. Microcosm Press, Inc., 2009.

Wie B., *Space Vehicle Dynamics and Control*, 2nd ed. AIAA Education Series, 2008.

Wittmann K., *Handbook of Space Technology*, 1st ed. Wiley, 2009.